Developing a Methodology for Optimal Design of the Combined System of Pleated Air Filters and Heating Elements for Filter Disinfection.

By

Ali Mirzazade Akbarpoor

A thesis submitted in partial fulfillment of the requirements for the degree of

Doctor of Philosophy

Department of Mechanical Engineering

University of Alberta

© Ali Mirzazade Akbarpoor, 2026

Abstract

Improper design and operation of heating, ventilation, and air conditioning (HVAC) systems can contribute to the transmission of pathogenic microorganisms in indoor environments. While air filters are traditionally deployed to control airborne pathogens' virulence, they can accumulate microbes over time and become breeding grounds for bacteria and fungi, posing significant biological hazards. To address this challenge, this thesis proposes a novel energy-efficient air disinfection approach that combines air filtration with thermal inactivation by heat. To maintain continuous filtration during operation, the system incorporates two side-by-side filtration units with identical filters that operate in sequence. While one unit undergoes thermal disinfection within an insulated enclosure, the other remains in service.

Three design concepts are developed and evaluated based on their mode of heat transfer and application strategy. The first concept is a fanless configuration that relies primarily on natural convection to disinfect a single-stage filter. The second concept employs forced convection using recirculating warm air to disinfect a single-stage filter. The third concept extends the warm-air-recirculation approach to two-stage filtration systems.

An experimental test rig is constructed to monitor the heat transfer performance of each design and to quantify the time and energy required to achieve the literature-based disinfection condition of maintaining a filter temperature of 65 °C for 10 minutes. Furthermore, a closed-loop aerosol wind tunnel accommodating the prototype of the disinfection unit was constructed to evaluate the system's particle removal efficiency and pressure drop at different duct airflow rates. The setup follows the ASHRAE 26 and 52.2 general requirements for measuring filter efficiency.

To support the design of the natural-convection-based system, Computational Fluid Dynamics (CFD) simulations are first conducted to identify heating-element configurations that promote uniform temperature distribution within the enclosure. The filters are excluded from the computational domain to reduce geometric complexity and computational cost. The 2D unsteady turbulent buoyancy-driven flow is simulated using Ansys Fluent 2023 R2. Five configurations are examined by varying the number of tubular heating elements, their spatial arrangement, and the enclosure geometry through the addition of a heating chamber. The numerical results indicate that incorporating a heating chamber beneath the frame and redistributing the heating elements to enhance preheating and mixing near the bottom of the enclosure significantly reduces temperature non-uniformity. Configurations demonstrating improved thermal uniformity are subsequently selected for experimental investigation with filters.

Next, prototypes of the natural-convection-based system, including a pleated filter with a minimum efficiency reporting value (MERV) of 11 and tubular heating elements, are manufactured and experimentally evaluated. Three configurations are tested over a range of heater set-point temperatures. The results revealed that the optimal configuration substantially reduces thermal non-uniformity across the filter surface, enabling the entire filter to reach the disinfection condition within approximately 35 minutes, with an energy consumption of 0.10 kWh per cycle. Flow characterization tests further demonstrate that the integration of heating elements and associated duct modifications does not significantly affect filtration efficiency and results in only a minor increase in pressure drop during normal operation.

To reduce the disinfection period, prototypes of a forced-convection-based system employing recirculating warm air for disinfecting a single-stage MERV 11 filter were developed. The impacts of warm inlet temperature and air recirculation rate within the disinfection units on the heat transfer performance of the system were experimentally investigated. The results showed that under optimal operating conditions, the filter achieves the disinfection criterion within 13 minutes, with a total energy consumption of 0.11 kWh per cycle. During normal operation, when both units remained open, the system maintained filtration efficiency equivalent to that of a standalone filter, with a negligible increase in pressure drop. During the disinfection period, when one unit was isolated, the submicron particle removal efficiency decreased, while large-particle removal increased, and the pressure drop rose significantly for only a short period, resulting in a minimal impact on the overall HVAC fan energy use.

Finally, the concept of thermal disinfection of single-stage filtration systems with warm-air recirculation was extended to two-stage filtration systems, comprising a MERV 8 pre-filter and either a MERV 11 or a MERV 13 main filter. The heat transfer and filtration performance of the system were evaluated experimentally at three inter-filter distances. A comparison of theoretical correlations for estimating the overall filtration efficiency of multi-stage systems with experimental results showed good agreement in normal operation, with some deviations during the disinfection period due to flow redistribution. Furthermore, changing the inter-filter distance has relatively minor impacts on the overall filtration efficiency and pressure drop compared to its effect on the disinfection process. Consequently, the energy performance of the disinfection system should be considered the primary criterion when determining the optimal distance between the pre-filter and the main filter.

Preface

This thesis is an original work by Ali Mirzazade Akbarpoor. The research was conducted at the University of Alberta Filtration Testing Laboratory (FTL) under the supervision of Prof. Alireza Nouri and the co-supervision of Prof. Mahdi Shahbakhti. The wind tunnel setup was designed in collaboration with Dr. Mahmood Salimi and constructed with the assistance of Dr. Mahmood Salimi, Adib Shabani, and Erfan Rasouli.

The content of each chapter has been fully or partially published or submitted to peer-reviewed journals [1–3]. As the first author, I made substantial contributions to all papers derived from this thesis. The contributions of the co-authors are as follows:

In Chapter 4, Dr. Mahmood Salimi and Adib Shabani collaborated in building the experimental setup.

In Chapters 5 and 6, Dr. Mahmood Salimi and Erfan Rasouli collaborated in building the test apparatus.

Acknowledgement

First and foremost, I would like to express my deepest gratitude to my supervisor, Prof. Alireza Nouri. It has been a great honour to work under his supervision. His professionalism, invaluable scientific feedback, patience, and mentorship made my PhD experience both fruitful and stimulating.

I would also like to sincerely thank my co-supervisor, Prof. Mahdi Shahbakhti, for his invaluable comments and dedication, which helped me reach important milestones throughout my PhD. I am also grateful to Dr. Yuxiang Chen for serving on my supervisory committee and for providing insightful comments that helped improve the quality of this dissertation.

I would like to extend special thanks to Dr. Mahmoud Salimi, who has been both a mentor and a peer coach to me. His good temper, along with his deep knowledge and expertise in various aspects of engineering, continually reassured me that no scientific challenge is unsolvable when approached collaboratively. I would also like to thank my labmates and friends, Adib Shabani and Erfan Rasouli, for their help in building the experimental setup used in this research.

I gratefully acknowledge the financial support provided by the Natural Sciences and Engineering Research Council of Canada (NSERC), Engineered Air, the Alberta Graduate Excellence Scholarship (AGES), the Lab2Market Validate Program, the Flight PS752 Commemorative Scholarship Program, the Alberta Innovates Graduate Student Scholarship (AIGSS), the Sadler Graduate Scholarship, and the Walter and Edith Fryers Graduate Scholarship.

I would like to express my sincerest appreciation to my parents for their endless care and for raising me with a love for science. I am also deeply grateful to my brother for his encouragement and continuous support throughout this journey.

Lastly, I would like to express my heartfelt gratitude to my loving, kind, patient, and supportive wife, Matin, who has stood beside me throughout my academic journey. Her scientific support as a member of our research group and as my co-author, together with her unwavering belief in me, helped me overcome many challenges along the way. I truly owe much of this achievement to her.

This thesis is dedicated to my beloved Matin and to my dear parents in Iran.

Table of Contents

List of Tables

List of Figures

Nomenclature

a_1	model constant in Eq. (3.3)
C	downstream particle concentration ($\mathrm{counts/cm^3}$)
c_P	specific heat capacity ($\mathrm{J/kg}$ K)
D	inter-filter distance (cm)
D_h	hydraulic diameter (cm)
D_P	particle diffusion rate ($\mathrm{m^2/s}$) in the Peclet number formula
D_ω	cross-diffusion term in Eq. (3.5) ($\mathrm{kg/m^3s^2}$)
d_f	filter fiber diameter (μm)
F_2	blending function in Eq. (3.3)
G_k	generation of k ($\mathrm{kg/m\ s^3}$)
G_ω	generation of ω ($\mathrm{kg/m^3s^2}$)
g	gravitational acceleration ($\mathrm{m/s^2}$)
H	filter pleat height (m)
h_{conv}	convection heat transfer coefficient ($\mathrm{W/m^2}$ K)
h_{sp}	specific enthalpy (kJ/kg)
I	identity tensor
K	permeability ($\mathrm{m^2}$)
k	thermal conductivity ($\mathrm{W/m}$ K), or turbulence kinetic energy ($\mathrm{m^2/s^2}$)
L_c	characteristic length (m)
m	mass (g)
n	number of samples
P_{ave}	average particle penetration
p	pressure (Pa)
Q	airflow rate ($\mathrm{m^3/h}$)
R_{ave}	average correlation ratio
S	strain rate magnitude ($\mathrm{s^{-1}}$)
S_k, S_ω	user-defined source terms in Eqs. (3.4) and (3.5)
S_M	momentum sink term ($\mathrm{N/m^3}$)

T	temperature (℃)
t	time (s)
t_0	relaxation time in Stokes number formula (s)
U	upstream particle concentration ($\mathrm{counts/cm^3}$)
V	velocity ($\mathrm{m/s}$)
W	filter pleat width (m)
$\dot{W}_{fan}$	fan power (kW)
Y_k	dissipation of k due to turbulence ($\mathrm{kg/m\ s^3}$)
Y_ω	dissipation of ω due to turbulence ($\mathrm{kg/m^3 s^2}$)
x, y, z	Cartesian coordinate (m)

Greek symbols

α	thermal diffusivity ($\mathrm{m^2/s}$)
α^*	low-Reynolds-number correction coefficient
β	thermal expansion coefficient ($\mathrm{K^{-1}}$)
δ	filter media thickness (m)
ε	media porosity, or turbulent dissipation rate ($\mathrm{m^2/s^3}$)
η	particle size removal efficiency
η_{fan}	fan efficiency in Eq. (5.6)
η_{motor}	motor efficiency in Eq. (5.6)
η_t	overall filtration efficiency in multi-stage filtration systems
μ	dynamic viscosity (Pa s)
μ_t	turbulent viscosity (Pa s)
ν	kinematic viscosity ($\mathrm{m^2/s}$)
ρ	density ($\mathrm{kg/m^3}$)
σ_k, σ_ω	model constants in Eqs. (3.4) and (3.5)
ω	specific dissipation rate ($\mathrm{s^{-1}}$)

Dimensionless terms

Co	Courant number ($V\Delta t/\Delta x$)
Da	Darcy number ($K/{L_c}^2$)
Gr	Grashof number ($g\beta(T_h - T_c){L_c}^3/\nu^2$)
Nu	Nusselt number ($h_{conv}L_c/k$)
Pe	Peclet number ($d_f V/D_P$)
Pr	Prandtl number (ν/α)
Ra	Rayleigh number ($g\beta(T_h - T_c){L_c}^3/\nu\alpha$)
Ra*	Modified Rayleigh number ($g\beta K(T_h - T_c)L_c/\nu\alpha$)
Re	Reynolds number (VL_c/ν)
Ri	Richardson number ($\mathrm{Gr}/\mathrm{Re}^2$)
Stk	Stokes number ($t_0 V/d_f$)

Subscripts

a	air
b	background
c	cold
e	estimated
h	hot
i	sample number
o	observed
s	solid
t	turbulent

Abbreviations

ASHRAE	American Society of Heating, Refrigerating and Air-Conditioning Engineers
BSL	BSL Biosafety Level
CFD	Computational Fluid Dynamics

CFL	Courant Friedrichs Lewy
DBF	Darcy Brinkman Forchheimer
DNS	Direct Numerical Simulation
EEAF	Electrically Enhanced Air Filter
ESP	Electrostatic Precipitator
FDM	Finite Difference Method
FEM	Finite Element Method
FVM	Finite Volume Method
HEPA	High-Efficiency Particulate Air filter
HVAC	Heating, Ventilation, and Air Conditioning
IAQ	Indoor Air Quality
LCT	Liquid Crystal Thermography
LES	Large-Eddy Simulation
LTE	Local Thermal Equilibrium
LTNE	Local Thermal Non-Equilibrium
MERV	Minimum Efficiency Reporting Value
OPC	Optical Particle Counter
PCM	Phase Change Material
PID	Proportional Integral Derivative
PIV	Particle Image Velocimetry
PM	Particulate Matter
PV	Photovoltaic
RANS	Reynolds-Averaged Navier-Stokes model
RNA	Ribonucleic Acid
SST	Shear Stress Transport
UV	Ultraviolet irradiation
UVGI	Ultraviolet Germicidal Irradiation
VOC	Volatile Organic Compound
WHO	World Health Organization

Chapter 1. Introduction

1.1 Overview and Problem Statement

Airborne pathogens are responsible for the spread of the most recent pandemics, such as H1N1 flu (swine flu) and the new coronavirus (SARS-CoV-2) and its highly transmissible variants (Delta and Omicron) [4–6]. The virulence of infectious and lethal diseases is rising due to globalization, increased travel and trade, urbanization, populated cities, changes in human behavior, reviving pathogens, and improper use of antibiotics [7]. The health and economic repercussions of pandemics are devastating [8]. For instance, according to the World Health Organization (WHO) record [9], more than 700 million COVID-19 cases were reported globally by the end of 2023, resulting in the death of approximately seven million individuals.

Respiratory activities such as breathing, speaking, coughing, and sneezing release pathogen-laden droplets and aerosols into indoor environments [10]. In enclosed spaces, these airborne contaminants can persist and be transported by airflows, making indoor air quality a critical factor in infection risk [11,12]. Heating, ventilation, and air conditioning (HVAC) systems play a key role in shaping indoor exposure, as ventilation rates, air recirculation, and airflow pathways can either mitigate or facilitate the transmission of airborne microorganisms [13,14]. Consequently, the design and operation of HVAC systems have received heightened attention as engineering controls for reducing airborne disease transmission, particularly in high-risk environments such as healthcare facilities.

Air filtration is one of the most widely implemented strategies within HVAC systems for controlling airborne contaminants [15]. Filters are effective at physically removing microorganisms from the air stream and are routinely employed in residential, commercial, and institutional buildings [16]. However, filtration is inherently a removal-based strategy and does not inactivate captured microorganisms. As a result, filters may accumulate viable biological material over time, raising concerns regarding their potential role as secondary sources of contamination during operation, maintenance, or disposal [12,17]. These limitations highlight the need for complementary approaches that address not only particle capture but also microbial inactivation within HVAC systems.

To overcome the shortcomings of filtration-only approaches, supplementary air-disinfection technologies have been proposed to inactivate microorganisms and reduce the risk of microbial accumulation [18]. Among the available inactivation methods, thermal treatment is particularly attractive due to its broad effectiveness against a wide range of bacteria, fungi, and viruses. Heat can penetrate porous media and inactivate microorganisms by denaturing essential proteins and enzymes [19–21]. While thermal inactivation has been widely used in non-aerosol applications, its integration into HVAC systems for disinfecting filters remains limited, largely due to concerns related to energy consumption, pressure drop, and system-level feasibility at the building scale.

To address the limitations of filtration-only approaches while maintaining continuous HVAC operation, this thesis investigates an integrated filtration–disinfection concept based on alternating modes of operation. The working principle of the proposed system is illustrated schematically in Figs. 1.1 to 1.3. As shown in Fig. 1.1, the device consists of two identical filtration units arranged side by side within a shared HVAC section. As can be seen in Fig. 1.2., each unit contains a pleated air filter housed within an enclosed frame equipped with heating elements.

During normal operation (Fig. 1.1a), both units remain open, allowing air to pass through the filters in parallel. This condition, referred to as the open-gates mode, where the dominant performance metrics are airflow characteristics, pressure drop, and particle removal efficiency. After a prescribed filtration period, one of the two units is temporarily isolated by closing its inlet and outlet gates, while the other unit remains open and continues filtering the incoming air. This condition defines the closed-gates mode, as illustrated in Fig. 1.1b.

In the closed-gates mode, airflow through the isolated unit is interrupted, and the heating elements are activated to raise the temperature of the enclosed filter to a level sufficient for microbial inactivation. The objective is to achieve the required disinfection temperature and exposure time directly on the filter media where microorganisms have accumulated, while preventing excessive heat from being released into the HVAC ductwork. By alternating the roles of the two units between open-gates and closed-gates modes, the system enables continuous air filtration alongside periodic thermal disinfection without requiring system shutdown or bypass (Fig. 1.3).

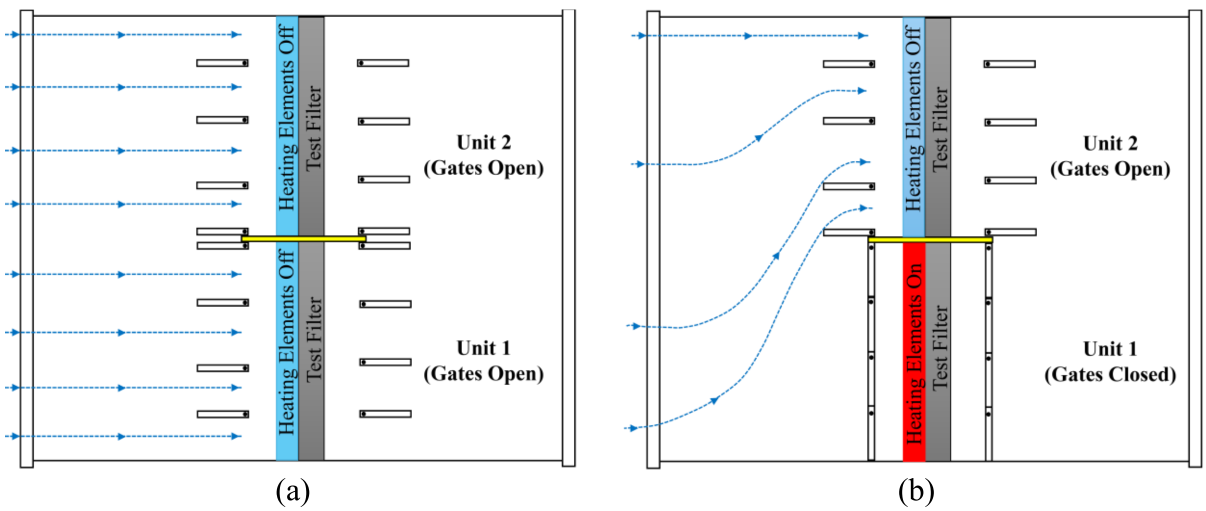

Fig. 1.1. A schematic view of the working principle of the disinfection technology proposed in the present thesis under two operation modes (a) open-gates mode, where two units remain open, and (b) closed-gates mode, where a single unit is isolated for disinfection.

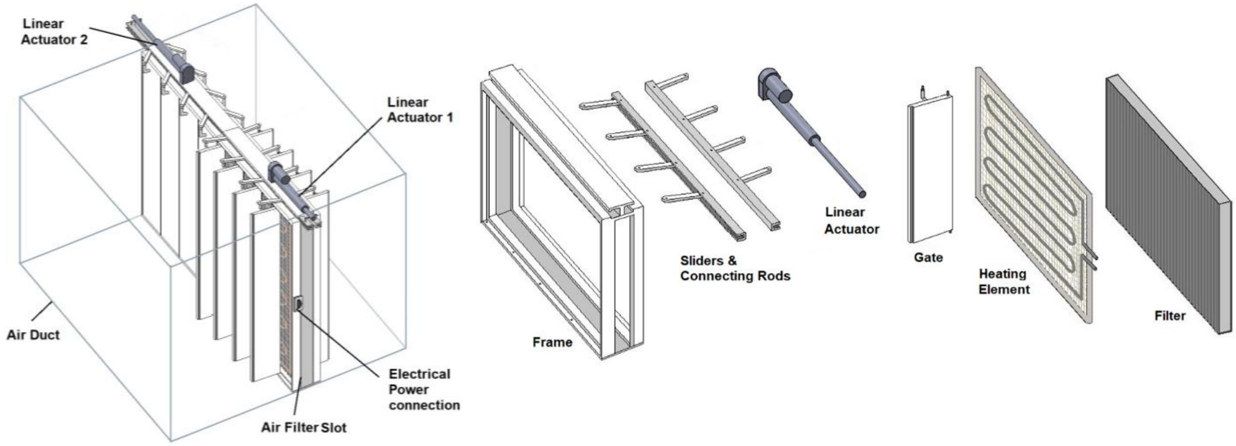

Fig. 1.2. Different elements of the disinfection system.

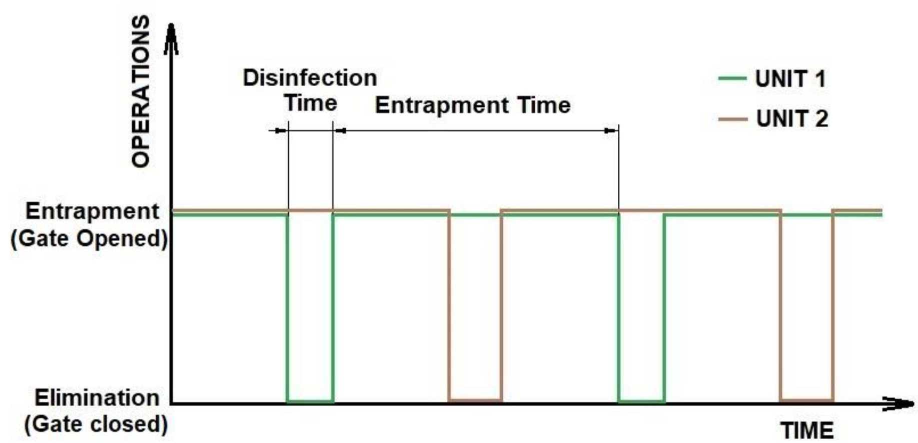

Fig. 1.3. Sequential entrapment-disinfection by filtration and heat application.

1.2 Research Questions

This thesis aims to answer the following research questions:

1. How do heating element arrangement and enclosure configuration impact temperature uniformity, energy consumption, and airflow resistance during thermal disinfection of HVAC filters?

2. To what extent does the application of the proposed technology affect the particle removal efficiency and pressure drop during the normal operation and disinfection period?

3. Is reliance on the buoyancy-driven flow sufficient to achieve uniform filter disinfection within a reasonable time frame, or is the integration of forced convection through external power/fans required to enhance disinfection efficiency and uniformity?

1.3 Research Objectives

The roadmap of this thesis to address the above research questions includes the following objectives:

- Assessing the feasibility of using buoyancy-driven heat transfer for achieving spatially uniform and energy-efficient thermal disinfection of pleated HVAC filters.
- Quantifying the impacts of system configuration, filter characteristics, and operating conditions on thermal performance, airflow characteristics, and particle removal efficiency during both open- and closed-gates modes.
- Developing practical design guidelines for integrating filter-level thermal disinfection technologies into HVAC duct systems without compromising ventilation performance.

1.4 Research Hypothesis

This section discusses the hypotheses related to the aforementioned research questions:

- Increasing the number of heating element tubes on the bottom side of the heating unit can achieve a more uniform temperature on the filter surface, counteracting the temperature difference caused by buoyancy-driven flow.

- For a given heating power, increasing the number of heating element passes reduces the required thermal exposure time but may introduce additional pressure losses and airflow non-uniformities, suggesting the existence of an optimal range of heating element passes.
- Given the low thermal conductivity of the solid matrix of the filter's porous media (e.g., non-woven polyester fibres) and the inherent temperature difference caused by buoyancy-driven flow, especially when the number of heating element passes is low, a significant temperature variation across the filter is expected. To mitigate this temperature difference between the top and bottom sides and the front and back faces of the filter, deploying air recirculation and leveraging forced convection can promote a more uniform temperature distribution across the filter surface, reducing the disinfection time.
- The time and energy required for thermal disinfection are expected to increase for filters with higher Minimum Efficiency Reporting Values (MERV) due to their lower porosity, higher pleat density, and higher thermal inertia.

1.5 Research Methodology

This thesis employs a combination of numerical simulations and experimental investigations to evaluate the stated hypotheses and address the research questions. Although the core concept of the proposed technology is heat-based disinfection of filters, three distinct system configurations are investigated: (i) a fanless system that relies solely on natural convection as the dominant heat-transfer mechanism for disinfecting a single filter; (ii) a forced-convection system employing fans and warm-air recirculation for disinfecting a single filter; and (iii) a warm-air-recirculation system, similar to the second system, designed for disinfecting a two-stage filtration system.

Computational Fluid Dynamics (CFD) simulations are conducted to examine various heating element and unit configurations for the fanless variant to identify arrangements providing improved temperature uniformity within the enclosure. For this purpose, computational domains are generated for all cases, and the full set of governing conservation equations is discretized and solved using Ansys Fluent 2023 R2. The heating element configuration identified through the numerical investigation provides the basis for the design and fabrication of the natural-convection-based (fanless) disinfection prototype accommodating HVAC filters.

The experimental component of this research consists of two main parts: (1) evaluation of the thermal and energy performance of the proposed disinfection system, and (2) assessment of filtration efficiency and pressure drop using a closed-loop aerosol wind tunnel.

The heat transfer and energy performance evaluation involves constructing physical prototypes of the disinfection system and developing a dedicated test facility equipped with temperature control, monitoring instrumentation, and energy-measurement capabilities.

The experimental evaluation of size-resolved particle removal efficiency and pressure drop is conducted using a fully recirculating closed-loop aerosol wind tunnel designed in accordance with ASHRAE 52.2 [22]. All developed prototypes are installed in the wind tunnel, and their performance is assessed under two operating conditions: normal operation, in which both units remain open, and disinfection mode, in which one unit is temporarily isolated.

Figure 1.4 presents an overview of the research methodology adopted in this thesis. As illustrated, the study begins with an in-depth literature review to identify existing research and technological gaps. This is followed by numerical simulations and experimental investigations of heat transfer, filtration efficiency, and pressure drop. The outcomes of these analyses are synthesized to establish practical design considerations for achieving energy-efficient, uniform filter disinfection with minimal airflow resistance.

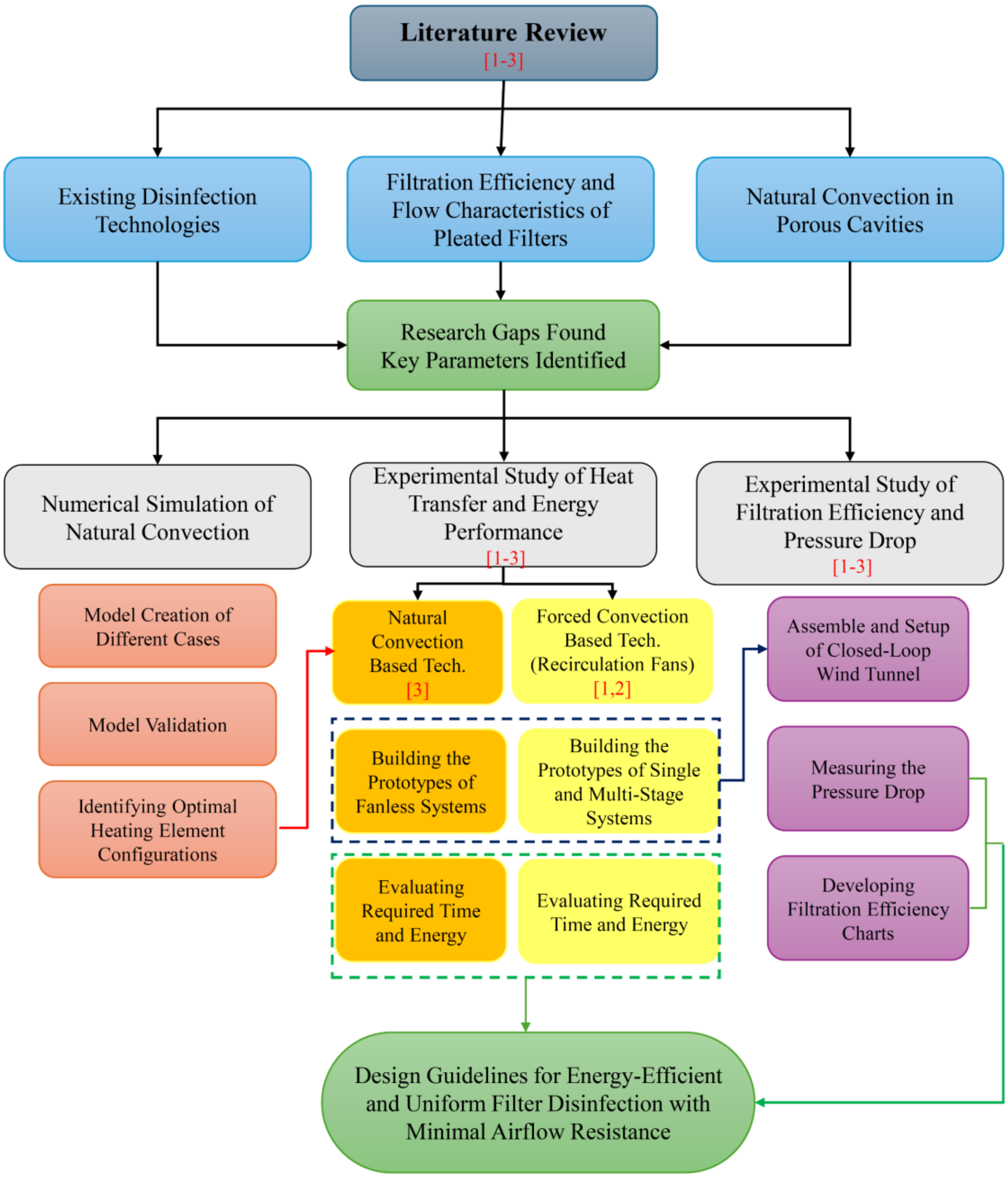

Fig. 1.4. Overall research methodology of this thesis.

1.6 Thesis Outline

This thesis follows a paper-based format and consists of seven chapters. The content of each chapter is briefly outlined below.

Chapter 1 presents an overview of the research background and problem statement, followed by the formulation of the research questions, objectives, hypotheses, methodology, and the overall structure of the thesis.

Chapter 2 provides a comprehensive literature review on the motivation for HVAC filter disinfection and existing air disinfection technologies, with a particular focus on heat-based disinfection approaches. The literature is organized into two mode-specific sections: one addressing flow performance and filtration metrics under open-gates operation, and the other focusing on natural convection and heat transfer phenomena relevant to closed-gates operation. The chapter concludes by identifying research gaps and summarizing the novelty and contributions of this thesis.

Chapter 3 focuses on the numerical simulation of buoyancy-driven flow in an enclosure containing tubular heating elements. This chapter presents the details of the CFD simulation, including model selection, mesh sensitivity analysis, and model validation. The numerical results provide the basis for the design of the fanless disinfection system investigated experimentally in Chapter 4.

Chapter 4 experimentally investigates the natural-convection-based thermal disinfection of HVAC filters. This chapter describes the experimental setup and procedures used to evaluate the heat-transfer performance and filtration efficiency of the fanless system.

Chapter 5 experimentally studies the forced-convection configuration employing fans and warm-air recirculation for disinfecting a single filter. The experimental setup and procedures for evaluating heat transfer performance, energy consumption, filtration efficiency, and pressure drop are presented in this chapter.

Chapter 6 experimentally evaluates the feasibility of warm-air recirculation in a two-stage HVAC filtration system comprising a low-MERV pre-filter and a higher-MERV main filter. This chapter introduces the advanced experimental facilities developed for this purpose, including a fully recirculating closed-loop aerosol wind tunnel compliant with ASHRAE Standard 52.2, as well as the heat-transfer performance setup for two-stage filter disinfection.

Chapter 7 summarizes the key findings of this thesis, discusses its limitations, and provides recommendations for future work.

Chapter 2. Literature Review & Research Gaps

2.1 Preface

As described in Chapter 1, the proposed disinfection technology in this thesis operates in two distinct modes: open-gate mode and closed-gate mode. In the open-gate mode, when the gates are open, the dominant performance metrics are flow characteristics, pressure drop, and particle removal efficiency. In contrast, during the closed-gate mode, the airflow is interrupted, and the heating elements are activated, transforming the problem into one governed by buoyancy-driven flow and heat transfer within an enclosure containing pleated porous media and external heat sources. Accordingly, the literature reviewed in this chapter is structured to provide background information relevant to both operating modes.

The discussion first establishes the motivation for filter disinfection and reviews existing disinfection technologies, with emphasis on hybrid filtration-disinfection approaches. The review then addresses the fundamental considerations associated with heat-based disinfection. Finally, the literature is organized into two mode-specific sections: one focusing on flow performance and filtration metrics under open-gate operation, and the other focusing on natural convection and heat transfer phenomena relevant to closed-gate operation.

Detailed reviews of specific configurations, numerical models, and experimental implementations are intentionally retained within the corresponding paper-based chapters to preserve their integrity as standalone studies. This chapter therefore, serves as a unifying framework that connects the broader research landscape to the individual contributions presented in the subsequent chapters.

2.2 Microbial Contamination of HVAC Filters

Installation of air filters in HVAC ductwork, as shown in Fig. 2.1, is the classical approach for controlling the virulence of airborne pathogens and reducing the concentration of bioaerosols in indoor environments [15]. Depending on their efficiency and structural characteristics, air filters can effectively entrap microorganisms through mechanisms such as diffusion, interception, and inertial impaction [23,24]. For instance, high-efficiency particulate air (HEPA) filters are capable of removing up to 99.97% of particles with a diameter of 0.3 µm, which corresponds to the most penetrating particle size among submicron aerosols [16].

Despite these advantages, air filters do not eliminate microorganisms; rather, they accumulate them over time (Fig. 2.2). As filters load with dust and organic matter, they may provide suitable conditions for microbial survival and growth, particularly when exposed to suitable temperature and humidity levels [12,17]. Consequently, contaminated filters can transition from passive removal devices to active reservoirs of biological material, raising concerns regarding their role as secondary sources of indoor contamination. Depending on filter type, loading condition, and airflow regime, a fraction of captured microorganisms may be re-entrained into the downstream air during normal operation [25,26]. Under transient operating conditions, such as fan start-up, shut-down, or sudden changes in airflow rate, this release can increase substantially [27,28]. Such episodic release events may lead to short-term spikes in bioaerosol concentration, increasing occupant exposure risk.

Given that filtration is only a removal strategy, not an "inactivation" approach, the microbe accumulation problem persists. Therefore, supplementary disinfection technologies should be adopted to inactivate microbes, prevent the creation of a medium for pathogen multiplication, and reduce the risk of episodic germ release into the building. This is particularly important during pandemics and in critical settings such as hospitals, clinics, and dental offices, where airborne pathogen concentrations may be high.

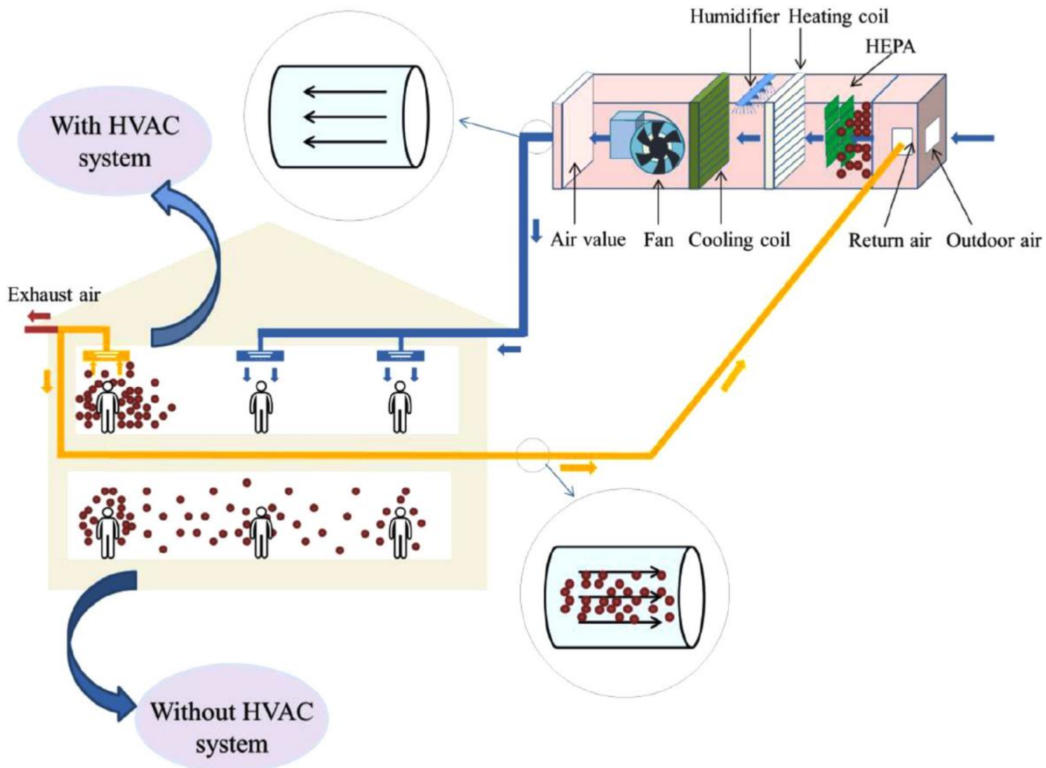

Fig. 2.1. A schematic view of controlling the virulence of airborne pathogens via filtration in HVAC systems (adapted from Ref. [15]).

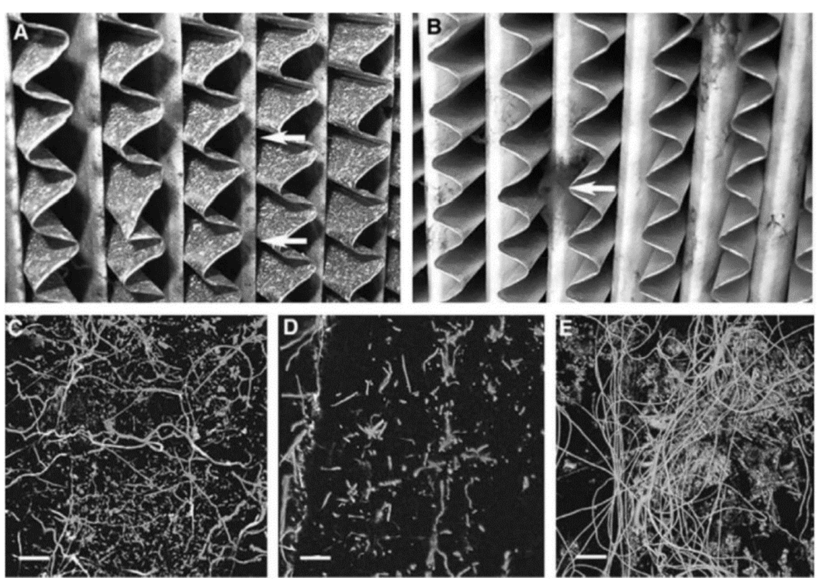

Fig. 2.2. Growth of microbes on the HEPA filters over time (adapted from Ref. [12]).

2.3 Overview of Air Disinfection Technologies

2.3.1 Standalone Air Disinfection Technologies

Several sterilization approaches have been introduced in the literature for the removal/inactivation of infectious microorganisms. A schematic view of different disinfection technologies available in the literature is illustrated in Fig. 2.3. These purification technologies can be categorized into physiochemical and biochemical technologies based on the inactivation mechanisms used in the sterilization process. The physiochemical technologies include conventional filters [17,29–31], electrostatic filters [12,29,32,33], antimicrobial filters [34–37], ultraviolet (UV) sterilization [34,38–41], photocatalysis oxidation [30,42–44], plasma [29,45–47], thermal treatment [48–50], ozonation [51–53] and microwave [30,54,55]. However, implementing botanical disinfectants [56–58] and herb fumigation [11,41,42] falls under the biochemical category and is less frequently applied in HVAC systems due to challenges associated with controllability, scalability, and standardization. A detailed comparison of these disinfection technologies and their capabilities in terms of pathogen removal or inactivation is provided in Chapter 5 of this thesis.

Notwithstanding the merits of standalone air disinfection technologies documented in the literature, their implementation is associated with high investment costs, high energy consumption, harmful byproducts, complex installation and maintenance, and long-term efficiency degradation. As a result, despite their technical potential, many standalone disinfection technologies remain difficult to deploy widely in continuously operated, occupied buildings [1,59,60].

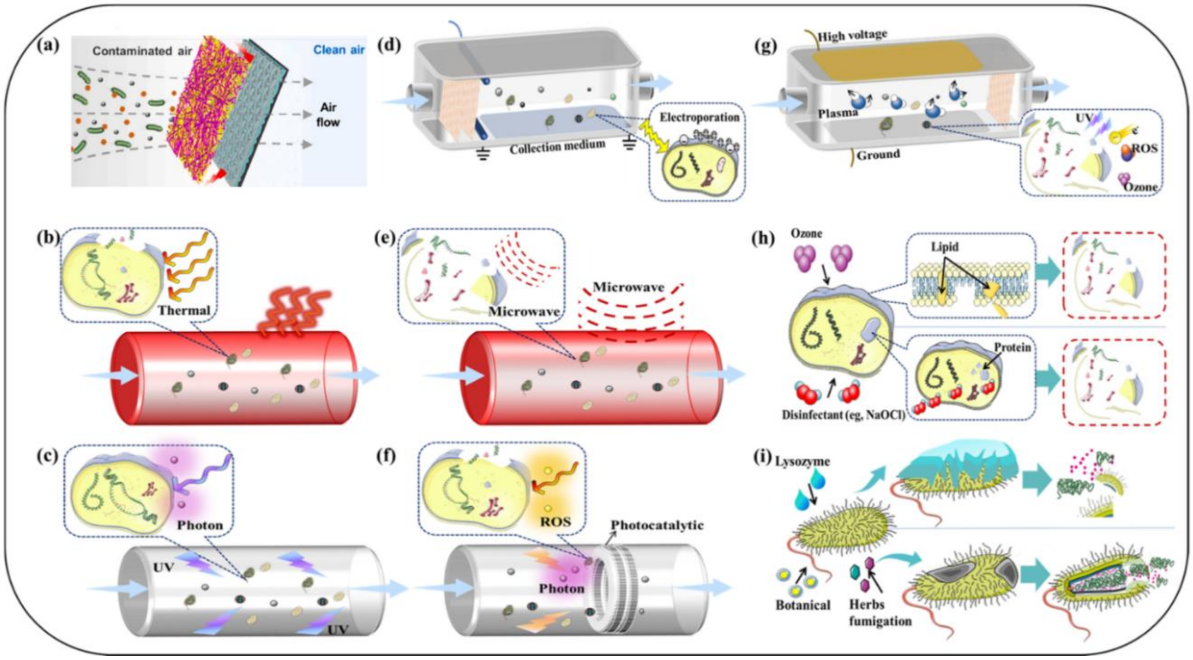

Fig. 2.3. A schematic representation of different disinfection technologies including (a) antimicrobial filtration, (b) thermal treatment, (c) UV, (d) electrostatic, (e) microwave, (f) photocatalysis, (g) plasma, (h) ozonation, and (i) botanical disinfectant and herbs fumigation (reproduced from Ref. [29]).

2.3.2 Filter-Assisted Hybrid Disinfection Technologies

Recognizing that HVAC filters serve as primary locations for microbial accumulation, various antibacterial and antiviral agents, such as quaternary ammonium phosphate, copper, nano-silver, carbon nanomaterials, and metal oxides (e.g., ZnO and TiO_2), have been extensively studied to inhibit microbial growth on filters [5]. However, their practical application remains limited due to material compatibility concerns and performance degradation over time [61]. Consequently, supplementary disinfection technologies have been hybridized with filtration to address the issue of filter colonization. The most common filter-assisted sterilization technologies in HVAC systems include electrostatic precipitators (ESPs), ultraviolet (UV) irradiation, photocatalysis, plasma-based systems, and thermal treatment for the decontamination of air filters.

The integrated system of an electrostatic precipitator (ESP) and an air filter utilizes corona discharge to enhance the physical removal of charged particles through Coulombic forces while simultaneously inactivating bioaerosols trapped within the filter by generating ions [62–64]. Feng et al. [62] developed a numerical model demonstrating that a well-designed hybrid system combining an electrically enhanced air filter (EEAF) with an ESP could achieve 100% disinfection of COVID-19, with a particle removal efficiency comparable to that of high-efficiency particulate air (HEPA) filters. However, the implementation of ESPs presents several challenges. One of the primary concerns is ozone generation, as ozone exposure is linked to respiratory and cardiovascular health risks, increased mortality, and the formation of secondary organic byproducts that can be even more hazardous than ozone [65,66]. Other drawbacks of ESP-based systems include high initial and maintenance costs, safety risks associated with high-voltage operation, the need for periodic component replacement, and the uncertainty regarding the ability of released ions to effectively penetrate the inhomogeneous porous structure of filters for inactivating entrapped particles [67,68]. These limitations must be carefully considered when designing combined ESP and air filtration systems.

The integrated system of ultraviolet (UV) light and air filters utilizes UV radiation to denature the DNA and RNA of bioaerosols accumulated on the filter surface and captured within the filter media. Numerous studies in the literature have examined the feasibility of UV-C lamps for disinfecting both HEPA and non-HEPA pleated filters [61,69]. Feng et al. [62] conducted computational fluid dynamics (CFD) simulations to evaluate the performance of a hybrid system combining UV lamps with pleated filters for inactivating SARS-CoV-2 aerosols trapped within the filter. Their findings indicated that the UV + filter system achieved 100% inactivation of COVID-19 bioaerosols at an airflow rate of 2120 cfm, with an energy consumption of 483 W. However, the integrated UV system with air filters has its own limitations. Susceptibility of UV lamps to the relative humidity [18], inaccessibility of UV light to the particles entrapped within dense porous media of filters [70], decrease in inactivation rate by an increase in the duct flow rate, and high energy consumption [18,62] are some of the challenges associated with the UV + filter system that should be tackled in the future development of this technology.

The hybridization of photocatalysis with filtration is another innovative approach explored in the literature. In photocatalysis, reactive oxygen species are generated under light exposure, acting as strong oxidants that destroy pathogens trapped within the filter [71,72]. ZnO and TiO_2 are commonly used photocatalysts, typically applied as coatings on filter fibers. However, their disinfection efficiency decreases at higher airflow rates, and their antibacterial effectiveness is limited when using sunlight as the light source, mandating integration with UV light for enhanced performance [71,73]. To address the challenges of common photocatalysts, Li et al. [71] proposed photocatalytic air filters fabricated from metal-organic frameworks (MOFs). The developed photocatalytic filter achieved 99.99% E. coli decontamination within 30 minutes and removed 97% of particulate matter (PM). Despite the effectiveness of employing filters with photocatalytic properties, ozone generation remains a major concern, posing challenges to the practical application of this technology in improving indoor air quality (IAQ) [74].

The hybrid system of plasma and air filtration utilizes corona discharge to generate ions capable of annihilating bioaerosols trapped within filter pores [18,75]. Hyun et al. [75] investigated the use of plasma for disinfecting MS2 bioaerosols filtered by a fiberglass filter. Their findings indicated that, in the bipolar mode of the ionizer, disinfection efficiency could reach 97.4% after 45 minutes of exposure. Li et al. [76] designed and evaluated a portable air purification system that integrates a corona discharge array (plasma) with metallic foam filtration. To mitigate ozone generation, a carbon filter was installed at the system's outlet. Their results demonstrated that the proposed device achieved a filtration efficiency of 91.5% and an antiviral efficiency of 99.32% in removing Influenza H1N1 bioaerosols after one hour of operation in a 50 m^3 test room. While the integration of filtration and plasma has shown promising results in portable air purifiers, ozone generation and ion byproducts remain significant concerns [18,75,77]. Furthermore, the application of this technology at larger scales and in centralized HVAC systems with high airflow demands requires further research and development, as it is associated with increased energy consumption and greater ozone byproduct production.

While the hybrid disinfection technologies discussed above demonstrate that filter-assisted inactivation of microorganisms can be highly effective, they also highlight persistent challenges related to energy demand, byproduct formation, scalability, and compatibility with continuous HVAC operation [59]. These approaches are therefore not pursued further in this thesis. Instead, the present work focuses on heat-based disinfection of HVAC filters, which offers broad-spectrum microbial inactivation without reliance on electrical discharges, ultraviolet radiation, or reactive chemical species. Heat-based approaches and their relevance to filter disinfection are discussed separately in the following section.

2.3.3 Filter-Assisted Heat-Based Disinfection Technologies

Among the various disinfection strategies discussed in the literature, heat-based inactivation has emerged as a particularly robust and broadly effective mechanism for microbial control [2,59,78]. Thermal disinfection relies on exposure to elevated temperatures that disrupt cellular membranes, denature proteins, and deactivate essential enzymes [19–21]. Unlike chemical, ultraviolet, or plasma-based approaches, heat-based disinfection does not depend on reactive species or electromagnetic radiation and therefore avoids the generation of harmful chemical byproducts during operation. Furthermore, heat has an excellent capability to penetrate the porous structure of the filters, exposing microorganisms trapped within the interior of the filter to lethal temperature–time conditions [2,59].

Another major advantage of heat-based disinfection is its broad applicability across different classes of microorganisms. Previous studies have shown that maintaining temperatures of 60–70 °C for about 10 minutes effectively inactivates vegetative bacteria, fungal spores, and enveloped viruses, including influenza and coronaviruses [29,79–85]. A detailed comparison of the required temperatures and exposure times for inactivating various microorganisms is provided in Chapter 5. While the exact thermal inactivation conditions vary across species, these temperature–time ranges provide a practical basis for thermal disinfection strategies compatible with HVAC applications.

Despite the demonstrated effectiveness of thermal inactivation, applying heat-based disinfection in HVAC systems poses practical challenges when continuous operation and system integration are considered. Several studies have explored filter-assisted thermal concepts in which elevated temperatures are generated locally and interact directly with the filtration process. Xie et al. [86], for example, proposed a hybrid thermal disinfection system that combined air filtration with a photovoltaic (PV) panel and a Trombe wall for the inactivation of *Klebsiella pneumoniae*. In their configuration, a portion of the bioaerosols was exposed to elevated temperatures within the Trombe wall air gap, while the remaining microorganisms were captured by a filter installed at the wall outlet. The continuous passage of warm air through the filter further inhibited bacterial survival and growth. Their numerical analysis showed that, under an average ambient temperature of 9.7 °C and a solar irradiance of 620.6 W/m², the air temperature at the Trombe wall outlet could reach approximately 75 °C, resulting in a substantial reduction in the concentration of pathogens retained within the filter over several hours of daytime operation. While this study demonstrated the feasibility of integrating passive thermal sources with filtration, the disinfection process remained highly dependent on environmental conditions and required extended exposure times.

An alternative filter-assisted thermal approach involves heat generation within the filter media. Yu et al. [87] developed a self-heating air filter fabricated from pleated nickel foam for the inactivation of SARS-CoV-2 and *Bacillus anthracis* spores. By applying Joule heating directly to the conductive filter medium, the authors demonstrated that increasing the filter temperature to approximately 200 °C resulted in inactivation efficiencies of 99.98% for the coronavirus and 99.99% for anthrax spores. However, achieving this temperature for a relatively small filter (24 cm × 30 cm × 1.6 cm) at an airflow rate of 10 L/min (0.35 cfm) required a power input of 500 W. In addition, key performance metrics relevant to HVAC applications, such as pressure drop and scalability to higher flow rates, were not reported.

These examples illustrate that, while filter-assisted heat-based disinfection can achieve high levels of microbial inactivation, existing implementations often rely on elevated temperatures, low airflow rates, or high energy input, highlighting the need for further investigation into energy-efficient, scalable, and HVAC-compatible thermal disinfection strategies.

The review presented in Sections 2.1–2.3 has established the motivation for filter disinfection and summarized existing disinfection technologies, with particular emphasis on filter-assisted and heat-based approaches. While these studies primarily focus on disinfection mechanisms, the practical implementation of such technologies in HVAC systems is inherently affected by system operation and the associated flow and heat transfer characteristics. As introduced in Chapter 1, the disinfection concept introduced in this thesis involves two distinct operating modes. Accordingly, the following sections review literature relevant to these operating conditions, beginning with filtration performance under open-gates mode and followed by buoyancy-driven flow and heat transfer phenomena under closed-gates conditions.

2.4 Open-Gates Mode: Flow Characteristics and Filtration Performance

The optimum performance of filters hinges on the particle removal efficiency and pressure drop. The optimal filter can provide desirable particle collection with minimal airflow resistance. The application of flat filters would impose excessive pressure drop, increase fan energy consumption, reduce filter efficiency, and accelerate filter aging [88,89]. To address these issues, pleated air filters are frequently employed in HVAC systems and air purifiers, in automobile engine intakes, and as protective masks in firefighting, the military, and chemical laboratories, etc. [90]. Implementing pleated geometries increases the filter surface area, reducing the filter face velocity and, therefore, improving particle collection [91]. Different fibrous media made of glass [92,93], polypropylene [94], polyester [95], and cellulose [93] fibers with different fiber diameters and permeabilities were considered as the filter media to provide the aimed efficiency.

Many researchers have used empirical studies, analytical approaches, and numerical simulations to examine the impact of geometric modifications to the pleat on the pressure drop, flow characteristics, and particle removal efficiency of unused pleated filters. Tronville & Sala [88] experimentally and numerically investigated the pressure drop within triangular pleated air filters. They demonstrated that the curve relating the number of mini-pleats to pressure drop within the filter media at different airflow rates was U-shaped. Consequently, increasing the pleat counts may not necessarily reduce the filter's pressure drop. Rebaï et al. [96] developed a semi-analytical 1-D model based on the similarity solution to determine the optimal pleat density for minimizing the airflow resistance. Their model benefits from the consideration of both pleat height and pleat density. However, they did not consider the impact of pleat density variation on particle penetration. Théron et al. [95] deployed Ansys Fluent software to evaluate the effect of varying the height and width of rectangular pleats on the pressure drop. It was observed that reducing the pleat height and increasing its width decreased the pressure drop.

Whether the filter is unused or contains dust layers [60], selecting the appropriate computational domain and airflow model to simulate flow characteristics in the vicinity of the pleated filters can be problematic. In most studies in the literature (e.g., [80,82–85]), a half or single pleat was selected as the 2-D computational domain due to the pleats' inherent symmetry. This is due to the complex geometry of pleated filters, in which the filter thickness is by far smaller than the filter height and width (Fig. 2.4). Therefore, although the simulation of all pleats as 3-D computational domains may evaluate the border effects more accurately [88,90], it increases the computational costs significantly. Furthermore, the airflow conditions within the duct and at the filter face, as well as the filter media properties, determine which models should be adopted to simulate airflow around and inside the pleated filters.

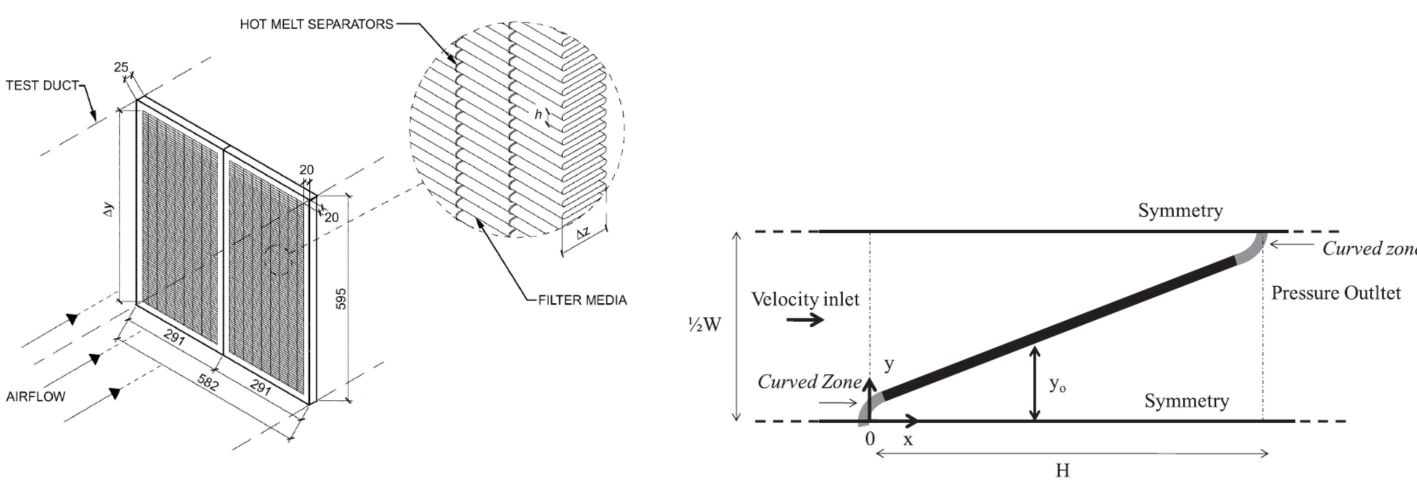

Fig. 2.4. Consideration of a half pleat for simulation of pressure drop and filtration efficiency in pleated air filters (adapted from Refs. [88] and [89]).

Table 2.1 summarizes studies on the flow characteristics, pressure drop, and particle penetration in the vicinity of pleated filters as porous media. In summary, several factors influence the pressure drop and particle removal efficiency of pleated air filters, including filter thickness, pleat density, pleat height and depth, airflow rate, filter face velocity, filter media thickness, and fibrous material properties. Understanding these factors is crucial for balancing filtration efficiency and pressure drop, resulting in more efficient, cost-effective systems.

Table 2.1. A summary of the literature on the pressure drop, flow characteristics, and particle removal efficiency of pleated air filters.

Filter Media Properties	**Geometrical Feature**	**Flow Characteristics**	**Computational Domain**	**Reference**
Cellulose fiber $K = 3.80 \times 10^{-11} m^2$ $\varepsilon = 0.8$	Pleated filters, triangular shaped, rectangular shaped: $H = 27 - 48\ mm$ $W = 2.0 - 3.5\ mm$	Laminar flow $V_{filtration}$= 0.07 $m\ s^{-1}$	2D 1/2 pleat	Del Fabbro et al. (2002) [93]
HEPA media (glass fiber) $K = 1.19 \times 10^{-12} m^2$ $\varepsilon = 0.92$	Pleated filters, triangular shaped, rectangular shaped: $H = 27 - 48\ mm$ $W = 2.0 - 3.5\ mm$	Laminar flow $V_{filtration}$ = 0.07 $m\ s^{-1}$	2D 1/2 pleat	Del Fabbro et al. (2002) [93]
$\delta = 0.38\ mm$ $K = 7.5 \times 10^{-12} m^2$	Pleated filters, triangular shaped: $H = 25\ mm$ $W = 3.2\ mm$	Turbulence models: RSM, Standard k-ε, RNG k-ε V_{inlet} = 0.5-2.0 $m\ s^{-1}$	3D and 2D 3.5 pleat	Tronville et al. (2003) [88]
$\delta = 1.45\ mm$ $K = 3.6 \times 10^{-10} m^2$	Pleated filters, triangular shaped, rectangular shaped: $H = 51\ mm$ $W = 12.5\ mm$	Laminar flow V_{inlet} = 0.39 $m\ s^{-1}$	1D semi-analytical solution and 2D numerical simulation	Rebaï et al. (2010) [96]

Note: K denotes the filter permeability; ε is the porosity; d_f is the fiber diameter; δ is the filter media thickness; H and W represent the pleat height and width, respectively; V_{inlet} is the duct inlet velocity; and $V_{filtration}$ is the filtration velocity, defined as the volumetric flow rate divided by the filtration face area.

Table 2.1. A summary of the literature on the pressure drop, flow characteristics, and particle removal efficiency of pleated air filters (continued).

Filter Media Properties	Geometrical Feature	Flow Characteristics	Computational Domain	Reference
HEPA media $\delta = 0.38\ mm$ $\varepsilon = 0.90 - 0.96$ $d_f = 6 - 15\ \mu m$	Pleated filters, triangular shaped, rectangular shaped: $H = 25.4\ mm$ $W = 1.3 - 8.5\ mm$	Laminar flow V_{inlet} = 0.2-0.1 $m\ s^{-1}$	2D 1 pleat	Fotovati et al. (2012) [92]
Polypropylene media $\delta = 0.30\ mm$ $K = 8.33 \times 10^{-13} m^2$	Pleated filters, rectangular shaped: $H = 50\ mm$ $W = 50\ mm$	Turbulence models: v2f, LES, DES, Standard k-ε, LRN k-ε V_{inlet} = 0.13 $m\ s^{-1}$ $V_{filtration}$= 0.072 $m\ s^{-1}$	2D 1/2 pleat	Feng et al. (2014) [94]
Coarse filter made of cotton and polyester fiber: $\delta = 2.8 \pm 0.7\ mm$ $K = 10^{-9} m^2$ $d_f = 13.8 \pm 4.4\ \mu m$ $\varepsilon = 0.92 \pm 0.010$	Pleated filters, triangular shaped: $H = 20 - 40\ mm$ $W = 50\ mm$	Turbulence models: Standard k-ε model and the Reynolds stress model (rsm) V_{inlet} = 0.6-5.6 $m\ s^{-1}$ $V_{filtration}$=0.09-0.81$m\ s^{-1}$	2D 1/2 pleat	Théron et al. (2017) [95]
$\delta = 0.6\ mm$ $K = 10^{-12} m^2$ $d_f = 3.14\ \mu m$ $\varepsilon = 0.92 \pm 0.010$	Pleated filters, triangular shaped: $H = 27 - 29\ mm$ $W = 24 - 26\ mm$	Turbulence models: Laminar model, the standard k-ε turbulence model and the transition SST model V-inlet = 0.67 $m\ s^{-1}$ $V_{filtration}$ = 0.27 $m\ s^{-1}$	2D 1/2 pleat	Mrad et al. (2021) [89]
$\delta = 0.6\ mm$ $K = 9.58 \times 10^{-12} m^2$ $d_f = 4.6\ \mu m$ $\varepsilon = 0.92 \pm 0.010$	Pleated filters, triangular shaped, rectangular shaped: $H = 20\ mm$ $W = 5.6 - 28\ mm$	Laminar model $V_{filtration}$ = 0.04 $m\ s^{-1}$	2D 1 pleat Periodic BC	Teng et al. (2022) [91]
Polyester fiber $\delta = 0.5\ mm$ $K = 1.92 \times 10^{-10} m^2$	Pleated filters, triangular shaped $H = 15\ mm$ $W = 15\ mm$	Turbulence model $k\text{–}\omega$ SST V_{inlet}= 0.9 $m\ s^{-1}$	2D 15 pleats	Rasouli et al. (2025) [60]

Note: K denotes the filter permeability; ε is the porosity; d_f is the fiber diameter; δ is the filter media thickness; H and W represent the pleat height and width, respectively; V_{inlet} is the duct inlet velocity; and $V_{filtration}$ is the filtration velocity, defined as the volumetric flow rate divided by the filtration face area.

2.5 Closed-Gates Mode: Natural Convection and Heat Transfer Performance

Porous media, characterized by their complex flow and heat transfer behavior, further complicate the natural convection process in enclosures. The interest in investigating natural convection flow and heat transfer in porous cavities extends beyond the proposed disinfection technology. In practice, understanding buoyancy-driven flow in enclosures incorporating porous media is crucial for various applications such as geothermal systems, heat exchangers, solar collectors, fuel cells, electronic cooling, crude oil production, etc. [97–100]. This section aims to provide a comprehensive review of free-convection flow and heat transfer in cavities partially or fully filled with porous media. The primary focus is on cases where internal bodies are present within the enclosures.

2.5.1 Experimental Studies of Natural Convection in Porous Enclosures

The experimental investigation of natural convection in enclosures containing porous media is of vital importance for the verification/validation of theoretical studies. However, only a few studies utilized heat transfer measurements and flow visualization techniques to investigate free convection in porous cavities.

One of the earliest empirical studies of buoyancy-driven flows in differentially heated cavities filled with a porous medium was conducted by Seki et al. [101]. They proposed a correlation for calculating the Nusselt number (Nu) on the hot vertical wall of porous cavities based on the Prandtl number, the Rayleigh number and the height-to-width ratio of the enclosure.

Belwafa et al. [102] conducted an experimental study on the natural convection flow in a cavity partially filled with a horizontal porous layer. They employed different conventional fibrous insulators as the porous media. The results indicated that the average Nu number on the cold wall rises as the air gap between the insulation layer and the cold wall increases. Therefore, they recommended that partial insulation be avoided in practical applications.

Song and Viskanta [103] experimentally and numerically studied free-convection flow and heat transfer in a differentially heated rectangular cavity, in which one half of the enclosure was filled with a vertical layer of an anisotropic porous medium, and the other half was the clear fluid region. They employed electrolysis dye generation for flow visualization. Comparing the experimental data with the mathematical modelling questioned the validity of adopting the laminar flow model at high Ra values (i.e., Ra $\sim 10^9$). Moreover, the results revealed that as the Rayleigh number and permeability of the porous layer increase and the aspect ratio of the cavity decreases, the penetration of fluid flow into the porous region increases.

Bagchi et al. [104] experimentally investigated the buoyancy-driven flow in a rectangular cavity containing a fluid-superposed porous medium subjected to localized heating at the lower boundary. They evaluated the impacts of the porous layer thickness and the heating element length on the heat transfer performance. It was observed that by increasing the porous layer-to-cavity height ratio, the average Nu on the heated wall decreased. However, the heater length ratio did not significantly affect the hot wall's average heat transfer coefficient.

Particle Image Velocimetry (PIV) is a non-intrusive optical flow-visualization technique widely used in experimental investigations of natural convection in cavities [105–108]. It offers significant advantages over traditional measurement methods. By seeding the fluid with tracer particles, PIV captures instantaneous velocity fields with high spatial resolution, enabling researchers to study complex flow patterns and vortices. The technique provides valuable insights into fluid dynamics, boundary-layer characteristics, and heat-transfer distribution within the cavity. Moreover, PIV's non-intrusive nature prevents perturbation of the flow, ensuring accurate and reliable data acquisition. Liu et al. [109] employed PIV for measuring the slip coefficient at the porous-fluid interface in a cavity partially filled with a vertical porous layer. Ataei-Dadavi et al. [110,111] utilized PIV and liquid crystal thermography (LCT) to visualize the velocity and temperature fields at pore scales in a differentially heated enclosure filled with large solid spheres forming a coarse porous medium. Various sphere materials, diameters and packing configurations were investigated. They concluded that the heat transfer rate in the porous cavity is lower than in the clear cavity, unless the porous medium is highly conductive.

The impacts of employing nanofluids [112,113], applying magnetic fields [113], and incorporating phase change materials (PCMs) [114] on the natural convection flow in porous enclosures have been explored experimentally in the literature. However, for the purposes of this thesis, the focus is directed towards a distinct aspect of the field. Therefore, this section intentionally avoids going into the complex details of those interactions.

Table 2.2 presents a comprehensive overview of experimental investigations concerning natural convection in enclosures that are either completely or partially filled with porous media. The table summarizes essential details, including the instrumentation, flow conditions, and geometric configurations used in these experiments.

Table 2.2. A summary of the experimental studies of natural convection in enclosures fully or partially filled with porous media.

Authors	Geometry	Properties	Instrumentations/results
Seki et al. (1978) [101]	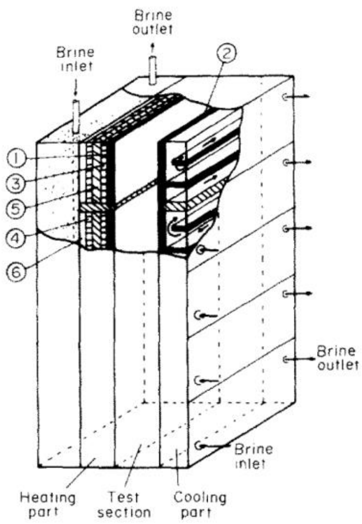	$1 \leq Ra^{*} \leq 10^{5}$ $1 \leq Pr \leq 200$ Height to width ratio of the cavity (H/W) varied between 5-26.	They proposed a correlation for the calculation of the Nu: $Nu^{*} = 0.627\, Pr^{0.13}(\frac{H}{W})^{-0.527} Ra^{*^{0.463}}$
Belwafa et al. (1991) [102]	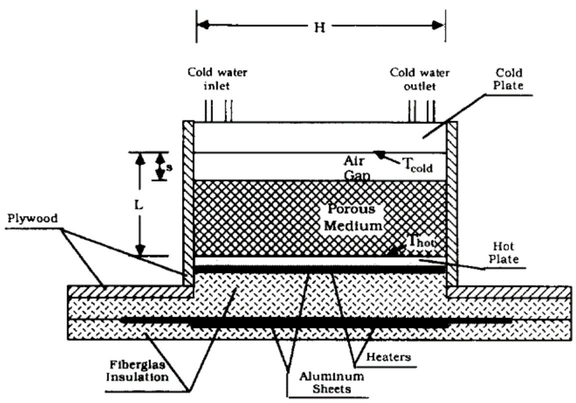	Three different samples as the porous media. $K_A = 1.8 \times 10^{-9}\ (m^2)$ $K_B = 1.3 \times 10^{-9}\ (m^2)$ $K_C = 4.9 \times 10^{-10}\ (m^2)$ $\varepsilon_A = 0.988$ $\varepsilon_B = 0.983$ $\varepsilon_C = 0.956$ $Ra \sim 10^{6}$	• Copper-constantan thermocouples were used for the temperature measurement. • Increasing the air gap at a constant porous thickness, increases the Nusselt number. • In practical applications, the partial insulation should be avoided.
Song and Viskanta (1994) [103]	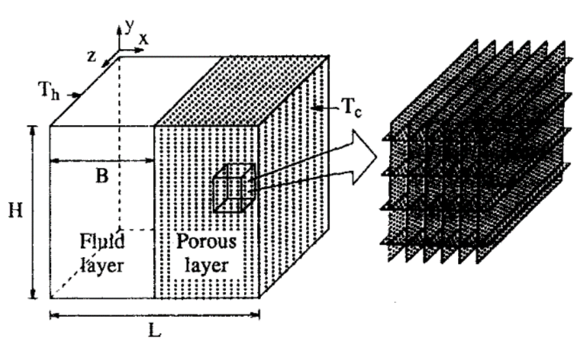	$\varepsilon = 0.629$ $\varepsilon = 0.744$ $\varepsilon = 0.801$ $Pr = 5.98$ $Pr = 6.47$ $Pr = 230$ $Ra \sim 10^{7} - 10^{9}$	• T-type thermocouples for measuring hot and cold walls temperatures. • 9 K-type thermocouples for evaluating the temperature of the porous section. • Electrolysis dye generation was utilized for flow visualization.

Table 2.2. A summary of the experimental studies of natural convection in enclosures fully or partially filled with porous media (Continued).

Authors	Geometry	Properties	Instrumentations/results
Bagchi et al. (2012) [104]	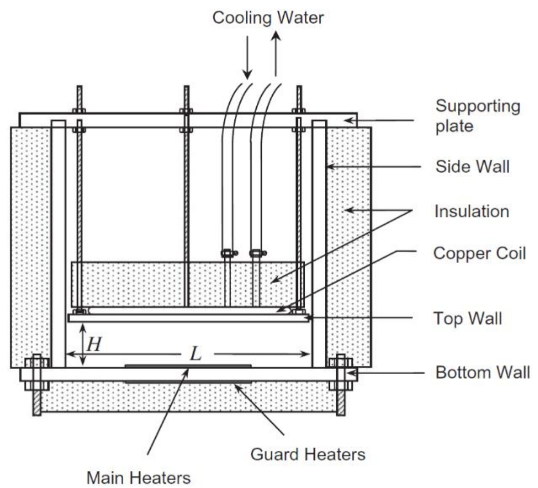	$\varepsilon = 0.38$ $Da = 4.04 \times 10^{-6}$ $10^7 \leq Ra \leq 10^9$ Four porous layer-to-cavity height ratios: 0.5, 0.67, 0.75, 1 Two heater-to-cavity length ratios: 0.11, 0.44	• E-type thermocouples were used for the temperature measurements. • With increasing the porous layer-to cavity height ratio, the average Nu on the heated wall decreases. • The heater length ratio does not have a significant effect on the average heat transfer coefficient of the hot wall.
Liu et al. (2013) [109]	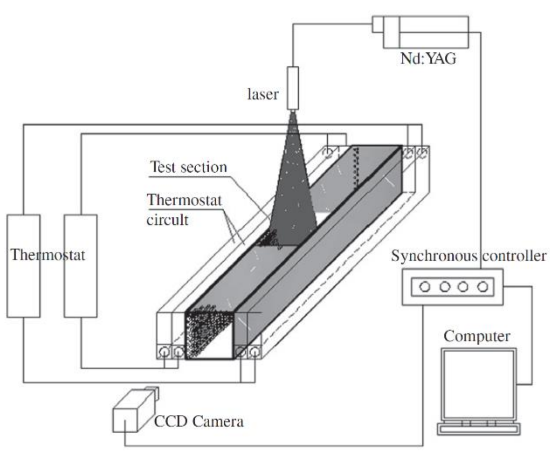	$\varepsilon = 0.908$ $K = 1.85 \times 10^{-6}\ (m^2)$ $10^4 \leq Ra \leq 10^6$	• PIV was used for the velocity measurement inside the porous, and at the porous/fluid interface. • They concluded that the dimensionless slip velocity at the interface of porous and fluid does not change along the height of the interface.
Solomon et al. (2017) [112]	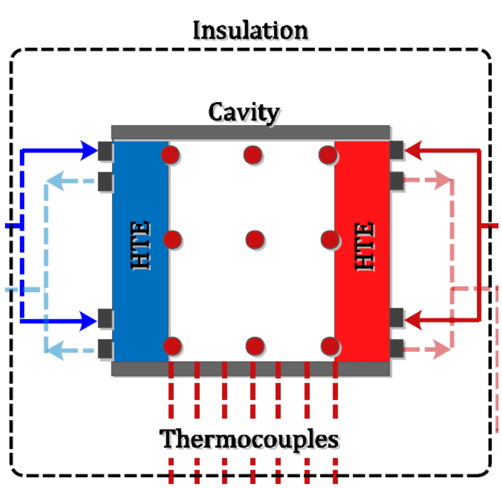	$\varepsilon = 0.249$ $K = 3.43 \times 10^{-7} (m^2)$ The range of the Rayleigh number for the clean cavity: $Ra \sim 10^8$ The range of the Rayleigh number for the porous cavity: $10^3 \leq Ra \leq 10^4$	• T-Type (OMEGA) thermocouple wires with a thickness of 0.25 mm and an accuracy of ±0.2 °C were utilized. • They utilized Berkovsky's equation for the validation of their experimental study. • By adding 0.05% of alumina nano-particles to the base fluid (water), the average Nu number increased by up to 10 %.

Table 2.2. A summary of the experimental studies of natural convection in enclosures fully or partially filled with porous media (Continued).

Authors	Geometry	Properties	Instrumentations/results
Ataei-Dadvi et al. (2019) [110]	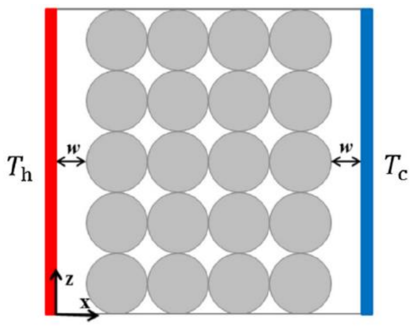	$10^7 \leq Ra \leq 10^9$ $Pr = 6.75$ $Pr = 7.63$ Different sphere solid materials (polypropylene, glass, steel, and brass) as large porous media were used for filling the cavity.	• LCT and PIV measurements, Pt100 resistance thermometers with an inaccuracy of ±0.03 ºC, PID controller for temperature. • They proposed a new correlation for the calculation of Nu number in cavities filled with coarse porous media. • The heat transfer rate within the porous cavity is lower than that of the clear cavity, unless the porous medium is highly conductive.
Ataei Dadvi et al. (2019) [111]	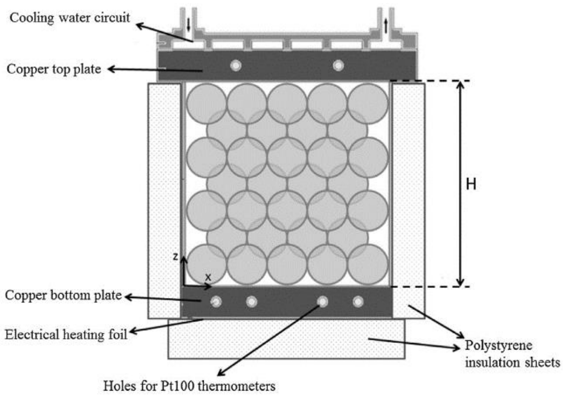	$10^7 \leq Ra \leq 10^9$ $Pr = 6.75$ $Pr = 7.63$ Different sphere solid materials (polypropylene, glass, steel, and brass) as large porous media were used for filling the cavity.	• LCT and PIV measurements, Pt100 resistance thermometers • At lower Ra numbers, no matter what the sphere material and size are, the measured Nu number in porous cavity is lower than that of the pure Rayleigh-Bénard convection. • However, at higher Ra numbers, the measured Nu number is rather similar in the two cases.
Qi et al. (2019) [113]	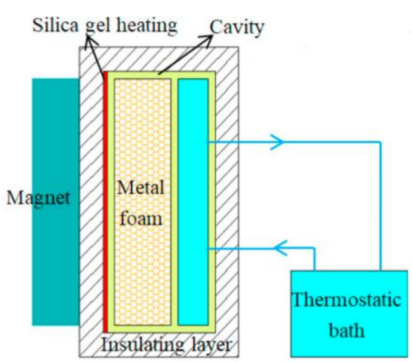	$\varepsilon = 0.94$ Copper metal foams with two different pores per inch values, but with similar porosity were used: PPI=5, 10 Tilt angles of cavity: 0°, 45°, 90°, 135°	• T-type thermocouples, silica gel heating sheet (Q=15 W) is used to provide a high constant temperature for the hot side of the cavity. • As the PPI increases, the average Nu number on the hot wall increases. • The highest heat transfer can be achieved in the cavity with a tilt angle of 90°.
Zhang et al. (2022) [114]	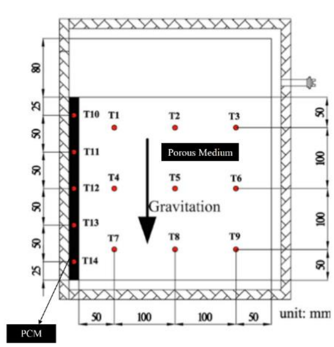	Different porous media, including iron and copper iron foams, were tested. $\varepsilon = 0.922\text{-}0.971$ Pores per inch values =10-35	• A 40-W silicone rubber heater was used for heating the cavity. • T-type thermocouples (Omega TT-T-30-SLE) for temperature measurement. • An infrared camera for capturing the temperature field of PCM. • Unlike small cavities, in large cavities, both conductive and convective regimes are significant.

2.5.2 Theoretical Studies of Natural Convection in Porous Enclosures

This section mainly focuses on theoretical and numerical studies of natural convection in porous enclosures. Accordingly, first, an overview of the current understanding of natural convection in porous enclosures without internal bodies will be provided. Then, the impacts of the presence of internal bodies on fluid flow patterns and convective heat transfer will be discussed.

2.5.2.1 Natural Convection in Porous Enclosures without Internal Bodies

Investigation of buoyancy-driven flow in rectangular cavities, fully or partially filled with porous media, can be found in earlier studies [103,115–119]. The accuracy of simulating the natural convection in porous beds is highly dependent on selecting the appropriate model for deriving momentum equations in porous regions. The well-known Darcy model is the most basic form relating pressure drop and velocity in porous media. According to Darcy's law, the frictional drag caused by the presence of the porous medium is directly proportional to the velocity [97,98].

While Darcy's model can be applied to a wide range of engineering applications, it loses accuracy in two cases. First, the Darcy model cannot consider the impact of no-slip conditions on the walls. This is particularly important in closely packed porous media. When the effect of the walls is substantial, the Darcy-Brinkman equation can be used to estimate the pressure drop, which can consider the near-wall-region effects [97,98]. Second, the Darcy model is not applicable when the inertia effects become significant at high fluid velocities. Hence, the Forchheimer term, which can consider the inertial impact, should be added to the momentum equations [97,98].

Beckermann et al. [117] carried out numerical and experimental studies to evaluate the natural convection in a vertical cavity partially filled with a porous medium. They adopted the Darcy-Brinkman-Forchheimer (DBF) model to derive the momentum equation in the porous region. The results indicated that at lower values of Da and Ra, the heat transfer in the porous region was dominated by conduction. Singh and Thorpe [119] compared the application of three different models, including Darcy, Brinkman-extended Darcy and Brinkman-Forchheimer-extended Darcy models, in simulating the natural convection in a cavity partially filled with a horizontal layer of a porous medium. It was concluded that for lower Darcy numbers (i.e., $\mathrm{Da} < 10^{-4}$), there was not a significant discrepancy between the three models. However, at higher values of the Darcy number, the Brinkman-Forchheimer-extended Darcy model was preferable as it considers the impact of inertia. Chen et al. [120] utilized DBF to study the free convection flow inside a cavity partially filled with two horizontal porous layers in its upper and bottom parts. It was observed that at constant values of Da and Ra numbers, increasing the thickness of the porous layers reduces the local Nusselt number, and this decrease in Nu is more significant for the upper part of the cavity.

Another vital factor that needs to be considered for the numerical simulation of buoyancy-driven flow in porous media is the validity of the local thermal equilibrium (LTE) assumption. By adopting LTE, an identical temperature will be considered for the solid matrix and the fluid phase at any given location within the porous medium. Numerous studies utilized LTE to simplify the analysis of heat transfer within porous media [120–124]. However, the LTE assumption loses applicability when the temperature difference between the solid and fluid phases becomes considerable. For instance, when the porous matrix has high thermal conductivity (e.g., metal foams and heat sinks) and there is a phase change or heat generation in the porous media, local thermal non-equilibrium (LTNE) approaches should be implemented instead.

Khashan et al. [125] used the Finite Volume Method (FVM) to simulate a non-Darcian flow in a porous enclosure. They evaluated the validity of the local thermal equilibrium assumption in porous media at various Rayleigh and Darcy numbers. The results indicated that neglecting the non-Darcian effects, especially the Forchheimer term, at higher Rayleigh numbers overestimates Nu and the LTNE values. Ghalambaz et al. [126] analyzed the impacts of the location of constant temperature elements on a conjugate free-convection heat transfer in an enclosure filled with a porous medium by considering the LTNE effect. The results revealed that the maximum heat transfer rate from the walls to the porous media occurred when both the heating and cooling elements were located at the center of the walls. Moreover, the lowest heat transfer rate occurred when the heating and cooling elements were near the top and bottom walls, respectively. Other aspects of employing the LTNE approach in simulating the free convection within porous cavities, such as applying linearly [127] or sinusoidal thermal boundary conditions [128], using nanofluids [129], saturating the porous region with non-Newtonian fluid [130], varying wall waviness [131], imposing magnetic field [132] have been thoroughly investigated in previously published works.

2.5.2.2 Natural Convection in Porous Enclosures with Internal Bodies

Numerous studies in the literature have investigated the flow and heat transfer characteristics of free-convection flow inside cavities partially or fully filled with porous media [122–124,133,134]. However, there are relatively fewer works that consider the effect of the existence of an internal obstruction inside enclosures containing porous media. These studies generally investigated the impact of varying the internal bodies' geometry, arrangements and boundary conditions on the heat transfer performance within rectangular cavities.

Based on the complexity of the problem, the Finite Difference Method (FDM) can be adopted to discretize the set of governing equations for simple geometries. Alomar et al. [135] utilized FDM to compare the heat transfer performance of the in-line and staggered arrangements of a bank of orthogonal heated elements in a square porous enclosure. They concluded that the heat transfer performance of the in-line configuration of the elements outperformed that of the staggered arrangement. Basher et al. [136] adopted FDM to investigate the buoyancy-driven flow in a square cavity filled with porous media, including vertical and horizontal heated elements. The results indicated that the application of horizontal elements could provide a more favorable heat transfer outcome.

For numerical investigation of more complex problems, such as natural convection flows in porous cavities embedding single or several cylinders, the Finite Element Method (FEM) and Finite Volume Method (FVM) can be implemented [99,137–142]. For instance, Khanafer et al. [99] and Alturaihi et al. [137] deployed FEM to study the steady natural convection in confined porous enclosures embedding a single cold and heated circular cylinder, respectively. Hussain et al. [138] numerically investigated the heat transfer rate of various cylinder geometries, including circle, triangle, rectangle, rhombus and ellipse inside a square enclosure partially filled with porous media and nanofluid. The results showed that the triangular heated cylinder has a higher heat transfer rate at similar boundary conditions. Abdulkadhim et al. [139] utilized COMSOL Multiphysics software to simulate the steady free-convection flow in a wavy enclosure partially filled with nanofluid and porous layers. It was observed that an increase in the thickness of the porous layer leads to a reduction in the average Nusselt number. Several studies numerically addressed the presence of a pair [140] or four circular [140,142] isothermal cylinders in porous cavities. Generally, the impact of the cylinder spacing on the time-averaged Nu of each cylinder is not significant at lower values of the Rayleigh number (i.e., when conduction is dominant). However, at higher Rayleigh numbers, the cylinders' average Nu increases with increasing transverse and horizontal distances between the embedded cylinders [141].

A summary of the numerical studies on the natural convection flow in porous enclosures containing internal bodies is provided in Table 2.3.

Table 2.3. A summary of the studies on the natural convection flow in porous enclosures containing internal bodies.

Internal Body	Steady/Unsteady	Numerical Method	Parameters	Computational Domain	Reference
Bank of **constant temperature orthogonal heated plates** in a square porous enclosure	Steady	FDM (LTNE Model)	$100 \leq Ra^* \leq 1000$ $Da = 10^{-5}$	2D	Alomar et al. (2021) [141]
Vertical and horizontal **heated elements** with **constant temperature** embedded in a square porous cavity	Steady	FDM (LTNE Model)	$200 \leq Ra^* \leq 1000$ $Da = 10^{-5}$	2D	Basher et al. (2022) [136]
Single cold cylinder embedded in a square porous cavity with a flexible wall	Steady	FEM	$10^3 \leq Ra \leq 10^4$ $Da = 10^{-2}$	2D	Khanafer et al. (2020) [99]
Single isothermal cylinder embedded in a square porous cavity with a flexible wall	Steady	FEM	$Ra = 1.4 \times 10^7 \&$ $Ra = 4.23 \times 10^7$ $Da = 10^{-2}$	2D	Alturaihi et al. (2020) [137]
Different **constant temperature heated** objects, including **circle, triangle, rectangle and ellipse** inside a square enclosure partially filled with porous media and nanofluid	Steady	FEM	$10^3 \leq Ra \leq 10^4$ $10^{-5} \leq Da \leq 10^{-1}$	2D	Hussain et al. (2019) [138]
Isothermal hot corrugated cylinders inside a wavy enclosure filled with nanofluid superposed in porous–nanofluid layers	Steady	FEM (COMSOL)	$10 \leq Ra \leq 10^6$ $10^{-5} \leq Da \leq 10^{-1}$	2D	Abdulkadhim et al. (2019) [139]
A **pair of isothermal hot cylinders** embedded in a square porous cavity	Unsteady	FEM	$10^3 \leq Ra \leq 10^6$ $10^{-4} \leq Da \leq 10^{-2}$	2D	Pal et al. (2018) [140]
Four isothermal hot cylinders embedded in a square porous cavity	Unsteady	FEM (COMSOL)	$10^3 \leq Ra \leq 10^6$ $10^{-4} \leq Da \leq 10^{-2}$	2D	Nammi et al. (2022) [141]
Four isothermal cold cylinders embedded in a square porous cavity with a flexible wall saturated with nanofluid and NEPCM-water	Unsteady	FVM (ANSYS FLUENT)	$10^4 \leq Ra \leq 10^6$ $Da = 10^{-3}$	2D	Hashemi-Tilehnoee et al. (2020) [142]

2.6 Novelty and Contributions

The literature reviewed in Section 2.3 revealed that, despite their potential, existing air disinfection technologies face several significant challenges, including high operational and capital costs, high energy consumption, generation of harmful byproducts, and complex installation and maintenance requirements. In addition, when it comes to disinfecting HVAC filters as reservoirs of captured microorganisms, heat-based disinfection emerges as the only viable approach capable of penetrating the porous structure of pleated filters without introducing chemicals or secondary byproducts. However, existing heat-based filter disinfection methods, such as self-heating filters [87], are often associated with high pressure drop, excessively elevated operating temperatures, and unintended heat addition to the HVAC system, while passive solar-based approaches [86] rely strongly on ambient and environmental conditions. These limitations collectively highlight the need for an energy-efficient, scalable, and HVAC-compatible heat-based filter disinfection technology.

From an operational perspective, the studies reviewed in Section 2.4 provided essential insights into investigating pleated air filters as porous media. However, to date, no detailed investigation has examined the combined effects of the presence of heating elements (cylinders), flow-control gates, and gate-opening/closing mechanisms on the pressure drop and particle removal efficiency of pleated HVAC filters. Furthermore, reviewing the studies of natural convection in porous enclosures in section 2.5 revealed that, to date, far too little attention has been paid to unsteady natural convection in confined enclosures containing pleated porous media and heating elements, especially under conditions relevant to HVAC applications. Most of the studies in the literature focused on laminar natural convection ($\mathrm{Ra} \leq 10^7$) and square porous media ($10^{-5} \leq \mathrm{Da}$). However, this thesis requires the investigation of turbulent natural convection ($10^8 \leq \mathrm{Ra}$) at lower

Darcy number ranges ($\mathrm{Da} \leq 10^{-9}$) in pleated filter media. The lack of studies addressing this regime constitutes a fundamental knowledge gap in the coupling of heat transfer, buoyancy-driven flow, and filtration media.

To address these research gaps, the present thesis will develop a methodology for the optimal design of the integrated system of pleated air filters and heating elements. The main novelty and research contributions of this thesis include:

1. Proposing a novel, energy-efficient air disinfection approach that combines air filtration with thermal inactivation.
2. Developing and evaluating multiple design concepts and prototypes for implementing the proposed technology in both single-stage and multi-stage filtration configurations.
3. Evaluating the energy performance of the system while measuring pressure drop and particle removal efficiency according to the ASHRAE 52.2 standard [22].
4. Investigating the effect of the existence of heating elements (cylinders) in the ductwork, the presence of flow-control gates, and gate opening/closing mechanisms on the pressure drop and the particle removal efficiency of pleated filters.
5. Examining the impact of heating element configurations on the unsteady turbulent buoyancy-driven flow within cavities containing pleated filters.
6. Identifying optimal geometric configurations and operating parameters that yield uniform temperature distributions and effective thermal disinfection across the filter surface for a natural-convection-based (fanless) system.
7. Determining optimal operating conditions for forced warm-air recirculation, including air recirculation rate and temperature, in cases where natural convection alone is insufficient to achieve uniform and effective disinfection.

Chapter 3. Numerical Simulation of Buoyancy-Driven Flow in an Enclosure Containing Tubular Heating Elements

3.1 Preface

This chapter provides guidelines for designing the experimental setup of the natural-convection-based system, which is described in detail in Chapter 4. The main objective is to use CFD simulations to explore various heating-element and filter-frame configurations that can reduce the temperature non-uniformity inherent to natural convection. The resulting optimal configurations are then tested experimentally with actual filters in Chapter 4 to verify their effectiveness under realistic operating conditions.

3.2 Problem Description

As discussed in Chapter 2, air filters have complex geometries and diverse material properties; therefore, explicitly including them in the computational domain would introduce unnecessary complexity, variability, and computational cost. By excluding the filter, this chapter can focus more efficiently on the core objective, identifying heating-element arrangements that produce uniform heating within the unit.

Figure 3.1 illustrates five different configurations considered for the system in the symmetrical plane. As is evident, each enclosure includes heat-generating cylinders (heating elements) with a diameter of 8 mm that increase the temperature of the air mainly by buoyancy-driven flow. The main idea is to investigate the impacts of changing the number of cylinders, heating element arrangements, and frame geometry on temperature distribution within the enclosed cavity. To this end, a constant amount of heat generation of approximately 1.2×10^6 ($\frac{W}{m^3}$) is applied to cylinders in all cases. Given the cylinder length in the spanwise (out-of-plane) direction is 30.5 cm, this heat generation rate corresponds to a total heat input of approximately 140 W and 180 W for configurations with 8 and 10 cylinders, respectively.

In Config. I, 8 cylinders are equally spaced in the center line of the enclosure. In Config. II, 8 cylinders are arranged in a way that the number of elements near the bottom of the frame be denser. In Config. III, a heating chamber is added below the unit frame to act as a mixing plenum, and 8 cylinders are positioned at varying distances. In Config. IV, all 8 cylinders are placed in the heating chamber. Configuration V investigates ten cylinders positioned at varying distances.

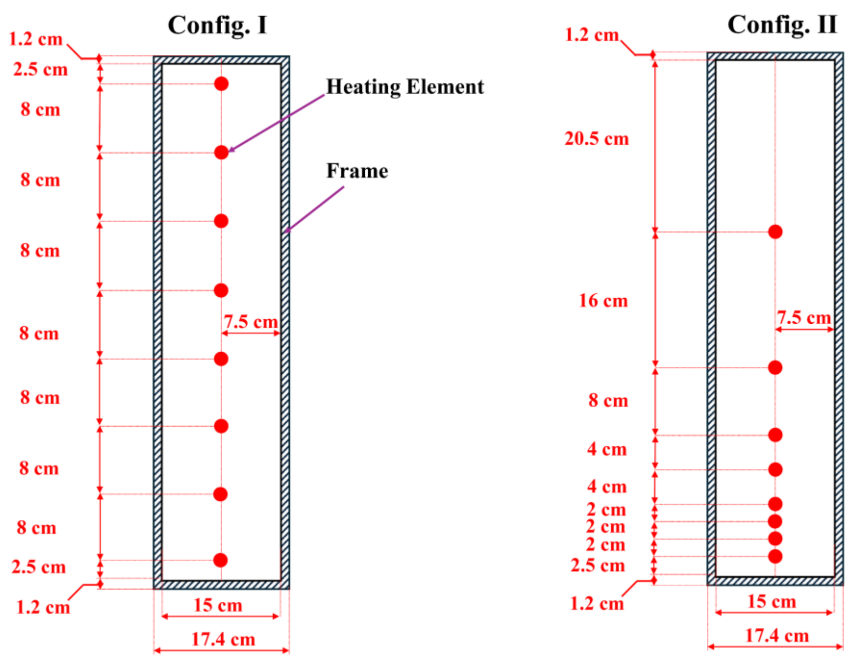

Fig. 3.1. A schematic representation of five different configurations considered for the numerical simulation.

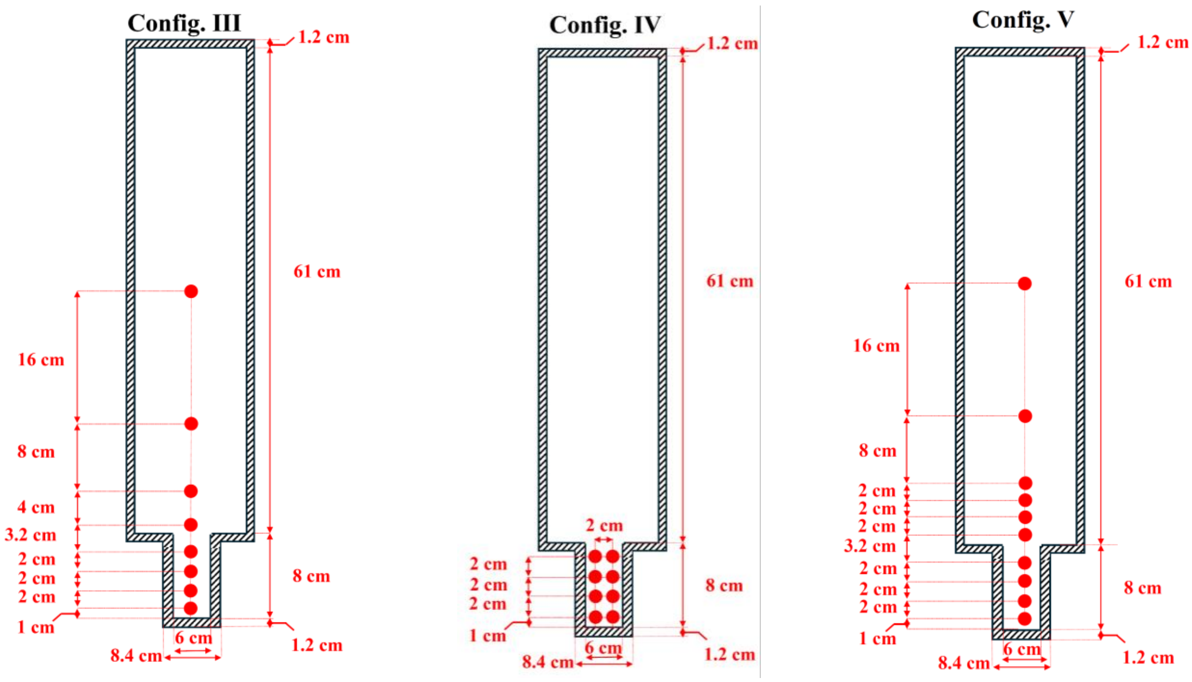

Fig. 3.1. A schematic representation of five different configurations considered for the numerical simulation (continued).

3.3 Assumptions

As portrayed in Fig. 3.1, the computational domain includes activated heating elements (cylinders), fluid region (air) and the polycarbonate frame. Constant heat generation (1.2×10^6) is applied to the cylinders, and all external walls are insulated. Simplifying assumptions will be implemented to reduce the complexity of the problem as follows:

1. The fluid in the enclosure is Newtonian.
2. The flow is assumed to be 2D. Owing to the geometric symmetry of the configuration and the thermally insulated boundary conditions on the walls, two-dimensional simulations are expected to provide accurate predictions for the range of Rayleigh numbers considered in this thesis ($Ra \sim 10^9$)[143,144]. Although the two-dimensional approximation entails some loss of accuracy near the walls, as it does not capture heat transfer in the spanwise (out-of-plane)

direction, it reduces the number of computational cells by approximately two orders of magnitude, thereby substantially lowering the computational cost. Therefore, by balancing accuracy and computational efficiency, the flow is modelled using a two-dimensional formulation.

3. The effect of viscous dissipation is neglected.
4. The radiation heat transfer is neglected. It is assumed that the heating elements and internal walls are covered with a thin aluminum foil.
5. The pressure work is neglected as the velocities in the natural convection are relatively low.
6. The thermophysical properties of the solid regions, encompassing the heating element and unit frame, are assumed to be constant and invariant with temperature.
7. The heating element was approximated as a homogeneous solid with equivalent thermophysical properties derived from an assumed volumetric composition of 80% MgO powder and 20% stainless steel, based on typical manufacturer specifications for thin-walled tubular heaters.

It should be noted that, since the heating element temperature exceeds 100 ºC in our study, the temperature difference between the hot and cold surfaces can easily exceed 28 ºC, the threshold for employing the Boussinesq approximation [145]. Hence, in this study, the Boussinesq approximation cannot be adopted; instead, density variations due to temperature must be fully retained. Moreover, according to Refs. [143,144], for the buoyancy-driven flow induced by a hot cylinder in a cold square cavity, the flow becomes fully turbulent when Ra $\geq 10^8$. In this study, like most real-world engineering applications, the Rayleigh number exceeds 10^8. Accordingly, to study the unsteady turbulent natural convection flow, this thesis employs the shear-stress transport $k{-}\omega$ Reynolds-Averaged Navier-Stokes (RANS) model, which has been shown to provide accurate results compared to experimental data and high-cost direct numerical simulation (DNS) and large-eddy simulation (LES) methods [146–148].

3.4 Mathematical Modelling

3.4.1 Governing Equations

Considering the assumptions mentioned in section 3.3, the governing equations for the unsteady turbulent natural convection flow with variable air properties can be derived as follows [98,145,149,150].

Clear fluid region (air):

Continuity equation:

$$\frac{\partial \rho_a}{\partial t} + \nabla \cdot \left(\rho_a \vec{V}\right) = 0 \tag{3.1}$$

Momentum equation:

$$\frac{\partial\left(\rho_a \vec{V}\right)}{\partial t} + \nabla \cdot \left(\rho_a \vec{V}\vec{V}\right) = -\nabla p + \nabla \cdot \left[(\mu + \mu_t)\left(\nabla\vec{V} + \nabla^T\vec{V} - \frac{2}{3}\left(\nabla \cdot \vec{V}\right)\bar{\bar{I}}\right) - \frac{2}{3}\rho_a k \bar{\bar{I}}\right] + \rho_a \vec{g} \tag{3.2}$$

where k is the turbulent kinetic energy, and μ_t denotes the turbulent viscosity, which can be calculated as follows [149]:

$$\mu_t = \frac{\rho_a k}{\omega} \frac{1}{max\left[\frac{1}{\alpha^*}, \frac{SF_2}{a_1}\right]} \tag{3.3}$$

in which ω represents the specific dissipation rate. α^* is the low-Reynolds-number correction coefficient, S is the strain rate magnitude, F_2 is the blending function, and a_1 is the model constant.

Turbulent kinetic energy:

$$\frac{\partial(\rho_a k)}{\partial t} + \nabla \cdot \left(\rho_a k \vec{V}\right) = \nabla \cdot \left[\left(\mu + \frac{\mu_t}{\sigma_k}\right)\nabla k\right] + G_k - Y_k + S_k \tag{3.4}$$

Specific dissipation rate:

$$\frac{\partial(\rho_a \omega)}{\partial t} + \nabla \cdot (\rho_a \omega \vec{V}) = \nabla \cdot \left[\left(\mu + \frac{\mu_t}{\sigma_\omega}\right) \nabla \omega\right] + G_\omega - Y_\omega + D_\omega + S_\omega \tag{3.5}$$

where σ_k and σ_ω are the model constants, G_k and G_ω show the generation terms, Y_k and Y_ω denote dissipation, D_ω represents the cross-diffusion term and S_k and S_ω are the user-defined source terms. The details of these parameters can be found in Ref. [149].

Energy equation:

$$\rho \frac{Dh_{sp,a}}{Dt} = \nabla \cdot ((k_a + k_t)\nabla T) \tag{3.6}$$

in which $h_{sp,a}$ is the specific enthalpy of air, D/Dt represents the total derivative, k_a is the air thermal conductivity, and k_t is the turbulent thermal conductivity, whose calculation details are provided in Ref. [149].

Solid regions (unit's frame and heating element):

$$\frac{\partial T_s}{\partial t} = \alpha_s \nabla^2 T_s \tag{3.7}$$

where α_s represents the thermal diffusivity of the solid regions.

It should be noted that Nusselt number (Nu), a key dimensionless heat-transfer parameter that will be used for validation against previous studies in Section 3.5.3, is defined as:

$$\mathrm{Nu} = \frac{hD}{k_a} = \frac{qD}{(T_h - T_c)} \tag{3.8}$$

in which D denotes the cylinder diameter, T_h and T_c are the temperatures of the hot and cold sources, respectively. q is the local heat flux over the cylinder wall, which can be determined as follows:

$$q = -k_a \frac{\partial T}{\partial n} \tag{3.9}$$

where n shows the outward normal direction at the cylinder wall.

3.4.2 Boundary and Initial Conditions

No-slip boundary conditions are considered for all solid surfaces, including the enclosure walls and the cylinder surface for the velocity field. The enclosure walls are assumed to be thermally insulated, while the cylinders are modelled as a solid region with uniform volumetric heat generation. The computational domain is initially at rest (no flow movement) and at a uniform temperature of 22 ºC. At no-slip walls, the turbulent kinetic energy is damped to zero, and the specific dissipation rate is imposed via the model's wall boundary condition.

The temperature-dependent thermophysical properties of air, including density (ρ), thermal conductivity (k), dynamic viscosity (μ), and specific heat capacity (C_p) are extracted from Ref [151]. The unit frame is assumed to be made of solid polycarbonate, and the properties are adopted based on the manufacturer's datasheet ($\rho = 1210\ \frac{kg}{m^3}$, $k = 0.2 \frac{W}{m.K}$, $C_p = 1250 \frac{J}{kg.K}$). Furthermore, for the heating element, based on Assumption 7 described in Section 3.3, the equivalent density and heat capacity were computed using volumetric, assuming a composition of 80% MgO powder and 20% AISI 304 stainless steel. The effective thermal conductivity was estimated using standard composite mixing rules, with the classical series and parallel composite conduction models providing lower and upper bounds, respectively [152]. The value adopted in the simulations corresponds to the average of these bounds. The resulting equivalent properties of the heating element used in the simulations are $\rho = 4500\ \frac{kg}{m^3}$, $k = 36.6 \frac{W}{m.K}$, $C_p = 900 \frac{J}{kg.K}$.

3.5 Numerical Method

3.5.1 Numerical Grid

The numerical grid was generated by first creating the geometry of the computational domain using Design Modeler software. The computational domain consists of the unit frame, the fluid region, and the heating elements (cylinders). Subsequently, Ansys Meshing was employed to generate the numerical grids. Figures 3.2 and 3.3 present the meshes for the configurations without and with a chamber, respectively.

As illustrated in Figs. 3.1a–c and 3.2a–c, the numerical grid comprises both structured and unstructured regions. Unstructured triangular elements with a size of 0.3 mm are used inside the heating cylinders, while structured quadrilateral elements are employed in the remaining regions of the domain. The mesh is locally refined near the surfaces of the heat-generating cylinders and along the internal walls of the frame and chamber. The height of the first near-wall cell was selected to ensure that the dimensionless wall distance satisfies $1 \leq y^{+} < 5$ [149]. Accordingly, the first-layer thickness was set to 0.2 mm near the cylinder surfaces and 0.3 mm near the internal frame walls. Furthermore, for all configurations, the minimum orthogonal quality exceeded 0.8, and the maximum skewness remained below 0.1, indicating a high-quality computational mesh [149].

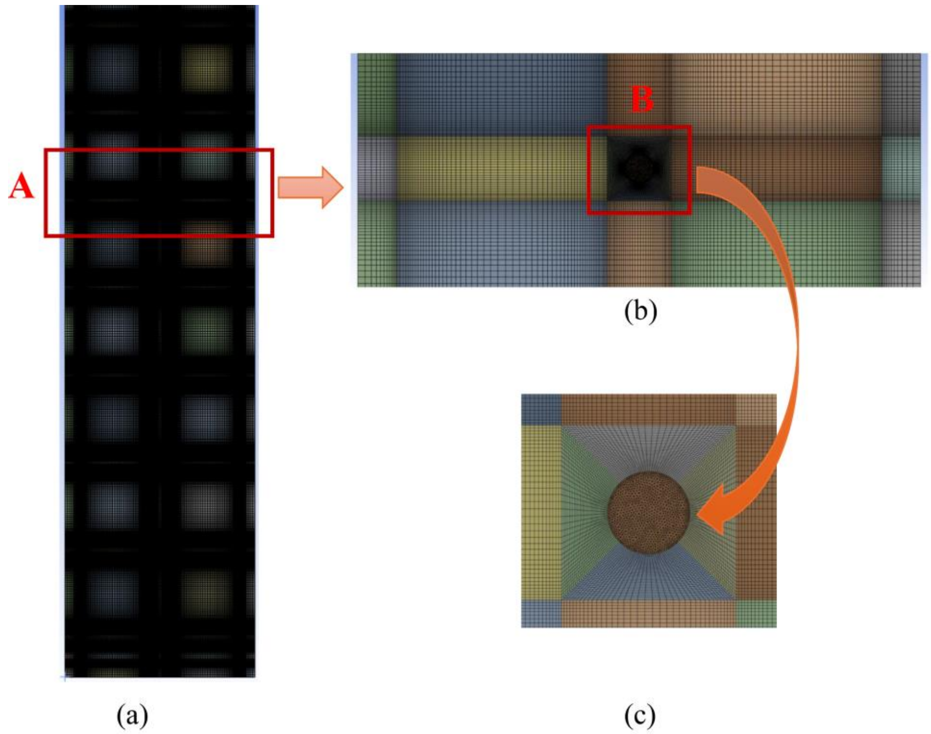

Fig. 3.2. A schematic view of the numerical grid for the unit without the chamber: (a) whole domain, (b) zoomed view of section A, and (c) zoomed view of section B.

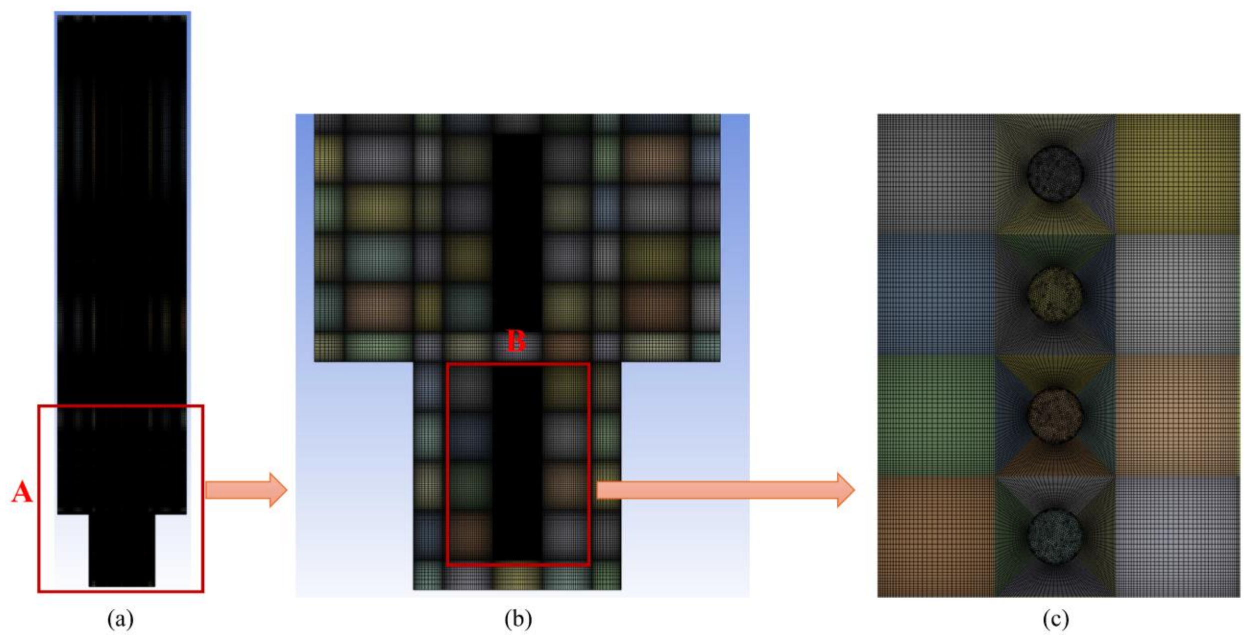

Fig. 3.3. A schematic view of the numerical grid for the unit with the chamber: (a) whole domain, (b) zoomed view of section A, and (c) zoomed view of section B.

3.5.2 Solver Setup

To simulate the conjugate heat transfer problem, the full set of governing equations, including the continuity equation, the Navier–Stokes equations, the transport equations for turbulent kinetic energy and its specific dissipation rate, and the energy equation, were discretized and solved using Ansys Fluent 2023 R2. A pressure-based solver was employed. Pressure interpolation was performed using the PRESTO! (Pressure Staggering Option) scheme, as recommended in Ansys Fluent Users' Guide for buoyancy-driven flows [149]. Second-order upwind discretization schemes were applied to the momentum, turbulent kinetic energy, specific dissipation rate, and energy equations to improve solution accuracy. Pressure–velocity coupling was achieved using the SIMPLE algorithm. A CFL[1]-based adaptive time-stepping approach was implemented, allowing the time step to vary between 0.005 s and 0.1 s, ensuring that the Courant number, $\mathrm{Co} = V\Delta t/\Delta x$, remained on the order of unity or lower. The convergence criteria were set to 10^{-6} for the energy equation and 10^{-3} for all other variables. All simulations were carried out for a total physical time of 600 s for each configuration.

3.5.3 Grid Independence

To ensure that the numerical results were independent of mesh resolution, a grid-independence study was performed. For this purpose, four computational grids were developed for Config. I, referred to as Case 1, Case 2, Case 3, and Case 4, containing 64,742, 123,412, 197,376, and 262,914 cells, respectively. The average Nusselt number over the cylinders was selected as the primary evaluation parameter, as it reflects both the heat transfer and flow characteristics of the system.

[1] Courant–Friedrichs–Lewy

Running the simulations for each case demonstrated that the solution did not converge for Case 1. Figure 3.4 depicts the mesh sensitivity analysis for Cases 2, 3, and 4. As is evident, refining the mesh from Case 3 to Case 4 has a negligible effect on the average Nusselt number (less than 0.6%). Therefore, considering both accuracy and computational cost, a mesh resolution comparable to Case 3 (approximately 197,000 elements) was adopted as the reference level of refinement for all configurations analyzed in this study.

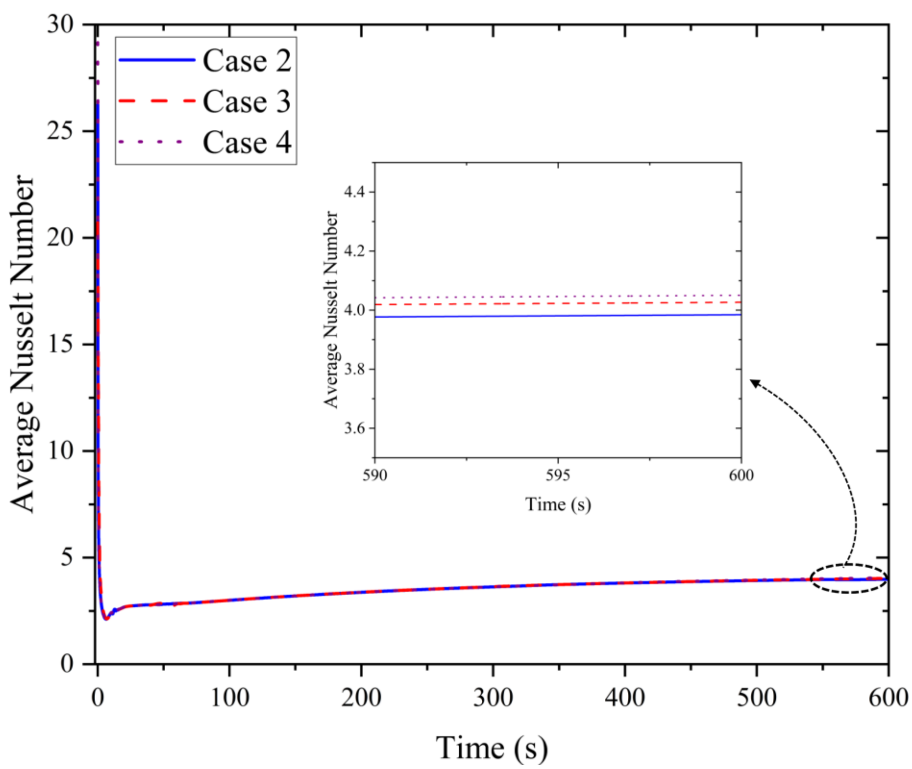

Fig. 3.4. Mesh-sensitivity analysis showing the effect of grid resolution on the average Nusselt number over the cylinders for Config. I during 600 s. The inset highlights the negligible difference between Cases 2–4 near the end of the simulation.

3.5.4 A Test of Validation

Experimental validation of unsteady turbulent natural convection requires non-intrusive optical measurement techniques, such as Particle Image Velocimetry (PIV) and Liquid Crystal Thermography (LCT), to resolve the velocity and temperature fields [110,111,153,154]. Implementing such techniques is beyond the scope of this thesis. Furthermore, to the best of the author's knowledge, no experimental or numerical studies have been reported in the literature that investigate the configurations considered in this work at high Rayleigh numbers (Ra $\geq 10^8$). Consequently, numerical results available in the literature for simpler geometries, specifically, 2D and 3D unsteady turbulent natural convection around a heated cylinder located at the center of a square enclosure with cold walls [143,144], were employed to validate the numerical methodology adopted in this thesis.

The geometry of the computational domain investigated in Refs. [143,144] is illustrated in Figs. 3.5a and b. The square cavity has dimensions of $D \times D$ and contains a centrally located cylindrical heat source maintained at a temperature of 303 K (T_h), while all cavity walls are held at a uniform cold temperature of 283 K (T_c). The cylinder radius (r_o) is equal to $0.2D$. A Rayleigh number of 10^8 is considered, corresponding to a cavity dimension of 0.36 m. While Aithal employed the Wilcox $k{-}\omega$ turbulence model in their study, the $k{-}\omega$ SST turbulence model was adopted in this thesis. Figure 3.6 compares the results of the current simulations with the corresponding 2D and 3D results reported by Aithal [143,144]. A schematic representation of the numerical grid used for the validation case is provided in Appendix A.

As shown, the local Nusselt number distributions on the cylinder wall at various angular positions measured from the top of the cylinder (φ), as well as on the cavity walls at different dimensionless distances from the center of the top wall (S), show good agreement between the 2D results of the present study and the 2D results reported in Ref. [143]. The discrepancies observed between the 2D results of this study and the 3D results of Aithal [143] are primarily attributed to neglecting heat transfer in the spanwise (out-of-plane) direction, as discussed in Section 3.3. Since 3D simulations require approximately two orders of magnitude more computational cells, adopting a 2D modelling approach represents a reasonable compromise between accuracy and computational efficiency. This approach is therefore considered adequate for comparing the heat-transfer performance of different configurations from an engineering perspective in this thesis.

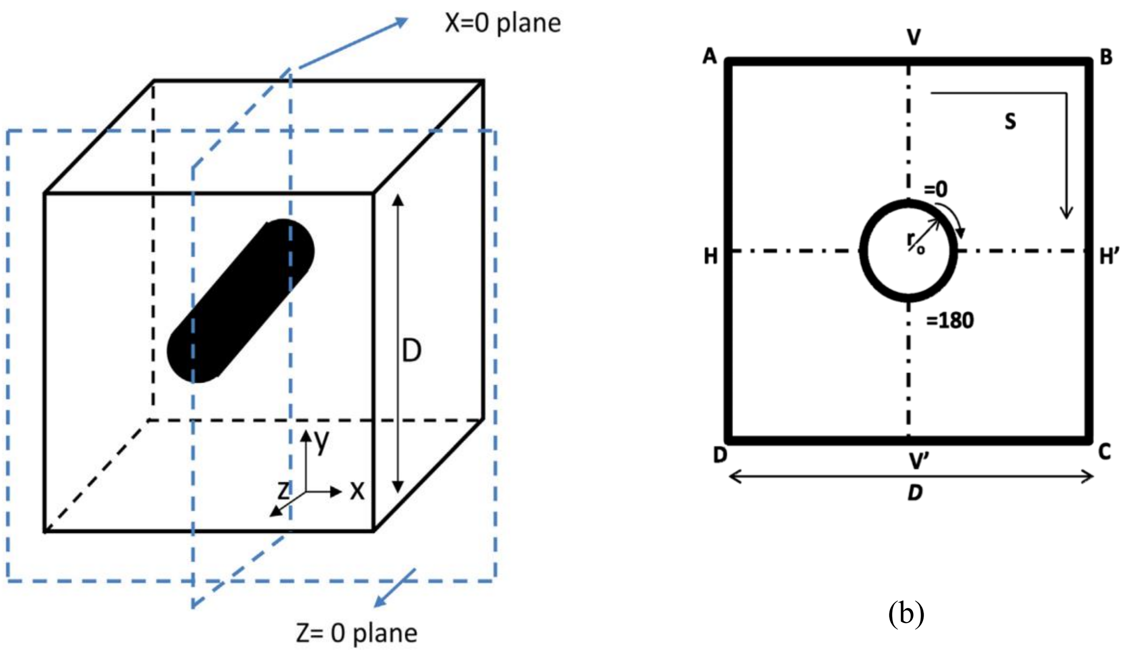

(a)

Fig. 3.5. Schematic representation of (a) 3D, and (b) 2D computational domains (extracted from Refs. [143,144]).

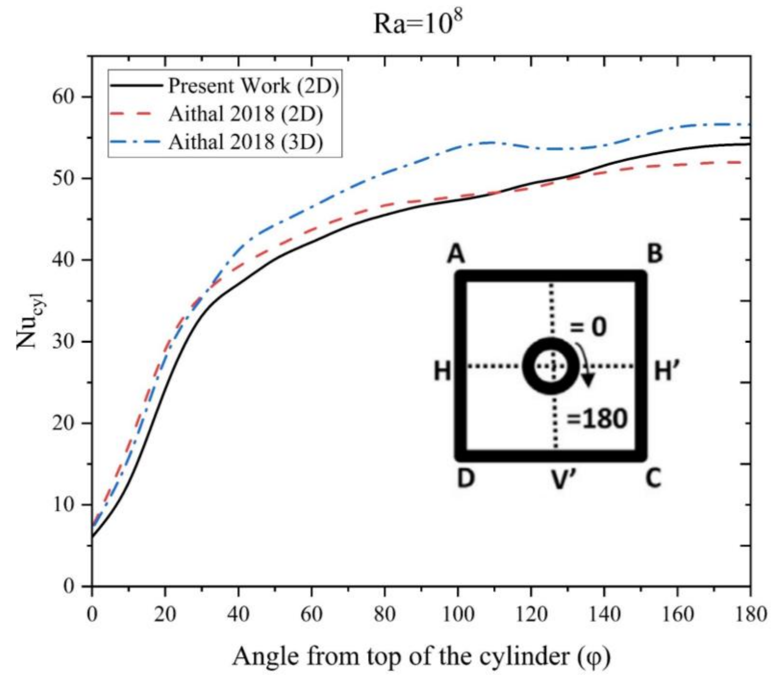

(a)

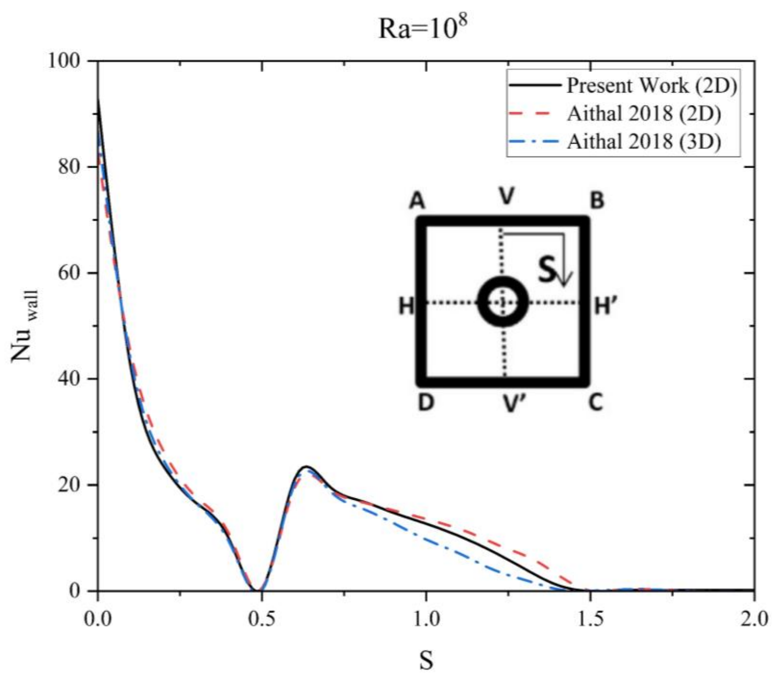

(b)

Fig. 3.6. Comparison of (a) local Nusselt number on the cylinder wall at various angular position, and (b) local Nusselt number on the enclosure walls at different dimensionless distances with Aithal 2018 [143].

3.6 Results and Discussion

Figure 3.7 presents the temperature contours in the enclosure for the five configurations at t = 600 s. Based on the temperatures at this time and the enclosure height as the characteristic length scale, the Rayleigh numbers for all configurations are slightly above 10^9, indicating fully turbulent natural convection. In this study, a mean Rayleigh number is evaluated using the mean temperature of all heating elements relative to the cold enclosure walls. It should be noted that the present problem is inherently transient; therefore, the temperature-based Rayleigh number is not constant and increases with time as the temperature difference between the heating elements and the surrounding air changes. Although some studies define modified Rayleigh numbers based on the heat generation [155–158], to the best of the author's knowledge, there is no single universal critical Rayleigh number for such cases. Consequently, a temperature-based Rayleigh number is adopted here to characterize the flow regime.

Figure 3.7a shows that adopting Config. I, in which eight heat-generating cylinders are equally spaced along the centerline of the enclosure, leads to pronounced temperature non-uniformity. Air in the vicinity of the cylinders is heated, its density decreases, and it rises due to buoyancy, forming distinct warm air plumes around the cylinders. As a result, the air temperature in the upper region of the enclosure becomes significantly higher than that near the bottom. Such temperature stratification must be mitigated before installing any filter inside the enclosure. Figure 3.7b indicates that redistributing the same number of cylinders with a denser arrangement near the bottom of the enclosure (Config. II) slightly reduces the temperature non-uniformity. However, the improvement remains limited and noticeable temperature gradients still persist between the bottom and top regions.

To address this issue, a heating chamber is installed beneath the enclosure frame to serve as a mixing plenum, preheating the air before it enters the main frame region. As illustrated in Figs. 3.7c and 3.7d, distributing the cylinders between the frame and the chamber with varying spacing (Config. III), substantially reduces the temperature difference within the enclosure. In contrast, placing all cylinders inside the heating chamber (Config. IV) is not effective, as the buoyant air plume generated in the chamber is not sufficiently strong to transport heated air to the upper region of the frame. Figure 3.7e (Config. V) indicates that increasing the number of cylinders to ten also improves temperature uniformity. However, the temperature difference between the bottom and top regions of the frame remains slightly larger than in Config. III. Although the additional cylinders introduce more energy into the system, they intensify the upward buoyant plume, which enhances vertical temperature stratification compared to Config. III.

Another important observation from Figs. 3.7a–e is the emergence of asymmetric temperature contours, particularly when the distance between cylinders decreases or when a heating chamber is added. Interactions between adjacent plumes, the enclosure walls, and adjacent cylinders at high Rayleigh numbers lead to flow instabilities and the formation of complex recirculating structures. Similar behaviour has been reported by Seo et al. [159], where interactions between multiple heated cylinders led to asymmetric flow patterns at $Ra = 10^6$. Furthermore, it can be observed that the cylinders' temperatures are not equal within each configuration. Cylinders located in regions where the surrounding air is warmer, or where adjacent cylinders are closer, exhibit higher surface temperatures. For example, in Config. I (Fig. 3.7a), the cylinder located near the top wall reaches a higher temperature than the one near the cold bottom wall. Since the same volumetric heat generation is imposed in all cylinders, those surrounded by warmer air transfer less heat to the fluid (according to Newton's law of cooling), leading to higher cylinder temperatures.

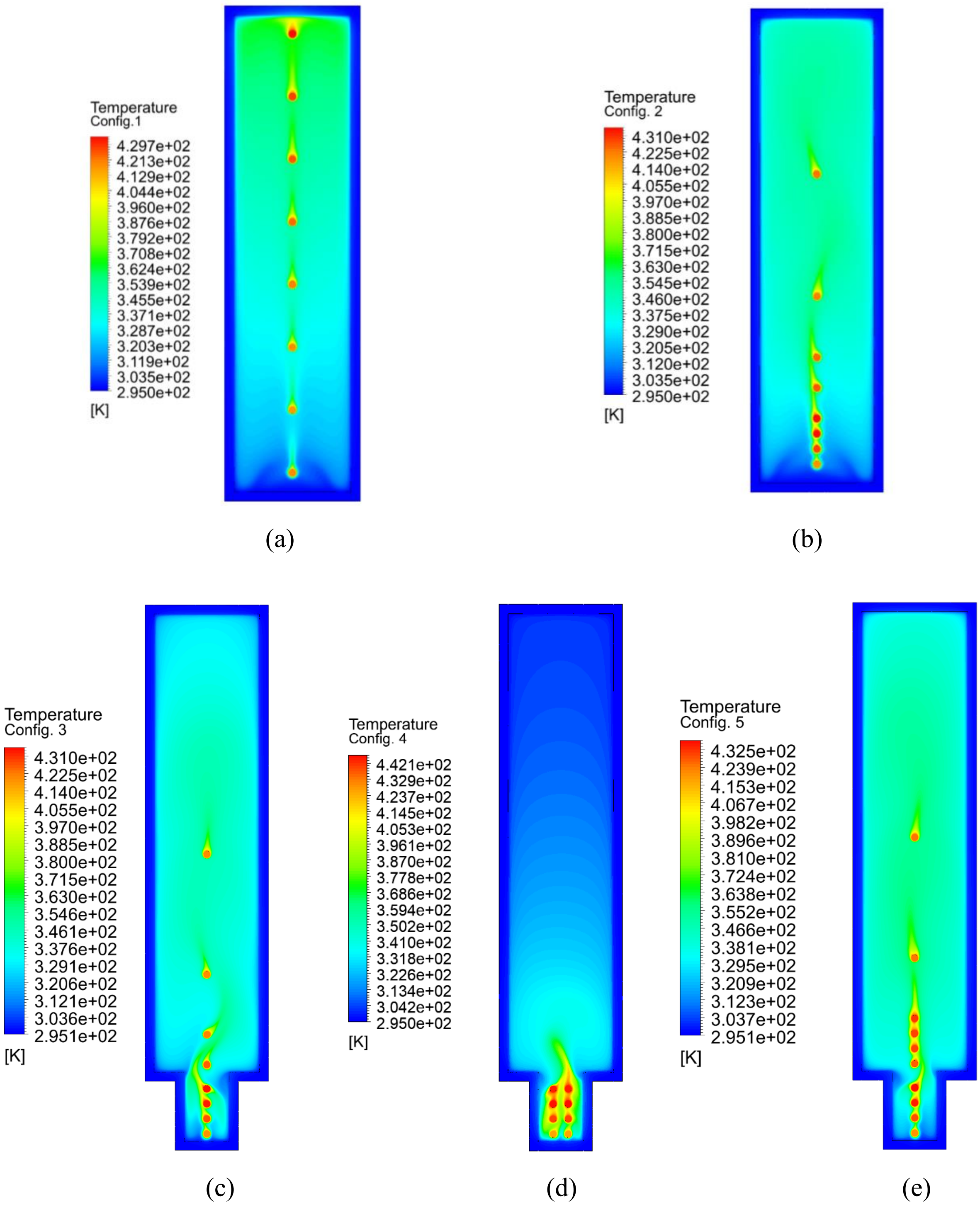

Fig. 3.7. Temperature contours in the enclosure for five different configurations at t = 600 s: (a) Config. I, (b) Config. II, (c) Config. III, (d) Config. IV, and (e) Config. V.

To quantitatively compare the temperature distribution among the different configurations, air temperature profiles were extracted along a vertical reference line located 3 cm to the right of the symmetry line, as shown in Fig. 3.8. The line illustrated in Fig. 3.8b represents the nominal location of the filter backside in the experimental setup described in Chapter 4. This reference line extends from 1 cm above the bottom wall to 1 cm below the top wall to account for the thickness of the filter frame. As evident in Fig. 3.8a, significant differences in temperature uniformity are observed among the five configurations. In Configuration I, the temperature difference along the reference line reaches approximately 65 K, confirming the strong vertical stratification previously observed in the contour plots. In contrast, adopting Configs. III and V reduces this temperature difference to approximately 15 K and 20 K, respectively, indicating a substantially more uniform temperature field within the enclosure.

In addition to the overall temperature difference, the shape of the temperature profiles provides further insight into the flow characteristics within the enclosure. In Config. I, the steep temperature gradient observed in the upper portion of the reference line indicates strong thermal stratification caused by concentrated upward buoyant plumes. This confirms that most of the heat accumulates near the top region due to limited mixing. In contrast, the much flatter profiles in Configs. III and V demonstrate enhanced mixing and more uniform heat distribution, as the heating chamber and redistributed elements weaken the direct plume-driven transport and promote lateral recirculation. Config. IV exhibits a relatively uniform temperature in the lower region but a noticeable drop toward the top, indicating that although preheating occurs in the chamber, the buoyant flow is insufficient to carry heated air effectively throughout the entire enclosure height.

Based on this quantitative assessment, Configs. III and V, which provide the most uniform temperature distributions, are selected for further investigation in Chapter 4 and will be compared with Configuration I when a filter is installed inside the enclosure.

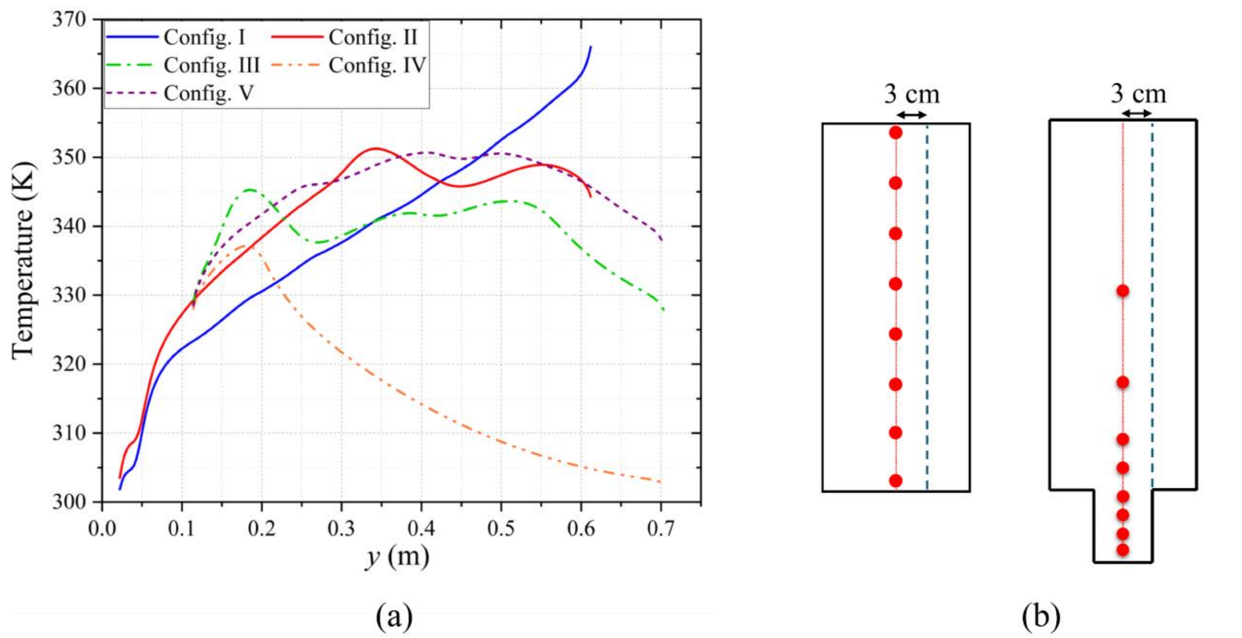

Fig. 3.8. (a) Air temperature profiles for five different configurations at t = 600 s. (b) Schematic representation of the vertical reference line used for data extraction, located 3 cm to the right of the symmetry line.

3.7 Summary of Chapter

This chapter numerically investigated the unsteady turbulent natural convection in an enclosure containing tubular heating elements. Five different configurations were examined by varying the number of heating elements, their spatial arrangement, and the geometry of the enclosure through the addition of a heating chamber.

Ansys Fluent software was implemented for CFD simulation of a two-dimensional, transient, conjugate heat-transfer system with temperature-dependent air properties. A detailed grid-independence study and validation against benchmark results from the literature confirmed the accuracy and reliability of the numerical approach adopted in this work.

The results showed that introducing a heating chamber beneath the frame and redistributing the heating elements to promote preheating and enhanced mixing near the bottom of the enclosure significantly reduced temperature non-uniformity within the cavity. Designs incorporating these features are therefore selected for experimental investigation with filters in Chapter 4 to evaluate the interaction between the heating system and filter performance under realistic operating conditions.

Chapter 4. Natural-Convection-Based Thermal Disinfection of Air Filters: Performance and Energy Evaluation in HVAC Systems

This paper was submitted to the Thermal Science and Engineering Progress.

Mirzazade Akbarpoor, A. Salimi, M., Rasouli, E., Shahbakhti, M., Nouri. A., *Natural-Convection-Based Thermal Disinfection of Air Filters: Performance and Energy Evaluation in HVAC Systems*, Journal of Thermal Science and Engineering Progress, 2026 (Under Review).

4.1 Preface

Bioaerosols can be effectively entrapped within the porous structure of HVAC filters. Nonetheless, conventional filters do not inactivate accumulated/multiplied microorganisms on the filter media, increasing the risk of pathogen release downstream. To address this challenge, this study presents a fanless, energy-efficient technology for the thermal disinfection of filters. During disinfection, buoyancy-driven flow transfers heat to the filter, eliminating the need for recirculating fans and the reliability and maintenance concerns associated with elevated-temperature operation. The system encompasses two identical filtration units operating parallelly, each containing a filter with a minimum efficiency reporting value (MERV) of 11 and tubular heating elements. To reduce the temperature non-uniformity inherent to natural convection, three system configurations were experimentally investigated over a range of heater set-point temperatures. The configurations differed in filter housing design and the arrangement of heating elements. A well-recognized criterion, maintaining a filter temperature of 65 °C for 10 min, was used to determine the required disinfection time and energy. Moreover, the aerodynamic performance of the system was evaluated using an ASHRAE 52.2-compliant wind tunnel at three air velocities (0.5, 0.75, and 1 m/s). The results revealed that the optimal configuration substantially reduces thermal non-uniformity across the filter, enabling the entire filter to reach the disinfection condition within approximately 35 min, with an energy demand of 0.10 kWh. Furthermore, flow characterization tests indicated that the presence of heating elements and duct modifications does not significantly affect filtration efficiency and results in a minor increase in pressure drop during normal filtration operation.

4.2 Introduction

The rapid global spread of airborne infectious diseases over the past two decades, encompassing SARS, H1N1 influenza, and most recently the COVID-19 pandemic, has highlighted the vulnerability of indoor environments to bioaerosol transmission [4–6]. In enclosed spaces, where people spend up to 90% of their daily lives [160], airborne pathogens can remain in the air for several hours and be transmitted over distances of up to hundreds of meters [10–12]. Factors such as population density, inadequate ventilation, and improper operation of HVAC systems further compound the risk, making indoor air quality (IAQ) [16,23,30] and thermal comfort [161–163] critical determinants of public health during pandemics and seasonal outbreaks.

Among engineering controls, filtration is a widely used and cost-effective measure for reducing airborne pathogen concentrations in recirculated air [23]. HVAC filters entrap particles through different mechanisms, offering a continuous means of removing pathogens from the airflow [23,24]. Several studies have demonstrated the effectiveness of HVAC filters in reducing exposure to bioaerosols and, consequently, reducing contamination rates in indoor environments [164–166].

Nonetheless, a growing body of evidence points to a major limitation of filtration-only approaches. HVAC filters accumulate microorganisms during service and can inadvertently become reservoirs for bacterial multiplication and fungal growth. Several field studies have documented the presence of viable bacteria and fungi on used filters in hospitals, commercial buildings, and residential systems [167–171]. Viral RNA of pathogens such as SARS-CoV-2 has also been detected on HVAC filters [172]. Under normal airflow conditions, loaded filters may release a small but measurable fraction of captured bioaerosols downstream [26]. During transient events, such as fan cycling or mechanical vibration, re-entrainment can increase substantially, with reported release fractions as high as 10–25% depending on loading conditions, airflow velocity, and filter media structure [27,28]. These findings underscore the necessity for complementary disinfection strategies that inactivate microorganisms within the filter rather than relying solely on mechanical capture.

Thermal treatment represents one of the most effective and reliable approaches for microbial inactivation [18,78]. Heat penetrates the porous media of filters efficiently [1,59], denaturing proteins and nucleic acids and thereby inactivating a wide spectrum of bacteria, fungi, and viruses [19–21]. Thermal exposure at approximately 65 °C for a duration of 10 min has been reported to substantially decrease the viability of a broad spectrum of HVAC-relevant microorganisms, including *Escherichia coli, Legionella pneumophila, Pseudomonas aeruginosa, Aspergillus spp.*, rhinoviruses, influenza viruses, and coronaviruses [79–84].

Despite the strong potential of heat-based inactivation, a few works have investigated thermally assisted filtration as a feasible approach for deactivating pathogens accumulated on filter media. Xie et al. [173] proposed a solar-assisted air-disinfection concept in which a photovoltaic (PV)-integrated Trombe wall was used to elevate the temperature of air flowing through the system, while a downstream filter collected bioaerosols. The combined effect of solar-induced heating and filtration enabled partial thermal inactivation of Klebsiella pneumoniae during daytime operation. Yu et al. [87] examined self-heating metal foams for capturing and destroying SARS-CoV-2 and *Bacillus anthracis*. Their results demonstrated that, with an electrical power input of 500 W, a pleated nickel foam specimen (24 cm × 30 cm × 1.6 cm) could reach 200 °C, achieving more than 99% inactivation of the collected microorganisms.

An alternative, energy-efficient heat-assisted filtration technology was developed in our prior works [1,60]. Unlike solar-assisted systems, this technology is not constrained by climate conditions or day-time availability, and it does not suffer from the high energy demand and pressure drop related to self-heating metallic filters. Our proposed system consists of two parallel units, each containing HVAC filters and a dedicated heating mechanism that enables continuous air filtration alongside thermal disinfection. By closing the gates of one unit and using internal fans to recirculate heated air to raise the filter temperature, the design effectively minimizes thermal losses and reduces the additional heat load on the HVAC system, while maintaining continuous filtration. The experimental findings demonstrated that a MERV 11 test filter could meet the disinfection target of 65 °C for 10 minutes with a modest energy input (0.11 kWh) and within only 13 minutes.

More recently, this concept was extended to a two-stage filtration configuration in which forced convection within insulated units enabled simultaneous thermal treatment of both a lower-MERV pre-filter and a higher-MERV main filter [59]. These developments highlight the potential of controlled forced convection in enclosed cavities containing filter media to achieve an energy-efficient thermal disinfection. However, the systems still rely on small recirculation fans to transfer heat to the test filters. In enclosures operating at elevated temperatures, fan reliability and maintenance demands increase, introducing long-term operational challenges, particularly for large or remote HVAC installations.

To overcome the limitations of fan-driven systems, natural convection, the focus of this study, can serve as the primary heat-transfer mechanism within insulated disinfection units. By eliminating moving parts (i.e., recirculating fans), buoyancy-driven heating can enhance system robustness, improve reliability, minimize maintenance, and reduce long-term operational costs. However, employing natural convection introduces a complex heat transfer problem. Thermal disinfection of pleated HVAC filters within a cavity constitutes a transient natural-convection process in an enclosure containing a porous medium. Considering the large dimensions of HVAC ducts in real-world applications, and a set point temperature higher than 65 °C for the heat-generating sources (e.g., tubular heating elements), the resulting buoyancy-driven flow can easily become turbulent ($Ra \geq 10^8$)[154].

Although the flow and heat transfer characteristics of buoyancy-driven flow inside rectangular cavities, including porous media, have been extensively studied, covering laminar [104,109,112,113,137,140,141], transitional, and turbulent regimes [108,174–177], to the best of the authors' knowledge, no work has examined natural convection in enclosures containing HVAC-grade porous media (filters). Moreover, the highly pleated structure of filters induces non-uniform thermal resistance, making it even more challenging to achieve spatially uniform surface temperatures, a crucial requirement for effective disinfection.

To address this gap, this study introduces a thermal disinfection approach for HVAC filters that relies on buoyancy-driven natural convection rather than forced airflow. Tubular heating elements are employed as heat sources within insulated enclosures to elevate the filter temperature primarily through buoyancy-driven flow, in contrast to earlier systems that relied on forced convection. To mitigate the temperature non-uniformity inherently associated with natural convection, a heating chamber is incorporated beneath the filter frame, and the configuration of the tubular heating elements is redesigned accordingly. In addition to evaluating heat-transfer performance, this study investigates the impact of these design modifications on airflow characteristics by comparing the particle removal effectiveness and flow resistance of the introduced design with those of a standard HVAC configuration. Section 2 outlines the system architecture and its operating principles in detail.

The main advances introduced in this work are outlined below.

1. Development of an innovative, energy-efficient, fanless air-disinfection technology that integrates air filtration with buoyancy-driven thermal inactivation.
2. Investigation of transient buoyancy-driven heat transfer within an enclosed cavity containing a pleated HVAC filter and multiple tubular heating elements.

3. Systematic evaluation of filter housing geometry, heating-element arrangement, and heater set-point temperature on temperature uniformity, and required time and energy to satisfy disinfection conditions (i.e., 65 °C for 10 min).
4. Experimental assessment of particle removal effectiveness and flow resistance for the introduced design using an advanced test facility complies with the testing requirements specified in ASHRAE Standard 52.2 (i.e., details of this standard are provided in Appendix B) [22].

4.3 Problem Description

Figures 4.1a and 1b depict the working principle of the proposed disinfection technology, comprising a pair of parallel modules arranged within a shared frame. As shown in Fig. 4.2, each unit comprises tubular heating elements, a filter housing, and a filter. During the normal operation, both units remain open and perform filtration, capturing airborne bioaerosols (Fig. 4.1a). After a defined operating period, a selected module is isolated through gate closure, after which tubular heaters are activated to raise the filter temperature to the specified level and sustain it for the required exposure duration. As discussed previously, existing studies suggest that an exposure temperature of 65 °C for 10 min is adequate for inactivating the most common bioaerosols. These parameters can be adjusted for microorganisms with higher thermal resistance. The supplied heat penetrates through the filter depth, inactivating the entrapped or reproduced microorganisms. Meanwhile, the other unit remains open and continues to filter the incoming air. By alternating the process between the two units, continuous filtration and periodic thermal decontamination can be achieved.

As illustrated in Fig. 4.2a, the proposed system in this study relies entirely on natural convection, without any mechanical assistance or fans to transfer heat to the filter surface. In this configuration, the tubular heating elements are positioned at equal spacing, which can lead to significant temperature non-uniformity due to buoyancy-induced upward motion of the heated air. To mitigate this effect, the unit design was modified (Fig. 4.2b) by adding a heating chamber beneath the frame and repositioning the heating elements at non-uniform vertical distances. The dimensions and layout of the developed disinfection system are shown in Fig. 4.2c. Further details of the considered configurations designed to address the temperature non-uniformity of the buoyancy-driven flow are provided in Section 4.4.1.

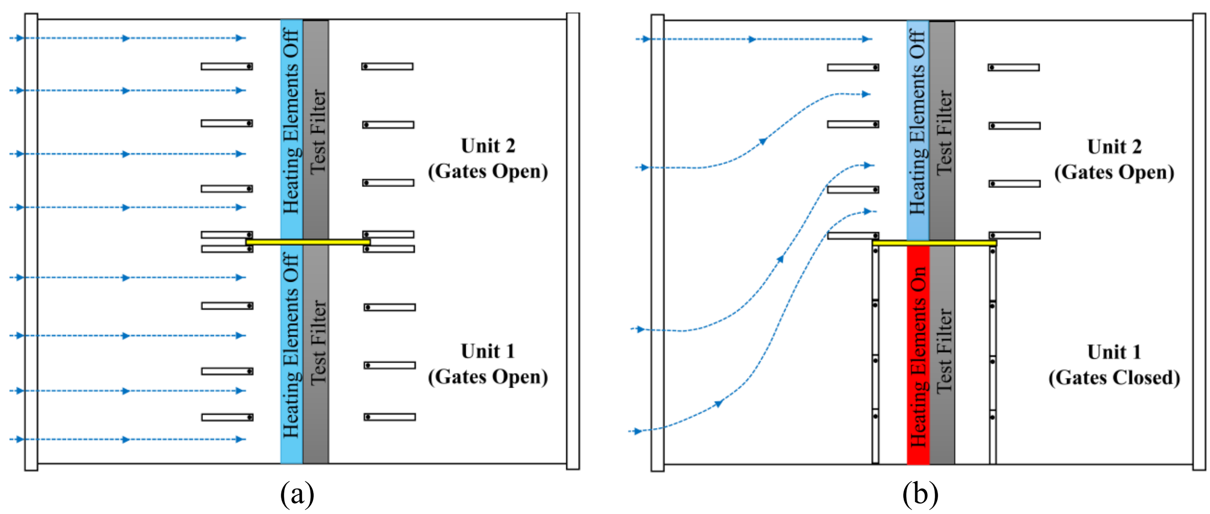

Fig. 4.1. Schematic illustrations of the operation of the disinfection units under two modes: (a) open-gates mode, where two units remain open, and (b) closed-gates mode, where a single module is isolated for thermal inactivation.

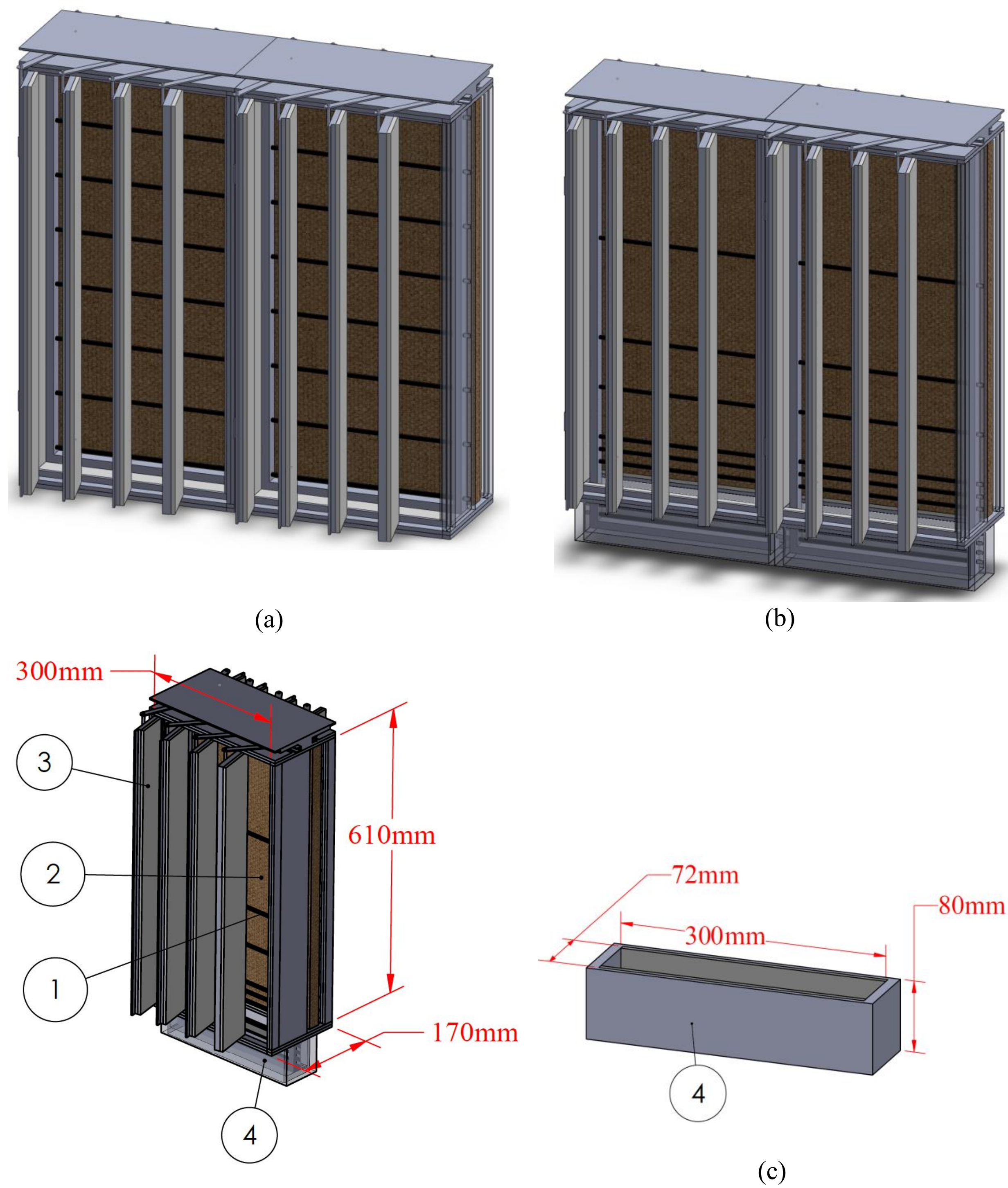

Fig. 4.2. Schematic representations of (a) the standard units with heating elements positioned at equal distances, (b) the modified units, where heating chambers are added beneath the units and the heating elements are at varying distances, and (c) the dimensions and layout of the introduced disinfection system, including 1: tubular heating elements, 2: test filter, 3: gates, and 4: chamber.

4.4 Methodology

The methodology adopted in this study comprises two parts: the development of an experimental setup to monitor the thermal performance of the buoyancy-driven system, and the implementation of a wind tunnel to evaluate the particle removal effectiveness and flow resistance of the proposed technology. These experimental setups are described in detail in Sections 4.4.1 and 4.4.2, respectively.

4.4.1 Heat Transfer Setup

Figure 3 demonstrates the test apparatus used to assess the heat transfer and energy consumption of the proposed disinfection system. The setup includes the prototype shown in Fig. 4.1, constructed from polycarbonate sheets. The prototypes are installed inside an aerosol wind tunnel, which is described in Section 4.4.2.

As noted earlier, to reduce temperature non-uniformity caused by buoyancy-driven flow in Config. 1, a medium-scale heating chamber, 6 cm wide and 8 cm tall, is added beneath the filter housings in the modified designs to accommodate a portion of the tubular heating elements. The chamber dimensions are selected as a representative, fixed geometry compatible with standard HVAC ductwork and typical retrofit constraints. The chambers are intended to provide adequate space for buoyancy-driven flow development and thermal mixing beneath the filter without introducing excessive flow resistance. Accordingly, the objective of this study is to evaluate the feasibility and thermal performance of natural-convection-based filter disinfection for this configuration, rather than to optimize chamber dimensions. Furthermore, unlike Config. 1, where eight tubular heating elements are spaced uniformly, Configs. 2 and 3 employ eight and ten heating elements, respectively, positioned at varying distances, as indicated in Fig. 4. Each tubular heating element has a nominal power of 300 W, a diameter of 8 mm, and a length of 30 cm. To regulate the heater's electrical current, pairs of heating elements are wired in series, and these pairs are then connected in parallel. In addition, as shown in Fig. 4.4, the internal walls of all prototypes are covered with aluminum foil to reduce radiative losses to the surroundings.

Figure 4.3 illustrates the experimental apparatus employed for thermal and energy performance assessment of the introduced disinfection system. A PID controller (OMEGA) is used to regulate the temperature of the heating elements. The test filter is a MERV 11 polyester filter, a representative mid-efficiency filter widely used in commercial and institutional HVAC systems, with a width of 30 cm, a height of 61 cm, and a thickness of 2.5 cm. The filter incorporates a medium with a thickness of 0.66 mm and a pleat packing density of 0.4 pleats per centimeter. As shown in Figs. 5a and b, 14 T-type thermocouples (OMEGA), each 0.08 mm in diameter and accurate to ±0.5 °C, are attached to the front and rear faces of the filter. In addition, two K-type thermocouples (0.08 mm diameter, ±1.0 °C accuracy) are attached to the heating element that reaches the highest temperature to monitor and control its set-point. Experimental observations indicate that the hottest heating element is the uppermost element in Config. 1 and the third element from the bottom in Configs. 2 and 3. All thermocouples are connected to a data logger (National Instruments) with 16 channels for temperature acquisition.

To determine the optimal heating performance, six set-point temperatures, including 100, 120, 140, 160, 170, and 180 °C, are tested for each configuration shown in Fig. 4.4. The filter-surface temperatures are continuously monitored, and once the disinfection criteria (65 °C for 10 minutes) are achieved, the total electrical energy consumption is recorded using a power meter (Poniie-PN2000). All heat-transfer experiments are conducted at an air flow of 2100 m^3/h, representing the maximum operating capacity of the centrifugal fan driving the test loop.

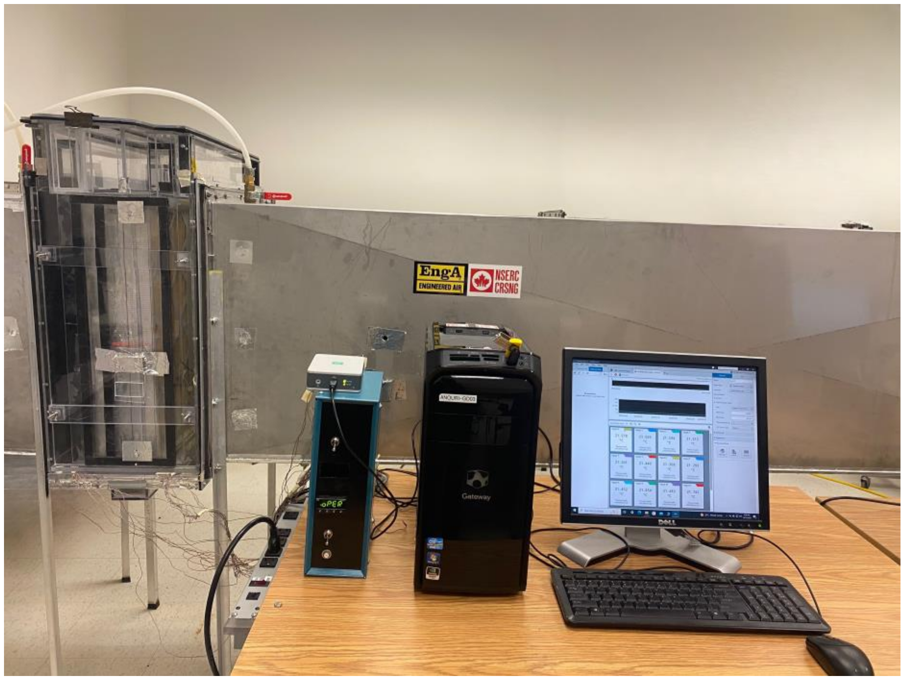

Fig. 4.3. The experimental setup of the temperature monitoring and energy consumption measurement of the proposed disinfection technology.

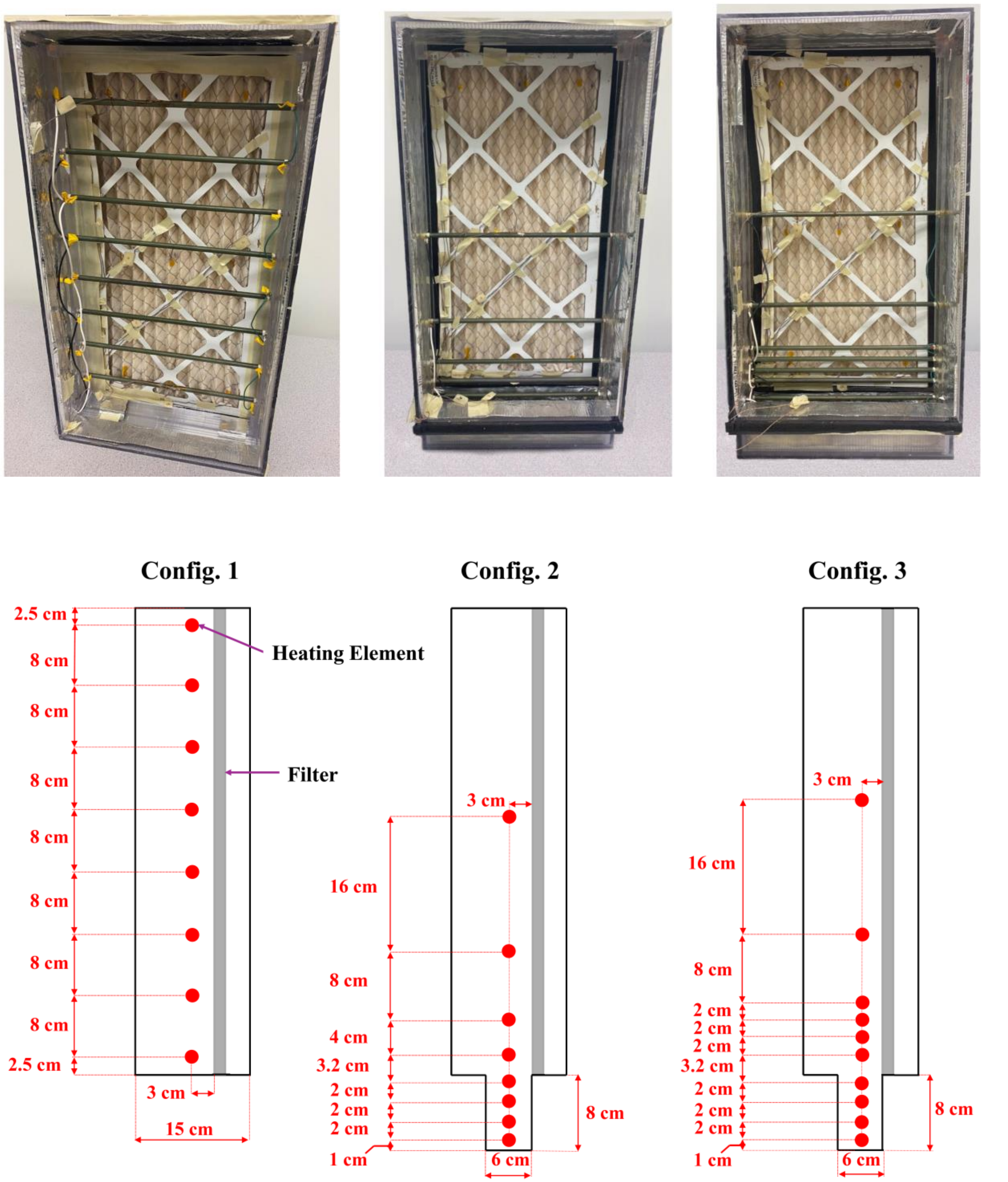

Fig. 4.4. Manufactured prototypes and schematic dimensions of the three configurations used in the heat-transfer experiments, including Config. 1, the standard unit equipped with eight heating elements spaced uniformly; Config. 2, a modified unit incorporating a heating chamber beneath the frame and eight heating elements arranged at non-uniform distances; and Config. 3, a modified unit incorporating a heating chamber beneath the frame and ten heating elements positioned at varying distances.

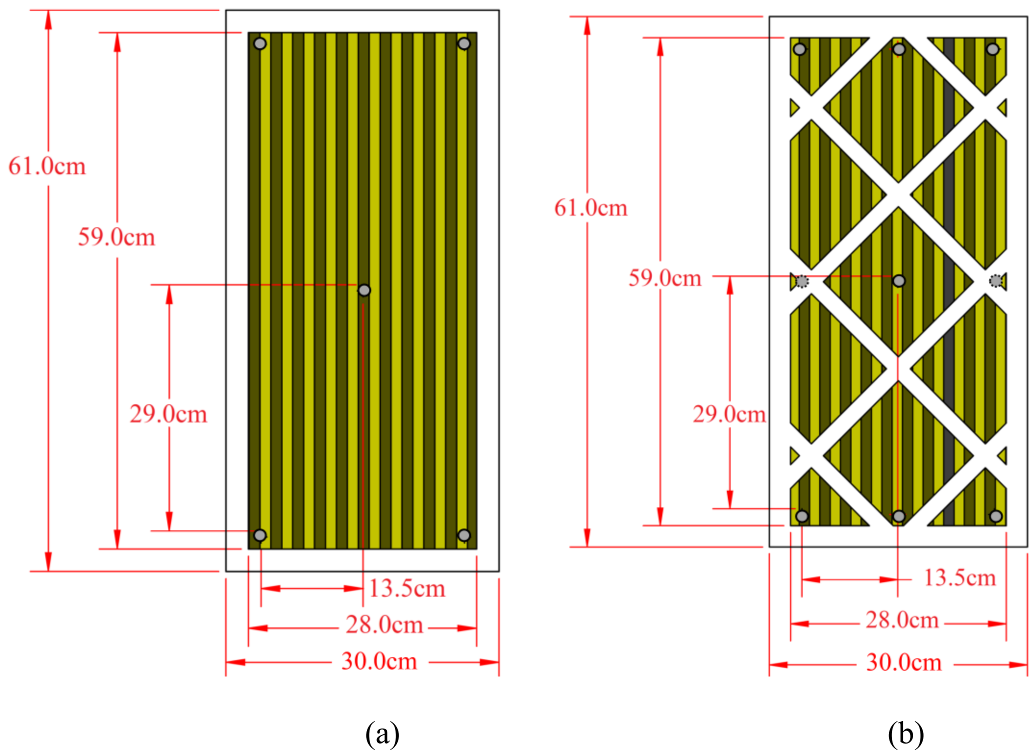

Fig. 4.5. Schematic representations of the thermocouple attachment points on the test filter, showing (a) the front face and (b) the rear face.

4.4.2 Advanced Filtration Efficiency Testing Facility

4.4.2.1 Experimental Apparatus

Figure 4.6 presents a layout of the closed-loop wind tunnel used to quantify particle removal performance and associated flow resistance of the proposed technology. The wind tunnel consists of an 18-m-long stainless-steel square duct with a 61 cm × 61 cm cross section. The test apparatus is designed in accordance with the ASHRAE 52.2 standard [22]. Detailed descriptions of the wind tunnel design and instrumentation are provided in our previous studies [1,59]. In this section, only the main components and testing principles are described.

As shown in Fig. 4.6, a centrifugal fan manufactured by Rosenberg recirculates air through the wind tunnel at the desired airflow rate. Aerosols are generated from a KCl solution using a TOPAS polydisperse generator and injected into the system. A TOPAS optical particle counter, coupled to a programmable switching valve, collects isokinetic samples upstream and downstream of the disinfection units. In addition, the pressure drop across the disinfection units is measured using a pressure transmitter (OMEGA) interfaced with an eight-channel data logger (National Instrument).

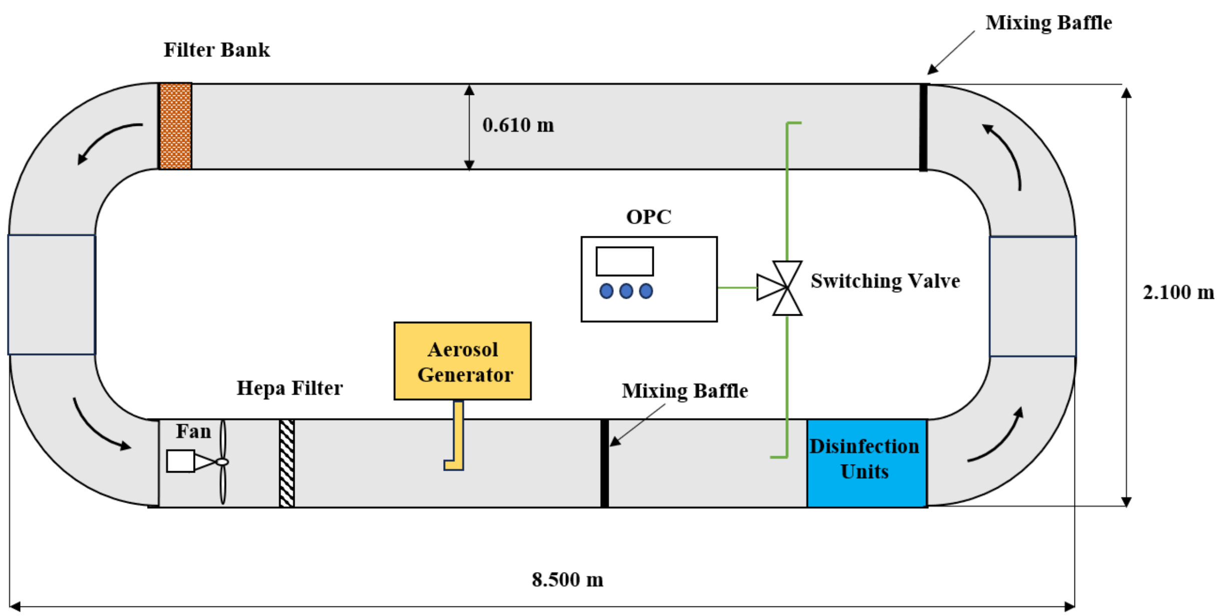

Fig. 4.6. A schematic view of the ASHRAE 52.2 complaint closed-loop aerosol wind tunnel.

4.4.2.2 Testing Methodology

To measure the filtration efficiency, the experiment is conducted in three steps. First, three background samples are collected sequentially at sampling points located before and after the system. Each sampling lasts one minute, followed by a one-minute rinse period before the subsequent measurement. In the second step, the aerosol generator is turned on, and sampling begins once the aerosol concentration stabilizes. Four upstream samples and three downstream samples are collected. One additional upstream sample is required because, according to ASHRAE 52.2, penetration is determined by comparing a downstream measurement with the average of the upstream measurements taken immediately before and after it. In the third step, the aerosol generator is turned off, and three additional background measurements are collected at both sampling locations. Finally, to determine the correction factor (R_{ave}), the disinfection system is removed from the wind tunnel, and all three steps are repeated.

It should be noted that each filtration efficiency test is repeated three times to ensure accurate and repeatable results.

The filtration efficiency of the proposed system can be calculated using the following formula:

$$\eta = (1 - \frac{P_{ave}}{R_{ave}}) \times 100 \tag{4.1}$$

in which, P_{ave} denotes the particle penetration, determined as follows:

$$P_{ave} = \frac{1}{n} \sum_{i=1}^{n} \frac{C_{i,o} - C_{b,ave}}{U_{i,e} - U_{b,ave}} \tag{4.2}$$

where $C_{b,ave}$ and $U_{b,ave}$ are the average downstream and upstream background concentrations, respectively. $C_{i,o}$ represents the observed downstream concentration directly measured by the particle counter. $U_{i,e}$ denotes the estimated upstream particle concentration, calculated as the average of the upstream samples collected before and after each downstream measurement.

In this study, the most optimal configuration in terms of heat transfer performance is first identified (Section 4.4.1). An optimal configuration is defined as one that meets the disinfection criteria in the shortest time, with lower energy consumption, and with reduced temperature non-uniformity across the filter surface. This configuration is then compared with the standard unit without heating elements in terms of filtration efficiency and pressure drop (Figs. 4.7a and b). For both cases, two operating modes are considered: the open-gates mode, in which both parallel units are open, and the closed-gates mode, in which only one unit is open. These tests are conducted at three prescribed duct air velocities: 0.5 m/s, 0.75 m/s, and 1.0 m/s. Notably, operating at duct velocities of 1.0 m/s or lower ensures that the closed-gates mode remains fully compliant with the isokinetic sampling requirements of ASHRAE 52.2.

(a) (b)

Fig. 4.7. Schematic representation of two side-by-side units used for flow characterization and filtration efficiency testing: (a) standard units (regular filter housing without heating elements) and (b) disinfectable units (modified filter housings incorporating a heating chamber and tubular heating elements).

4.5 Results and Discussion

4.5.1 Thermal Performance of the System

Figures 4.8a-f depict the temporal temperature variation of the MERV 11 test filter at different heating element set-point temperatures for Configuration 1 (no chamber and equal spacing between the eight elements). As evident from the results, this configuration exhibits significant temperature non-uniformity across the filter surface due to the formation of a strong buoyant plume around the heating elements. Increasing the heating element set-point temperature from 100 °C to 180 °C further amplifies this non-uniformity. This can be attributed to an increase in the Rayleigh number at higher temperatures, an indication of stronger natural convection flow that transfers a larger portion of heat toward the upper region of the enclosure. As shown, when the set-point temperature rises from 100 °C (Fig. 4.8a) to 180 °C (Fig. 4.8f), corresponding to an increase in the Rayleigh number from 1.05×10^9 to 1.26×10^9, the temperature difference across the filter surface increases from approximately 25 °C to over 60 °C. Furthermore, increasing the heating element set-point temperature beyond 180 °C, or maintaining 180 °C for more than 20 minutes, is not recommended, as the filter temperature exceeds 100 °C, potentially compromising its structural integrity and degrading its performance [178,179].

Figures 4.9a–f depict the temperature box plots of the test filter over time at different heating element set-point temperatures for Configuration 2, encompassing a chamber and eight heating elements positioned at varying distances. A comparison between Figs. 4.8 and 4.9 indicates that, at a constant heating element temperature, employing Config. 2 significantly reduces temperature non-uniformity across the filter surface compared to Config. 1. As an example, at a heater set-point of 180 °C, the temperature difference across the filter surface after one hour was reduced from about 60 °C in Config. 1 (Fig. 4.8f) to roughly 22 °C in Config. 2 (Fig. 4.9f). This improvement demonstrates that incorporating a chamber with a denser arrangement of heating elements near the bottom of the unit frame mitigates the non-uniformity induced by natural convection. The chamber, accommodating heating elements beneath the unit frame, effectively acts as a mixing plenum, driving preheated air upward toward the lower section of the filter and ensuring a more uniform lateral heat distribution compared to Config. 1. Furthermore, unlike Config. 1, the filter in Config. 2 consistently reaches the required 65 °C disinfection threshold across its entire surface at set-point temperatures of 170–180 °C.

Figures 4.10a-f demonstrate the temperature evolution of the filter over time at heating element set-point temperatures ranging from 100 °C to 180 °C for Configuration 3. A comparison between Fig. 4.10 and the corresponding results in Figs. 4.8 and 4.9 shows that, while Config. 3 exhibits substantially lower temperature non-uniformity than Config. 1, it shows inferior thermal uniformity compared to Config. 2. Specifically, at a constant heating element set-point temperature, adding two additional tubular elements in the main unit section of Config. 3 increases temperature non-uniformity relative to Config. 2. For instance, at a set-point temperature of 170 °C, the temperature difference across the filter surface after one hour is approximately 22 °C in Config. 2 (Fig. 4.9e), whereas it rises to about 28 °C in Config. 3 (Fig. 4.10e). This is primarily due to the fact that, while employing ten tubular elements in Config. 3 instead of eight in Config. 2 increases the total heat input, it also intensifies the buoyancy-driven circulation within the main unit, resulting in a stronger upward thermal plume and reduced thermal uniformity. As shown in Figs. 4.9 and 4.10, even though the average filter temperature in Config. 3 is slightly higher than that in Config. 2, the greater temperature non-uniformity leads to a delayed achievement of the disinfection condition.

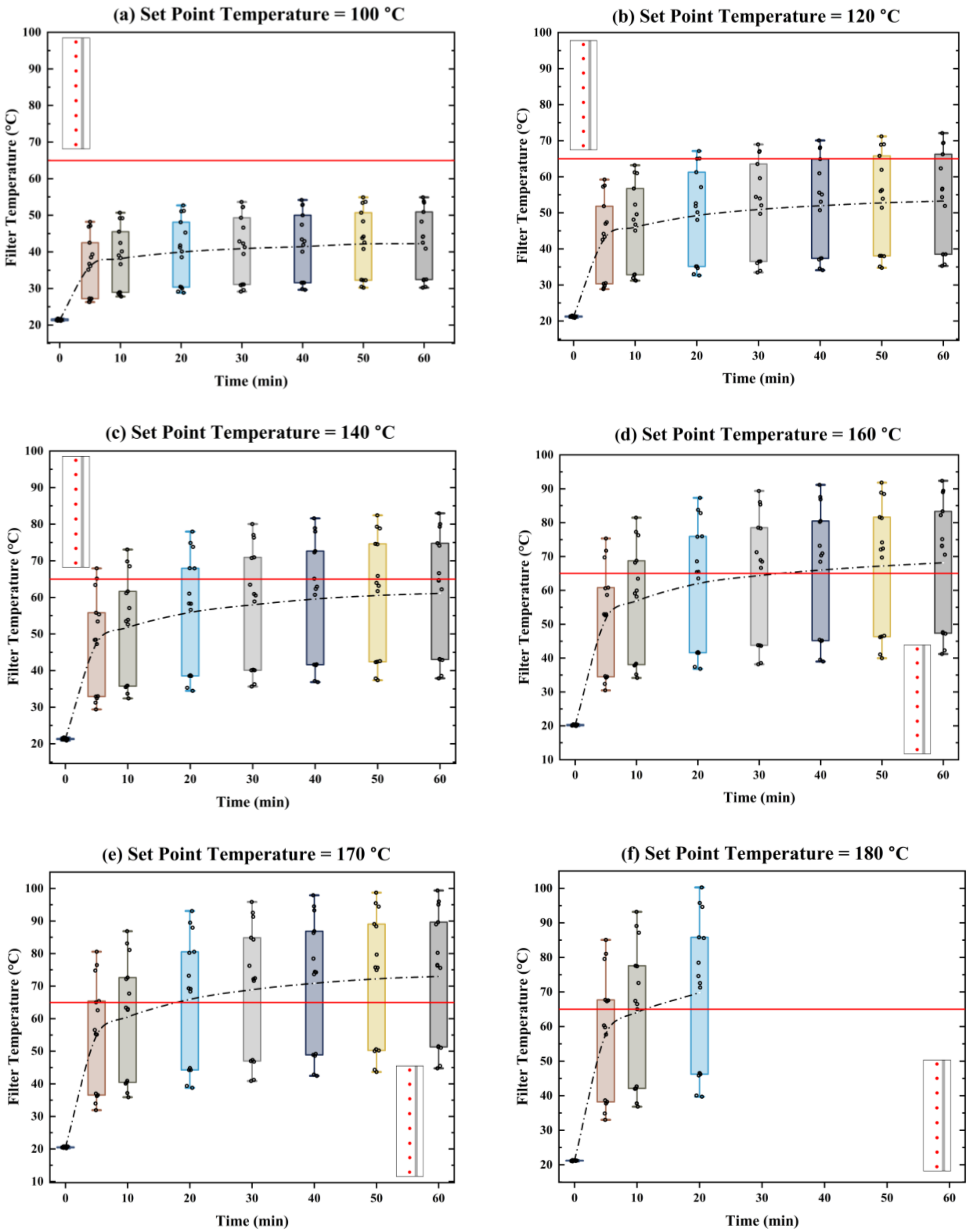

Fig. 4.8. Temporal evolution of filter temperature for Configuration 1 (unit with no chamber, and equal spacing between the eight elements) at different heating element set-point temperatures: (a) 100 °C, (b) 120 °C, (c) 140 °C, (d) 160 °C, (e) 170 °C, and (f) 180 °C. A simplified schematic of Config. 1 is embedded within the subfigures for reference, while detailed geometry is provided in Fig. 4.4. The 65 °C inactivation criterion is shown as a horizontal reference line.

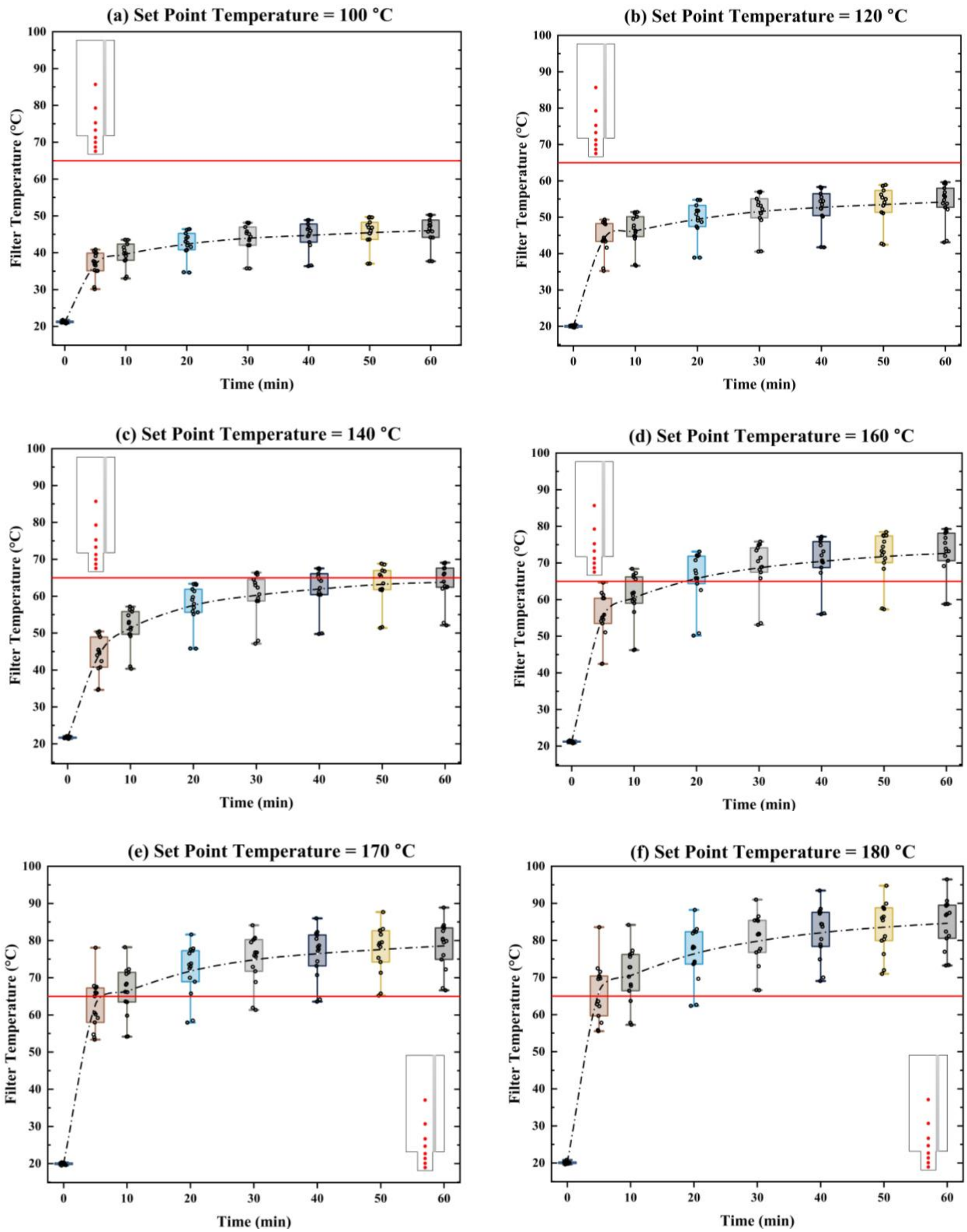

Fig. 4.9. Temporal evolution of filter temperature for Configuration 2 (unit with chamber and eight heating elements positioned at varying distances) at different heating element set-point temperatures: (a) 100 °C, (b) 120 °C, (c) 140 °C, (d) 160 °C, (e) 170 °C, and (f) 180 °C. A simplified schematic of Config. 2 is embedded within the subfigures for reference. The 65 °C inactivation criterion is shown as a horizontal reference line.

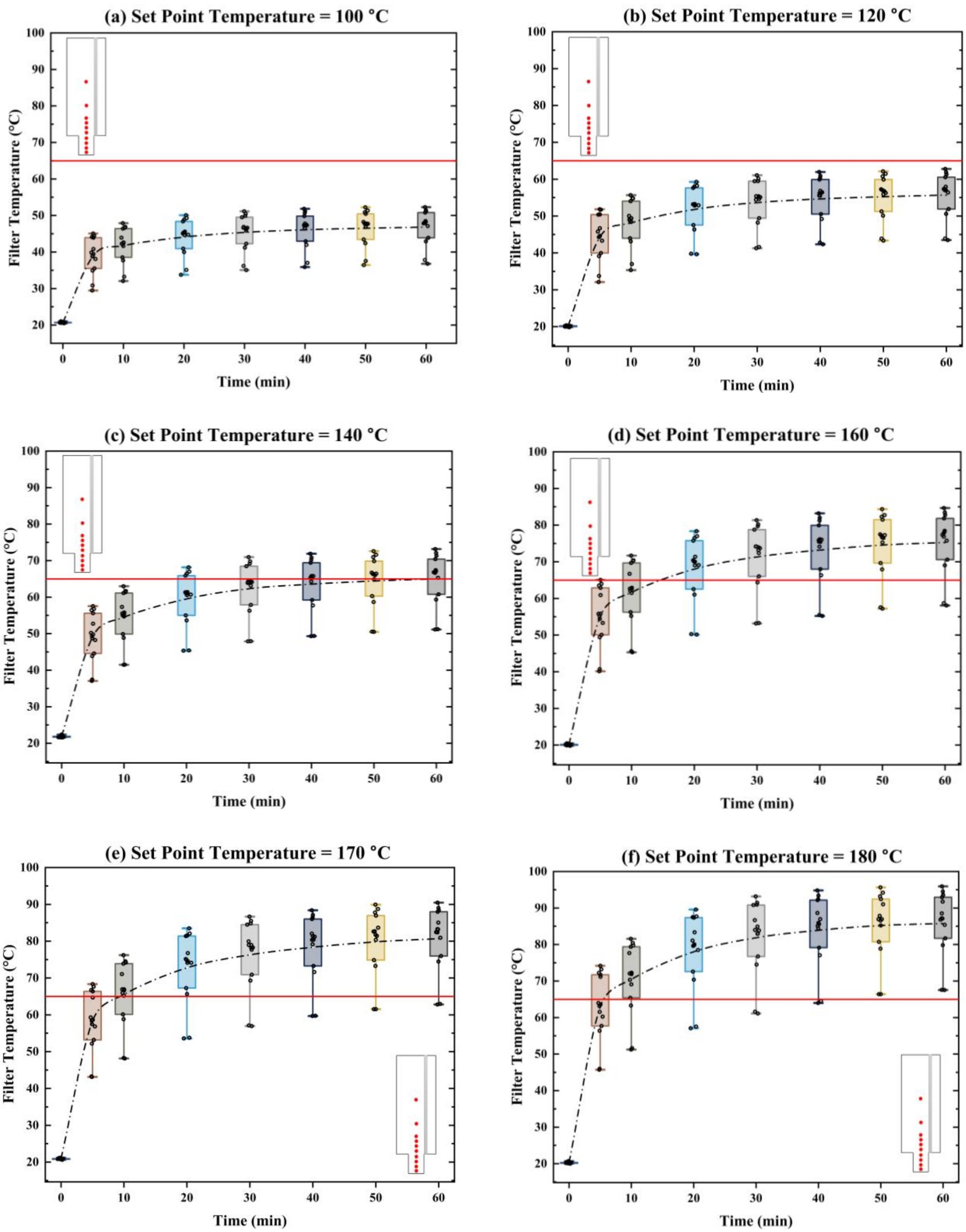

Fig. 4.10. Temporal evolution of filter temperature for Configuration 3 (unit with chamber and ten heating elements positioned at varying distances) at different heating element set-point temperatures: (a) 100 °C, (b) 120 °C, (c) 140 °C, (d) 160 °C, (e) 170 °C, and (f) 180 °C. A simplified schematic of Config. 3 is embedded within the subfigures for reference. The 65 °C inactivation criterion is shown as a horizontal reference line.

4.5.2 Energy Demand Evaluation

Figure 4.11 compares the required energy consumption and operating duration among the tested configurations that achieved the literature-based disinfection criterion, reaching 65 °C and maintaining it for 10 minutes. As shown in Fig. 4.11, adopting Config. 2 with a heating element set-point temperature of 180 °C provides the filter disinfection condition in 35 minutes (25 minutes to reach 65 °C plus 10 additional minutes to ensure complete inactivation of captured bioaerosols) with an energy consumption of only 0.10 kWh per disinfection cycle. This energy requirement is substantially lower than that of Config. 3, which requires approximately 50 minutes and consumes 0.14 kWh to meet the same disinfection condition. Therefore, among all tested cases, Config. 2 offers the most optimal performance, as it meets the disinfection criteria faster, consumes less energy, and maintains better temperature uniformity across the filter surface.

The proposed system in this study operates solely based on natural convection, with no mechanical assistance or fan used for heat transfer. Comparing the present system with the heat-driven filter disinfection technology introduced in Ref. [1] shows that the required energy for disinfecting the same test filter is comparable or even lower (0.10 kWh in the present study versus 0.11 kWh in Ref. [1]). Although the forced-convection-based system in Ref. [1] achieved disinfection in 13 minutes, which is shorter than the 35 minutes required by the present free-convection system, this difference has a negligible effect on the overall energy demand of the HVAC system's central fan. Moreover, eliminating the recirculating fan in the proposed system enhances reliability, as it removes the need for axial fans that would otherwise have to operate at elevated air temperatures (up to 105 °C) and therefore require frequent maintenance.

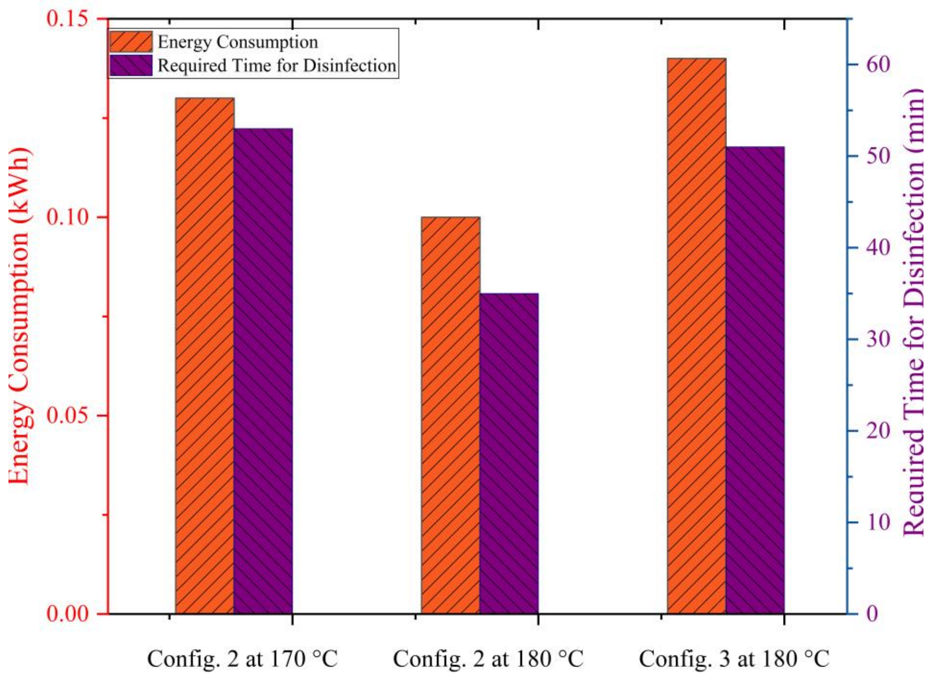

Fig. 4.11. Comparison of electrical energy consumption and the required time to reach the disinfection conditions for configurations that successfully achieved the disinfection conditions.

4.5.3 Filtration Efficiency of the Disinfection System

Figures 4.12a-c illustrate the size-resolved particle removal efficiencies of the standard (Fig. 4.7a) and disinfectable units (Fig. 4.7b) under different operating modes and duct velocities. The standard units consist of two side-by-side filter housings that can be opened or closed and contain no chamber or heating elements. The disinfectable units correspond to Config. 2, in which a chamber and eight heating elements with varying spacing were added downstream of the filter.

According to Figs. 4.12a-c, at all tested duct velocities (0.5, 0.75 and 1 m/s), the filtration efficiencies of the standard and disinfectable units are nearly identical in the open-gates mode, where both units are open. This indicates that incorporating a chamber and heating elements downstream of the filters has only a minor influence on particle capture performance. Similarly, in the closed-gates mode, where one of the two parallel units is sealed, the size-resolved efficiencies of the standard and disinfectable units remain comparable.

A more pronounced difference emerges when comparing the open- and closed-gates modes for each unit type. Closing one unit forces the entire flow to pass through the adjacent unit, effectively doubling filtration face velocity. This increase in face velocity reduces the removal of submicron particles, as diffusion-driven capture (Brownian motion) becomes less effective at higher velocities. Conversely, the capture of particles larger than 1 μm increases due to enhanced inertial impaction at elevated velocities. These trends are consistently observed across all three duct velocities.

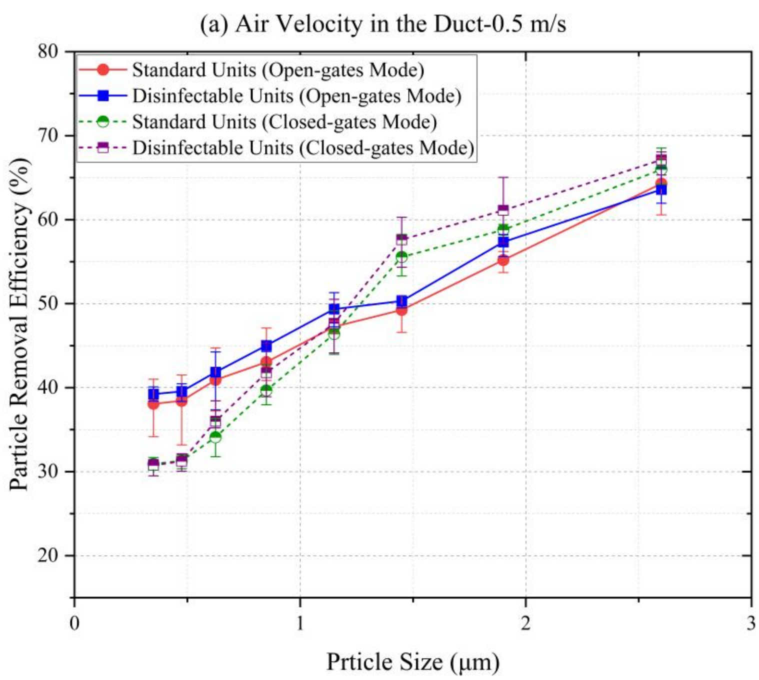

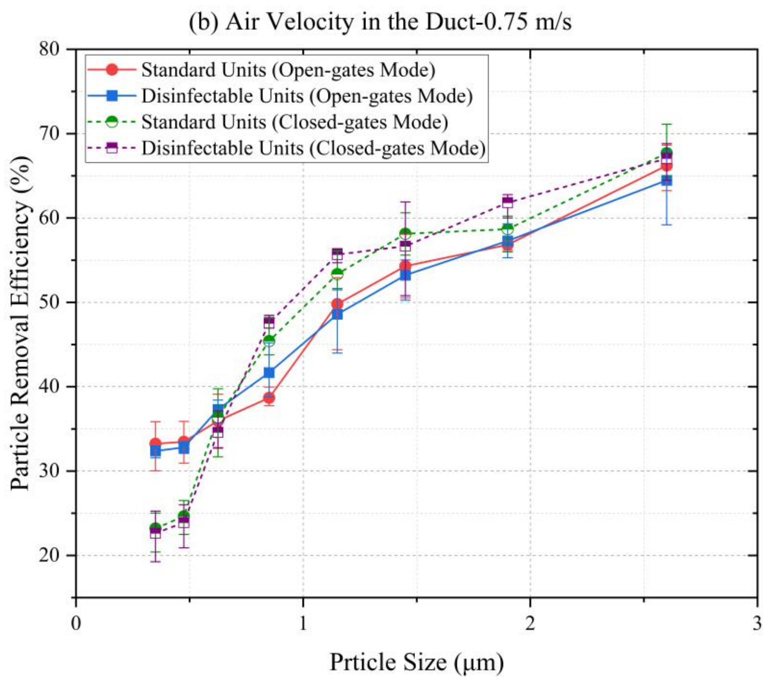

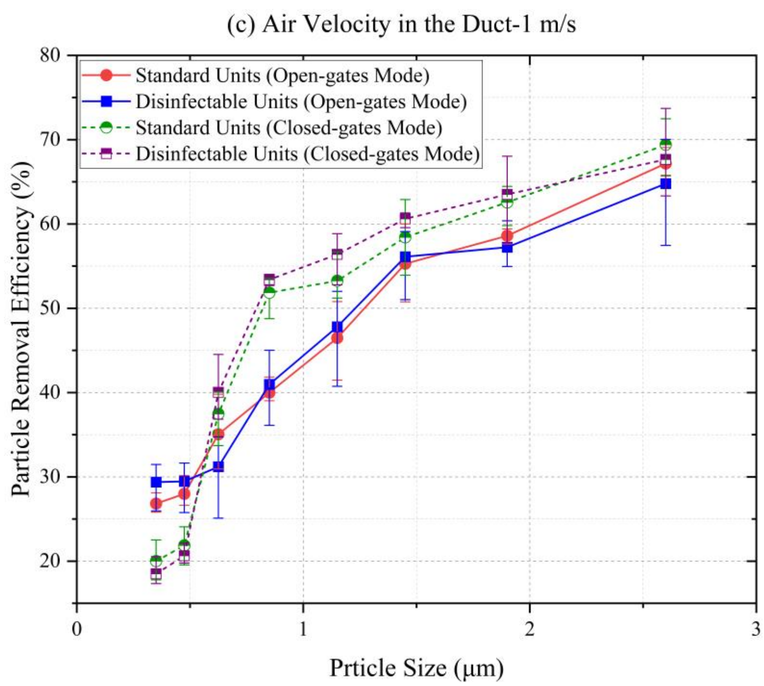

Fig. 4.12. Size-resolved filtration efficiency of the standard units (two side-by-side filter housings containing MERV 11 test filters) and the disinfectable units (the same filter housings modified by adding a chamber and eight heating elements downstream of the MERV 11 test filters) under two operating modes: open-gates mode (both units open) and closed-gates mode (one unit closed). Results are shown for air velocities of (a) 0.5 m/s, (b) 0.75 m/s, and (c) 1 m/s.

4.5.4 Pressure Drop of the System

Figure 4.13 depicts the pressure drop of the disinfectable and standard units at different airflow rates under both open- and closed-gates operating modes. In the open-gates mode, where both parallel units are open, the pressure drop increases linearly with the airflow rate for both configurations. This trend is consistent with Darcy's law [98], which indicates that the pressure loss across the filter varies linearly with volumetric flow rate at low velocities. A comparison between the two configurations shows only a minor increase of approximately 5 Pa in the disinfectable units, indicating that adding the downstream chamber and heating elements introduces only a small additional resistance when both units are open.

When one of the units is closed, the pressure drop for both configurations rises substantially compared with the open-gates mode, nearly tripling at a flow rate of 2000 m^3/h, and the pressure–flow relationship becomes nonlinear. Closing one unit forces the entire airflow through the adjacent unit, doubling the filter face velocity. At these higher velocities, inertial effects become comparable to viscous drag, so both linear (Darcy) and quadratic (inertial) terms contribute to the pressure drop. The difference in pressure drops between the disinfectable and standard units is also more pronounced in the closed-gates mode (about 15 Pa), mainly due to additional drag from the heating elements and contraction–expansion losses in the chamber.

Although temporary gate closure increases pressure drop during the disinfection process, the impact on total HVAC fan energy use is very small. Each disinfection cycle lasts only about 35 minutes, which is negligible compared to the HVAC system's full operational period. The only practical requirement is to ensure the HVAC fans can supply the necessary airflow during this short-term increase in system pressure drop.

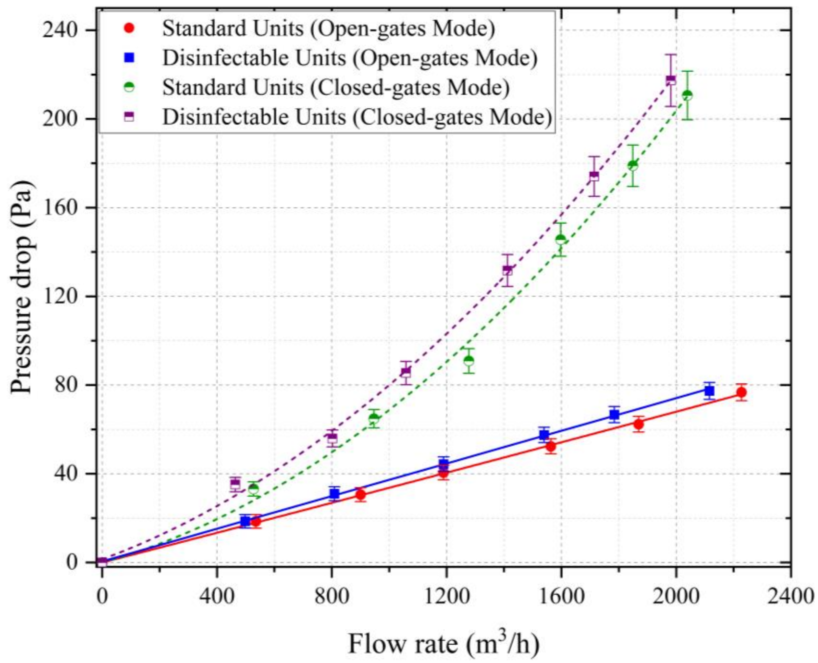

Fig. 4.13. A comparison between the pressure drop of the standard and disinfectable units at different airflow rates under two operating modes: open-gates mode (two units open) and closed-gates mode (single unit closed).

4.6 Conclusions

This study examined the feasibility of disinfecting HVAC filters using a buoyancy-driven, fan-independent thermal process. In the proposed system, heat generated by tubular heating elements was transferred to the filter media through natural convection within an insulated housing. The effect of heating element arrangement and the inclusion of a heating chamber beneath the disinfection unit on temperature uniformity, disinfection duration, and energy demand was systematically examined. Experiments were conducted at six heater set-point temperatures ranging from 100 to 180 °C, using a disinfection criterion of maintaining the filter at 65 °C for 10 min. Moreover, the particle removal effectiveness and flow resistance of the system were evaluated using an ASHRAE 52.2–compliant filtration test facility under both normal operation (open-gates mode) and disinfection operation (closed-gates mode), at different duct velocities. The principal findings of this work are summarized as follows.

(1) With eight heating elements equally spaced and without employing the heating chamber beneath the filter housings (Config. 1), the disinfection criteria cannot be achieved over the entire filter surface within a reasonable time frame without causing filter degradation.

(2) Introducing a heating chamber and repositioning the eight heating elements with a higher density near the lower section of the unit (Config. 2) substantially improved temperature uniformity across the filter. At a heater set-point of 180 °C, this configuration achieved the prescribed disinfection condition within 35 min, with an energy consumption of approximately 0.1 kWh per cycle.

(3) At a constant heater set-point temperature, adding additional heaters in the main unit section (Config. 3), intensified the natural convection circulation within the main unit, resulting in a stronger upward thermal plume and reduced thermal uniformity across the filter, and consequently delayed the disinfection period compared to Config. 2.

(4) At all duct velocities, incorporating the chamber and heating elements downstream of the test filter has a negligible impact on size-resolved particle removal. During disinfection, however, closure of one unit increased the face velocity through the remaining open filter, decreasing submicron particle removal while increasing the capture of larger particles.

(5) Adding the chamber and heating element introduced only a small additional resistance during the normal operation. During the disinfection process, although temporary gate closure almost tripled the pressure drop, the impact on total HVAC fan energy use is limited. Each disinfection cycle lasts only about 35 minutes, which is negligible compared to the HVAC system's full

operational period. The only practical requirement is to ensure the HVAC fans can supply the necessary airflow during this short-term increase in system pressure drop.

Acknowledgements

This research was supported by the Natural Sciences and Engineering Research Council of Canada (NSERC) via the Alliance program (Grant No. 567653-21) and by Engineered Air through its endowed support of HVAC Engineering at the University of Alberta.

Chapter 5. Forced-Convection-Based Thermal Disinfection of Air Filters: Performance and Energy Evaluation in HVAC Systems

This paper was published in the Journal of Building Engineering.

Mirzazade Akbarpoor, A., Salimi, M., Rasouli, E., Shahbakhti, M., Nouri. A., *A heat-driven disinfection technology for enhancing indoor air quality in HVAC Systems*, Journal of Building Engineering, 2025 (Published).

5.1 Preface

Heating, ventilation, and air conditioning (HVAC) filters are traditionally deployed to control airborne pathogens. However, filters may accumulate microbes over time and become breeding grounds for pathogens. Any disturbance may release some of these microorganisms into the environment. This study proposes a novel, energy-efficient air disinfection approach employing recirculating warm air sequentially within two side-by-side enclosures to inactivate microorganisms captured in HVAC filters. An experimental setup assesses the impacts of warm inlet temperature and air recirculation rate within the disinfection units on the heat transfer performance of the system. Furthermore, a closed-loop aerosol wind tunnel accommodating the technology prototype has been constructed per ASHRAE 52.2 to evaluate the filtration efficiency and pressure drop at various duct airflow rates. The test filter has a Minimum Efficiency Reporting Value (MERV) of 11. The test filter reached 65 °C in about 3 minutes under optimal conditions and was maintained at or above this temperature for 10 minutes to meet literature-based thermal inactivation criteria. The total energy consumption per disinfection cycle was 0.11 kWh. During normal operation, the system maintained filtration efficiency equivalent to that of a standalone filter, with a negligible increase in pressure drop. In disinfection mode, the submicron particle removal efficiency decreased, while large-particle removal increased, and the pressure drop rose significantly (140 Pa at 2000 m^3/h), but only during a short period (13 minutes), resulting in a minimal impact on the overall HVAC fan energy use. This study provides practical insights for HVAC system designers and facility managers on integrating energy-efficient disinfection technology into buildings to improve indoor air quality.

5.2 Introduction

Airborne pathogens are responsible for the spread of the most recent pandemics, such as H1N1 flu (also known as swine flu) and the new coronavirus (SARS-CoV-2), as well as its highly transmissible variants (Delta and Omicron) [4–6]. The virulence of infectious and lethal diseases is increasing due to globalization, increased travel and trade, urbanization, population growth in cities, changes in human behavior, the resurgence of pathogens, and the improper use of antibiotics [7]. The health and economic repercussions of pandemics are devastating [8]. For instance, according to the World Health Organization (WHO) record [9], more than 770 million COVID-19 cases were reported globally by the end of 2024, resulting in the death of approximately seven million individuals.

Improper design and operation of the heating, ventilation, and air conditioning (HVAC) systems, such as low ventilation rates, inadequate air circulation, and the transmission of pathogenic microorganisms via HVAC ductwork, can facilitate the spread of pathogens [16,23,30]. Inadequate ventilation rate increases the probability of infection as infectious aerosols can accumulate indoors [16,29]. Recirculated air may reintroduce microorganisms not fully captured by filters [180], and microbial growth can also occur within ducts and filters [30,72], further increasing the risk of transmission. Since human beings spend most of their time in indoor environments, providing desirable thermal comfort conditions [161–163] and indoor air quality (IAQ) factors in enclosed spaces through HVAC systems is of vital importance. Properly designed and operated HVAC systems can substantially improve IAQ [181], thereby reducing the susceptibility of occupants to airborne diseases [30]. For instance, improved mechanical ventilation in classrooms has been associated with up to an 80% reduction in COVID-19 transmission [182], hospital studies show that higher outdoor air exchange rates limit influenza, tuberculosis, and rhinovirus risks to below

1% [183], and an intervention in day care centres demonstrated that increasing effective clean airflow reduced infection risk by more than 50% and illness-related absenteeism by 32% [184].

The installation of air filters in HVAC ductwork is a classical approach for controlling the virulence of airborne pathogens [15]. Depending on the filter efficiency, filters can effectively entrap microorganisms. For instance, high-efficiency particulate absorbing (HEPA) filters can remove 99.97% of 0.3 microns' diameter particles, which have the most penetration among different submicron particles [16].

Notwithstanding the advantages of air filtration, filters may accumulate microbes over time and even become a breeding ground for fungi and bacteria, rendering the filter a biologically hazardous object of significant concern [12,17]. Field and laboratory studies have demonstrated the colonization of HVAC filters by different fungi, such as *Aspergillus* and *Penicillium,* as well as various bacteria, including *Escherichia coli* and *Pseudomonas spp*., with viable microorganisms detected in both MERV-rated and HEPA filters across hospitals, offices, and schools [167–171]. Recently, viral particles, including SARS-CoV-2 RNA, have also been recovered from HVAC filters [172]. According to the literature, depending on the filter types and airflow conditions, contaminated filters can release up to 1% of these microorganisms under normal operation [26] to substantially higher levels (up to 25%) under transient conditions such as fan restarts [27,28].

Therefore, supplementary disinfection technologies should be adopted to inactivate microbes, prevent the creation of a medium for pathogen multiplication, and mitigate the risk of episodic germ release into the building [25].

5.2.1 Existing Disinfection Technologies in the Literature

Several sterilization approaches have been introduced in the literature for the removal or inactivation of infectious microorganisms. These purification technologies can be categorized into physicochemical and biochemical technologies based on the inactivation mechanisms used in the sterilization process. The physicochemical technologies include conventional filters [17,29,30,185], electrostatic filters [12,29,32,33], antimicrobial filters [34–37], ultraviolet germicidal irradiation (UVGI) [34,38–41,186], photocatalysis oxidation [30,42–44], plasma [29,45–47], thermal treatment [49,50], ozonation [51–53,187] and microwave [30,54,55]. However, implementing botanical disinfectants [56–58] and herb fumigation [29,188] belongs to the biochemical category.

Table 1 provides a targeted synthesis of representative peer-reviewed studies on air disinfection technologies relevant to HVAC applications. Through targeted searches in Scopus, Web of Science, ScienceDirect, and PubMed using combinations of general and technology-specific keywords (e.g., air disinfection, air purification technologies, HVAC filters, electrostatic filters, "antimicrobial filters, UV disinfection HVAC, photocatalytic oxidation, plasma air disinfection, thermal disinfection air, and ozonation), we identified approximately 200 relevant publications on disinfection technologies. From these, more than 30 representative studies were selected to highlight the reported advantages and limitations of different approaches. Readers seeking broader coverage of the literature are referred to recent systematic and critical reviews [18,29,30,72,180]. Notably, biochemical disinfections are excluded from Table 5.1 as they are less common in HVAC applications. As is evident in Table 5.1, notwithstanding the merits of the available technologies, their implementation is associated with high investment costs, high energy consumption, harmful by-products, complicated installation and maintenance, and degradation in long-term efficiency.

Table 5.1. Characteristics of different disinfection technologies proposed in the literature.

Technology	Description	Removal /Inactivation	Advantages	Disadvantages
Conventional Filters [29,30]	Use the adsorption capability of fibrous materials to capture microorganisms via impaction, diffusion and interception.	Removal	Low-cost, convenient installation, commercially available.	Higher efficiency filters may increase pressure drop, but the relationship is not universal and depends on filter structure, thickness, and MERV class [185], microbial growth and secondary contamination have been reported on loaded filters [12,17].
Electrostatic Filters [32,33]	Collection of microorganisms by the electrostatic force caused by by the opposite charged Coulomb force, image force and polarization force.	Mainly removal, partial inactivation	High efficiency across a wide range of particle sizes, lower pressure drop compared to conventional fibrous filters, commercially available.	High initial cost relative to conventional filters, efficiency can decline over time due to dust accumulation and aging, electric field is easy to break down [12,29].
Antimicrobial Filters [34,35]	Use antimicrobial agents or coatings on the filter to inactivate entrapped bioaerosols.	Removal and inactivation	Reducing the risk of downstream release helps limit microbial growth during service life	Inactivate specific microbes, not all of them, higher initial costs compared to conventional filters, degradation in removal efficiency, and may increase pressure drop compared to untreated filters [36,37].
Ultraviolet Germicidal Irradiation (UVGI) [38,39,186]	Produce short-wavelength electromagnetic waves, with the peak irradiance traditionally occurring at approximately 254 nm. These high-energy waves effectively target the DNA, controlling the replication of pathogens. Recent developments in far-UVC show potential for safe operation in occupied spaces with a lower wavelength (200–230 nm).	Inactivation	High microbial inactivation efficiency across a broad range of pathogens, conventional 254 nm systems are commercially available, low airflow resistance, does not require chemicals.	UV light can be blocked by objects, adverse health effects of conventional UVGI on the skin (erythema) and eyes (photokeratitis), UV radiation exposure is carcinogenic, in-duct UVGI efficiency highly depends on operating conditions (e.g., duct airflow rate, air temperature, and relative humidity), far-UVC systems are not yet widely commercialized and typically have shorter lamp lifetimes compared to traditional mercury lamps, increases added heat to the HVAC system [34,38,40,41,186].
Photocatalysis Oxidation [42,43]	Use light in combination with oxidation to produce reactive oxygen species that can inactivate microorganisms and degrade organic pollutants . Primarily, TiO_2 is used as the catalyst to accelerate the photoreaction.	Inactivation	Potential to inactivate a range of microorganisms and degrade volatile organic compounds can operate continuously when coupled with UV.	Easily produces secondary pollutants (aldehydes and ketones), with a reduction in effectiveness over time due to dirt buildup, and a low catalyst lifetime [30,42,44].
Plasma [45,46]	Harness an external electric field to generate electrons, which, upon contact with bioaerosols, leads to the direct interaction of reactive chemical species, causing damage to airborne microorganisms.	Inactivation	Efficient for a wide range of pollutants, reducing the growth of adhering fungi, elimination of clinging odours.	May generate harmful by-products, including ozone, carbon monoxide, particulate matter, and formaldehyde, and requires a professional technician for operation; not cost-effective for large spaces [29,47].

Table 5.1. Characteristics of different disinfection technologies proposed in the literature (continued).

Technology	Description	Removal /Inactivation	Advantages	Disadvantages
Thermal Treatment [49]	Use high temperature (either dry heat or moist heat) to destroy bioaerosols by denaturing the enzymes and proteins.	Inactivation	High inactivation efficiency with deep penetration, does not impose excessive pressure loss, avoids chemical additives.	Requires high operating temperature, high energy consumption, not cost-effective for large spaces, increases added heat to the HVAC system, causes thermal deformation in some materials, more applicable in food industry and sterilizing medical equipment [50].
Ozonation [51,52]	Use the corona discharge to produce ozone that inactivates microorganisms by damaging their cell membrane and proteins.	Inactivation	Inactivates a broad range of microorganisms, rapid reaction mechanism.	Generates ozone and secondary contaminants, causes respiratory problems, should not be used in occupied spaces, unstable and must be applied with monitored concentration just before use [51,53,187].
Microwave [30,54]	Operates via electromagnetic waves at frequencies of 300 to 3000 MHz. The generated non-ionizing electromagnetic radiation denatures cells through induced heat.	Inactivation	Rapid sterilization, does not produce by-products.	Microwave energy is weakly absorbed by air and requires microwave-absorbing materials. Exposure to radiation poses risks to the well-being of individuals, but is more efficient in the food industry [55].

As far as HVAC filters decontamination is concerned, several disinfection technologies have been used in the literature, though each faces practical limitations. The integration of electrostatic precipitators (ESPs) with air filters has shown enhanced removal of charged particles and partial inactivation of bioaerosols; however, it is hindered by ozone generation, secondary by-products, and high operational costs [62–68]. UV-integrated filters, applied to both HEPA and non-HEPA media, suffer from poor penetration into dense structures, humidity sensitivity, reduced performance at high duct velocities, and high energy demand [18,61,62,69,70,189]. Photocatalytic coatings (e.g., TiO_2, ZnO) applied to filter fibers are capable of inactivating entrapped microorganisms. However, their application is limited by reduced efficiency at high airflow, reliance on UV irradiation, and the risk of ozone generation [71–74]. Plasma-assisted filtration has shown effectiveness in portable devices, but ozone and ion by-products, together with elevated energy consumption, limit its viability for central HVAC systems [18,75,77].

Thermal treatment of HVAC filters has also been explored and, given its direct relevance to the present work, is reviewed separately in Section 5.2.2.

5.2.2 Thermal Inactivation

Among various disinfection methods, thermal inactivation is of interest to this study. Thermal inactivation is a powerful tool against most infectious agents. Heat has excellent penetration capabilities that can annihilate highly infectious agents by denaturing their enzymes and proteins [19–21]. The two main parameters for a successful sterilization process by heat are temperature and exposure time. Table 5.2 presents the required temperature and exposure time for inactivating various common airborne microorganisms, including bacteria, fungi, and viruses. As is evident, most pathogenic agents can be inactivated with sustained heat at approximately 65 °C for around 10 minutes. This suggests that heat holds significant potential for disinfecting microorganisms accumulated on HVAC filters.

Table 5.2. The required temperature and exposure time for thermal inactivation of various airborne pathogens.

Species	Microorganism	Inactivation Temperature (ºC)	Exposure Time (min)	Reference
Bacteria	Escherichia coli	60	0.7-2.7	[79]
	Mycobacterium tuberculosis	80	20	[190]
	Legionella pneumophila	60	2	[80]
	Pseudomonas aeruginosa	65	5	[81]
Fungi	Aspergillus	60	10	[191]
	Penicillium	60	10	[191]
	Mucor	60	10	[191]
Viruses	Rhinovirus (Common cold)	60	10	[82]
	MERS-CoV	65	0.5	[192]
	Human influenza	55.6	30	[78]
	MS2	70	< 30	[193]
	Avian influenza	65 70	10 1	[83]
	SARS-CoV	70	3	[78]
	SARS-CoV-2 (COVID-19)	56 65 70	30 10 5	[84] [84] [34]

Although thermal inactivation of viruses by heat is an established and widely applied method in "non-aerosol" applications, to the best of the authors' knowledge, its utilization for inactivating pathogenic aerosols in HVAC systems remains limited. Soni et al. [194] conducted a numerical investigation of a solar-assisted system for the thermal inactivation of bioaerosols. The proposed system comprises a heating section (consisting of a solar collector and an auxiliary electrical heater), a porous unit, a disinfection chamber, and a cooling unit. The obtained results indicated that, even with an optimal porosity of 0.9, the pressure drop across the porous region is approximately 5 kPa. Furthermore, they deduced that the system's efficiency during the daytime is merely 37%, while it can reach 91% at nighttime operation.

Xie et al. [173] introduced an innovative passive solar heating solution for disinfecting bioaerosols. They assessed the feasibility of using a Trombe wall to inactivate COVID-19 viruses in a test room with dimensions of 6 m × 3 m × 3 m in Xining, Qinghai Province, China. The results showed that at an average ambient temperature of 18.8 °C and average solar irradiance of 638.9 W/m^2, the proposed system could provide 37 m^3/h of clean air for three hours with a single-pass inactivation rate of 89.3% for SARS-CoV and MERS-CoV, and 24 m^3/h of clean air for 78 minutes with an inactivation rate of 59.1% for SARS-CoV-2. In a recent study, Xie et al. [86] introduced an innovative thermal inactivation system combining air filtration with a hybrid photovoltaic (PV) panel and Trombe wall system for the decontamination of *Klebsiella pneumonia*. Their numerical analysis indicated that, with an average ambient temperature of 9.7 °C and solar irradiance of 620.6 W/m^2, the air temperature at the Trombe wall outlet could reach 75 °C, effectively reducing the concentration of pathogens trapped in the filter over several hours during the daytime.

Yu et al. [87] developed a novel self-healing filter composed of pleated nickel foams for inactivating the COVID-19 virus and *Bacillus anthracis* (anthrax spores). Experimental results demonstrated that increasing the filter temperature to 200 °C resulted in the inactivation of 99.98% of the coronavirus and 99.99% of the anthrax spores. Achieving the required temperature for a self-heating filter with dimensions of 24 cm × 30 cm × 1.6 cm at an airflow rate of 10 l/min (0.6 m^3/h) required a power input of 500 W. However, no information was provided regarding the associated pressure drop.

Thermal inactivation solutions proposed in the literature face several challenges that hinder their application in large HVAC systems and real-world settings. Issues include low thermal efficiency, limited reliability of solar-driven technologies for daytime use, brief exposure times in Trombe walls, high energy consumption, pressure drops associated with metallic foams, undesirable added heat during HVAC cooling modes, and high maintenance costs. To address the deficiency of the existing technologies, the present study proposes a novel solution based on the thermal inactivation of HVAC filters in insulated units. The disinfection process utilizes a combination of air filters to trap microorganisms and thermal inactivation by heating elements to destroy the captured pathogens. Since heat transfer occurs within an insulated enclosure, energy consumption and unwanted added heat to the HVAC ductwork are minimized. Details on the device's working principle are provided in Section 5.3. In summary, the key innovations and contributions of this study are:

1. Proposing a novel, energy-efficient approach for air disinfection combining filtration with thermal inactivation.
2. Assessing the system's heat transfer and energy performance.
3. Evaluating pressure drop and size-resolved particle removal efficiency of the system in a closed-loop aerosol wind tunnel meeting ASHRAE 52.2 standards [22].
4. Determining optimal operating conditions, including warm air set-point temperature and air recirculation rate within the disinfection units.

5.3 Description of the Problem

The working principle and the elements of the introduced technology in the present study are depicted in Fig 5.1. The disinfection device includes two side-by-side units (Fig. 5.1a). Each sterilizing unit consists of a filter, a heating element (i.e., heating wires), and axial fans, all enclosed within a closed system (Figs. 5.1b and 1c).

As is evident in Fig. 5.1b, axial fans and the heating element are positioned beneath the frame, hence referred to as "external fans" hereafter. Both units are initially open, and the heating elements and axial fans are turned off for filtration. After some time, one of the units is isolated by closing its gates, and then the heating elements and external fans are turned on. The external fans blow air toward the heating element, and the warm air enters the unit containing the filter through the provided inlet, transfers heat to the filter and recirculates through the recirculation outlet and the adjacent duct. The target is to raise the filter temperature to 65 °C and maintain it for 10 minutes to inactivate microorganisms. At the same time, the other unit is open and continues its work for entrapping microbes. By repeating this process sequentially (Fig. 5.2), the two units can capture and eliminate pathogens in HVAC systems. It should be noted that as the heat transfer process from the heating elements to the pleated filters occurs within an insulated enclosure, it avoids releasing excessive heat into the HVAC system. Hence, the introduced technology is projected to be cost-effective, safe and environmentally friendly for purifying air contaminated with bio-aerosol particles.

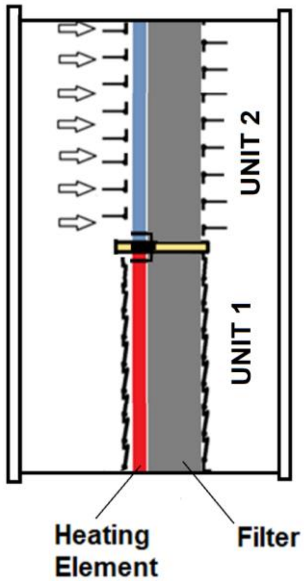

(a)

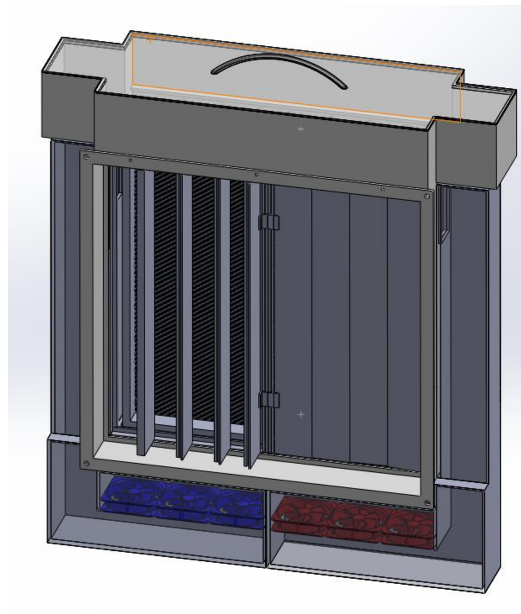

(b)

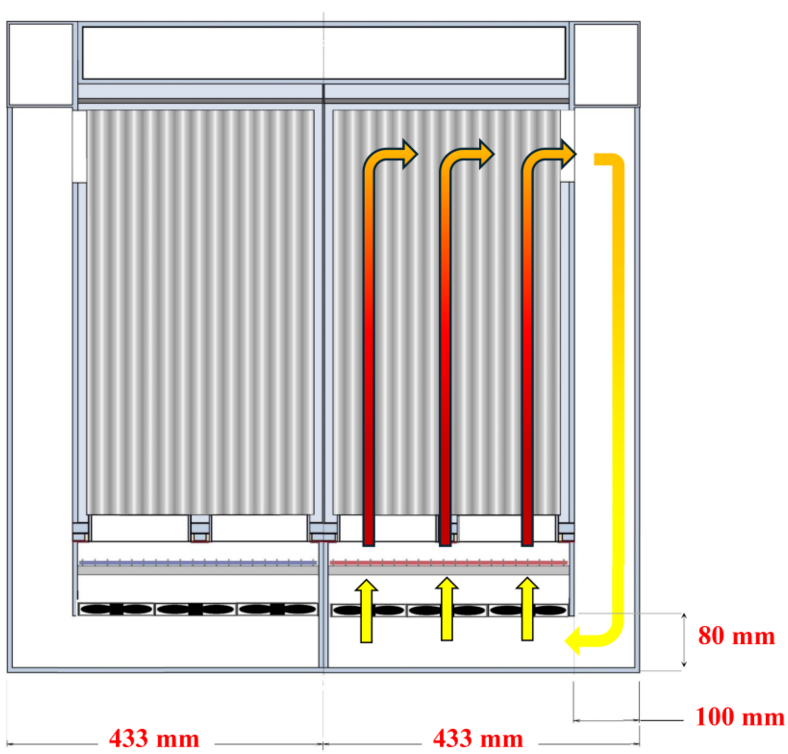

(c)

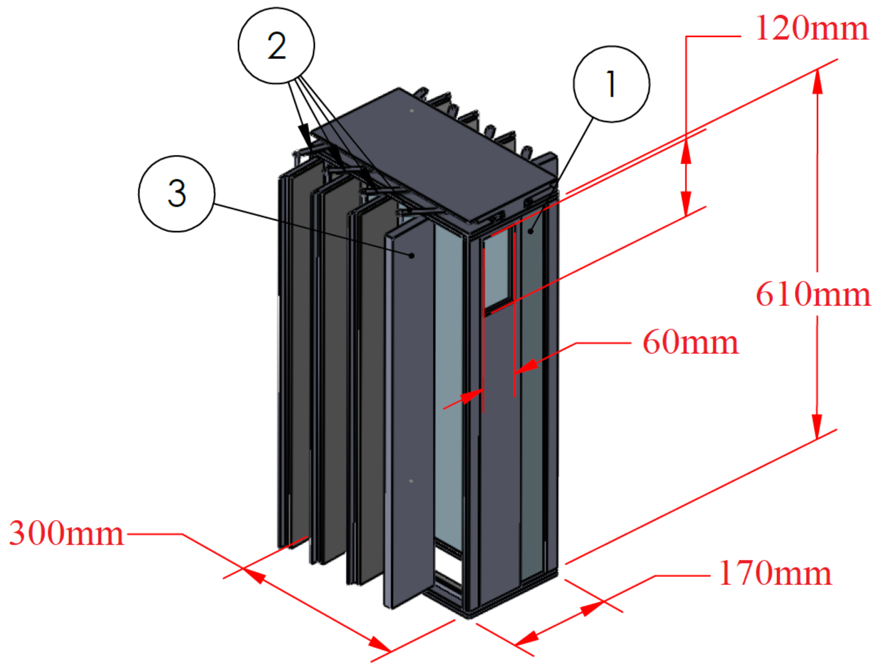

(d)

Fig. 5.1. A schematic view of (a) the working principle, (b) prototype, (c) flow direction, and (d) dimensions and the elements of the disinfection technology proposed in the present study, including 1: filter, 2: sliders, and 3: gates.

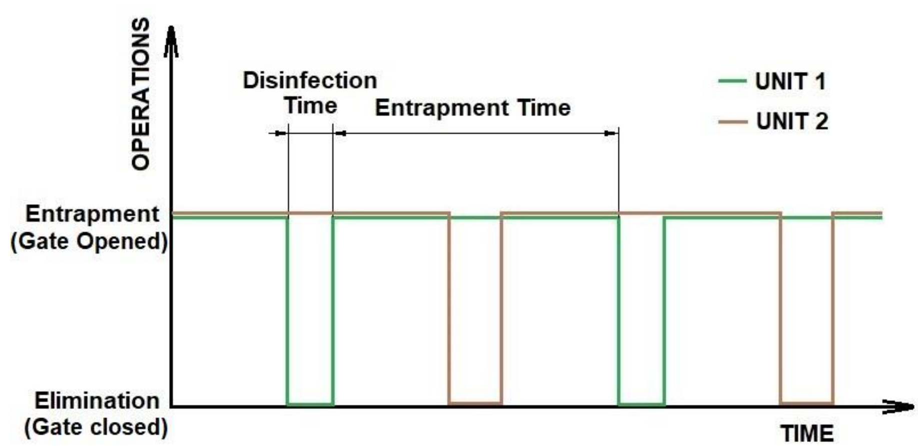

Fig. 5.2. Sequential entrapment-disinfection by filtration and heat application.

5.4 Methodology

The experimental study in this work includes investigating the energy performance of the proposed disinfection system and evaluating the filtration efficiency and pressure drop of the unit in a closed-circuit aerosol wind tunnel that can accommodate the device prototype.

5.4.1 Experimental Setup of the Energy and Heat Transfer Performance Evaluation

The experimental setup for evaluating the heat transfer performance of the system comprises an enclosed cavity, a pleated filter, a heating element, a data monitoring and acquisition system, a temperature-controlling unit, and a closed-loop wind tunnel (Fig. 5.3a) that accommodates the device prototype (Fig. 5.3b) for simulating real-world applications. Considering the availability, cost, and desirable thermal properties (i.e., low thermal conductivity, low thermal expansion, and higher melting points), solid and twin-wall polycarbonate sheets are used for manufacturing the prototype, as they are readily available in various thicknesses and sizes on the market. Several rotating gates are considered for the opening and closing mechanism (Fig. 5.2b). Four axial fans (airflow rate of 74 m^3/h and energy consumption of 1.7 W each) and the heating element (nichrome heating wires supplying 800 W) are installed under the frame. A PID controller (OMEGA-CN32PT-145) is deployed to provide a constant temperature heat source. Sixteen T-type thermocouples (OMEGA) with a diameter of 0.08 mm and an accuracy of ±0.5 ºC are employed to monitor the filter surface. The test filter used in this study is a MERV 11 filter with a thickness of 1 inch (2.54 cm) and dimensions of 12 inches × 24 inches (30.48 cm × 61.0 cm). The filter is made of polyester fibers, with a media thickness of 0.66 mm and a pleat density of 0.4 pleats/cm. Nine thermocouples are fixed at the filter face, five thermocouples are connected to the filter back (Fig. 5.3c), and two thermocouples are installed before the external fans and after the heating element in the recirculation duct. A sixteen-channel data logger (NI-9213) is utilized to collect temperature data. Additionally, to monitor the energy consumption of the proposed sterilizing system during the disinfection period, a power meter (Poniie-PN2000) is used. All frame surfaces and eight gates are covered with aluminum foil (i.e., emissivity less than 0.1) to reduce radiation dissipation to the surroundings.

To determine the optimal operating conditions, the energy performance of the disinfection system will be tested at four different recirculation flow rates for external fans (88, 148, 223, and 296 m^3/h) and three different inlet air set-point temperatures (85, 95, and 105°C). In all cases, the wind tunnel airflow rates will be kept constant at 2100 m^3/h (i.e., the maximum airflow rate in our wind tunnel). Following this, the most optimal operating condition identified in these tests will be further evaluated under varying wind tunnel flow rates (0 and 2100 m^3/h) to assess the impact on the system's heat and energy performance.

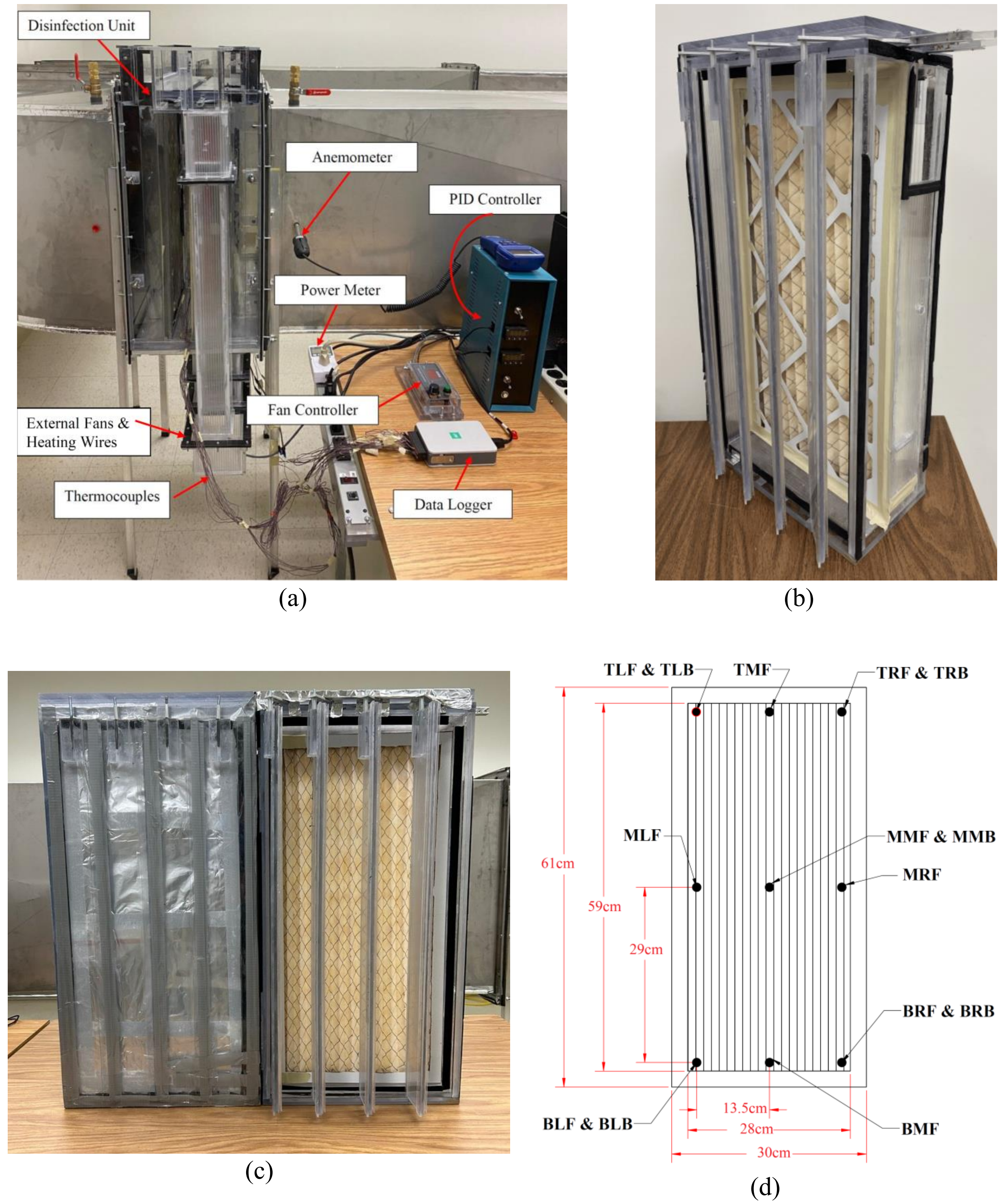

Fig. 5.3. A representation of (a) the experimental setup of the heat transfer performance monitoring, (b) the manufactured prototype, (c) side-by-side units and (d) the location of thermocouples on the filter (Hint: First Letter - Vertical Position (T: Top, M: Middle, B: Bottom); Second Letter - Horizontal Position (L: Left, M: Middle, R: Right); Third Letter - Depth (F: Front, B: Back)).

5.4.2 Measurement of the Particle Removal Efficiency and Pressure Drop

This study will follow ASHRAE 52.2 [22] and ASHRAE Guideline 26 [195] for designing the aerosol wind tunnel that can determine the particle removal efficiency and pressure drop of the suggested disinfection system. These standards outline the critical dimensions and arrangements of the test apparatus, as well as the required features of various equipment (e.g., aerosol generator and particle counter), to ensure a reliable result in air filter testing (Appendix B).

It is essential to highlight that ASHRAE 52.2 primarily focuses on the guidelines for designing an open-loop wind tunnel. However, the present study centers on the utilization of a closed-loop aerosol wind tunnel. The emphasis on a closed-loop system arises from its distinct advantages, including the ability to maintain consistent air velocity and particle concentration profiles with greater ease. Moreover, closed-loop wind tunnels offer enhanced safety features, reduced noise levels, and lower energy consumption, positioning them as a more efficient and sustainable alternative [196]. Consequently, to take advantage of the recirculating wind tunnels, some studies have modified the open-loop wind tunnel proposed in ASHRAE 52.2 [197–199]. By following the same procedure in this study, the closed-circuit aerosol wind tunnel, as specified in ASHRAE 52.2, can be obtained as shown in Fig. 5.4. This is a fully recirculating air testing facility designed to serve as a platform for refining the prototype design and evaluating the filtration efficiency of various air cleaning devices. We manufactured and assembled different sections of the recirculating ductwork (Appendix C) and installed the required test equipment within the closed-loop wind tunnel (Fig. 5.5).

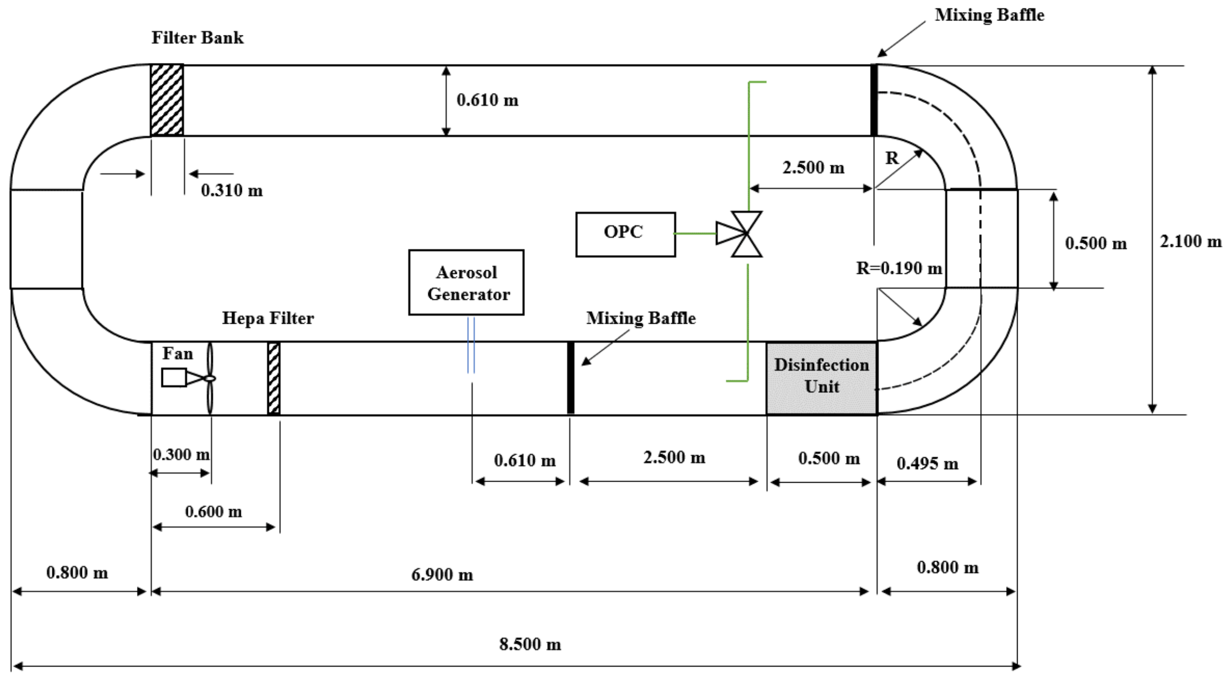

Fig. 5.4. Dimensions of the required closed-loop wind tunnel and the location of the instruments (NB. dimensions are not proportional).

Fig. 5.5. Advanced filtration testing assembly and setup.

The filtration performance is evaluated through controlled air circulation within the 18-m stainless steel ductwork, which has a cross-section of 61 cm × 61 cm, facilitated by a centrifugal fan (Rosenberg GKHM 280-CIB). To maintain consistency, the air velocity at the test section will be kept constant throughout the entire testing duration. Simultaneously, the aerosol generation system releases KCl aerosols into the system at a constant rate. The aerosol generation system includes a polydisperse aerosol generator (TOPAS ATM240/S) supplied by a 5-bar oil-free compressed air source. The aerosols are generated from a highly concentrated aqueous KCl solution (25g of KCl per 100 ml of ionized water). According to the ASHRAE 52.2 design guideline, two mixing baffles with a 40% open area on their perforated diffusion plates are installed before the upstream and downstream sampling locations.

The measurement of particle removal efficiencies is performed using a single Optical Particle Counter (OPC) (TOPAS-LAP340/L) connected to a sample switching valve (TOPAS-SYS520/S) that can automatically switch between upstream and downstream sampling. To ensure isokinetic sampling is provided, two isokinetic sampling probes manufactured by TSI are connected to external vacuum pumps (TSI model 3032) at both upstream and downstream sampling points. An isokinetic coupler manufactured by TSI is then utilized as an interface, providing a second isokinetic sample between the sampling probe and the inlet to the sample switching valve connected to the OPC. A differential low-pressure transmitter (OMEGA-PX655-05DI) connected to a data logger (NI-USB-6002) will measure the pressure loss across the prototype under both closed and open gate conditions. At the same time, a thermo-anemometer (TSI-9535) will be used to measure the airflow rate at the sampling locations. It should be noted that throughout all experiments, the wind tunnel air temperature and relative humidity remained stable within 22 ± 3 °C and 50% ± 2% RH, respectively.

The particle size removal efficiency (η) of an air cleaning device can be defined as follows [200]:

$$\eta = \left(1 - \frac{\text{Downstream particle concentration}}{\text{Upstream particle concentration}}\right) \times 100 = (1 - \frac{P_{ave}}{R_{ave}}) \times 100 \tag{5.1}$$

in which P_{ave}, the average penetration, represents the portion of aerosols that penetrates the filter and can be obtained using Eq. (5.2) [22]. R_{ave}, the average correlation ratio, is a correction factor and can be determined with Eq. (5.2) when the test device is not installed [201].

$$P_{ave} = \left(\sum_{i=1}^{n} P_i\right) \Big/ n = \left(\sum_{i=1}^{n} \frac{C_{i,o} - C_{b,ave}}{U_{i,e} - U_{b,ave}}\right)/n \tag{5.2}$$

where $C_{i,o}$ and $U_{i,e}$ are the observed downstream concentration and the estimated upstream concentration, respectively, $C_{b,ave}$ and $U_{b,ave}$ represents the average concentration of the background samples collected before and after the aerosol generation at the downstream and upstream data collection points, respectively. While $C_{i,o}$ is simply observed in OPC, Eqs. (5.3) to (5.5) should be used for calculating $U_{i,e}$, $C_{b,ave}$ and $U_{b,ave}$ as follows:

$$U_{i,e} = \frac{U_{i,o} + U_{(i+1),o}}{2} \tag{5.3}$$

$$U_{b,ave} = \left(\sum_{i=1}^{n} U_{i,o,b}\right)/n \tag{5.4}$$

$$C_{b,ave} = \left(\sum_{i=1}^{n} C_{i,o,b}\right)/n \tag{5.5}$$

It should be noted that the required number of background samples can be ascertained based on the data quality relations (i.e., explained in Section 10.6.2 of ASHRAE Standard 52.2 [22]). In this study, three background samples at each of the sampling locations were collected. Furthermore, the data quality determines the sampling period and the total number of data collected. In this regard, four and three samples were recorded at upstream and downstream sampling points, respectively. In the present work, a one-minute purging in the sample switching valve, followed by a 30-second rinsing within the OPC, and eventually a one-minute data collection during each sampling, could meet ASHRAE 52.2 requirements.

For designing the experiment, the filtration efficiency and pressure drop of a standalone 24 in × 24 in × 1 in (61 cm × 61 cm × 2.54 cm) MERV 11 filter are compared with those of the proposed disinfection technology at different operating conditions, including when both units are open, and when one of the units is closed. Each of the side-by-side units contains a MERV-11 filter identical to the abovementioned standalone filter in properties but different in dimensions (12 in × 24 in × 1 in). These three cases will be tested at duct velocities of 0.5, 0.75, and 1 m/s. It should be noted that when one of the units is closed, the maximum air velocity in the duct, at which the ASHRAE 52.2 requirements for isokinetic sampling can be satisfied, is 1 m/s.

5.4.3 Uncertainty Analysis

Table 5.3 presents the uncertainties associated with various measured parameters in this study, including temperature, energy consumption, air velocity, pressure drop, and filtration efficiency. Following the procedure described in Ref [202], the combined standard uncertainty, including specifications of measurement instruments provided by the manufacturer, and uncertainty estimates from repeated readings (repeatability) are calculated.

Table 5.3. Combined standard uncertainty values of the quantified parameters.

Quantity	Combined Standard Uncertainty
Temperature	± 0.46 °C
Electrical Energy Consumption	± 1.4 W
Air Velocity	± 0.05 m/s
Pressure Drop	± 5 Pa
Filtration Efficiency	± 5%

5.5 Results and Discussion

5.5.1 Evaluating the Heat Transfer Performance of the System

Figures 5.6a-d illustrate the variation of temperature with time at various locations on the test filter under a recirculation flow rate of 296 m^3/h and an inlet air set-point temperature of 85°C. As is evident, the temperature on the filter's front surface is higher in the bottom and middle regions compared to that of the top region. This pattern arises due to the predominance of forced convection over buoyancy-driven flow on the front surface (i.e., the Richardson number (Ri) order of magnitude in this work is 0.001, which is by far lower than one). As warm air enters the unit, it transfers heat to the filter, the surrounding air within the cavity, and the unit frame. This heat exchange causes the temperature of the advective air stream to decrease progressively as it reaches the upper regions of the filter. Consequently, the upper section of the filter front exhibits a relatively lower temperature.

Furthermore, as shown in Fig. 5.6, the backside of the filter consistently exhibits a lower temperature than the front, with the lowest temperature observed at the bottom of the back surface. This difference is because, as illustrated in Fig. 5.1, the backside of the filter is not in direct contact with the incoming warm air. Instead, heat is conducted from the front surface to the back. In contrast to the front surface, where forced convection dominates, the back surface primarily experiences buoyancy-driven flow, resulting in higher temperatures in the upper regions of the filter's back compared to the lower regions.

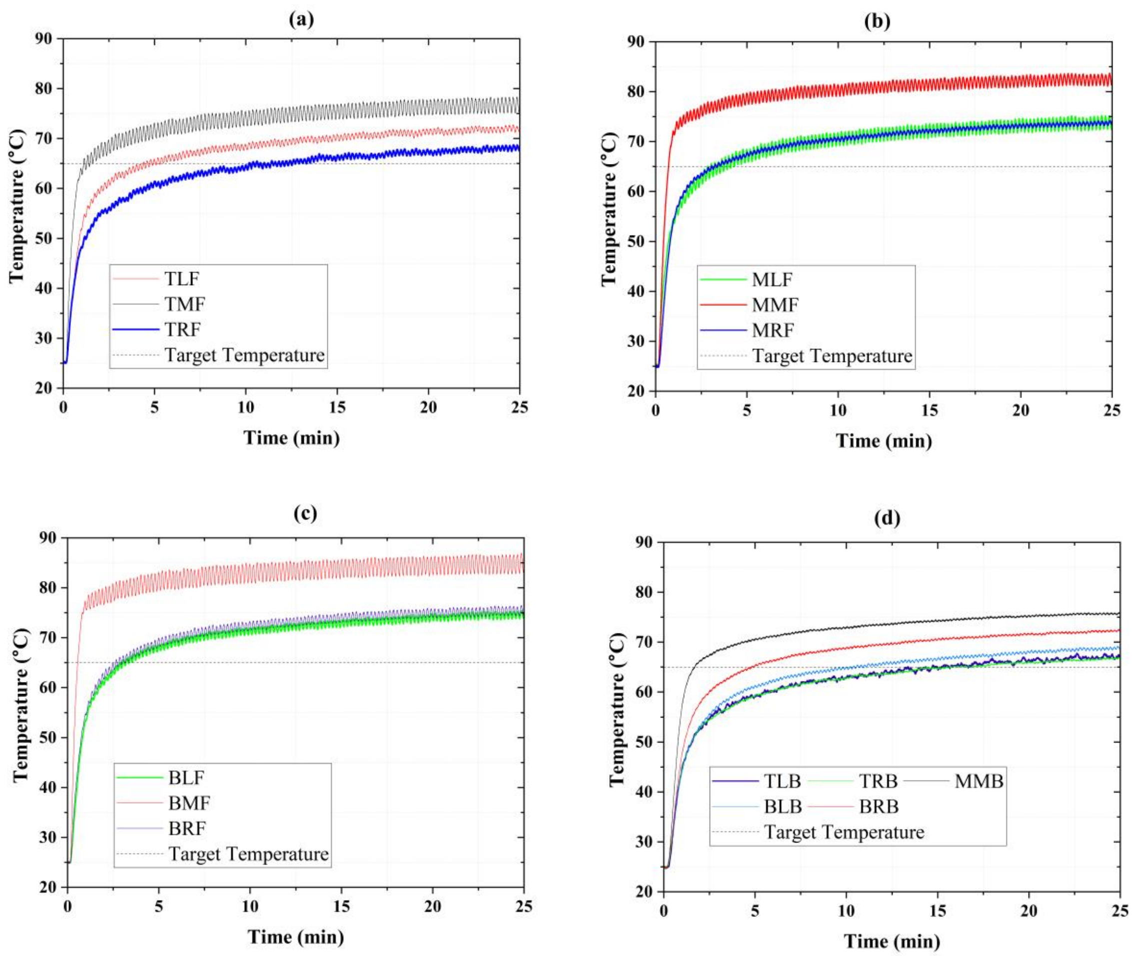

Fig. 5.6. Temperature variation at different locations on the filter, including (a) top of the front surface, (b) middle of the front surface, (c) bottom of the front surface, and (d) filter back surface, over time for a 1-in MERV 11 filter at a recirculation flow rate of 296 m^3/h and warm inlet air set point temperature of 85°C. Abbreviations related to these figures are specified in Fig 5.3.

Figure 5.7 illustrates the variation of temperature distribution on the filter surface over time at different recirculation flow rates of the fans. To achieve the required disinfection temperature of 65°C, the minimum value of the box plot must be above the horizontal red line. As shown in Figs. 5.7a-c, at an airflow rate of 88 m^3/h, the target disinfection temperature cannot be reached within a reasonable timeframe. At a recirculation flow rate of 148 m^3/h (Figs. 5.7d-f), the filter reaches the target temperature merely when the warm inlet temperature is set as high as 105°C. However, the time required to attain this condition remains long (exceeding 20 minutes). When the recirculating flow rate is increased to 223 m^3/h (Fig. 5.7g), decontamination is achievable at a lower inlet temperature of 85°C; however, the required time remains substantial. A further increase in both the warm inlet temperature and the recirculating flow rate significantly reduces the time necessary to reach the disinfection temperature at the filter (Figs. 5.7i-l). As illustrated in Fig. 5.7l, at a recirculating airflow rate of 296 m^3/h and an inlet temperature of 105°C, the entire filter area reaches the target temperature (65°C) in less than five minutes. This effect arises because higher recirculating airflow rates enhance convective heat transfer at the filter's front surface, allowing the minimum filter temperature to reach the target disinfection level more rapidly (Figs. 5.8a-c). In other words, at a constant inlet temperature, with an increase in the airflow rate, the minimum filter temperature increases. Furthermore, it should be noted that, according to Fig. 5.7, at a constant warm inlet temperature, increasing the recirculation flow rate can significantly reduce the temperature difference within the filter, resulting in a more uniform temperature distribution due to enhanced convection heat transfer.

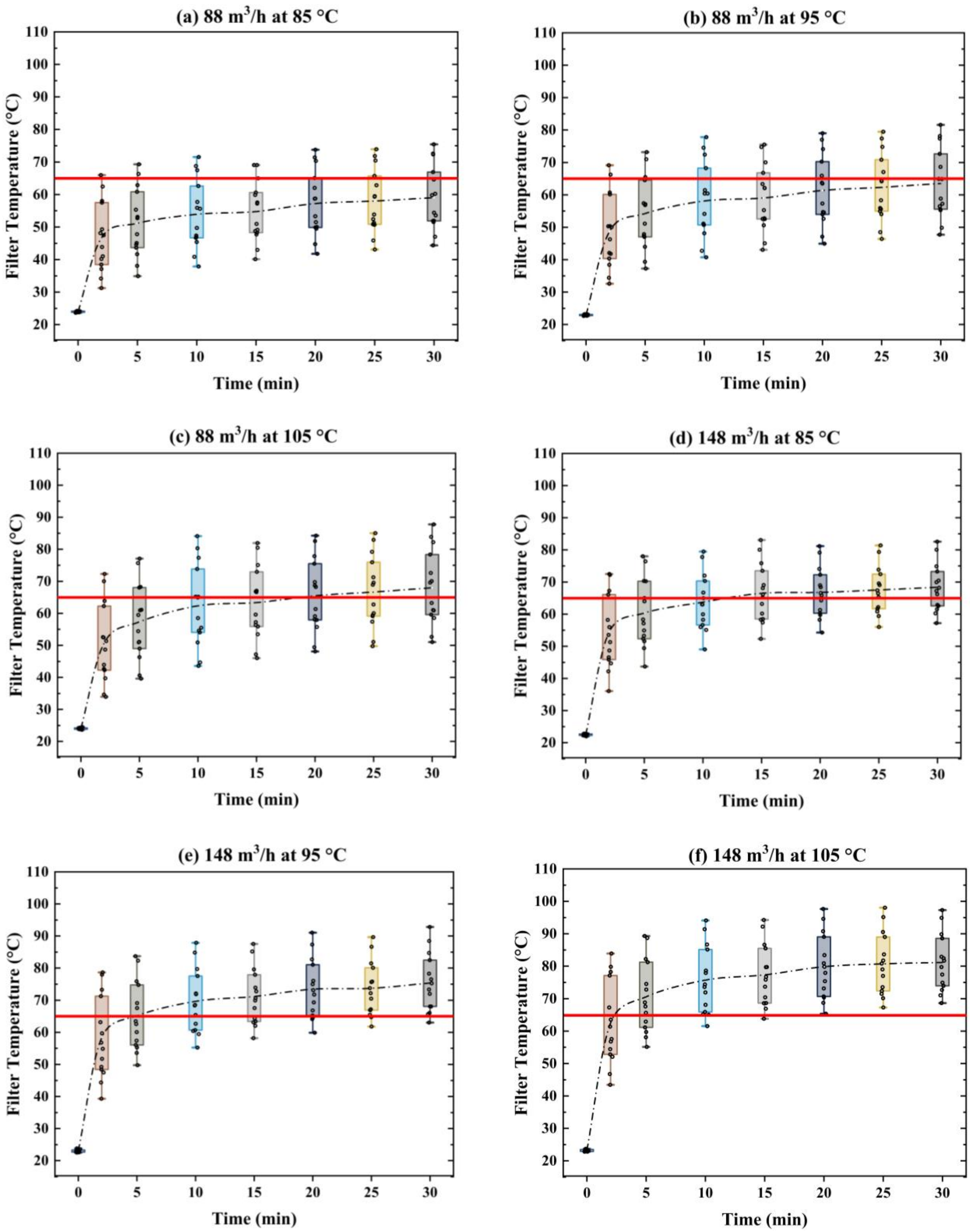
(a) 88 m3/h at 85 °C
(b) 88 m3/h at 95 °C
(c) 88 m3/h at 105 °C
(d) 148 m3/h at 85 °C
(e) 148 m3/h at 95 °C
(f) 148 m3/h at 105 °C
Filter Temperature (°C)
Time (min)
20
30
40
50
60
70
80
90
100
110
0
5
10
15
20
25
30

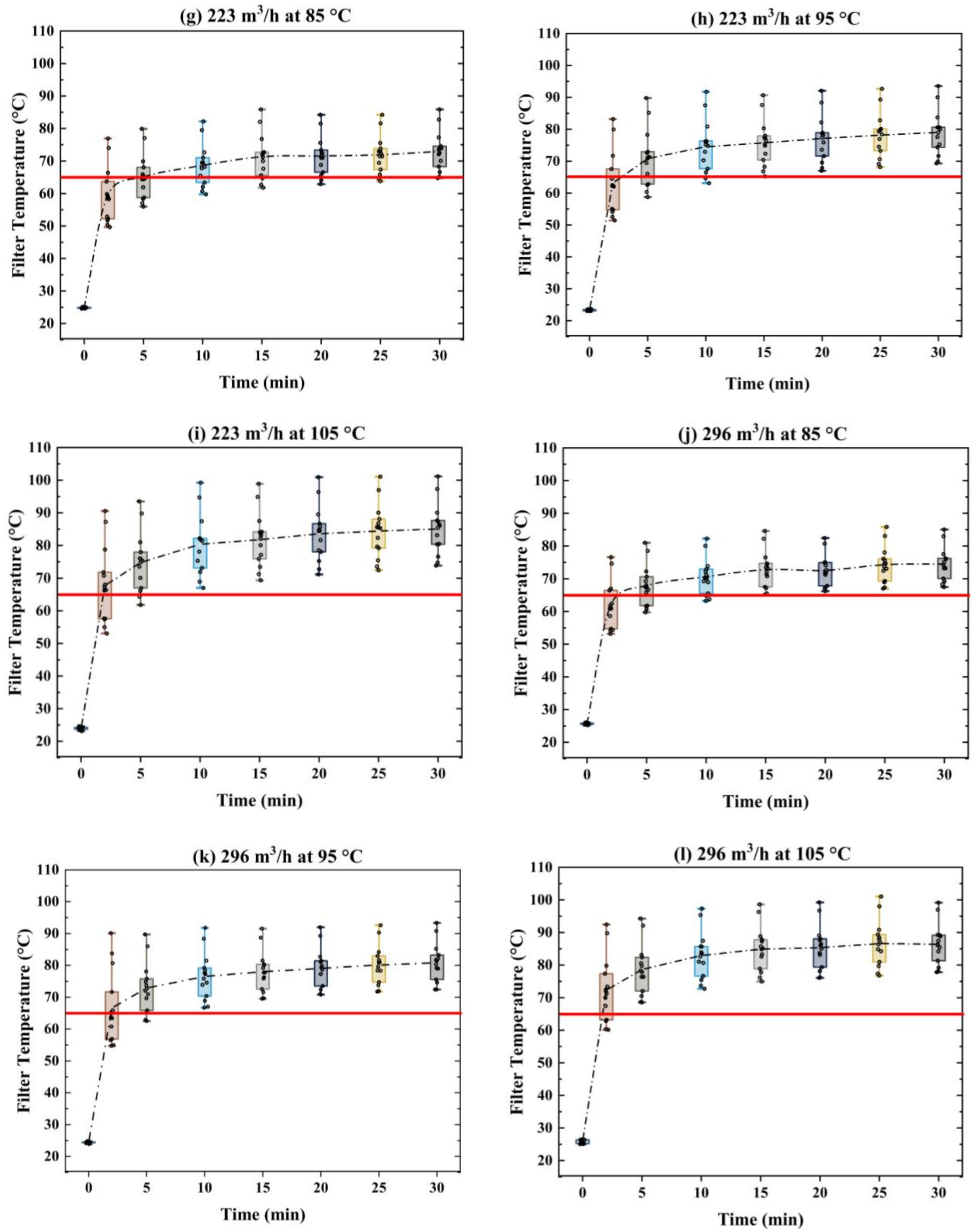

Fig. 5.7. Filter temperature profiles over 30 minutes at varying inlet air temperatures and recirculation flow rates, including (a) 88 m³/h at 85 °C, (b) 88 m³/h at 95 °C, (c) 88 m³/h at 105 °C, (d) 148 m³/h at 85 °C, (e) 148 m³/h at 95 °C, (f) 148 m³/h at 105 °C, (g) 223 m³/h at 85 °C, (h) 223 m³/h at 95 °C, (i) 223 m³/h at 105 °C, (j) 296 m³/h at 85 °C, (k) 296 m³/h at 95 °C, and (l) 296 m³/h at 105 °C.

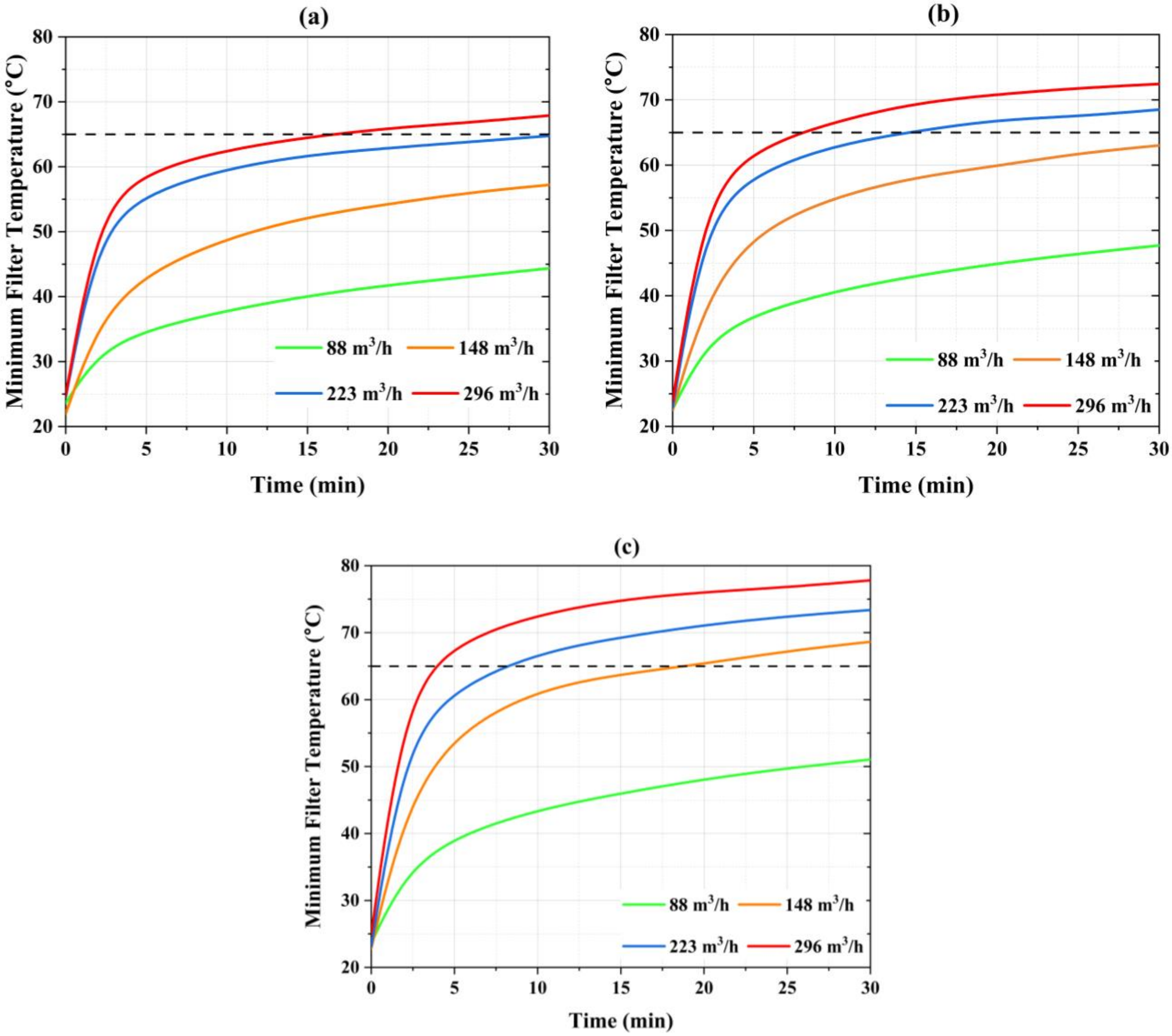

Fig. 5.8. Variation of the minimum filter temperature over time at different recirculation flow rates, with constant warm inlet temperatures of (a) 85 °C, (b) 95 °C, and (c) 105 °C.

5.5.2 Evaluating the Energy Performance of the System

The energy performance of the proposed disinfection technology depends on two key factors: (1) the electrical energy consumption, which includes the power required to operate the external fans (for air recirculation) and to raise the system temperature; and (2) the time required to achieve effective disinfection. Figure 5.9 compares the energy consumption and disinfection duration across six cases that can achieve the target filter surface temperature of 65 °C within a reasonable timeframe. To ensure microorganism inactivation, the system must maintain this temperature for a sufficient period, set at 10 minutes in this study, as indicated in Table 5.2, to effectively destroy the COVID-19 virus. As illustrated in Fig. 5.8, when the inlet air temperature is set to 105 °C, and the recirculation rate is 296 m^3/h, the filter temperature reaches 65 °C in approximately 3 minutes. Maintaining this condition for an additional 10 minutes ensures the elimination of microorganisms that have become trapped in the filter. According to Fig. 5.9, under these operating conditions, the filter is decontaminated in 13 minutes, with a total energy consumption of just 0.11 kWh, including both fan and heating element power.

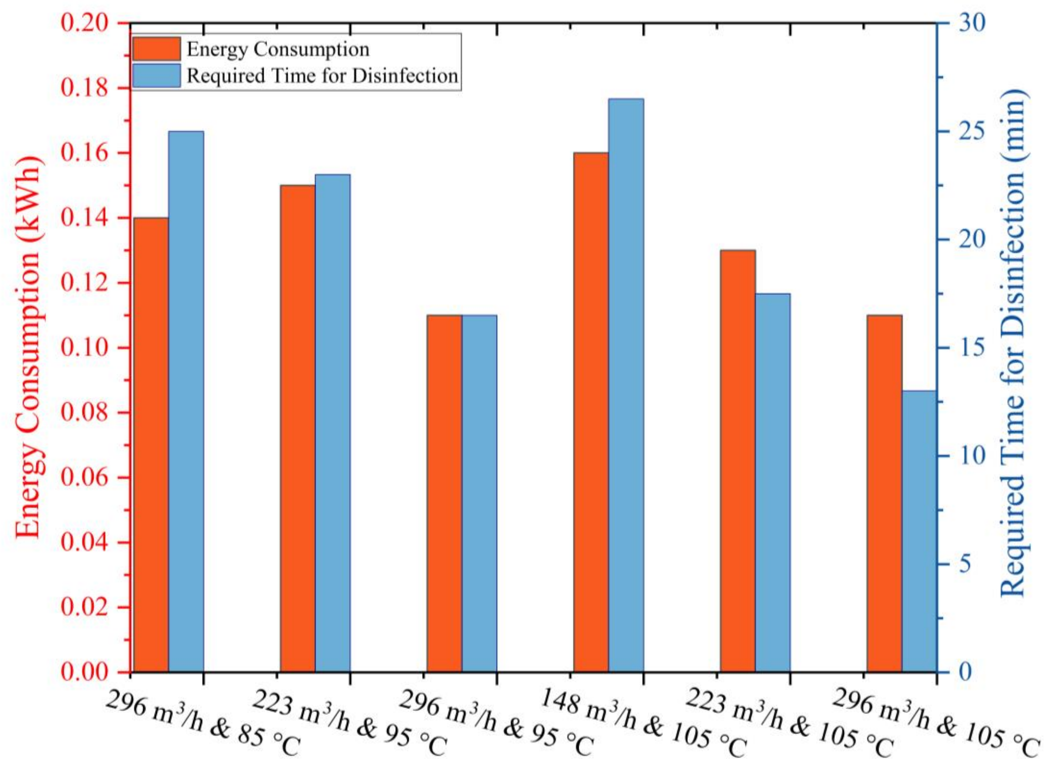

Fig. 5.9. Comparing energy consumption and required time for disinfection between cases, meeting the disinfection criteria.

The cumulative disinfection energy over the service life of a filter depends on the frequency of disinfection and filter properties, including pleat density (number of pleats/cm), media material (commonly made of synthetic polymer, and fiberglass fibers [203–205]), thickness, porosity and dimensions. The exact disinfection frequency will vary with the application (e.g., residential, commercial, or healthcare facilities), environmental conditions (e.g., relative humidity and dust loading [169,206]) and operational circumstances (e.g., pandemic outbreaks). Assuming one disinfection cycle per day and a three-month service life of the tested filter, the cumulative disinfection energy, based on a disinfection duration of 13 minutes and an energy consumption of 0.11 kWh per cycle, is approximately 9.9 kWh.

All previous cases were examined at the maximum reachable flow rate of 2100 m^3/h in the closed-loop wind tunnel. To assess the dependency of energy performance on the flow rate, tests were conducted at a warm inlet set-point temperature of 105 °C and a recirculation rate of 296 m^3/h, comparing scenarios where the wind tunnel was turned off (no flow) and operating at maximum flow (2,100 m^3/h). The results, depicted in Fig. 5.10, reveal that the wind tunnel flow rate has a negligible impact on the average filter temperature within the unit. Furthermore, the measured energy consumptions in these scenarios were not significantly different, with values of 0.11 kWh and 0.10 kWh recorded for the maximum and zero flow conditions within the wind tunnel, respectively. This outcome highlights the insulating effect of the twin-wall polycarbonate sheets deployed in the system. With a thermal conductivity of approximately 0.05 W/m·K, these sheets effectively minimize heat dissipation to the surrounding air, ensuring consistent energy efficiency regardless of the duct flow rate.

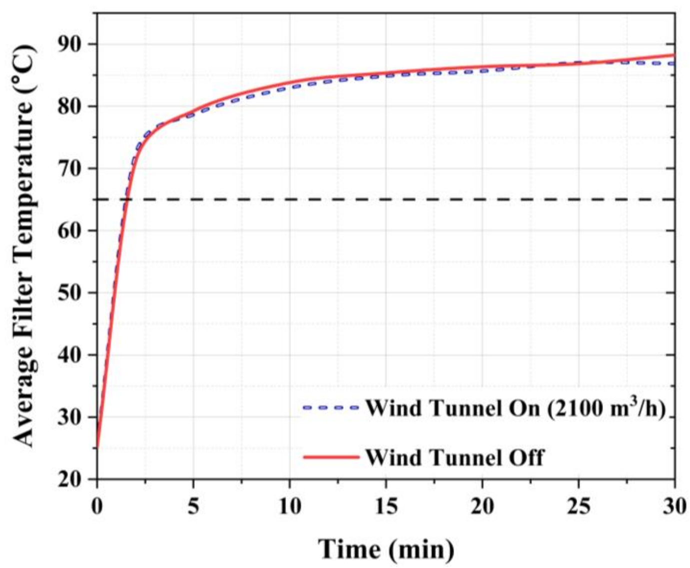

Fig. 5.10. Investigating the impact of airflow rate within the wind tunnel ductwork on the average filter temperature at the warm inlet air temperature of 105 °C, and fans' recirculation flow rate of 296 m^3/h.

5.5.3 Evaluating Filtration Efficiency of the Technology

Figure 5.11 demonstrates the particle removal efficiency of the standalone test filter at air velocities of 0.5, 0.75 and 1 m/s within the wind tunnel. As can be seen, for submicron particles, where diffusion is the dominant filtration mechanism, increasing the air velocity reduces the filtration efficiency. This stems from the fact that the diffusion caused by the Brownian motion of tiny particles is inversely proportional to the Peclet number (advection rate to diffusion rate) [207] and, therefore, air velocity. However, according to Fig. 5.11, increasing the air velocity enhances the filtration efficiency for particles larger than one micron, as the inertial impaction, which is directly proportional to the Stokes number (ratio of a characteristic time of a particle to that of the flow) [207], and consequently, air velocity, is the primary filtration mechanism.

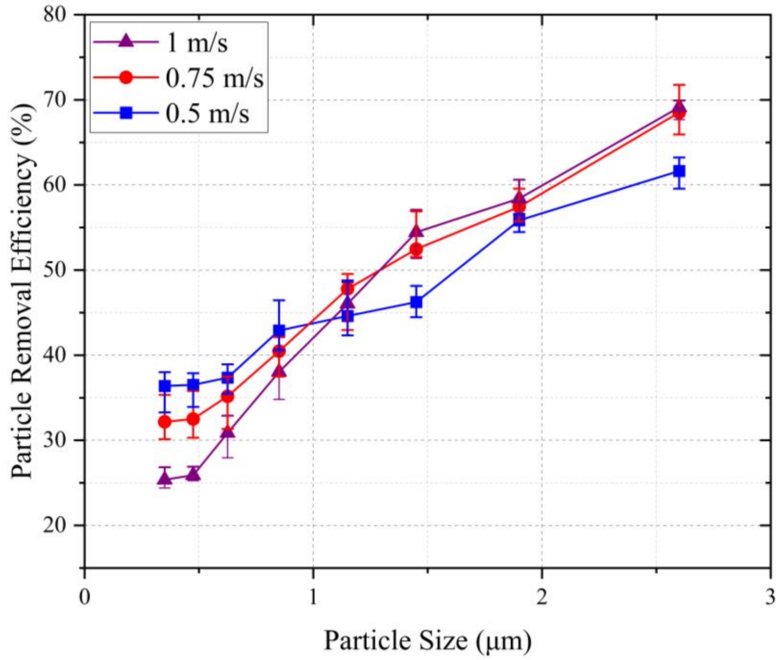

Fig. 5.11. Size-resolved particle removal efficiency of a standalone 1-in MERV 11 filter at different air velocities.

Figures 5.12a-c compare the size-resolved particle removal efficiency between the standalone MERV-11 filter and the disinfection units proposed in this study. As depicted in Figs. 5.12a-c, there is no significant difference in filtration efficiency between the standalone filter and the open-gates mode, where two side-by-side units are fully open. This result suggests that the gates and frames of the installed disinfection units have a minor impact on filtration efficiency when both units are open. However, according to Figs. 5.12a-c, when one of the units gets closed, the filtration efficiency reduces for submicron particles and increases for large particles. During the closed-gates operating mode, the air velocity of the adjacent open unit will be doubled. Therefore, due to the rise in the filter face velocity, the diffusion of submicron particles reduces, leading to a decrease in the filtration efficiency. Nonetheless, for large particles, an increase in the filter face velocity improves the particle capturing by the inertial impaction. Consequently, the penetration of the larger particles from the upstream to the downstream of the filter is lessened.

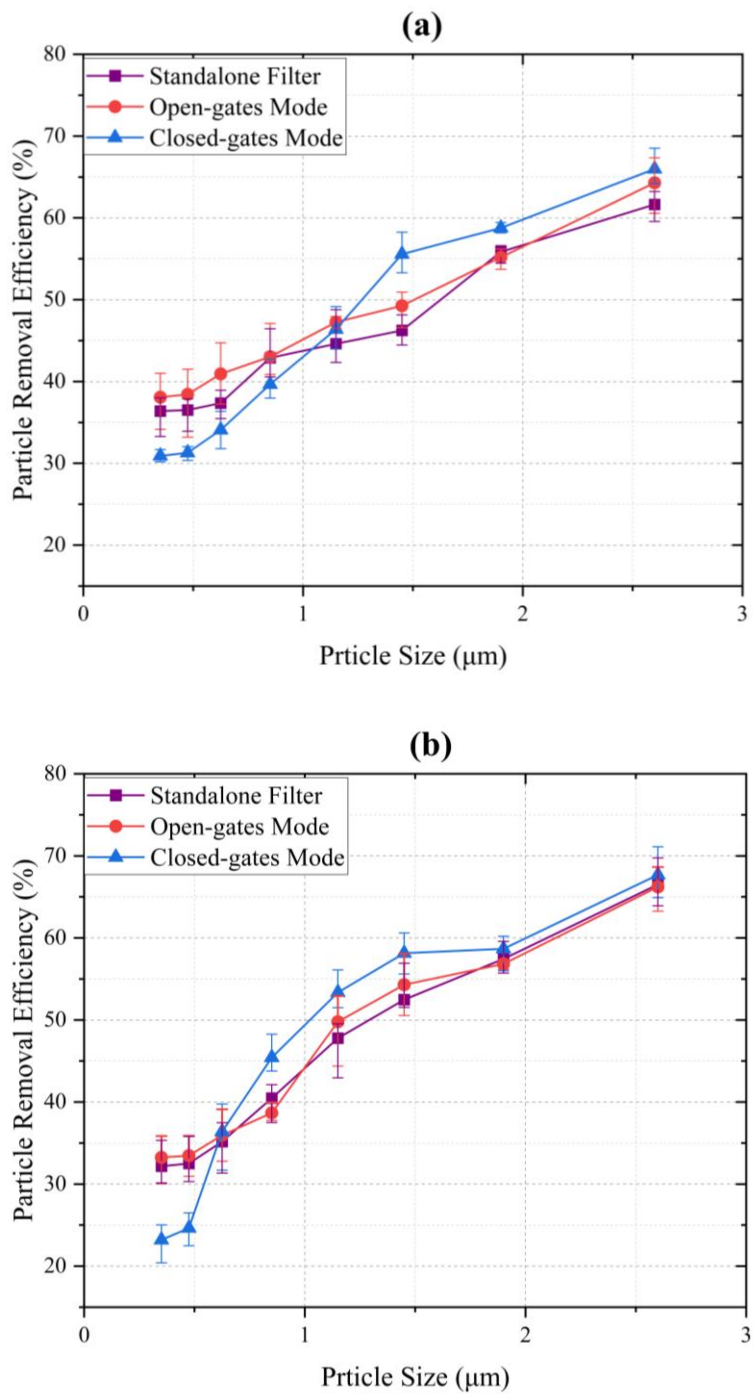

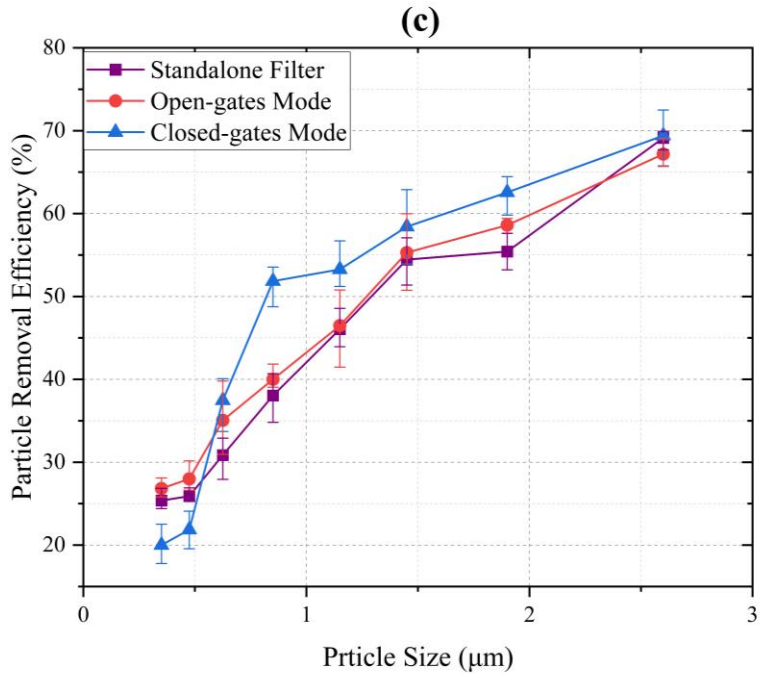

Fig. 5.12. Comparison of the filtration efficiency between the three cases, including the standalone MERV-11 filter, open-gate mode (two open units with MERV-11 filters), and closed-gate mode (one unit closed, one unit open with the MERV-11 filter) at a duct velocity of (a) 0.5 m/s, (b) 0.75 m/s, and (c) 1 m/s.

5.5.4 Evaluating the Pressure Drop of the Disinfection System

Figure 5.13 illustrates the pressure drop associated with three configurations, including standalone filter, open-gates mode, and closed-gates mode, at varying duct airflow rates. As shown, the open-gates mode, which involves the installation of the proposed disinfection system with the gates open, has a negligible impact on the pressure drop compared to the standalone filter. Even at a high airflow rate of 2000 m^3/h, the pressure drop increase in the open-gates mode is less than 5% (approximately 3 Pa) relative to the standalone filter. This indicates that, under normal operating conditions, the introduction of the disinfection system does not impose significant flow resistance.

In contrast, during the disinfection period, when one of the units is insulated by closing its gates (closed-gates mode), the pressure drop increases considerably. The difference between the pressure drop in the closed-gates mode and the standalone filter rises with increasing airflow rates. For instance, at an airflow rate of 2000 m^3/h, the pressure drop increases from 65 Pa for the standalone filter to approximately 205 Pa in the closed-gates mode. This substantial increase in pressure drop in the closed-gates mode is due to the change in airflow rate. When one unit is closed, the airflow passing through the adjacent filter doubles, leading to a sharp increase in air velocity at the filter front face. In porous media, such as HVAC filters, the pressure drop is affected by both frictional drag and inertial resistance. According to Darcy's law, frictional drag is directly proportional to velocity, while inertial resistance scales with the square of the air velocity. Therefore, the doubled air velocity results in significantly higher resistance and a corresponding increase in pressure drop.

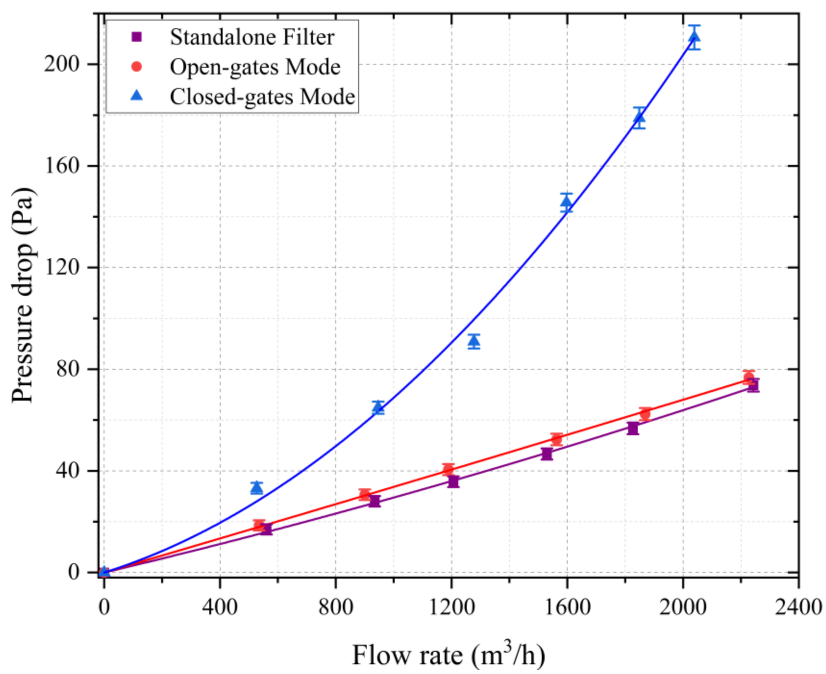

Fig. 5.13. Comparison of the pressure drop vs airflow rate between the three cases, including the standalone MERV-11 filter, the open-gate mode, and the closed-gate mode.

The additional flow resistance introduced during the disinfection period increases the power demand on the main HVAC system fan to maintain the required airflow. This additional fan power can be estimated as Eq. (5.6) [164]:

$$\dot{W}_{fan} = \frac{Q.\Delta p_{add}}{\eta_{motor}.\eta_{fan}} \tag{5.6}$$

in which $\dot{W}_{fan}$ is the fan power, Δp_{add} represents the additional pressure drop, and η_{motor} and η_{fan} are the efficiencies of the motor, and the fan, respectively. For an airflow rate of 2000 m^3/h, the additional pressure drop during the disinfection period is 140 Pa. Assuming constant motor and fan efficiencies of 90% and 60%, respectively, based on the manufacturer's catalogue [208], and a disinfection duration of only 13 minutes per unit, the additional energy consumed by the fan during disinfection ($\dot{W}_{fan}$ × Disinfection Duration) is approximately 0.03 kWh per unit. Therefore, although the increase in pressure drop during disinfection is notable, the short duration (about 13 minutes per unit) ensures that this temporary rise has a negligible impact on the HVAC system's overall energy consumption over its operational cycle.

5.5.5 Practical Prospects and Limitations

The parallel application of the existing disinfection technologies summarized in Table 5.1 with conventional filtration can present practical challenges, in particular, may not effectively decontaminate filters that can serve as potential secondary sources of contamination. Furthermore, integrating HVAC filters with other disinfection technologies may introduce risks associated with ozone and secondary by-product generation, particularly in electrostatic precipitator (ESP), plasma, and photocatalytic systems. The limited penetration of UV light into the porous fibrous structure of filters, combined with its high energy consumption (e.g., approximately 0.48 kWh for decontamination of a 20 cm × 20 cm test filter, as reported in Ref. [189]), further constrains the adoption of UV-assisted filtration.

Existing technologies on thermal disinfection of filters also encounter certain practical challenges. For instance, a pressure drop on the order of 5 kPa was reported in the approach introduced by Soni et al. [194], while elevated operating temperature requirements and the possibility of significant pressure losses associated with metallic foams, as well as current uncertainties in the reliability of solar-driven technologies, may hinder broader HVAC implementation.

In contrast, the present study demonstrates that applying recirculating warm air within an insulated enclosure can effectively disinfect a pleated MERV 11 filter in 13 minutes, consuming only about 0.11 kWh per cycle, while adding a minor additional load on HVAC fans during disinfection and without compromising filtration efficiency. The technology also avoids ozone-related concerns, as no reactive species are detected during our tests. Owing to its apparent robustness, relatively low energy consumption, and modular design, the system can be amenable to implementation in large-scale HVAC applications.

In terms of practical deployment, the design and placement of the disinfection unit may vary depending on the HVAC system size and configuration. A single disinfection module can be installed at the end of a return-air duct upstream of the central ventilation unit. In larger commercial buildings, schools, or healthcare facilities, multiple modules may be strategically distributed within the duct system or mounted near supply outlets serving individual zones. The proposed technology is particularly suited for pleated filters. For HEPA filters with greater depth and surface density, the required disinfection time could become excessively long, limiting the method's practicality. Additionally, the system requires adequate installation space for the warm air recirculation duct, which may not be available in compact or retrofit applications.

It should be noted that live microorganisms were not used in the present experiments; instead, literature-based thermal inactivation data were employed to validate the concept. Future work will involve biological testing using live microorganisms in a controlled test apparatus to safely quantify the efficiency of microbial inactivation on loaded filter media at different temperatures and exposure times.

5.6 Conclusions

To address the deficiency of existing disinfection technologies in HVAC systems, this study proposes a novel disinfection system that combines conventional air filtration with heating to entrap and inactivate pathogens. The inventive device operates by recirculating warm air in an insulated cavity that contains HVAC filters. The heat transfer performance of the system was investigated experimentally at various operating conditions, including different warm inlet temperatures (85, 95, and 105 °C) and recirculation rates within the units (88, 148, 223, and 296 m^3/h). Furthermore, a closed-loop aerosol wind tunnel accommodating the system prototype was developed following the ASHRAE 52.2 standard. This aerosol wind tunnel was then deployed to evaluate the size-resolved filtration efficiency and pressure drop of the proposed disinfection system at varying duct airflow rates and different operating modes. The main findings are as follows:

(1) An increase in the warm inlet temperature and the recirculating flow rate significantly decreases the time required to reach the disinfection temperature at the filter.

(2) At a warm inlet air temperature of 105 °C, and units' air recirculation rate of 296 m^3/h, the proposed system increases the temperature of a 1-in MERV-11 filter from room temperature to 65 °C in only 3 minutes. Maintaining this condition for an additional 10 minutes ensures the

elimination of entrapped COVID-19 viruses within the filter. To do so, the total energy consumption of the disinfection system is 0.11 kWh.

(3) An increase in the air velocity within the ductwork decreases the particle-capturing mechanism of submicron aerosols. However, for large particles, a rise in the duct flow rate increases inertial impaction and, therefore, filtration efficiency.

(4) The introduced system does not affect the particle removal efficiency compared to a standalone filter when the gates of two side-by-side units are open (open-gates mode). However, during the disinfection process, when one of the units is isolated, the particle removal efficiency of submicron particles decreases, whereas the filtration efficiency of large particles increases compared to a standalone test filter.

(5) Under normal operating conditions (open-gates mode), the addition of the proposed disinfection system does not impose significant flow resistance compared to a standalone filter. However, during the disinfection period (closed-gates mode), the pressure drop increases considerably. Even though the increase in pressure drop during the disinfection period is considerable, the disinfection duration is short (approximately 13 minutes per unit). Consequently, this temporary increase in pressure drop would not significantly affect the total energy consumption of the HVAC fans over the system's operational cycle.

Acknowledgements

The authors gratefully acknowledge the financial support provided by the Natural Sciences and Engineering Research Council of Canada (NSERC) through its Alliance program (Grant No. 567653-21) and by Engineered Air through its endowment in HVAC Engineering at the University of Alberta. We also extend our sincere thanks to Alberta Innovates for supporting this work through the Alberta Innovates Graduate Student Scholarship (AIGSS).

Chapter 6. An Energy-Efficient Heat-Driven Technology for Airborne Pathogen Inactivation: Integration of Two-Stage HVAC Filtration with Thermal Disinfection

This paper was published in Applied Thermal Engineering.

Mirzazade Akbarpoor, A., Salimi, M., Rasouli, E., Shahbakhti, M., Nouri. A., *Two-stage HVAC filtration systems: Performance assessment and thermal disinfection for air purification*, Applied Thermal Engineering, 2026 (Published).

6.1 Preface

Air filters are widely used in HVAC systems to control the transmission of airborne microorganisms. However, their application is associated with frequent maintenance, accumulation and release of bioaerosols. To address these issues, the present study proposes a novel thermal disinfection approach integrated into a two-stage filtration system comprising a MERV 8 pre-filter and either MERV 11 or MERV 13 main filter. To maintain continuous airflow, the system employs two side-by-side units with the same filters sequentially disinfected via forced convection heating while maintaining continuous filtration. A closed-loop aerosol wind tunnel, based on the ASHRAE 52.2 standard, was implemented to evaluate the filtration efficiency and pressure drop of the system at various configurations and operating modes, including normal operation (both units open) and a disinfection period (one unit closed). Moreover, a heat transfer setup was developed to measure the required time and energy consumption for meeting the literature-based thermal inactivation criteria (10 minutes exposure to 65 °C) across three inter-filter distances. A comparison of the theoretical correlation for estimating the overall filtration efficiency of multi-stage systems with experimental results confirmed good agreement in normal operation, with some deviations during the disinfection period due to flow redistribution. Furthermore, changing the inter-filter distance has relatively minor impacts on the overall filtration efficiency and pressure drop compared to its effect on the disinfection process. Consequently, the energy performance of the disinfection system should be considered the primary criterion when determining the optimal distance between the pre-filter and the main filter.

6.2 Introduction

Indoor air quality (IAQ) has attained significant importance in modern society and the post-COVID-19 pandemic era. Individuals spend approximately 90% of their time in enclosed spaces and inhale an average of 15-20 m^3 of air daily [68,160]. Poor IAQ and reduced thermal comfort [161–163] pose significant health risks, especially when the indoor environment is contaminated with pathogenic microorganisms [74]. Heating, ventilation and air conditioning (HVAC) systems are held accountable for maintaining indoor air quality and thermal comfort.

The prominent role of proper HVAC systems design illustrated itself during the virulence of pandemics such as SARS, Influenza H1N1, and COVID-19, which collectively caused widespread morbidity and mortality over the last two decades [18]. Air filtration is a widely adopted strategy for controlling airborne microorganisms' transmission in HVAC systems due to its cost-effectiveness, ease of implementation, and viability in removing air contaminants [23]. According to ASHRAE recommendations in 2021, high-efficiency filters with a Minimum Efficiency Reporting Value (MERV) of 13 or higher should be used to reduce the spread of airborne pathogens [209]. Published works in the literature have illustrated that MERV 13 filters effectively lower infection risks in enclosed spaces [164–166]. Nonetheless, rising filtration efficiency beyond MERV 13 provides slight surplus advantages in reducing aerosolized pathogens concentrations [164,200].

Notwithstanding their effectiveness, the application of HVAC filters is associated with several challenges. Filters require frequent maintenance due to particulate matter accumulation, leading to increased pressure drop and fan energy consumption [12,64,210]. Furthermore, considering that filtration is an entrapment mechanism and does not inactivate captured microorganisms, bioaerosols may accumulate on the filter surfaces over time, contributing to fungi and spores' growth in the presence of moisture and organic particles [211,212]. This colonization degrades filtration performance and turns filters into secondary pollutant sources, increasing the risk of pathogens re-aerosolization during the fan restart cycles and filter replacement [26,206].

One of the well-established solutions to mitigate rapid clogging and the need for frequent replacement of HVAC filters is the implementation of multi-stage filtration systems. Multi-stage filtration, widely applied in commercial buildings and health care facilities, employs inexpensive coarse pre-filters to protect the main stage filters with higher MERV ratings [213,214]. This configuration extends the service life of the main filter by reducing its particulate load and, therefore, maintains filtration efficiency and lowers operational costs [207,215,216].

For instance, Tian et al. [216,217] experimentally evaluated various pre-filter and main filter combinations and found that a G4 pre-filter (equivalent to MERV 8) provided the best balance of efficiency and longevity, offering the longest protection period for high-efficiency filters such as F9 and E11 (corresponding to MERV 16). Specifically, adding a G4 upstream extended the service life and dust-holding capacity of an E11 filter by 3.8 and 3.6 times, respectively. In a related study, Tian et al. [215] showed that while a G4 pre-filter improved the service duration of melt-blown F9 and PTFE E11 filters, it unexpectedly reduced the lifespan of a cellulose-based F7 filter, highlighting that the effectiveness of pre-filters depends strongly on the main filter media.

Wu et al. [200] experimentally investigated the performance of two-stage filtration systems, including pre-filters (MERV 6, MERV 8, and an electrostatic enhanced air filter (EEAF)) and MERV 11 filters. The results revealed that the combination of MERV 8 and MERV 11 filters obtained a superior quality factor (filtration efficiency to pressure drop ratio) compared to other combinations, where 50 % of particles within the size range of 0.1 to 1 μm were removed at an air duct velocity of 1 m/s.

Despite the effectiveness of multi-stage filtration systems in delaying the clogging of high-efficiency filters, they cannot prevent the re-aerosolization of bioaerosols and the release of particles downstream [74]. Therefore, supplementary disinfection technologies should be hybridized with filtration to address the filter colonization issue.

Several filter-assisted sterilization technologies have been reported, including electrostatic precipitators (ESPs), ultraviolet (UV) irradiation, photocatalysis, and plasma treatment. ESPs enhance particle removal by corona discharge but are hindered by ozone generation, harmful by-products, high costs, and safety risks from high-voltage operation [62–68]. UV-based systems can disinfect both HEPA and non-HEPA filters [61,69], yet their effectiveness is reduced by high humidity, limited penetration into filter pores, declining performance at higher duct flows, and high energy use [18,62,70]. Photocatalytic coatings, typically based on TiO_2 or ZnO, generate reactive oxygen species to inactivate pathogens [71,72], but their efficiency decreases at high airflow rates and sunlight-only conditions, while ozone generation remains a concern [71,73]. Plasma-assisted systems show promise in portable devices [18,75], but large-scale HVAC integration is limited by ozone and ion by-products as well as high energy demands [18,75,77].

The application of thermal treatment is another viable approach for air filter decontamination. Among various disinfection technologies, thermal inactivation, which is the focus of this study, demonstrates superior efficiency [18]. Unlike previously mentioned disinfection methods, heat can penetrate excellently. The key factors determining the effectiveness of heat-based disinfection are temperature and exposure time, both of which depend on the characteristics of the target microorganisms [19–21].

Studies examining used HVAC filters have identified frequent colonization by bacteria such as *Bacillus, Staphylococcus, Pseudomonas*, and *E. coli*; fungi such as *Aspergillus* and *Penicillium*; and viral RNA from pathogens including SARS-CoV-2 [167–170,206,218,219]. Research suggests that maintaining a temperature of approximately 65 °C for 10 minutes is sufficient to inactivate many common microorganisms found in HVAC systems, including vegetative bacteria (e.g., *E. coli* [79], *Legionella pneumophila* [80], and *Pseudomonas aeruginosa* [81]), and viruses (e.g., rhinovirus [82], avian influenza [83], and SARS-CoV-2 [84]). It should be noted that while certain fungal spores such as *Aspergillus niger* and *Penicillium citrinum* are reported to have lethal temperatures in the relatively low range of 45–56 °C under dry heat treatment [29], which suggests that exposure to 65 °C could be sufficient for significant inactivation, achieving complete inactivation of heat-resistant fungal spores typically requires conditions more severe than 65 °C for 10 minutes [85]. Therefore, maintaining 65 °C for 10 minutes was selected in this study as a conservative benchmark condition representing effective thermal inactivation for the majority of relevant microorganisms while remaining practical for HVAC-scale application.

Despite the high antiviral and antibacterial efficiency of heat treatment, only a limited number of studies have explored the integration of air filtration with thermal disinfection [78]. Xie et al. [86] reported that a hybrid system combining a photovoltaic (PV) panel, a Trombe wall, and an air filter achieved over 60% reduction of *Klebsiella pneumoniae* bioaerosols. Yu et al. [87] introduced a self-heating nickel foam filter that inactivated >99.9% of SARS-CoV-2 at the filter temperature of 200 °C but required 500 W for a relatively small filter (24 cm × 30 cm), raising scalability concerns.

Table 6.1 compares the capabilities of different filter disinfection methods proposed in the literature. As is evident, high energy consumption, risk of high voltage, generation of harmful by-products, short life span, and large-scale scalability are the main barriers to the application of existing technologies. Furthermore, despite the specified advantages of the multi-stage filtration system, none of the previously published studies focused on integrating thermal disinfection into multi-stage HVAC filtration. Current thermal approaches, while effective, often face challenges such as high energy consumption or limited scalability. Thus, there remains a critical need for an energy-efficient, scalable solution that ensures both high filtration efficiency and effective disinfection of accumulated pathogens.

Table 6.1. Comparing the existing filter disinfection technologies in the literature with the proposed technology in this study.

Technology	Energy Efficient	High Inactivation Efficiency	No Harmful By-products	No Risk of High Voltage	Long Life Span	Portable Air Purifiers	Scalability in HVAC
ESP + Filter		✓				✓	
UVC + Filter		✓	✓	✓		✓	✓
Photocatalysis + Filter	✓			✓		✓	
Plasma + Filter		✓				✓	
Heat + Filter (Existing Techs.)		✓	✓				
Proposed Tech. (Present Work)	✓	✓	✓	✓	✓	✓	✓

To fill this research gap, this study proposes a novel heat-based technology for the disinfection of a two-stage filtration system, including a pre-filter (MERV 8) and different main-stage filters (MERV 11 and MERV 13). By combining the two-stage system with thermal inactivation, the proposed system can prevent rapid clogging of the main filter and inactivate accumulated pathogens. Moreover, by employing two insulated side-by-side units, the system is energy-efficient and easily installed in HVAC systems. Unlike plasma, photocatalysis, or ESP-based systems, thermal disinfection of filters relies solely on heat and therefore does not produce ozone or other reactive oxygen species [220]. Previous studies have shown that volatile organic compound (VOC) emissions from filter materials remain negligible below 100 °C, and that any minor release originates mainly from desorption of pre-existing compounds on dust-loaded filters rather than from the filter media itself [221–225].

While two-stage filtration systems have been extensively studied for filtration performance, no previous work has investigated their disinfection and how filter spacing affects flow characteristics and disinfection efficiency. The present study provides a new experimental framework for understanding the coupled aerodynamic and thermal performance of multi-stage HVAC filters in both normal and disinfection modes. Details on the disinfection device's working principle are provided in Section 6.3. The main novelties and contributions of the present work can be summarized as follows:

1. Proposing a novel, energy-efficient method for disinfecting two-stage HVAC filtration systems.

2. Evaluating the pressure drop and filtration efficiency of the two-stage system in a recirculating aerosol wind tunnel based on ASHRAE 52.2 standard [52].

3. Assessing the accuracy of theoretical correlation for estimating the overall filtration efficiency of multi-stage systems in different operating modes.

4. Determining the optimal distance between the pre-filter and the main-stage filter, which can provide energy-efficient disinfection without lowering filtration efficiency.

6.3 Problem Description

Figures 6.1 and 6.2 illustrate the operating principles and components of the proposed disinfection technology investigated in this study. As depicted in Fig. 6.1, the disinfection module consists of two identical units arranged side by side, each comprising a pre-filter and a main-stage filter.

Initially, both units remain open, with heating elements and axial fans turned off, allowing the two-stage filtration system to capture bioaerosols effectively. After a specific operational period, depending on the installation environment or the concentration of microorganisms, one of the disinfection modules is isolated by closing its gates (Unit 1 in Fig. 1). In the isolated unit, the heating element and recirculation fans are activated. These axial fans direct airflow upwards toward heating wires positioned beneath the filters, causing heated air to flow through a slot into the space between the pre-filter and the main-stage filter. The heated air rises, transferring heat to the filters through forced convection, and subsequently recirculates via the designated recirculation duct. This heating process continues until both filters reach the targeted disinfection temperature, and the exposure duration is sufficient to ensure the destruction of all targeted bioaerosols trapped within the filters.

In this study, the targeted temperature and exposure time are set at 65 °C and 10 minutes, respectively, parameters effective in disinfecting the most common pathogens, as previously discussed. Upon completion of the thermal disinfection process, the heating element and recirculation fans are deactivated, and the isolated unit is reopened. Throughout the disinfection process of one unit, the adjacent unit (Unit 2) remains fully operational, continuing the capture of microorganisms. Sequential repetition of this process ensures continuous disinfection of both units.

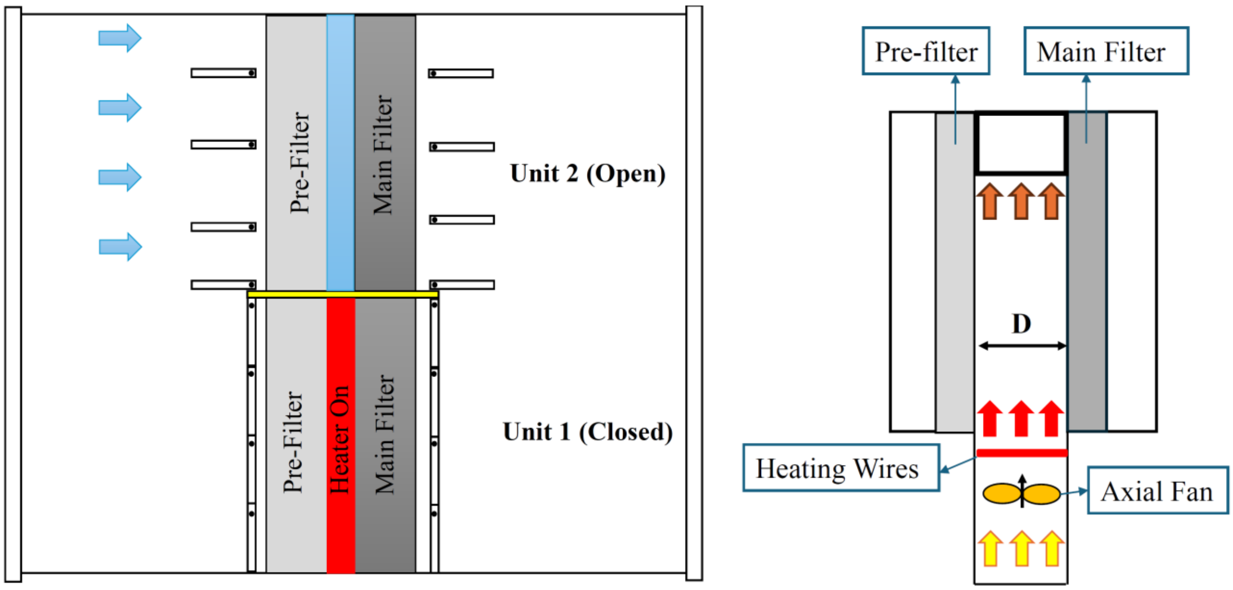

(Top view) (Side view)

Fig. 6.1. Schematic diagram demonstrating the disinfection approach utilized in the two-stage filtration system investigated in this study.

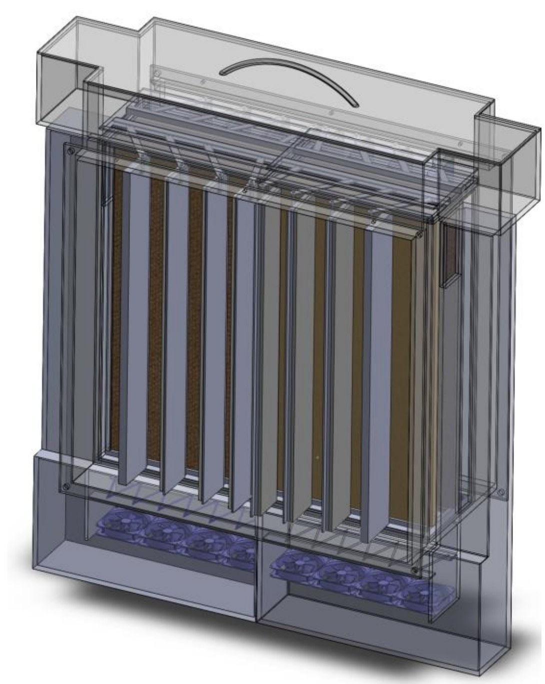

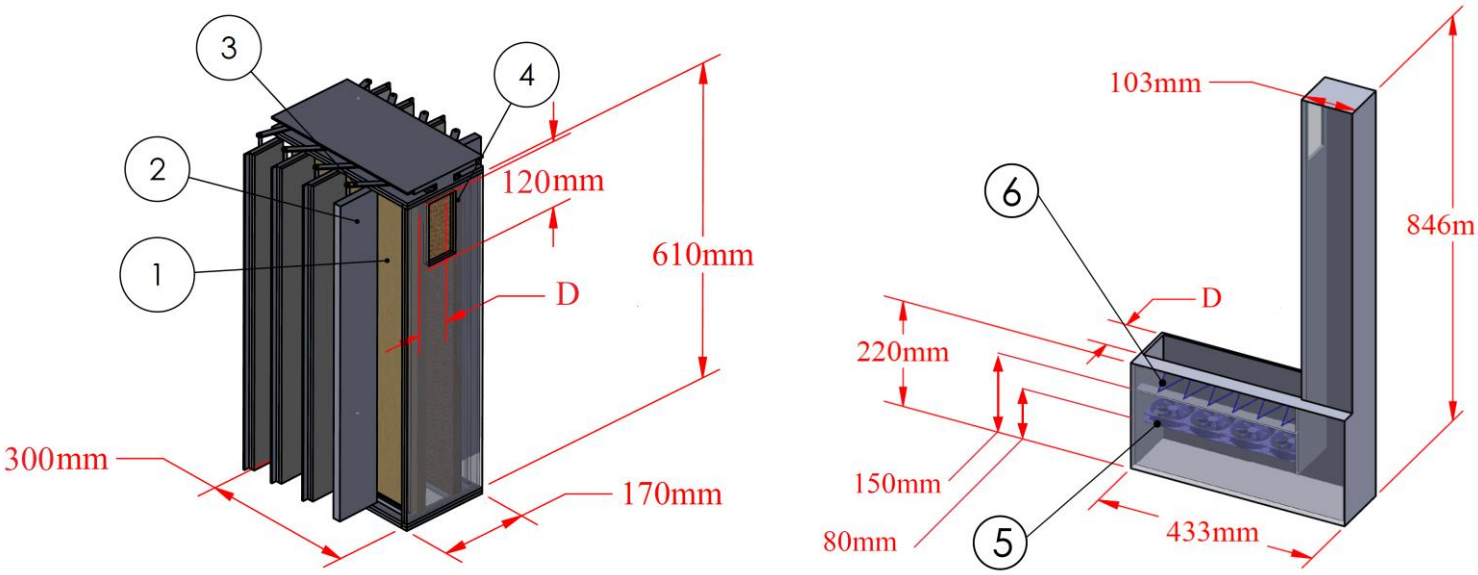

Fig 6.2. Technical schematic depicting the layout and dimensions (mm) of the heat-driven filter disinfection system, including 1: pre-filter, 2: gates, 3: sliders, 4: main filter, 5: axial recirculating fans and 6: the heating element.

6.4 Methodology

The investigation of the performance of the proposed technology includes an experimental evaluation of the filtration efficiency and pressure drop of the two-stage system in a closed-loop aerosol wind tunnel, as well as an assessment of the heat transfer and energy performance of the disinfection units. Therefore, the methodology in this work is divided into two sections.

6.4.1 Fully Recirculating Aerosol Wind Tunnel

For the sake of measuring the particle removal efficiency and pressure of the two-stage filtration system, a closed-loop aerosol wind tunnel with a total length of about 18 m and a cross-section of 0.61 m × 0.61 m meeting ASHRAE 52.2 [22] and Guideline 26 [195] was employed (Figs. 6.3 and 4). A centrifugal fan is implemented to circulate air within the ductwork and maintain the airflow at a desirable value during the test. A poly-disperse aerosol generator filled with KCl solution (25 gr KCl per 0.100 liter of ionized water) injects aerosols into the wind tunnel. Two mixing baffles are installed at the upstream and downstream sampling locations to provide a uniform particle distribution. Isokinetic samplers connected to vacuum pumps collect aerosols upstream and downstream of the test section. An automated sample switching unit is used to switch between the isokinetic sampling lines before and after the filter. This switching valve allows measuring filtration efficiency with a single optical particle counter (OPC). Furthermore, a pressure transmitter connected to a data logger is employed to measure the pressure drop of the two-stage filtration system. The specifications of all equipment utilized for filtration efficiency tests are detailed in Table 6.2.

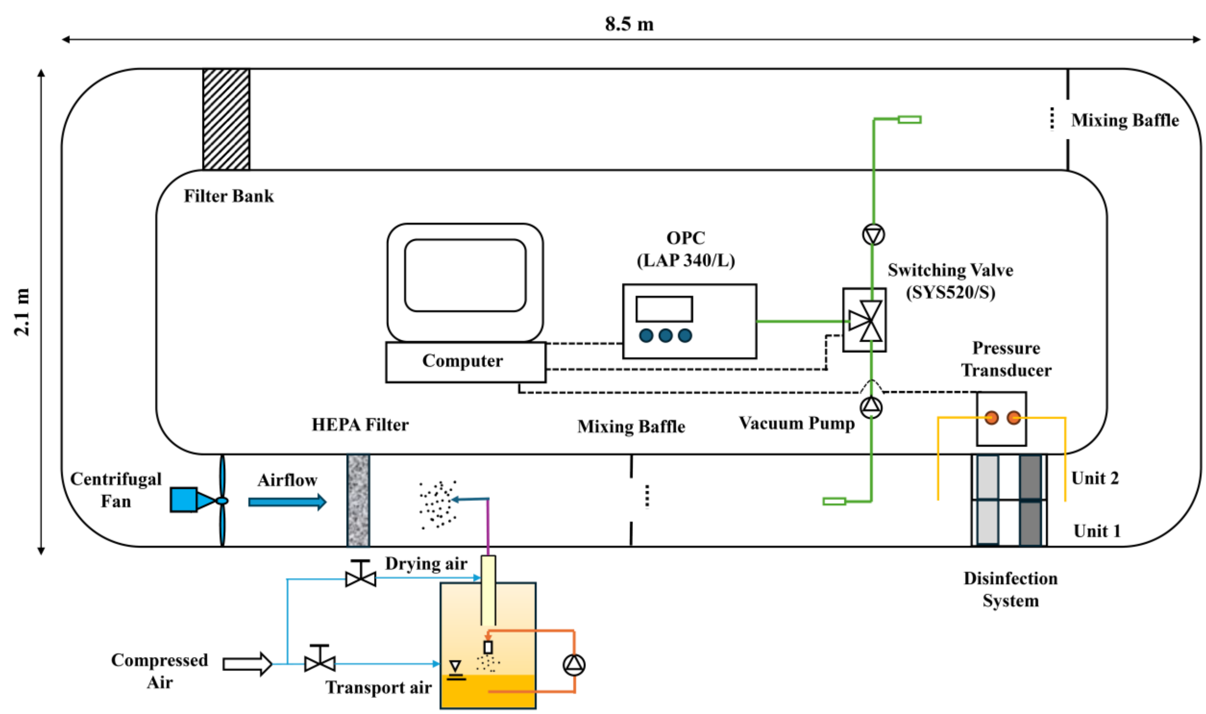

Fig. 6.3. A schematic diagram of the recirculating aerosol wind tunnel.

Fig. 6.4. Experimental setup for evaluating filtration efficiency and pressure drop.

Table 6.2. Specifications of the equipment implemented for testing the filtration efficiency and pressure drop of the disinfection system.

Instrument	Model / Specifications
Centrifugal fan	Rosenberg GKHM 280-CIB
Aerosol generator	TOPAS-ATM240/S (generates aerosols in the size range of 0.3 to 10 µm, fed by a 5-bar compressed air)
Optical particle counter (OPC)	TOPAS-LAP 340/L (measures aerosol concentration (#/cm^3) for particle diameter of 0.2 to 10 µm)
Isokinetic coupler and sampling probe	TSI- P/N 1130011
Vacuum pump	TSI model 3032 (produces flow rates up to 5 L/min)
Sample switching valve	TOPAS- SYS520/S
Differential pressure transmitter	OMEGA-PX655-05DI, accuracy ± 3 Pa
Data logger	NI-USB-6002
Thermo-anemometer	TSI-9535, accuracy ± 0.05 m/s
Mixing baffle	Manufactured according to ASHRAE 52.2 with a 40 % open area on the perforated diffusion plates

The filtration efficiency of a particle removal system can be determined using the following expression [200,201]:

$$\eta = (1 - \frac{P_{ave}}{R_{ave}}) \times 100 \tag{6.1}$$

where P_{ave} denotes the average penetration, representing the fraction of aerosols that pass through the filter (Eq. (6.2)). The term R_{ave} refers to the average correlation ratio, which acts as a correction factor and is determined from Eq. (6.2) when the filtration device is absent.

$$P_{ave} = \left(\sum_{i=1}^{n} \frac{C_{i,o} - C_{b,ave}}{U_{i,e} - U_{b,ave}}\right)/n \tag{6.2}$$

Here, $C_{i,o}$ and $U_{i,e}$ correspond to the observed downstream and estimated upstream concentrations, respectively. The terms $C_{b,ave}$ and $U_{b,ave}$ represent the average concentrations of background samples recorded before and after aerosol generation at the respective sampling locations (Eqs. (6.3) and (4)). While $C_{i,o}$ can be directly measured using an optical particle counter (OPC), the estimation of $U_{i,e}$ requires the application of Eq. (6.5):

$$U_{b,ave} = \left(\sum_{i=1}^{n} U_{i,o,b}\right)/n \tag{6.3}$$

$$C_{b,ave} = \left(\sum_{i=1}^{n} C_{i,o,b}\right)/n \tag{6.4}$$

$$U_{i,e} = \frac{U_{i,o} + U_{(i+1),o}}{2} \tag{6.5}$$

In this study, three background samples were collected at each sampling location. Furthermore, data quality considerations implied the total number of samples and the duration of each sampling period. Accordingly, four samples were recorded at the upstream location and three at the downstream location, while the duration of each sampling period was one minute.

Theoretically, the total filtration efficiency of two-stage filtration systems, including a pre-filter and a main-stage filter that are placed in series, can be estimated as follows [200,226]:

$$\eta_t = 1 - (1 - \eta_{\text{pre-filter}})(1 - \eta_{\text{main-filter}}) \tag{6.6}$$

In the present work, single-stage and two-stage filtration configurations will be tested in the wind tunnel. Each configuration will be examined under two different operating conditions: the normal operation mode, wherein both units are open and the disinfection mode, where one of the units is closed. Each side-by-side unit contains an identical pleated filter in the single-stage filtration system. Three different pleated filters, including MERV 8, MERV 11 and MERV 13, will be examined. The specifications of the test filters are summarized in Table 6.3. All filters have dimensions of 12 in × 24 in × 1 in (30.48 cm × 61 cm × 2.54 cm). For the two-stage filtration system, this work considers combinations of MERV 8 as a pre-filter, with MERV 11 and MERV 13 as the main-stage filter. Three different spacing distances (D) of 2 cm, 4 cm, and 6 cm between the two filters will be investigated. It should be noted that the air duct velocity will remain constant at 0.75 m/s for all experimental tests conducted in this study. At this velocity, ASHRAE's isokinetic sampling conditions can be met for particle diameters ranging from 0.3 to 3 μm in our test rig when one unit is closed.

Table 6.3. Specifications of the test filters.

MERV	Fiber Material	Thickness (mm)	Pleat Density (Pleat/cm)	Total Filter Mass* (g)	Effective Thermal Mass** ($J.K^{-1}$)
8	Polyester	0.53	0.33	135.53	171.7
11	Polyester	0.66	0.40	173.97	221.3
13	Polypropylene	0.73	0.60	200.51	318.2

* Each filter consists of filter media, a cardboard frame, and aluminum wire.
** The total effective heat capacity (thermal mass) is estimated using the following formula:

$$(mc_p)_{total} = \sum_i m_i c_{p,i}$$

in which m_i and $c_{p,i}$ specify the mass and the specific heat capacity of the component i of the filter.

6.4.2 Evaluation of Energy Consumption and Heat Transfer

As shown in Fig. 6.5, the prototype of the disinfection system was fabricated using polycarbonate sheets according to the dimensions provided in Fig. 6.2. All frame walls were covered with aluminum foil to minimize radiation heat loss. Axial fans and heating wires were installed beneath the system.

Figure 6.6 depicts the experimental setup developed to evaluate the time and energy required to disinfect the proposed two-stage filtration system. A proportional-integral-derivative (PID) controller was used to maintain a constant inlet-air temperature throughout the tests. Figure 6.7 illustrates the transient warm-air inlet temperature regulated by the PID controller during a 60-minute operation. The controller maintained the inlet-air temperature at approximately 95 ± 2 °C. The minor oscillations observed are attributed to the short thermal and transport lag between the heater surface and the thermocouple location (i.e., 7 cm above the heating wires). Because all tests were conducted at the same flow rate (296 $m^3\ h^{-1}$) and setpoint temperature (95 °C), the controller performance was nearly identical across all configurations; therefore, only one representative curve is presented.

The multi-stage filtration system consists of a pre-filter (MERV 8) followed by a main filter (MERV 11 or MERV 13). Twelve T-type thermocouples were mounted on each filter (seven on the front face and five on the rear face), for a total of 24 thermocouples, to monitor filter temperatures. The placement of these thermocouples on the filters is illustrated in Figs. 6.8a & b. As shown in Fig. 6.1, the rear face of the pre-filter and the front face of the main filter are directly exposed to forced convection from the recirculating warm air, while the opposite faces are primarily influenced by natural convection. Because of flow direction and lateral heat losses, the lowest temperatures on the forced-convection faces occur near the upper side edges, whereas on the natural-convection faces, the bottom and side regions are the coldest. Thermocouples were therefore positioned at these locations to capture both maximum- and minimum-temperature zones, ensuring that once the minimum points reached 65 °C, all other areas of the filters had already exceeded this temperature. Moreover, two thermocouples were installed immediately before the fans and after the heating wires. Two sixteen-channel data loggers recorded the temperature data. A power meter was also installed to measure energy consumption. The specifications of all instruments are summarized in Table 6.4.

To investigate energy performance, three inter-filter distances (D) of 2 cm, 4 cm, and 6 cm were tested, consistent with the filtration efficiency measurements. For all cases, the temperature of the air entering the enclosure was maintained at 95 °C to ensure that the filter media would not undergo permanent degradation [178,179]. The recirculation flow rate of the axial fans within the unit and the airflow rate in the wind tunnel were kept at 296 m^3/h and 2100 m^3/h, respectively.

Fig. 6.5. Manufactured prototype for thermal disinfection of the two-stage filtration systems.

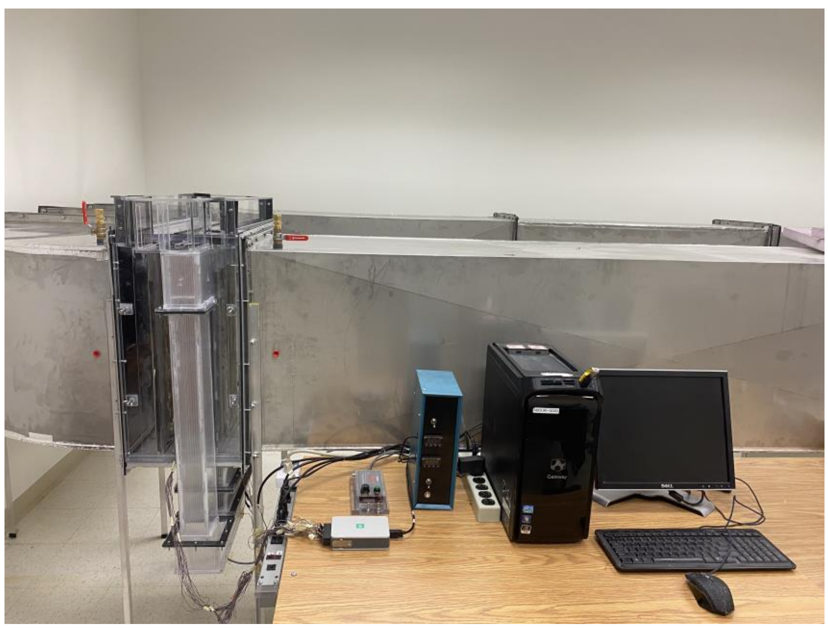

Fig. 6.6. Experimental setup for evaluating heat transfer and energy performance of the disinfection unit accommodated in the wind tunnel.

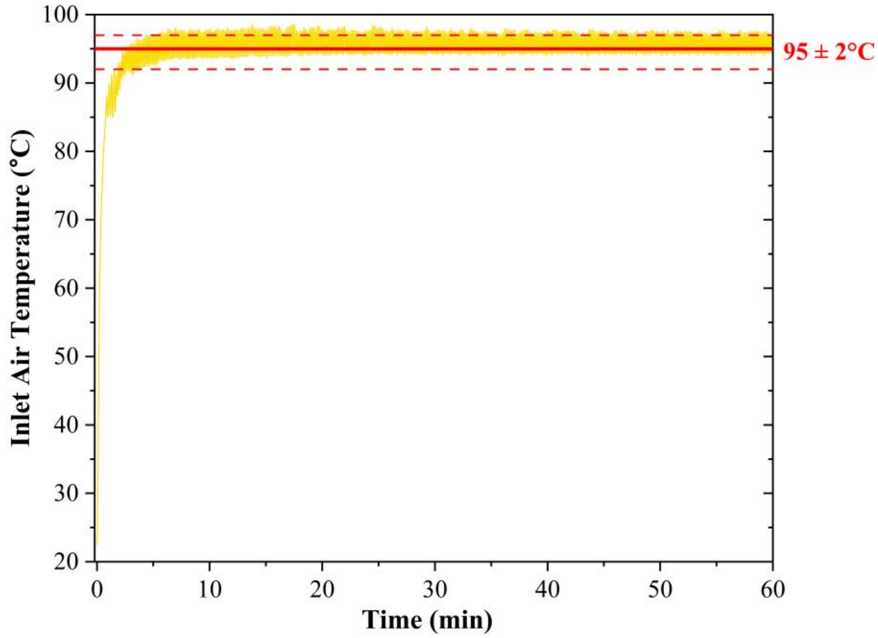

Fig. 6.7. Variation of the warm-air inlet temperature regulated by the PID controller during a 60-minute operation. The red dashed lines indicate the ±2 °C range around the 95 °C setpoint (red solid line).

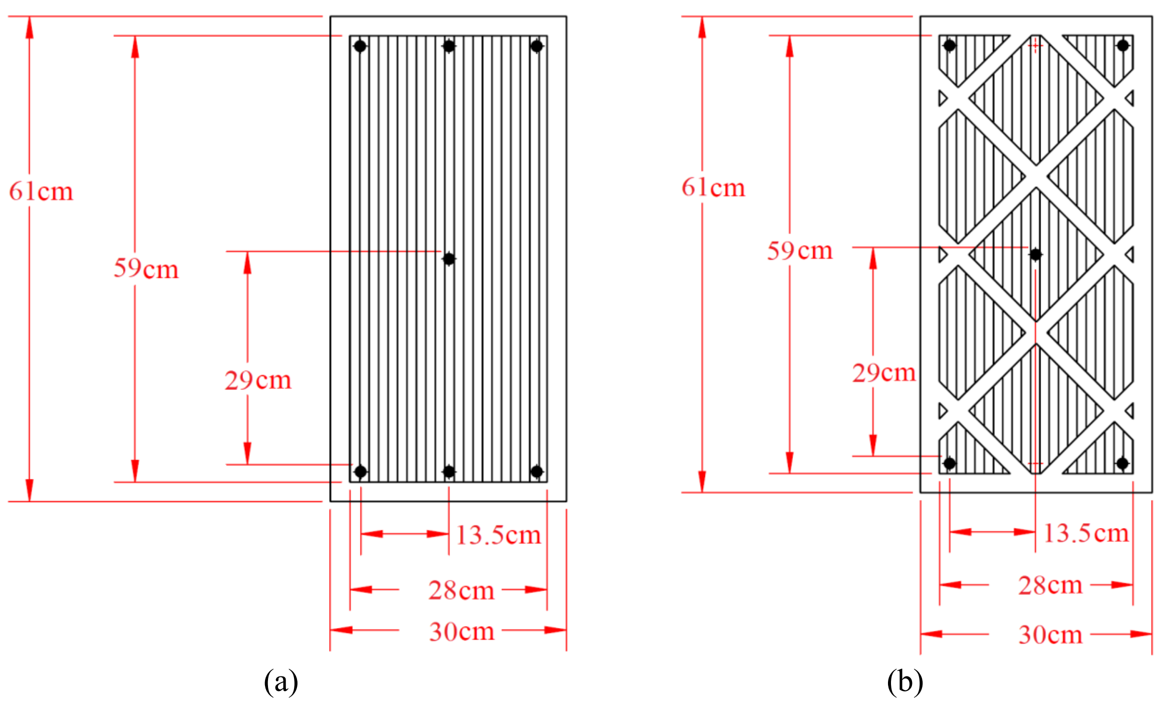

Fig. 6.8. The installation locations of thermocouples for temperature monitoring on pre-filter and main filter (a) front and (b) back surfaces.

Table 6.4. Specifications of the equipment utilized for monitoring the heat transfer performance.

Instrument	Model / Specifications
PID controller	OMEGA-CN32PT-145
Thermocouples	OMEGA-T-type -with a diameter of 0.08 mm and accuracy of ±0.5 ºC
Data loggers	NI-9213
Power meter	Poniie-PN2000

6.5 Results and Discussion

6.5.1 Filtration Performance of the System in Different Operating Modes

Figure 6.9 demonstrates the particle size removal efficiency of different filter configurations involving standalone filters and two-stage filtration systems when both units are open (Fig. 6.9a), and one of the units is closed (Fig. 6.9b). The inter-filter distance for the two-stage system in this section is kept constant at 2 cm. As can be seen, no matter whether both units are open or one of the units is closed, adding a MERV 8 pre-filter before a MERV 11 filter significantly improved the overall filtration efficiency in both submicron and large particle ranges. However, employing a MERV 8 pre-stage filter upstream of a MERV 13 filter only improves the particle removal efficiency of larger particles (more than 0.6 µm). Therefore, the presence of the MERV 8 pre-filter prior to the MERV 13 filter has a more protective role in preventing the clogging of the primary filter rather than significantly improving the filtration efficiency. Furthermore, comparing Figs. 6.9a & b reveals that for both standalone filters and two-stage filtration systems, closing the gates of one of the units reduces the filtration efficiency of submicron particles and increases the particle removal of particles larger than 0.6 µm. This is due to the fact that when both units are open, the air passing through each of the filters has a velocity of 0.75 m/s. When one of the units is isolated (i.e., no air passage for disinfection), the air velocity in the adjacent open unit will be doubled. An increase in the air velocity reduces the diffusion of the tiny particles and, consequently, lessens filtration efficiency within the submicron range. However, for the larger particles, an increase in the air velocity is associated with an increase in the inertial impaction and, therefore, enhancement of the removal of the larger particles.

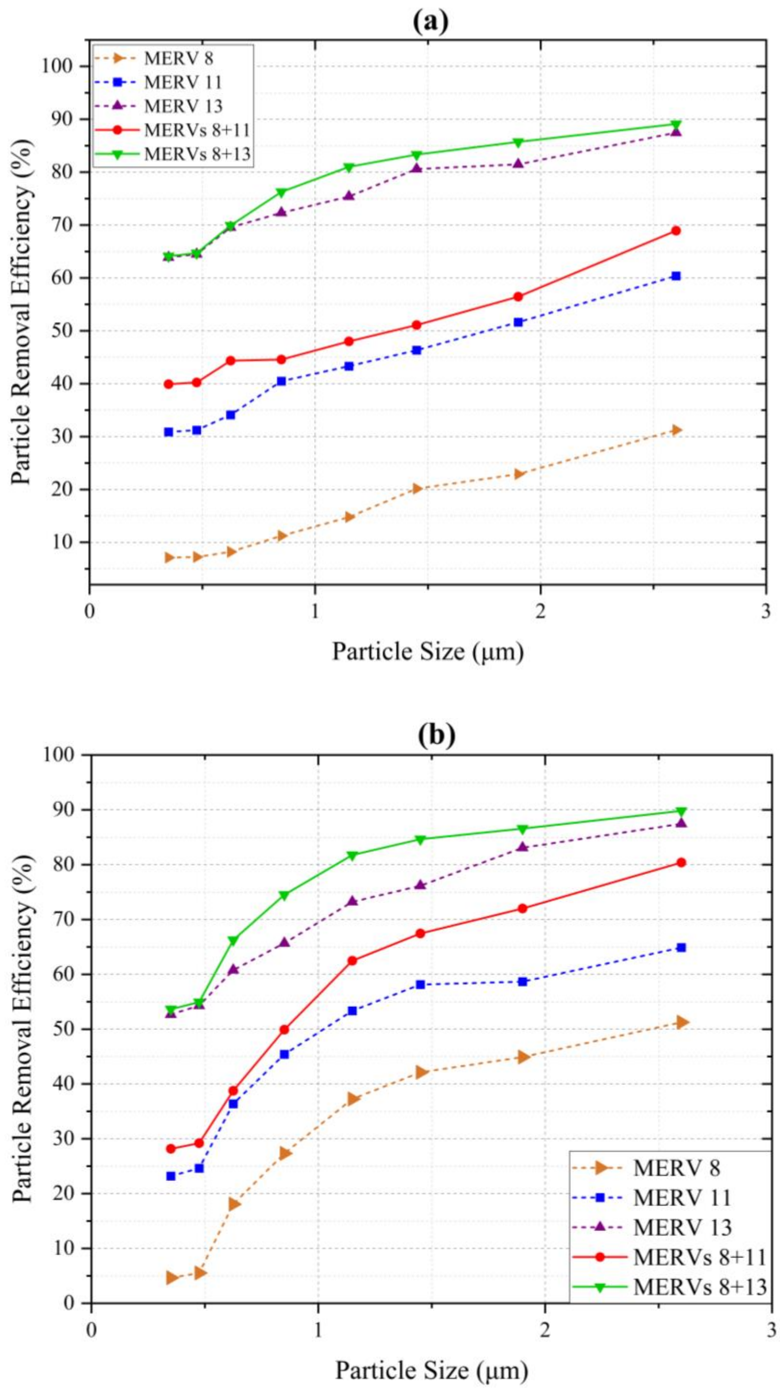

Fig. 6.9. Particle removal efficiency of standalone MERV filters (MERV 8, 11, and 13) and two-stage configurations (MERV 8 + 11 and MERV 8 + 13) at a duct velocity of 0.75 m/s. Subfigures (a) and (b) show results under normal operation mode (both units active) and disinfection mode (one unit isolated), respectively.

6.5.2 Effect of Distance Between the Filters on the Filtration Efficiency

Figures 6.10 and 11 illustrate the impacts of changing the inter-filter spacing on the efficiency of the combined filtration system of MERV 8 + MERV 11 and MERV 8 + MERV 13, respectively. As is evident, MERV 8 + MERV 11 shows a more noticeable variation across the different spacings, particularly under disinfection mode. In contrast, for MERV 8 + MERV 13, the efficiency curves for the three spacings of 2 cm, 4 cm and 6 cm are nearly indistinguishable across the entire particle size range. This suggests that the localized flow redistribution due to the change in the gap size between the two filters has a less profound effect on the filtration efficiency of MERV 8 + MERV 13, providing a more robust performance. The more pronounced dependence of the MERV 8 + MERV 11 configuration on flow redistribution arises from its higher permeability and coarser fiber structure, making its performance more sensitive to local flow non-uniformities and particle re-entrainment. In contrast, the finer and denser MERV 13 media establish a more uniform velocity field and enhance diffusional capture of submicron particles, thereby lessening the impact of inter-filter gap variations.

Figures 6.10 and 6.11 compare the predicted overall removal efficiencies based on the classical series-filter efficiency equation (Eq. (6.6)) with those of the measured data in the experiments. According to the provided figures, while the ideal theoretical model matches well with the measured data for MERV 8 + MERV 13 when the gates are open (Fig. 6.11a), its accuracy reduces slightly under closed gates mode (Fig. 6.11b) or MERV 8 + MERV 11 combination (Figs. 6.10a & b) due to the deviation from ideal independent filtration performance. This discrepancy between the experimental measurements and theoretical prediction stems from the more profound impact of flow redistribution within the gap on the performance of the combined system of MERV 8 + MERV 11 compared to that of MERV 8 + MERV 13, and flow disturbance, non-uniform distribution of airflow between two filters, and particle re-entrainment caused by closing the adjacent unit.

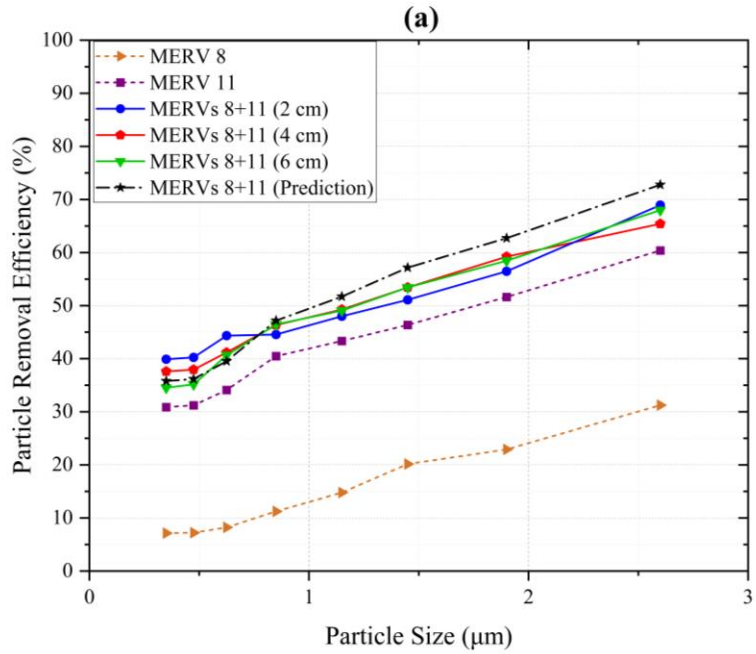

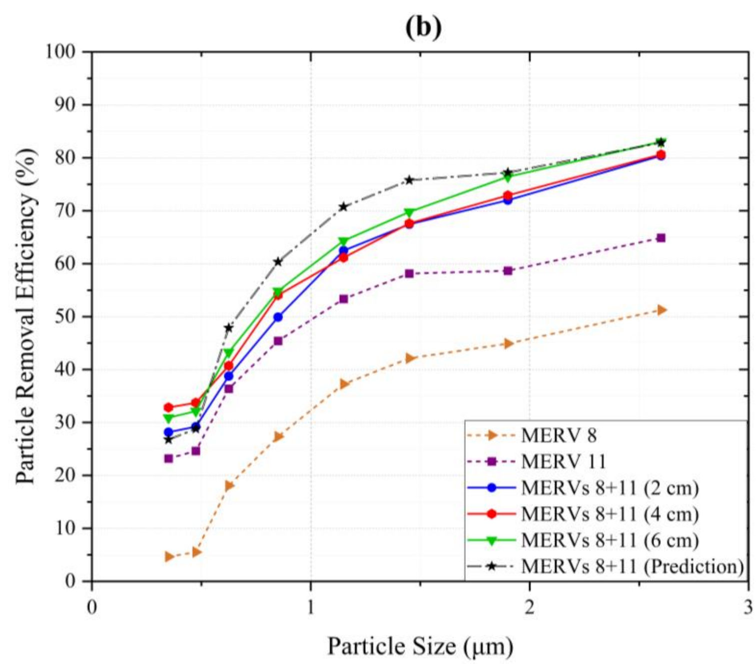

Fig. 6.10. Particle removal efficiency of a two-stage filtration system (MERV 8 + MERV 11) at a duct velocity of 0.75 m/s, evaluated at different inter-filter distances (2 cm, 4 cm, and 6 cm). Subfigure (a) shows results for the normal operation mode, and (b) for the disinfection mode. Experimental data are compared with single-stage filter performance (MERV 8 and MERV 11) and theoretical predictions.

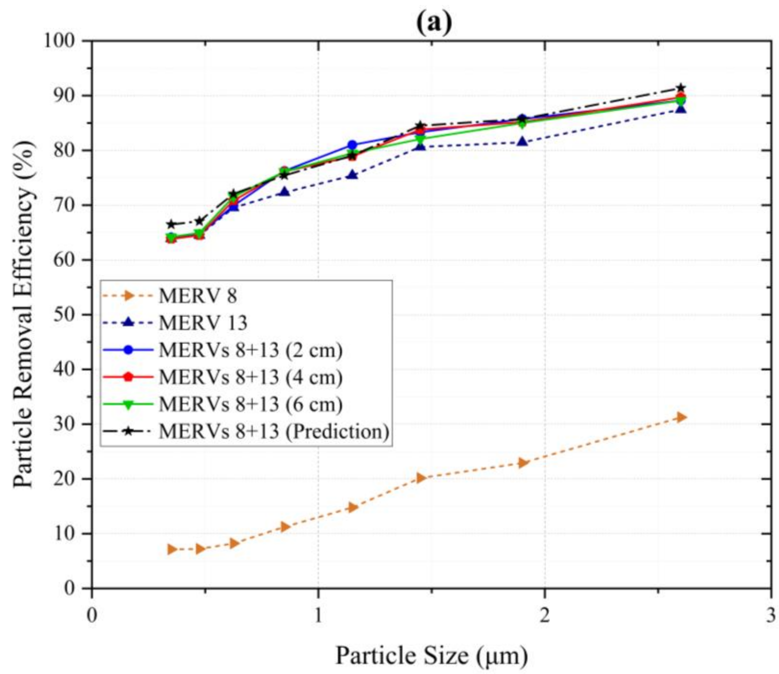

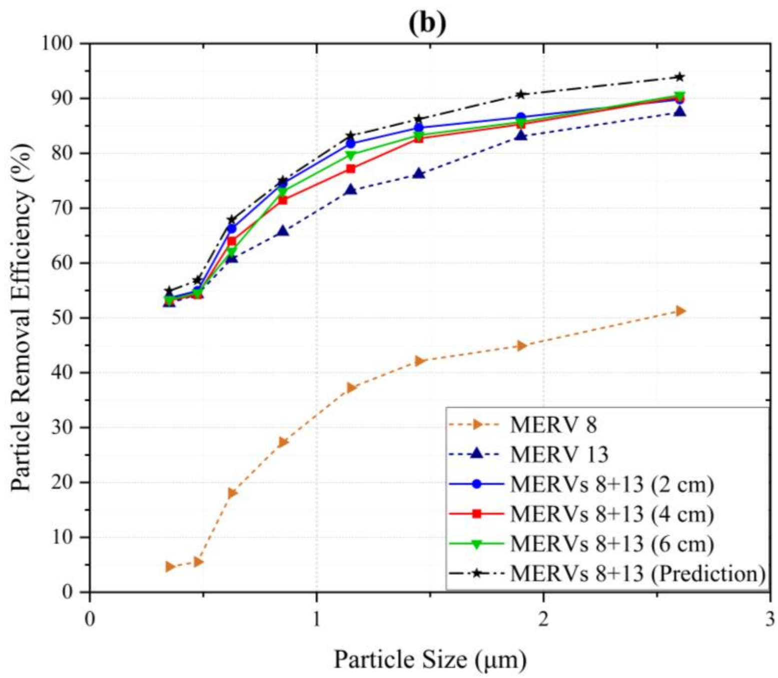

Fig. 6.11. Particle removal efficiency of a two-stage filtration system (MERV 8 + MERV 13) at a duct velocity of 0.75 m/s and varying inter-filter distances (2 cm, 4 cm, 6 cm). Subfigure (a) shows results under normal operation mode (both units open), and (b) under disinfection mode (one unit isolated). Experimental data are compared with single-stage filter performance (MERV 8 and MERV 13) and theoretical predictions.

6.5.3 Pressure Drop of the System

Figures 6.12a & b illustrate the pressure drop of the single-stage and the two-stage filtration systems with an inter-filter distance of 2 cm in normal operation (both units active) and disinfection (one unit isolated) modes, respectively. As is evident, no matter whether a single filter or a two-stage filtration system is employed, at a constant airflow rate within the duct, closing one of the units almost tripled the pressure drop compared to that of the normal operation mode. When one of the units is closed, the airflow rate passing through the filters installed within the open unit is doubled. According to Darcy's law, the pressure drop caused by the frictional drag within a porous medium as a filter is directly proportional to the filter face velocity. Therefore, the twofold increase of the filter face velocity doubles the pressure drop. The additional increase arises from the head loss caused by flow convergence and divergence when one of the units is closed, as well as from the growing significance of inertial resistance (Forchheimer term) within the porous filter media [98]. Under normal operation, the viscous term dominates, resulting in an almost linear pressure–velocity trend. In contrast, when one unit is closed and the face velocity doubles, the inertial resistance becomes significant, leading to the non-linear (curved) pressure–flow behavior observed in the disinfection mode.

Figures 6.13a-d depict the impact of inter-filter distance on the pressure drop of the two-stage filtration systems for both operating modes at different airflow rates. According to the provided figures, changing the distance between the pre-stage MERV 8 filter and the primary stage filter (MERV 11 or MERV 13) from 2 cm to 6 cm has an insignificant effect on the pressure drop of the system. In other words, the variation in the localized flow redistribution at different gaps does not impact the pressure drop.

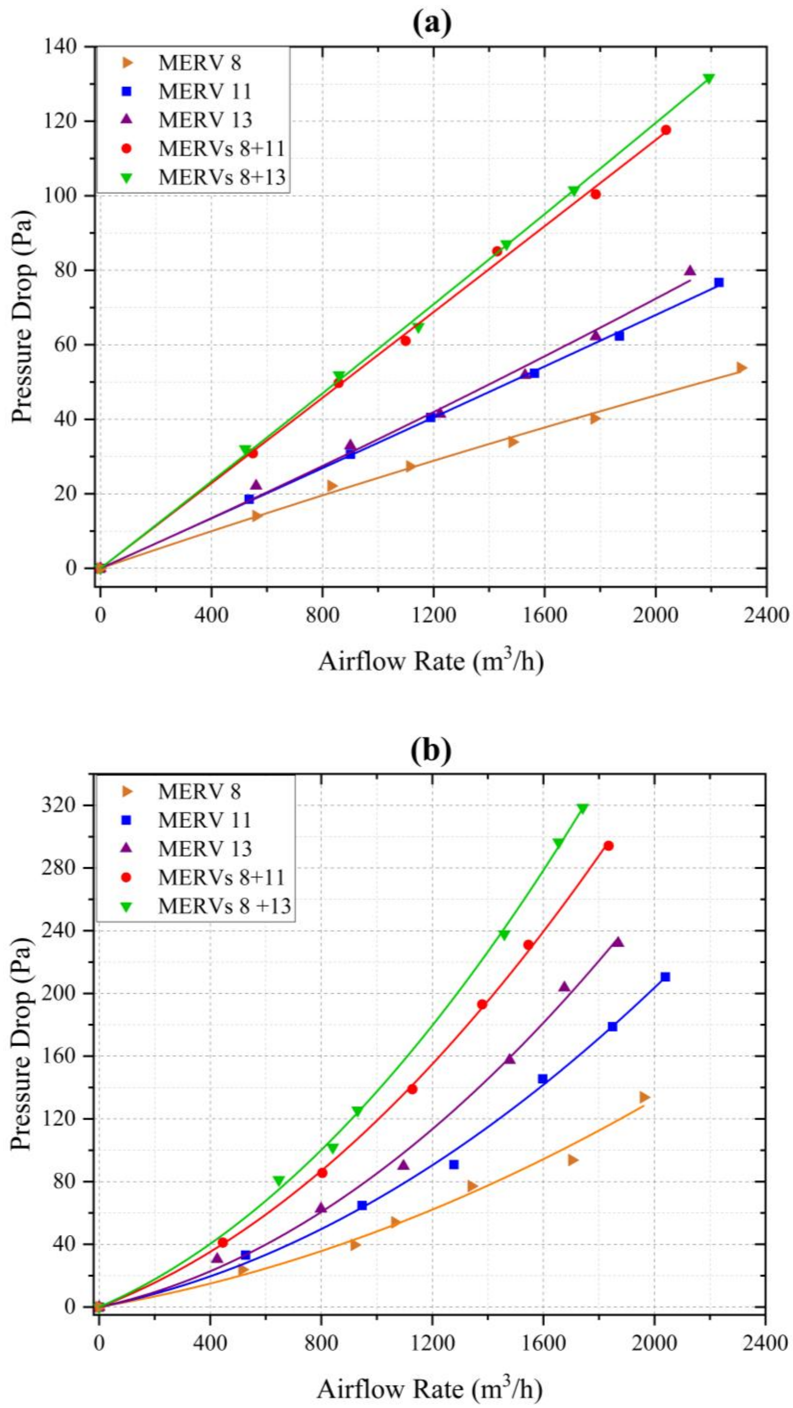

Fig. 6.12. Pressure drop as a function of airflow rate for single-stage (MERV 8, MERV 11, MERV 13) and two-stage (MERV 8 + 11, MERV 8 + 13) filtration systems with an inter-filter distance of 2 cm under two operating modes: (a) normal operation and (b) disinfection modes.

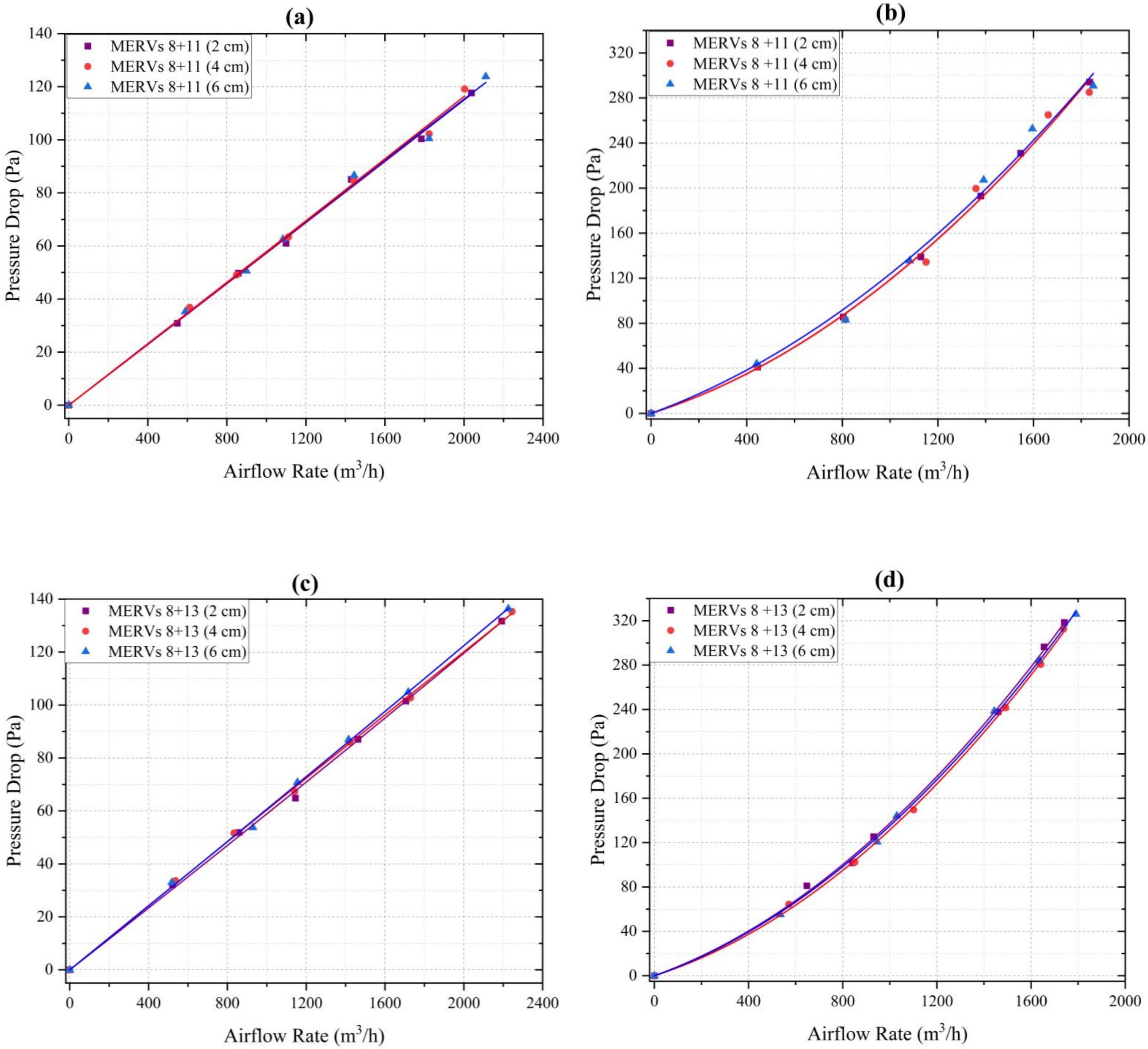

Fig. 6.13. Pressure drop across two-stage filtration systems as a function of airflow rate, evaluated for different inter-filter distances and operating modes. Subfigures (a) and (b) show results for the MERV 8 + MERV 11 configuration under normal operation and disinfection modes, respectively. Subfigure (c) and (d) correspond to the MERV 8 + MERV 13 configuration in the same modes.

6.5.4 Heat Transfer Performance of the Disinfection System

Figures 6.14a-f and 6.15a-f illustrate the temperature variation of the pre-filter and main filter over time at various inter-filter distances for the MERV 8 + MERV 11 and MERV 8 + MERV 13 configurations, respectively. To achieve thermal disinfection (defined as reaching 65°C), the lower whisker of the box plot must lie above the red horizontal line. Each box plot represents the temperature distribution at successive time intervals.

For both two-stage configurations, increasing the distance between the pre-stage and main-stage filters results in a longer time required for the filter surfaces to reach the disinfection temperature. At a constant recirculation flow rate of 296 m^3/h provided by the axial fans within the unit, decreasing the inter-filter distance from 6 cm to 2 cm increased the mean air velocity between the two filters from 4.5 m/s to 13.7 m/s. Consequently, the Reynolds number (Re_{D_h}) rose from 2.47×10^4 to 2.78×10^4. According to the Gnielinski correlation [227], the convection heat transfer coefficient (h) is directly proportional to Re_{D_h}, and inversely proportional to D_h. Hence, as the inter-filter distance decreases, both the increase in Re_{D_h} and the reduction in D_h act synergistically to enhance the convective heat transfer on the front surface of the main filter and the rear surface of the pre-filter. This leads to a higher heat-transfer rate from the warm air to the filters and a correspondingly shorter time required to reach the target disinfection temperature.

Furthermore, a comparison of Figs. 6.14 and 6.15 reveals that the time required to achieve thermal disinfection is significantly longer for the MERV 8 + MERV 13 system than for the MERV 8 + MERV 11 system. This is because the MERV 13 filter used in this study possesses a higher pleat density and thicker media, which increase its overall thermal mass. Moreover, the MERV 13 medium is made of polypropylene, which has a higher specific heat capacity (1.9 $kJ\ kg^{-1}\ K^{-1}$) than the polyester medium used in MERV 11 (1.2 $kJ\ kg^{-1}\ K^{-1}$). According to Table 3, the effective heat capacities were estimated as 172 J K^{-1}, 221 J K^{-1}, and 318 J K^{-1} for the MERV 8, 11, and 13 filters, respectively. This indicates that the MERV 13 filter possesses approximately 45% higher thermal mass than MERV 11 and nearly 85% higher than MERV 8. Therefore, the MERV 8 + MERV 13 configuration requires more energy compared to MERV 8 + MERV 11 to raise the filter temperature to the disinfection target temperature and maintain it for 10 more minutes.

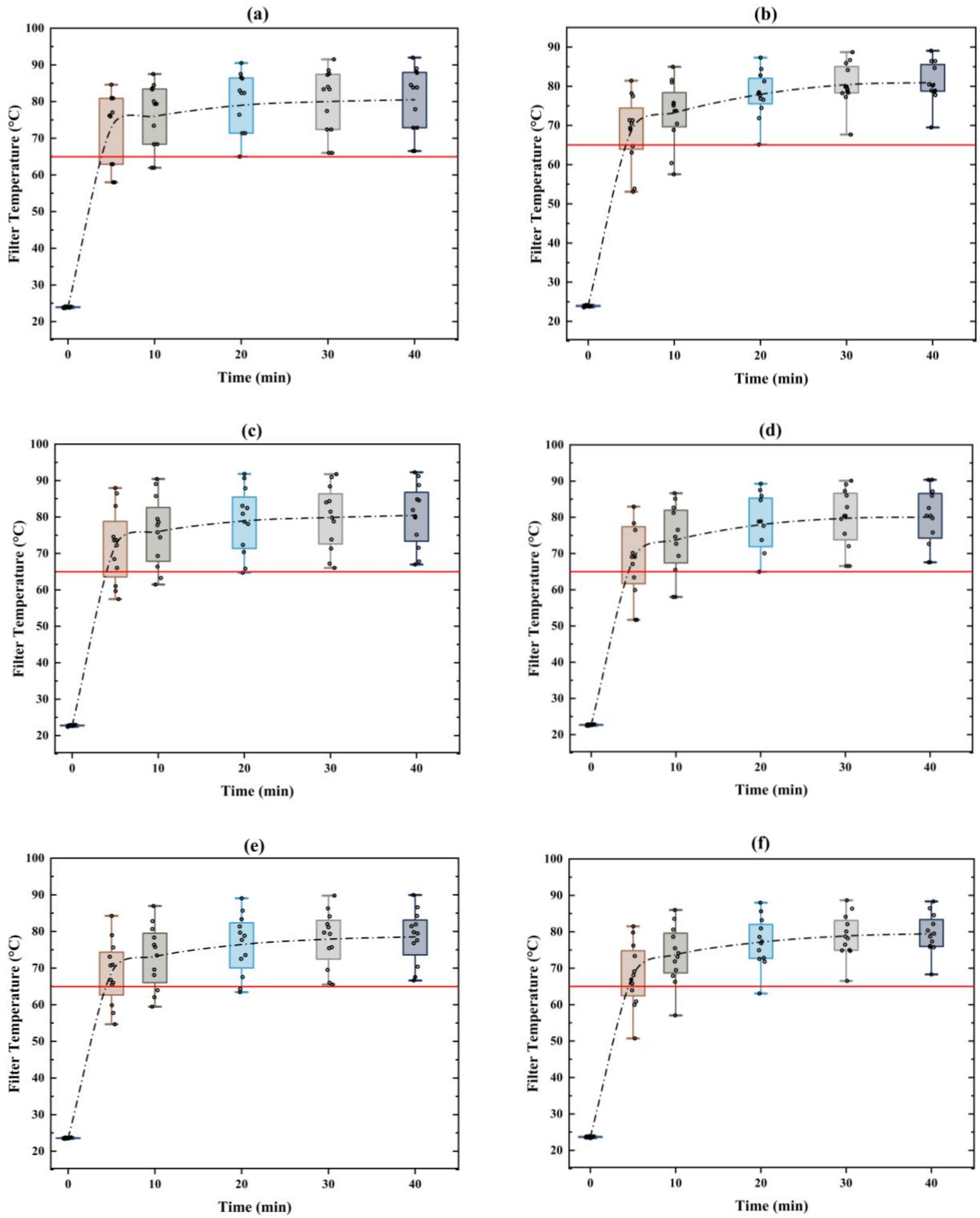

Fig. 6.14. Filter temperature evolution in a two-stage filtration system (MERV 8 pre-filter + MERV 11 main filter) at varying inter-filter distances. Subfigures (a), (c), and (e) show the temperature profiles of the pre-filter at an inter-filter distance of 2 cm, 4 cm, and 6 cm, respectively, while (b), (d), and (f) show those of the main filter at an inter-filter distance of 2 cm, 4 cm, and 6 cm, respectively. The red horizontal line indicates the thermal disinfection threshold (65 °C).

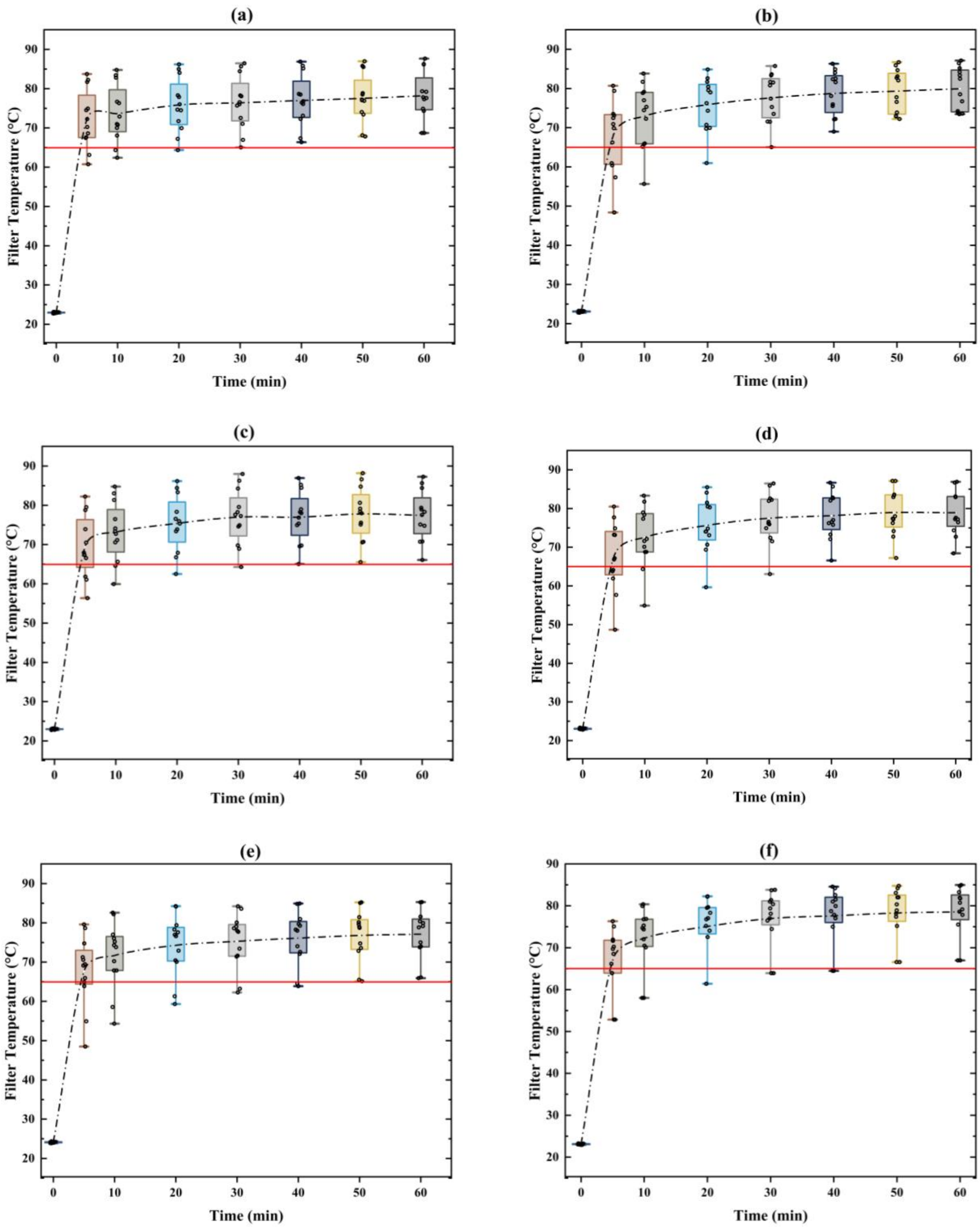

Fig. 6.15. Filter temperature variation over time for a MERV 8 + MERV 13 two-stage filtration system at different inter-filter distances. Subfigures (a), (c), and (e) show the temperature profiles of the pre-filter at an inter-filter distance of 2 cm, 4 cm, and 6 cm, respectively, while (b), (d), and (f) show those of the main filter at an inter-filter distance of 2 cm, 4 cm, and 6 cm, respectively. The red horizontal line indicates the 65 °C threshold required for thermal disinfection.

6.5.5 Required Time and Energy for Disinfection of the Two-Stage System

The intersection points between the horizontal line and the minimum temperature in the box plots of Figs. 6.14 and 6.15 represent the moment when all points on the pre-filter and main filter surfaces reach the target disinfection temperature. Maintaining this temperature for 10 minutes ensures the required exposure time to inactivate most airborne pathogens, including SARS-CoV-2 (COVID-19).

Figure 6.16 presents the energy consumption and total time required for disinfection, i.e., defined as the time needed to reach 65 °C plus 10 minutes of exposure, for the different two-stage filtration configurations. As shown, for the MERV 8 + MERV 11 system, increasing the inter-filter distance from 2 cm to 6 cm raises the electrical energy consumption from 0.18 kWh to 0.24 kWh and extends the required disinfection time from 30 minutes to 36 minutes. Similarly, for the MERV 8 + MERV 13 system, increasing the distance from 2 cm to 6 cm raises the energy consumption from 0.24 kWh to 0.34 kWh and the required time from 39 minutes to 58 minutes.

Since previous sections have demonstrated that changes in the inter-filter distance have relatively minor effects on the filtration efficiency and pressure drop compared to their impact on the disinfection process, the energy performance of the disinfection system should be considered the primary criterion when determining the optimal distance between the pre-filter and main filter. Based on the results, regardless of whether a MERV 11 or MERV 13 filter is used as the main filter, maintaining an inter-filter distance of 2 cm minimizes both the time and energy required for disinfection without compromising overall filtration efficiency or pressure drop.

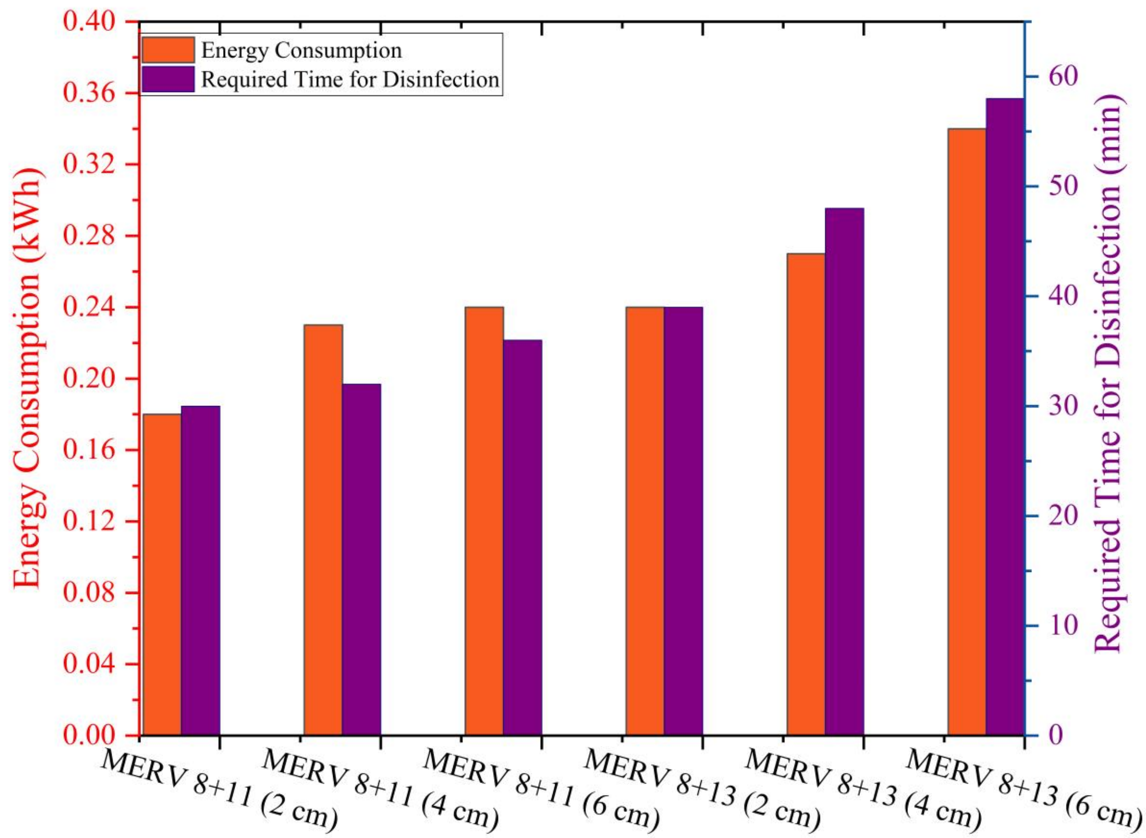

Fig. 6.16. The required energy and time for disinfecting the two-stage filtration systems at different inter-filter distances.

6.6 Conclusions

This study introduces a novel thermal disinfection approach for two-stage filtration systems, combining a MERV 8 pre-filter with a MERV 11 or MERV 13 main filter. The system, composed of two insulated side-by-side units, enables continuous filtration and sequential heat-based disinfection. The system's performance was evaluated at various configurations in a fully recirculating aerosol wind tunnel constructed in accordance with ASHRAE 52.2. Moreover, the system's heat transfer performance was experimentally investigated at different inter-filter distances. The key findings are as follows:

(1) Integrating a MERV 8 pre-filter upstream of a MERV 11 filter improves overall filtration efficiency for both submicron and coarse particles, whereas in the MERV 8 + MERV 13 system the pre-filter primarily serves to protect the main filter from clogging.

(2) Theoretical correlations predict the total filtration efficiency accurately under normal operation but deviate slightly during disinfection mode due to flow redistribution and particle re-entrainment.

(3) Closing one unit during disinfection approximately triples the pressure drop relative to normal operation as a result of increased face velocity and inertial losses.

(4) For both MERV 8 + MERV 11 and MERV 8 + MERV 13 configurations, the increased face velocity during disinfection diminishes capture of submicron particles by diffusion while enhancing inertial impaction of larger particles.

(5) Variation in inter-filter distance exerts minimal impact on overall filtration efficiency and pressure drop, yet substantially impacts the energy consumption and time required for effective disinfection.

Acknowledgements

The authors gratefully acknowledge the financial support provided by the Natural Sciences and Engineering Research Council of Canada (NSERC) through its Alliance program (Grant No. 567653-21) and by Engineered Air through its endowment in HVAC Engineering at the University of Alberta.

Chapter 7. Conclusion and Future Research

7.1 Summary of Key Findings and Conclusions

This thesis developed and validated a novel heat-based air disinfection approach that integrates conventional HVAC filtration with thermal inactivation by heat. To evaluate the feasibility, thermal performance, and operational implications of this concept, both numerical simulations and controlled experimental investigations were conducted. The experimental study included heat transfer performance monitoring, energy consumption assessment, and size-resolved filtration efficiency and pressure drop measurements performed in an ASHRAE 52.2-compliant closed-loop aerosol wind tunnel. The heat-based disinfection strategy was implemented and systematically assessed in three distinct system configurations: (i) a fanless system relying mainly on natural convection for disinfecting a single filter, (ii) a forced-convection system employing fans and warm-air recirculation for disinfecting a single filter; and (iii) a warm-air-recirculation system, similar to the second variant, designed for disinfecting a two-stage filtration system. The key findings of this thesis are summarized below:

- **Numerical Investigation of Natural Convection in a Cavity Including Heat-Generating Cylinders:**
    - A two-dimensional, unsteady turbulent CFD model was developed to investigate buoyancy-driven flow in an enclosure containing tubular heating elements. Five different configurations were examined by varying the number of heating elements, their spatial arrangement, and the geometry of the enclosure through the addition of a heating chamber.
    - Validation against benchmark results from the literature confirmed the accuracy and reliability of the adopted numerical methodology.

- The simulations showed that the system operates in a high-Rayleigh-number turbulent regime ($Ra > 10^9$), where strong buoyant plumes induce significant vertical temperature stratification and flow asymmetry.
- By introducing a heating chamber beneath the frame and redistributing the heating elements to promote preheating and enhanced mixing near the bottom of the enclosure, the temperature non-uniformity within the cavity was significantly reduced.

- **Natural-Convection-Based Thermal Disinfection of Single-Stage Filtration Systems:**
  - This system demonstrated that full-surface thermal disinfection of a pleated MERV 11 filter is feasible without mechanical systems (e.g., fans). Incorporating a heating chamber beneath the filter frame enabled the filter to reach the target disinfection condition (65 °C for 10 minutes) within approximately 35 minutes, with an energy consumption of 0.1 kWh.
  - Compared to configurations without geometric modification, the chamber-based design significantly reduced temperature stratification and achieved more uniform heating across the filter surface, confirming the numerical predictions of Chapter 3 and validating the design methodology.
  - Although the natural-convection approach provides a mechanically simple, reliable and energy-efficient solution, the relatively long disinfection period motivated the development of forced-convection configurations to accelerate thermal disinfection.
  - At all duct velocities, incorporating the chamber and heating elements downstream of the test filter has a negligible impact on filtration efficiency. During disinfection, however, closure of one unit increased the face velocity through the remaining open filter, decreasing submicron particle removal while increasing the capture of larger particles.

- Adding the chamber and heating element introduced only a small additional resistance during normal operation compared to a standalone filter. During the disinfection process, although temporary gate closure almost tripled the pressure drop, the impact on total HVAC fan energy use is limited.

- **Forced-Convection-Based Thermal Disinfection of Single-Stage Filtration Systems:**
  - The forced-convection configuration with recirculating warm air significantly reduced disinfection time compared to the fanless natural-convection approach. Under optimal operating conditions, the MERV 11 test filter reached 65 °C in approximately 3 minutes and was fully disinfected within 13 minutes, with an energy consumption of approximately 0.11 kWh per cycle.
  - Increasing the recirculation flow rate and inlet temperature enhanced convective heat transfer at the filter surface, reduced temperature non-uniformity, and shortened the time required to achieve the target inactivation condition.
  - The introduced system does not affect the particle removal efficiency compared to a standalone filter when the gates of two side-by-side units are open. However, during the disinfection process, when one of the units is isolated, the particle removal efficiency of submicron particles decreases, whereas the filtration efficiency of large particles increases compared to a standalone test filter.
  - During normal operation (open-gates mode), the integration of the disinfection unit does not introduce a significant additional pressure drop compared to a standalone filter. Although pressure drop increases during the short disinfection period (closed-gates mode), the limited duration of thermal treatment (≈ 13 minutes per cycle) ensures that the overall impact on HVAC fan energy consumption remains minimal.

- **Forced-Convection-Based Thermal Disinfection of Two-Stage Filtration Systems:**
    - Adding a MERV 8 pre-filter upstream of a MERV 11 filter enhances the filtration efficiency for both submicron and large particles. However, employing the pre-filter before the MERV 13 filter has a more protective role in preventing the clogging of the primary filter rather than a considerable improvement in overall efficiency.
    - Theoretical predictions of filtration efficiency of multi-stage systems agree well with experimental results in normal operation mode. However, under disinfection mode, deviations were observed due to flow redistribution and particle re-entrainment effects of the closed-adjacent unit.
    - During the disinfection process of both MERV 8 + MERV 11 and MERV 8 + MERV 13 systems, the filtration efficiency of submicron particles decreases while that of larger particles increases compared to normal operation mode due to higher face velocities at the filter surface.
    - Although variation in inter-filter distance (2-6 cm) has minimal impact on overall filtration efficiency and pressure drop, it significantly affects thermal performance. Reducing the gap improves convective heat transfer, thereby minimizing disinfection time and electrical energy consumption (approximately 0.18-0.34 kWh depending on configuration), establishing energy performance as the primary design criterion for spacing selection.

7.2 Contributions and Implementation

7.2.1 Contributions

This thesis contributes to the fields of heat transfer, HVAC engineering, and indoor air quality in three interconnected areas: buoyancy-driven heat transfer in porous enclosures, experimental methodologies for evaluating filter disinfection technologies, and filtration performance of pleated filters under disturbed aerodynamic conditions.

In terms of heat transfer, this research extends current understanding of natural convection in porous enclosures by investigating unsteady, turbulent, buoyancy-driven flow in cavities containing pleated porous media and internal heat-generating elements. The flow conditions examined correspond to Rayleigh numbers exceeding 10^9 and Darcy numbers on the order of 10^{-9}. These conditions differ significantly from those commonly investigated in the literature, where studies have largely focused on laminar natural convection in square porous enclosures with $Ra < 10^7$and $10^{-5} \leq Da \leq 10^{-1}$. Moreover, this thesis establishes the role of enclosure geometry and internal heat-source distribution in controlling temperature stratification within buoyancy-driven cavities. Strategic placement of heating elements and the introduction of a mixing chamber mitigate vertical thermal stratification and promote more uniform temperature fields within the enclosure, providing a design-oriented modelling framework for fanless thermal systems in which buoyancy-driven flow governs heat transfer.

Experimentally, this thesis introduces a comprehensive evaluation methodology for filter disinfection technologies that simultaneously considers thermal performance, electrical energy consumption, size-resolved filtration efficiency, and pressure drop. Unlike most previous studies that isolate either heat transfer or filtration performance, the proposed methodology enables holistic system assessment and captures the coupled interactions between heat transfer, filtration efficiency, and flow resistance within HVAC-integrated disinfection systems.

With respect to filtration performance, this thesis advances knowledge of air filtration under disturbed aerodynamic conditions and in multi-stage filtration configurations. The work provides the first systematic investigation of the influence of flow-obstructive elements within HVAC ductwork on the pressure drop and size-resolved particle removal efficiency of pleated filters across both submicron and larger particle ranges. In addition, the research examines the role of inter-filter spacing in two-stage filtration systems and its implications for pressure drop and overall filtration efficiency. The study also identifies limitations in commonly used theoretical correlations for predicting the efficiency of filters arranged in series when aerodynamic disturbances become significant.

7.2.2 Implementation

This thesis provides a structured design framework for HVAC engineers and indoor air quality (IAQ) specialists to implement a cost-effective, byproduct-free, and mechanically simple thermal disinfection technology within existing ventilation systems. Owing to its robustness, relatively low energy demand, and modular design, the system can be amenable to implementation in large-scale HVAC applications. The design and placement of the disinfection unit may vary depending on the HVAC system size and configuration. A single disinfection module can be installed at the end of a return-air duct upstream of the central ventilation unit. In larger commercial buildings, schools, or healthcare facilities, multiple modules may be strategically distributed within the duct system or mounted near supply outlets serving individual zones.

By offering both a fanless configuration and a forced-convection recirculation design, this work provides flexibility for different operational priorities. The fanless system offers mechanical simplicity, reduced maintenance requirements, and enhanced reliability in settings where extended disinfection time is acceptable. In contrast, the forced-convection configuration significantly reduces thermal disinfection duration, making it suitable for applications requiring rapid disinfection cycles. This dual-approach strategy allows system designers to select an implementation pathway aligned with building-specific performance, energy, and operational constraints.

In addition to the disinfection technology itself, this thesis resulted in the design, manufacturing, assembly, and commissioning of an ASHRAE 52.2-compliant closed-loop aerosol wind tunnel. This advanced experimental facility enables simultaneous measurement of size-resolved filtration efficiency and pressure drop under controlled conditions and can be utilized for evaluating a wide range of air-cleaning and disinfection technologies beyond the scope of this study. The developed testing infrastructure, therefore, represents an additional long-term contribution supporting future research and technology validation efforts.

7.3 Limitations and Recommendations for Future Research

7.3.1 Research Limitations

The findings of this thesis should be interpreted within the defined scope of the numerical and experimental framework adopted in this study.

From a numerical standpoint, the filter media were excluded from the computational domain, and a 2D model was employed to reduce computational cost while enabling parametric investigation of multiple configurations. Although this approach provided valuable design-oriented insights into temperature distribution and flow characteristics, it does not capture 3D flow structures or detailed porous-media interactions between the heating elements and the filter fibres. Furthermore, this thesis did not aim to experimentally resolve the fundamental physics of unsteady turbulent natural convection. Advanced non-intrusive measurement techniques such as Particle Image Velocimetry (PIV) or Liquid Crystal Thermography (LCT), which are typically required for full experimental validation of transient buoyancy-driven flow fields, were beyond the scope of this work. Instead, the numerical model was validated against established benchmark studies for simplified geometries available in the literature.

With respect to the experimental investigation, direct microbiological validation of pathogen inactivation was not conducted. The study focused on thermal performance, energy consumption, filtration efficiency, and pressure drop measurements using surrogate aerosol particles. Conducting live microorganism inactivation experiments within the large-scale wind tunnel facility would require Biosafety Level 2 (BSL-2) or Biosafety Level 3 (BSL-3) containment, which exceeds the design and safety specifications of the available laboratory infrastructure. Consequently, biological inactivation efficacy was inferred from established time-temperature criteria reported in the literature rather than from direct bioassay measurements.

7.3.2 Recommendations for Future Research

Potential avenues for future research emerging from the scope and findings of this thesis are listed below:

- **Inclusion of pleated filters as porous media in CFD simulations:**

  Future numerical studies may incorporate the filter directly within the computational domain as a pleated porous medium. This would extend the current unsteady natural convection model to a coupled problem involving natural convection, radiation heat transfer, and porous-media flow. Such modelling would enable investigation of the effects of filter pleat geometry (number of pleats, aspect ratio, pleat shape) and media properties (thickness, permeability, porosity, thermophysical characteristics) on thermal performance and temperature uniformity.

- **Geometric optimization of fanless configurations:**

  Parametric CFD studies can be conducted to optimize heating chamber aspect ratio and heating-element arrangement to further reduce temperature stratification and energy consumption in buoyancy-driven systems.

- **Optimization of forced-convection recirculation design:**

  Numerical modelling of the recirculating warm-air system can be performed to optimize duct location, flow distribution, and recirculation path geometry in order to minimize disinfection time and improve thermal efficiency.

- **Fundamental experimental investigation of unsteady natural convection:**

  Advanced non-intrusive measurement techniques, such as Particle Image Velocimetry (PIV) and Liquid Crystal Thermography (LCT), can be employed to characterize flow transitions, plume interactions, and transient flow structures within cavities containing internal heat sources.

- **Microbiological validation using live microorganisms:**

  Bio-validation studies conducted under appropriate biosafety conditions (e.g., BSL-2/BSL-3 facilities) are recommended to directly quantify inactivation efficiency and confirm the biological effectiveness of the proposed technology.

- **Assessment of cyclic heating and filter aging:**

Long-term studies are required to evaluate the impact of repeated thermal disinfection cycles on filtration efficiency, pressure drop, structural integrity, and overall filter lifespan.

- **Impacts of environmental conditions on the performance:**

  Future investigations should examine the effect of airflow temperature and relative humidity within the duct on required disinfection energy and heat transfer performance to establish operational guidelines across different climatic conditions.

References and Appendices

References

[1] A. Mirzazade Akbarpoor, M. Salimi, E. Rasouli, M. Shahbakhti, A. Nouri, A heat-driven disinfection technology for enhancing indoor air quality in HVAC systems, Journal of Building Engineering. 115 (2025) 114513. https://doi.org/10.1016/j.jobe.2025.114513.

[2] A. Mirzazade Akbarpoor, M. Salimi, E. Rasouli, M. Shahbakhti, A. Nouri, An energy-efficient heat-driven technology for airborne pathogen inactivation: integration of two-stage HVAC filtration with thermal disinfection, Applied Thermal Engineering. (2026) 129140. https://doi.org/https://doi.org/10.1016/j.applthermaleng.2025.129140.

[3] A. Mirzazade Akbarpoor, M. Salimi, A. Shabani, M. Shahbakhti, A. Nouri, Natural-Convection-Based Thermal Disinfection of Air Filters: Performance and Energy Evaluation in HVAC Systems, Thermal Science and Engineering Progress. (Submitted on Jan 31, 2026).

[4] H.Y. Kek, S.B. Mohd Saupi, H. Tan, M.H. Dzarfan Othman, B.B. Nyakuma, P.S. Goh, W.A. Hamood Altowayti, A. Qaid, N.H. Abdul Wahab, C.H. Lee, A. Lubis, S.L. Wong, K.Y. Wong, Ventilation strategies for mitigating airborne infection in healthcare facilities: A review and bibliometric analysis (1993 to 2022), Energy and Buildings. 295 (2023) 113323. https://doi.org/10.1016/j.enbuild.2023.113323.

[5] S. Mallakpour, E. Azadi, C.M. Hussain, Fabrication of air filters with advanced filtration performance for removal of viral aerosols and control the spread of COVID-19, Advances in Colloid and Interface Science. 303 (2022). https://doi.org/10.1016/j.cis.2022.102653.

[6] A. Aganovic, G. Cao, J. Kurnitski, P. Wargocki, New dose-response model and SARS-CoV-2 quanta emission rates for calculating the long-range airborne infection risk, Building and Environment. 228 (2023) 109924. https://doi.org/10.1016/j.buildenv.2022.109924.

[7] Y. Shang, H. Li, R. Zhang, Effects of pandemic outbreak on economies: Evidence from business history context, Frontiers in Public Health. 9 (2021) 146. https://doi.org/10.3389/fpubh.2021.632043.

[8] G. Verikios, The dynamic effects of infectious disease outbreaks: The case of pandemic influenza and human coronavirus, Socio-Economic Planning Sciences. 71 (2020) 100898. https://doi.org/10.1016/J.SEPS.2020.100898.

[9] WHO Coronavirus (COVID-19) Dashboard, (2024). https://covid19.who.int/data.

[10] Priyanka, O.P. Choudhary, I. Singh, G. Patra, Aerosol transmission of SARS-CoV-2: The unresolved paradox, Travel Medicine and Infectious Disease. 37 (2020) 101869. https://doi.org/10.1016/J.TMAID.2020.101869.

[11] H. Kulkarni, C.M. Smith, D.D.H. Lee, R.A. Hirst, A.J. Easton, C. O'Callaghan, Evidence of respiratory syncytial virus spread by aerosol time to revisit infection control strategies?, American Journal of Respiratory and Critical Care Medicine. 194 (2016) 308–316. https://doi.org/10.1164/RCCM.201509-1833OC/SUPPL_FILE/DISCLOSURES.PDF.

[12] G. Liu, M. Xiao, X. Zhang, C. Gal, X. Chen, L. Liu, S. Pan, J. Wu, L. Tang, D. Clements-Croome, A review of air filtration technologies for sustainable and healthy building ventilation, Sustainable Cities and Society. 32 (2017) 375–396. https://doi.org/10.1016/j.scs.2017.04.011.

[13] J.C. Luongo, J. Brownstein, S.L. Miller, Ultraviolet germicidal coil cleaning: Impact on heat transfer effectiveness and static pressure drop, Building and Environment. 112 (2017) 159–165. https://doi.org/10.1016/j.buildenv.2016.11.022.

[14] D. Menzies, J. Popa, J.A. Hanley, T. Rand, D.K. Milton, Effect of ultraviolet germicidal lights installed in office ventilation systems on workers' health and wellbeing: Double-blind multiple crossover trial, Lancet. 362 (2003) 1785–1791. https://doi.org/10.1016/S0140-6736(03)14897-0.

[15] Combating the virus in the air & coronavirus air filtration strategies | Camfil, (2023). https://www.camfil.com/en-us/insights/life-science-and-healthcare/virus (accessed March 2, 2023).

[16] W. Zheng, J. Hu, Z. Wang, J. Li, Z. Fu, H. Li, J. Jurasz, S.K. Chou, J. Yan, COVID-19 Impact on Operation and Energy Consumption of Heating, Ventilation and Air-Conditioning (HVAC) Systems, Advances in Applied Energy. 3 (2021) 100040. https://doi.org/10.1016/j.adapen.2021.100040.

[17] M. Baselga, J.J. Alba, A.J. Schuhmacher, Impact of needle-point bipolar ionization system in the reduction of bioaerosols in collective transport, Science of the Total Environment. 855 (2023) 158965. https://doi.org/10.1016/j.scitotenv.2022.158965.

[18] X. Zeng, C. Li, Z. Li, Z. Tao, M. Li, Review of research advances in microbial sterilization technologies and applications in the built environment, Journal of Environmental Sciences (China). 154 (2025) 314–348. https://doi.org/10.1016/j.jes.2024.09.026.

[19] G. Kampf, A. Voss, S. Scheithauer, Inactivation of coronaviruses by heat, Journal of Hospital Infection. 105 (2020) 348–349. https://doi.org/10.1016/j.jhin.2020.03.025.

[20] K.R. Wigginton, B.M. Pecson, T. Sigstam, F. Bosshard, T. Kohn, Virus inactivation mechanisms: impact of disinfectants on virus function and structural integrity, Environmental Science & Technology. 46 (2012) 12069–12078. https://doi.org/10.1021/es3029473.

[21] R.J. Fischer, D.H. Morris, N. van Doremalen, S. Sarchette, M.J. Matson, T. Bushmaker, C.K. Yinda, S.N. Seifert, A. Gamble, B.N. Williamson, Effectiveness of N95 respirator decontamination and reuse against SARS-CoV-2 virus, Emerging Infectious Diseases. 26 (2020) 2253. https://doi.org/10.3201/eid2609.201524.

[22] American Society of Heating, Refrigerating, and Air-Conditioning Engineers (ASHRAE), Standard 52.2, Method of testing general ventilation aircleaning devices for removal efficiency by particle size, (2017).

[23] A. Giampieri, Z. Ma, J. Ling-Chin, A.P. Roskilly, A.J. Smallbone, An overview of solutions for airborne viral transmission reduction related to HVAC systems including liquid desiccant air-scrubbing, Energy. 244 (2022) 122709. https://doi.org/10.1016/j.energy.2021.122709.

[24] G. Berry, I. Beckman, H. Cho, A comprehensive review of particle loading models of fibrous air filters, Journal of Aerosol Science. 167 (2023) 106078. https://doi.org/10.1016/J.JAEROSCI.2022.106078.

[25] American Society of Heating, Refrigerating, and Air-Conditioning Engineers (ASHRAE), technical resources, HVAC system maintenance and filter replacement during the COVID-19 pandemic, (2020).

[26] K. Morisseau, A. Joubert, L. Le Coq, Y. Andres, Quantification of the fungal fraction

released from various preloaded fibrous filters during a simulated ventilation restart, Indoor Air. 27 (2017) 529–538. https://doi.org/10.1111/ina.12330.

[27] Y. Qian, K. Willeke, V. Ulevicius, S.A. Grinshpun, Particle reentrainment from fibrous filters, Aerosol Science and Technology. 27 (1997) 394–404. https://doi.org/10.1080/02786829708965480.

[28] M.C. Verdenelli, C. Cecchini, C. Orpianesi, G.M. Dadea, A. Cresci, Efficacy of antimicrobial filter treatments on microbial colonization of air panel filters, Journal of Applied Microbiology. 94 (2003) 9–15. https://doi.org/10.1046/j.1365-2672.2003.01820.x.

[29] L. Song, J. Zhou, C. Wang, G. Meng, Y. Li, M. Jarin, Z. Wu, X. Xie, Airborne pathogenic microorganisms and air cleaning technology development: A review, Journal of Hazardous Materials. 424 (2022). https://doi.org/10.1016/j.jhazmat.2021.127429.

[30] Z. Liu, S. Ma, G. Cao, C. Meng, B.J. He, Distribution characteristics, growth, reproduction and transmission modes and control strategies for microbial contamination in HVAC systems: A literature review, Energy and Buildings. 177 (2018) 77–95. https://doi.org/10.1016/j.enbuild.2018.07.050.

[31] J. Liu, Z. Yu, Z. Liu, D. Qin, J. Zhou, G. Zhang, Performance Analysis of Earth-air Heat Exchangers in Hot Summer and Cold Winter Areas, in: Procedia Engineering, Elsevier Ltd, 2017: pp. 1672–1677. https://doi.org/10.1016/j.proeng.2017.10.342.

[32] D. Das, A. Waychal, On the triboelectrically charged nonwoven electrets for air filtration, Journal of Electrostatics. 83 (2016) 73–77. https://doi.org/10.1016/j.elstat.2016.08.004.

[33] S.-H. Huang, C.-W. Chen, Y.-M. Kuo, C.-Y. Lai, R. McKay, C.-C. Chen, Factors affecting

filter penetration and quality factor of particulate respirators, Aerosol and Air Quality Research. 13 (2013) 162–171. https://doi.org/10.4209/aaqr.2012.07.0179.

[34] G. Berry, A. Parsons, M. Morgan, J. Rickert, H. Cho, A review of methods to reduce the probability of the airborne spread of COVID-19 in ventilation systems and enclosed spaces, Environmental Research. 203 (2022) 111765. https://doi.org/10.1016/j.envres.2021.111765.

[35] R. Zendehdel, M.M. Amini, M. Hajibabaei, M.J. Nasiri, M.J. Jafari, M.K. Alavijeh, Doping metal–organic framework composites to antibacterial air filter development for quality control of indoor air, Environmental Progress & Sustainable Energy. 41 (2022). https://doi.org/10.1002/ep.13909.

[36] Y. Ju, T. Han, J. Yin, Q. Li, Z. Chen, Z. Wei, Y. Zhang, L. Dong, Bumpy structured nanofibrous membrane as a highly efficient air filter with antibacterial and antiviral property, Science of the Total Environment. 777 (2021) 145768. https://doi.org/10.1016/j.scitotenv.2021.145768.

[37] C. Balagna, R. Francese, S. Perero, D. Lembo, M. Ferraris, Nanostructured composite coating endowed with antiviral activity against human respiratory viruses deposited on fibre-based air filters, Surface and Coatings Technology. 409 (2021) 126873. https://doi.org/10.1016/j.surfcoat.2021.126873.

[38] H. Luo, L. Zhong, Ultraviolet germicidal irradiation (UVGI) for in-duct airborne bioaerosol disinfection: Review and analysis of design factors, Building and Environment. 197 (2021) 107852. https://doi.org/10.1016/j.buildenv.2021.107852.

[39] E.F. Dunn, A. Akhtar, A. Dunn, S. Lacey, E. Pauley, C. Powers, J. McKee, D. Petereit,

Evaluating an ultraviolet C system for use during SARS-CoV2 pandemic and personal protective equipment shortage, Advances in Radiation Oncology. 6 (2021) 100636. https://doi.org/10.1016/j.adro.2020.100636.

[40] American Society of Heating, Refrigerating, and Air-Conditioning Engineers (ASHRAE), Handbook, Chapter 62: Ultraviolet Air and Surface Treatment, (2019).

[41] M. Raeiszadeh, B. Adeli, A critical review on ultraviolet disinfection systems against COVID-19 outbreak: applicability, validation, and safety considerations, Acs Photonics. 7 (2020) 2941–2951. https://doi.org/10.1021/acsphotonics.0c01245.

[42] A.H. Mamaghani, F. Haghighat, C.-S. Lee, Photocatalytic oxidation technology for indoor environment air purification: The state-of-the-art, Applied Catalysis B: Environmental. 203 (2017) 247–269. https://doi.org/10.1016/j.apcatb.2016.10.037.

[43] J. Mo, Y. Zhang, Q. Xu, Y. Zhu, J.J. Lamson, R. Zhao, Determination and risk assessment of by-products resulting from photocatalytic oxidation of toluene, Applied Catalysis B: Environmental. 89 (2009) 570–576. https://doi.org/10.1016/j.apcatb.2009.01.015.

[44] S.O. Hay, T. Obee, Z. Luo, T. Jiang, Y. Meng, J. He, S.C. Murphy, S. Suib, The viability of photocatalysis for air purification, Molecules. 20 (2015) 1319–1356. https://doi.org/10.3390/molecules20011319.

[45] A. Bisag, P. Isabelli, R. Laurita, C. Bucci, F. Capelli, G. Dirani, M. Gherardi, G. Laghi, A. Paglianti, V. Sambri, Cold atmospheric plasma inactivation of aerosolized microdroplets containing bacteria and purified SARS-CoV-2 RNA to contrast airborne indoor transmission, Plasma Processes and Polymers. 17 (2020) 2000154. https://doi.org/10.1002/ppap.202000154.

[46] D. Dobrynin, G. Fridman, Y. V Mukhin, M.A. Wynosky-Dolfi, J. Rieger, R.F. Rest, A.F. Gutsol, A. Fridman, Cold plasma inactivation of Bacillus cereus and Bacillus anthracis (anthrax) spores, IEEE Transactions on Plasma Science. 38 (2010) 1878–1884. https://doi.org/10.1109/TPS.2010.2041938.

[47] T. Chen, J. O'Keeffe, COVID-19 in indoor environments—Air and surface disinfection measures, National Collaborating Centre for Environmental Health: Vancouver, BC, Canada. (2020) 1–25. https://ncceh.ca/resources/evidence-reviews/covid-19-indoor-environments-air-and-surface-disinfection-measures.

[48] X. Kang, W. Gao, B. Wang, B. Yu, L. Guo, B. Cui, A.M. Abd El-Aty, Effect of moist and dry-heat treatment processes on the structure, physicochemical properties, and in vitro digestibility of wheat starch-lauric acid complexes, Food Chemistry. 351 (2021) 129303. https://doi.org/10.1016/j.foodchem.2021.129303.

[49] J.H. Jung, J.E. Lee, C.H. Lee, S.S. Kim, B.U. Lee, Treatment of fungal bioaerosols by a high-temperature, short-time process in a continuous-flow system, Applied and Environmental Microbiology. 75 (2009) 2742–2749. https://doi.org/10.1128/AEM.01790-08.

[50] B. Bharti, H. Li, Z. Ren, R. Zhu, Z. Zhu, Recent advances in sterilization and disinfection technology: A review, Chemosphere. 308 (2022) 136404. https://doi.org/10.1016/j.chemosphere.2022.136404.

[51] L.M. Vasilyak, Physical methods of disinfection (a review), Plasma Physics Reports. 47 (2021) 318–327. https://doi.org/10.1134/S1063780X21030107.

[52] F. Masotti, L. Vallone, S. Ranzini, T. Silvetti, S. Morandi, M. Brasca, Effectiveness of air

disinfection by ozonation or hydrogen peroxide aerosolization in dairy environments, Food Control. 97 (2019) 32–38. https://doi.org/10.1016/j.foodcont.2018.10.022.

[53] A.J. Brodowska, A. Nowak, K. Śmigielski, Ozone in the food industry: Principles of ozone treatment, mechanisms of action, and applications: An overview, Critical Reviews in Food Science and Nutrition. 58 (2018) 2176–2201. https://doi.org/10.1080/10408398.2017.1308313.

[54] Y. Kang, S. Kato, Thermal and non-thermal germicidal effects of microwave radiation on microbial agents, Indoor and Built Environment. 23 (2014) 1080–1091. https://doi.org/10.1177/1420326X13490180.

[55] C. Wang, L. Song, Z. Zhang, Y. Wang, X. Xie, Microwave-induced release and degradation of airborne antibiotic resistance genes (ARGs) from Escherichia coli bioaerosol based on microwave absorbing material, Journal of Hazardous Materials. 394 (2020) 122535. https://doi.org/10.1016/j.jhazmat.2020.122535.

[56] S. Angulo-Milhem, M. Verriele, M. Nicolas, F. Thevenet, Full-scale determination of essential oil diffusion: Impact on indoor air quality, Atmospheric Environment. (2023) 120141. https://doi.org/10.1016/j.atmosenv.2023.120141.

[57] S. Panikar, G. Shoba, M. Arun, J.J. Sahayarayan, A.U.R. Nanthini, A. Chinnathambi, S.A. Alharbi, O. Nasif, H.-J. Kim, Essential oils as an effective alternative for the treatment of COVID-19: Molecular interaction analysis of protease (Mpro) with pharmacokinetics and toxicological properties, Journal of Infection and Public Health. 14 (2021) 601–610. https://doi.org/10.1016/j.jiph.2020.12.037.

[58] B. Han, J.-S. Kang, H.-J. Kim, C.-G. Woo, Y.-J. Kim, Investigation of antimicrobial activity

of grapefruit seed extract and its application to air filters with comparison to propolis and shiitake, Aerosol and Air Quality Research. 15 (2015) 1035–1044. https://doi.org/10.4209/aaqr.2014.09.0208.

[59] A. Mirzazade Akbarpoor, M. Salimi, E. Rasouli, M. Shahbakhti, A. Nouri, An energy-efficient heat-driven technology for airborne pathogen inactivation: integration of two-stage HVAC filtration with thermal disinfection, Applied Thermal Engineering. 284 (2026) 129140. https://doi.org/10.1016/j.applthermaleng.2025.129140.

[60] E. Rasouli, M. Salimi, A. Mirzazade Akbarpoor, M. Shahbakhti, A. Nouri, Effect of Aerodynamic Disturbances on Particle Detachment from Fibrous Filters in an Air Disinfection System, Journal of Building Engineering. (2025) 114653. https://doi.org/10.1016/j.jobe.2025.114653.

[61] M. Shang, Y. Kong, Z. Yang, R. Cheng, X. Zheng, Y. Liu, T. Chen, Removal of virus aerosols by the combination of filtration and UV-C irradiation, Frontiers of Environmental Science and Engineering. 17 (2023) 1–9. https://doi.org/10.1007/s11783-023-1627-y.

[62] Z. Feng, S.J. Cao, J. Wang, P. Kumar, F. Haghighat, Indoor airborne disinfection with electrostatic disinfector (ESD): Numerical simulations of ESD performance and reduction of computing time, Building and Environment. 200 (2021). https://doi.org/10.1016/j.buildenv.2021.107956.

[63] Z. Feng, W. Pan, H. Zhang, X. Cheng, Z. Long, J. Mo, Evaluation of the performance of an electrostatic enhanced air filter (EEAF) by a numerical method, Powder Technology. 327 (2018) 201–214. https://doi.org/10.1016/j.powtec.2017.12.054.

[64] Z. Feng, Z. Long, T. Yu, Filtration characteristics of fibrous filter following an electrostatic

precipitator, Journal of Electrostatics. 83 (2016) 52–62. https://doi.org/10.1016/j.elstat.2016.07.009.

[65] EPA, Air quality criteria for ozone and related photochemical oxidants, Molecular and Cellular Biochemistry. 9 (2006) 131–3.

[66] Y. Zhu, Z. Wei, X. Yang, S. Tao, Y. Zhang, W. Shangguan, Comprehensive control of PM 2.5 capture and ozone emission in two-stage electrostatic precipitators, Science of The Total Environment. 858 (2023) 159900. https://doi.org/10.1016/j.scitotenv.2022.159900.

[67] D.S. de Almeida, L.D. Martins, M.L. Aguiar, Air pollution control for indoor environments using nanofiber filters: A brief review and post-pandemic perspectives, Chemical Engineering Journal Advances. 11 (2022) 0–7. https://doi.org/10.1016/j.ceja.2022.100330.

[68] M. Zhang, J. Liu, X. Liu, X. Zhang, Evaluation and prediction of fibrous filters' operating performance in residential fresh air system, Building and Environment. 255 (2024) 111441. https://doi.org/10.1016/j.buildenv.2024.111441.

[69] W. Nakpan, M. Yermakov, R. Indugula, T. Reponen, S.A. Grinshpun, Inactivation of bacterial and fungal spores by UV irradiation and gaseous iodine treatment applied to air handling filters, Science of the Total Environment. 671 (2019) 59–65. https://doi.org/10.1016/j.scitotenv.2019.03.310.

[70] J. Liu, J. Liu, Y. Fan, P. Wang, Combination of UV radiation with 3D structure media filter for indoor air disinfection, in: E3S Web of Conferences, EDP Sciences, 2022. https://doi.org/10.1051/e3sconf/202235605054.

[71] P. Li, J. Li, X. Feng, J. Li, Y. Hao, J. Zhang, H. Wang, A. Yin, J. Zhou, X. Ma, B. Wang,

Metal-organic frameworks with photocatalytic bactericidal activity for integrated air cleaning, Nature Communications. 10 (2019). https://doi.org/10.1038/s41467-019-10218-9.

[72] V. Pertegal, E. Riquelme, J. Lozano-Serra, P. Cañizares, M.A. Rodrigo, C. Sáez, E. Lacasa, Cleaning technologies integrated in duct flows for the inactivation of pathogenic microorganisms in indoor environments: A critical review of recent innovations and future challenges, Journal of Environmental Management. 345 (2023). https://doi.org/10.1016/j.jenvman.2023.118798.

[73] F. Chen, X. Yang, H.K.C. Mak, D.W.T. Chan, Photocatalytic oxidation for antimicrobial control in built environment: a brief literature overview, Building and Environment. 45 (2010) 1747–1754. https://doi.org/10.1016/j.buildenv.2010.01.024.

[74] L.F. González, A. Joubert, Y. Andrès, M. Liard, C. Renner, L. Le Coq, Filtration performances of HVAC filters for PM10 and microbial aerosols— Influence of management in a lab-scale air handling unit, Aerosol Science and Technology. 50 (2016) 555–567. https://doi.org/10.1080/02786826.2016.1167833.

[75] J. Hyun, S.G. Lee, J. Hwang, Application of corona discharge-generated air ions for filtration of aerosolized virus and inactivation of filtered virus, Journal of Aerosol Science. 107 (2017) 31–40. https://doi.org/10.1016/j.jaerosci.2017.02.004.

[76] J. Li, H. Gao, C. Lan, L. Nie, D. Liu, X. Lu, K. (Ken) Ostrikov, Plasma air filtration system for intercepting and inactivation of pathogenic microbial aerosols, Journal of Environmental Chemical Engineering. 11 (2023). https://doi.org/10.1016/j.jece.2023.110728.

[77] C.W. Park, J.H. Byeon, K.Y. Yoon, J.H. Park, J. Hwang, Simultaneous removal of odors,

airborne particles, and bioaerosols in a municipal composting facility by dielectric barrier discharge, Separation and Purification Technology. 77 (2011) 87–93. https://doi.org/10.1016/j.seppur.2010.11.024.

[78] M.S. Vlaskin, Review of air disinfection approaches and proposal for thermal inactivation of airborne viruses as a life-style and an instrument to fight pandemics, Applied Thermal Engineering. 202 (2022) 117855. https://doi.org/10.1016/j.applthermaleng.2021.117855.

[79] G. Cebrián, S. Condón, P. Mañas, Physiology of the inactivation of vegetative bacteria by thermal treatments: Mode of action, influence of environmental factors and inactivation kinetics, Foods. 6 (2017) 1–21. https://doi.org/10.3390/foods6120107.

[80] J. Bartram, Legionella and the prevention of legionellosis, World Health Organization, 2007.

[81] W.H. Organization, Boil water. Technical Brief, WHO/FWC/WSH/15.02. Geneva: World Health Organization, 2015.

[82] Y.-H. Wang, X.-L. Wang, J. Song, Q.-Q. Song, X.-N. Luo, D. Xia, J. Han, Inactivation of human rhinovirus due to heat, UV irradiation and chemical disinfectants, Journal of Antivirals & Antiretrovirals. 09 (2017) 96–101. https://doi.org/10.4172/1948-5964.1000170.

[83] S. Zou, J. Guo, R. Gao, L. Dong, J. Zhou, Y. Zhang, J. Dong, H. Bo, K. Qin, Y. Shu, Inactivation of the novel avian influenza A (H7N9) virus under physical conditions or chemical agents treatment, Virology Journal. 10 (2013) 1–5. https://doi.org/10.1186/1743-422X-10-289.

[84] Z. gang Wu, H. yun Zheng, J. Gu, F. Li, R. long Lv, Y. yun Deng, W. zhou Xu, Y. qmg Tong, Effects of different temperature and time durations of virus inactivation on results of real-time fluorescence PCR testing of COVID-19 viruses, Current Medical Science. 40 (2020) 614–617. https://doi.org/10.1007/s11596-020-2224-y.

[85] T.S. Suryanarayanan, M.B. Govindarajulu, E. Thirumalai, M.S. Reddy, N.P. Money, Agni's fungi: Heat-resistant spores from the Western Ghats, southern India, Fungal Biology. 115 (2011) 833–838. https://doi.org/10.1016/j.funbio.2011.06.011.

[86] H. Xie, H. Jia, J. Ji, Y. Qian, H. Meng, J. Li, Y. Mu, Performance analysis of a novel air filtration and sterilization PV-Trombe wall, Building and Environment. 265 (2024) 111953. https://doi.org/10.1016/j.buildenv.2024.111953.

[87] L. Yu, G.K. Peel, F.H. Cheema, W.S. Lawrence, N. Bukreyeva, C.W. Jinks, J.E. Peel, J.W. Peterson, S. Paessler, M. Hourani, Z. Ren, Catching and killing of airborne SARS-CoV-2 to control spread of COVID-19 by a heated air disinfection system, Materials Today Physics. 15 (2020). https://doi.org/10.1016/j.mtphys.2020.100249.

[88] P. Tronville, R. Sala, Minimization of resistance in pleated-media air filter designs: Empirical and cfd approaches, HVAC and R Research. 9 (2003) 95–106. https://doi.org/10.1080/10789669.2003.10391058.

[89] W. Mrad, F. Theron, A. Joubert, N. Zgheib, L. Le Coq, Local variations of air velocity in the vicinity of filter pleats in transitional airflow regime – Experimental and numerical approaches, Separation and Purification Technology. 268 (2021) 118658. https://doi.org/10.1016/J.SEPPUR.2021.118658.

[90] M. Sedlar, T. Krátký, J. Langer, Numerical and Experimental Investigation of Three-

Dimensional Flow in Combined Protective Canister Filters, Fluids. 7 (2022) 171.

[91] G. Teng, G. Shi, J. Zhu, Influence of pleated geometry on the pressure drop of filters during dust loading process: experimental and modelling study, Scientific Reports 2022 12:1. 12 (2022) 1–16. https://doi.org/10.1038/S41598-022-24838-7.

[92] S. Fotovati, S.A. Hosseini, H. Vahedi Tafreshi, B. Pourdeyhimi, Modeling instantaneous pressure drop of pleated thin filter media during dust loading, Chemical Engineering Science. 66 (2011) 4036–4046. https://doi.org/10.1016/J.CES.2011.05.038.

[93] L. Del Fabbro, J.C. Laborde, P. Merlin, L. Ricciardi, Air flows and pressure drop modelling for different pleated industrial filters, Filtration & Separation. 39 (2002) 34–40. https://doi.org/10.1016/S0015-1882(02)80055-6.

[94] Z. Feng, Z. Long, Q. Chen, Assessment of various CFD models for predicting airflow and pressure drop through pleated filter system, Building and Environment. 75 (2014) 132–141. https://doi.org/10.1016/J.BUILDENV.2014.01.022.

[95] F. Théron, A. Joubert, L. Le Coq, Numerical and experimental investigations of the influence of the pleat geometry on the pressure drop and velocity field of a pleated fibrous filter, Separation and Purification Technology. 182 (2017) 69–77. https://doi.org/10.1016/j.seppur.2017.02.034.

[96] M. Rebaï, M. Prat, M. Meireles, P. Schmitz, R. Baclet, A semi-analytical model for gas flow in pleated filters, Chemical Engineering Science. 65 (2010) 2835–2846. https://doi.org/10.1016/J.CES.2010.01.014.

[97] D.A. Nield, A. Bejan, Convection in porous media, Springer, 2006.

[98] M.K. Das, P.P. Mukherjee, K. Muralidhar, Equations Governing Flow and Transport in Porous Media, in: Modeling Transport Phenomena in Porous Media with Applications, 1st ed., Springer, 2018: pp. 15–42.

[99] K. Khanafer, K. Vafai, Effect of a circular cylinder and flexible wall on natural convective heat transfer characteristics in a cavity filled with a porous medium, Applied Thermal Engineering. 181 (2020) 115989. https://doi.org/10.1016/J.APPLTHERMALENG.2020.115989.

[100] A. Souche, M. Dabrowski, T.B. Andersen, Modeling thermal convection in supradetachment basins: example from western N orway, Geofluids. 14 (2014) 58–74.

[101] N. Seki, S. Fukusako, H. Inaba, Heat transfer in a confined rectangular cavity packed with porous media, International Journal of Heat and Mass Transfer. 21 (1978) 985–989. https://doi.org/10.1016/0017-9310(78)90190-4.

[102] J.E. Belwafa, K. Vafai, An experimental investigation of heat transfer in a partially filled horizontal enclosure, Experimental Thermal and Fluid Science. 4 (1991) 369–373. https://doi.org/10.1016/0894-1777(91)90054-U.

[103] M. Song, R. Viskanta, Natural convection flow and heat transfer within a rectangular enclosure containing a vertical porous layer, International Journal of Heat and Mass Transfer. 37 (1994) 2425–2438. https://doi.org/10.1016/0017-9310(94)90284-4.

[104] A. Bagchi, F.A. Kulacki, Experimental study of natural convection in fluid-superposed porous layers heated locally from below, International Journal of Heat and Mass Transfer. 55 (2012) 1149–1153. https://doi.org/10.1016/j.ijheatmasstransfer.2011.09.056.

[105] X. Zhang, G. Su, J. Yu, Z. Yao, F. He, PIV measurement and simulation of turbulent thermal free convection over a small heat source in a large enclosed cavity, Building and Environment. 90 (2015) 105–113. https://doi.org/10.1016/j.buildenv.2015.03.015.

[106] X. Zhang, J. Yu, G. Su, Z. Yao, P. Hao, F. He, Statistical analysis of turbulent thermal free convection over a small heat source in a large enclosed cavity, Applied Thermal Engineering. 93 (2016) 446–455. https://doi.org/10.1016/j.applthermaleng.2015.10.011.

[107] A. Vasiliev, A. Sukhanovskii, P. Frick, A. Budnikov, V. Fomichev, M. Bolshukhin, R. Romanov, High Rayleigh number convection in a cubic cell with adiabatic sidewalls, International Journal of Heat and Mass Transfer. 102 (2016) 201–212. https://doi.org/10.1016/j.ijheatmasstransfer.2016.06.015.

[108] A. Weppe, F. Moreau, D. Saury, Experimental investigation of a turbulent natural convection flow in a cubic cavity with an inner obstacle partially heated, International Journal of Heat and Mass Transfer. 194 (2022) 123052. https://doi.org/10.1016/j.ijheatmasstransfer.2022.123052.

[109] F. Liu, B. Chen, L. Wang, Experimental and numerical estimation of slip coefficient in a partially porous cavity, Experimental Thermal and Fluid Science. 44 (2013) 431–438. https://doi.org/10.1016/j.expthermflusci.2012.08.004.

[110] I. Ataei-Dadavi, N. Rounaghi, M. Chakkingal, S. Kenjeres, C.R. Kleijn, M.J. Tummers, An experimental study of flow and heat transfer in a differentially side heated cavity filled with coarse porous media, International Journal of Heat and Mass Transfer. 143 (2019) 118591. https://doi.org/10.1016/J.IJHEATMASSTRANSFER.2019.118591.

[111] I. Ataei-Dadavi, M. Chakkingal, S. Kenjeres, C.R. Kleijn, M.J. Tummers, Flow and heat

transfer measurements in natural convection in coarse-grained porous media, International Journal of Heat and Mass Transfer. 130 (2019) 575–584. https://doi.org/10.1016/j.ijheatmasstransfer.2018.10.118.

[112] A. Brusly Solomon, M. Sharifpur, T. Ottermann, C. Grobler, M. Joubert, J.P. Meyer, Natural convection enhancement in a porous cavity with Al2O3-Ethylene glycol/water nanofluids, International Journal of Heat and Mass Transfer. 108 (2017) 1324–1334. https://doi.org/10.1016/j.ijheatmasstransfer.2017.01.009.

[113] C. Qi, J. Tang, Z. Ding, Y. Yan, L. Guo, Y. Ma, Effects of rotation angle and metal foam on natural convection of nanofluids in a cavity under an adjustable magnetic field, International Communications in Heat and Mass Transfer. 109 (2019) 104349. https://doi.org/10.1016/j.icheatmasstransfer.2019.104349.

[114] S. Zhang, L. Pu, S. Mancin, Z. Ma, L. Xu, Experimental study on heat transfer characteristics of metal foam/paraffin composite PCMs in large cavities: Effects of material types and heating configurations, Applied Energy. 325 (2022) 119790. https://doi.org/10.1016/j.apenergy.2022.119790.

[115] O. V. Trevisan, A. Bejan, Mass and heat transfer by natural convection in a vertical slot filled with porous medium, International Journal of Heat and Mass Transfer. 29 (1986) 403–415. https://doi.org/10.1016/0017-9310(86)90210-3.

[116] J.L. Lage, A. Bejan, The resonance of natural convection in an enclosure heated periodically from the side, International Journal of Heat and Mass Transfer. 36 (1993) 2027–2038. https://doi.org/10.1016/S0017-9310(05)80134-6.

[117] C. Beckermann, S. Ramadhyani, R. Viskanta, Natural Convection Flow and Heat Transfer

Between a Fluid Layer and a Porous Layer Inside a Rectangular Enclosure, Journal of Heat Transfer. 109 (1987) 363–370. https://doi.org/10.1115/1.3248089.

[118] C. Beckermann, R. Viskanta A N, Natural convection in vertical enclosures containing simultaneously fluid and porous layers, J. Fluid Nech. (1988) 257–284. https://doi.org/10.1017/S0022112088000138.

[119] A.K. Singh, G.R. Thorpe, Natural convection in a confined fluid overlying a porous layer-a comparison, Indian Journal of Pure and Applied Mathematics. 26 (1995) 81–95.

[120] X.B. Chen, · P Yu, · Y Sui, · S H Winoto, · H T Low, H.T. Low, Natural Convection in a Cavity Filled with Porous Layers on the Top and Bottom Walls, Transp Porous Med. 78 (2009) 259–276. https://doi.org/10.1007/s11242-008-9300-2.

[121] M. Sathiyamoorthy, T. Basak, S. Roy, I. Pop, Steady natural convection flow in a square cavity filled with a porous medium for linearly heated side wall(s), International Journal of Heat and Mass Transfer. 50 (2007) 1892–1901. https://doi.org/10.1016/J.IJHEATMASSTRANSFER.2006.10.010.

[122] A.J. Chamkha, M.A. Ismael, Natural convection in differentially heated partially porous layered cavities filled with a Nanofluid, Numerical Heat Transfer; Part A: Applications. 65 (2014) 1089–1113. https://doi.org/10.1080/10407782.2013.851560.

[123] F.J. Guerrero-Martínez, P.L. Younger, N. Karimi, S. Kyriakis, Three-dimensional numerical simulations of free convection in a layered porous enclosure, International Journal of Heat and Mass Transfer. 106 (2017) 1005–1013. https://doi.org/10.1016/J.IJHEATMASSTRANSFER.2016.10.072.

[124] A.S. Abdulwahed, L.F. Ali, Numerical investigation of natural convection in a square enclosure partially filled with horizontal layers of a porous medium, Heat Transfer. 52 (2023) 874–889. https://doi.org/10.1002/HTJ.22720.

[125] S.A. Khashan, A.M. Al-Amiri, I. Pop, Numerical simulation of natural convection heat transfer in a porous cavity heated from below using a non-Darcian and thermal non-equilibrium model, International Journal of Heat and Mass Transfer. 49 (2006) 1039–1049. https://doi.org/10.1016/j.ijheatmasstransfer.2005.09.011.

[126] M. Ghalambaz, A. Tahmasebi, A.J. Chamkha, D. Wen, Conjugate local thermal non-equilibrium heat transfer in a cavity filled with a porous medium: Analysis of the element location, International Journal of Heat and Mass Transfer. 138 (2019) 941–960. https://doi.org/10.1016/J.IJHEATMASSTRANSFER.2019.03.073.

[127] F. Wu, W. Zhou, G. Wang, X. Ma, Y. Wang, Numerical simulation of natural convection in a porous cavity with linearly temperature distributions under the local thermal nonequilibrium condition, Numerical Heat Transfer; Part A: Applications. 68 (2015) 1394–1415. https://doi.org/10.1080/10407782.2015.1052316.

[128] F. Wu, W. Zhou, X. Ma, Natural convection in a porous rectangular enclosure with sinusoidal temperature distributions on both side walls using a thermal non-equilibrium model, International Journal of Heat and Mass Transfer. 85 (2015) 756–771. https://doi.org/10.1016/J.IJHEATMASSTRANSFER.2015.02.039.

[129] A.I. Alsabery, R. Mohebbi, A.J. Chamkha, I. Hashim, Effect of local thermal non-equilibrium model on natural convection in a nanofluid-filled wavy-walled porous cavity containing inner solid cylinder, Chemical Engineering Science. 201 (2019) 247–263.

[130] M. Aneja, A. Chandra, S. Sharma, Natural convection in a partially heated porous cavity to Casson fluid, International Communications in Heat and Mass Transfer. 114 (2020) 104555. https://doi.org/10.1016/J.ICHEATMASSTRANSFER.2020.104555.

[131] K. Khanafer, B. Al-Azmi, A. Marafie, I. Pop, Non-Darcian effects on natural convection heat transfer in a wavy porous enclosure, International Journal of Heat and Mass Transfer. 52 (2009) 1887–1896.

[132] K. Al-Farhany, M.F. Al-dawody, D.A. Hamzah, W. Al-Kouz, Z. Said, Numerical investigation of natural convection on Al2O3–water porous enclosure partially heated with two fins attached to its hot wall: under the MHD effects, Applied Nanoscience (Switzerland). 13 (2023) 555–572. https://doi.org/10.1007/S13204-021-01855-Y/METRICS.

[133] A. Filiz, B. Bayta¸s, · A Cihat, Thermal Non-equilibrium Natural Convection in a Square Enclosure with Heat-Generating Porous Layer on Inner Walls, Transport in Porous Media. 120 (2017) 167–182. https://doi.org/10.1007/s11242-017-0914-0.

[134] F. Keramat, A. Azari, H. Rahideh, M. Abbasi, A CFD parametric analysis of natural convection in an H-shaped cavity with two-sided inclined porous fins, Journal of the Taiwan Institute of Chemical Engineers. 114 (2020) 142–152. https://doi.org/10.1016/J.JTICE.2020.09.011.

[135] O.R. Alomar, N.M. Basher, A.A. Yousif, Natural convection heat transfer from a bank of orthogonal heated plates embedded in a porous medium using LTNE model: A comparison between in-line and staggered arrangements, International Journal of Thermal Sciences. 160 (2021) 106692. https://doi.org/10.1016/J.IJTHERMALSCI.2020.106692.

[136] N.M. Basher, O.R. Alomar, I.A. Mohamed, Impact of using single heated obstacle on natural convection inside porous cavity under non-Darcy flow and thermal non-equilibrium model: A comparison between horizontal and vertical heated obstacle arrangements, International Communications in Heat and Mass Transfer. 133 (2022) 105925. https://doi.org/10.1016/J.ICHEATMASSTRANSFER.2022.105925.

[137] M.H. Alturaihi, L. Jassim, A.R. Alguboori, L.J. Habeeb, H.K. Jalghaf, Porosity influence on natural convection heat transfer from a heated cylinder in a square porous enclosure, Journal of Mechanical Engineering Research and Developments. 43 (2020) 236–254.

[138] S.H. Hussain, M.S. Rahomey, Comparison of Natural Convection Around a Circular Cylinder with Different Geometries of Cylinders Inside a Square Enclosure Filled with Ag Nanofluid Superposed Porous Nanofluid Layers, Journal of Heat Transfer. 141 (2019). https://doi.org/10.1115/1.4039642/365778.

[139] A. Abdulkadhim, H.K. Hamzah, F.H. Ali, A.M. Abed, I.M. Abed, Natural convection among inner corrugated cylinders inside wavy enclosure filled with nanofluid superposed in porous–nanofluid layers, International Communications in Heat and Mass Transfer. 109 (2019) 104350. https://doi.org/10.1016/J.ICHEATMASSTRANSFER.2019.104350.

[140] G. Chandra Pal, N. Goswami, S. Pati, Numerical investigation of unsteady natural convection heat transfer and entropy generation from a pair of cylinders in a porous enclosure, Numerical Heat Transfer; Part A: Applications. 74 (2018) 1323–1341. https://doi.org/10.1080/10407782.2018.1507887.

[141] G. Nammi, D.K. Deka, S. Pati, L. Baranyi, Natural convection heat transfer within a square porous enclosure with four heated cylinders, Case Studies in Thermal Engineering. 30

(2022) 101733. https://doi.org/10.1016/J.CSITE.2021.101733.

[142] M. Hashemi-Tilehnoee, A.S. Dogonchi, S.M. Seyyedi, M. Sharifpur, Magneto-fluid dynamic and second law analysis in a hot porous cavity filled by nanofluid and nano-encapsulated phase change material suspension with different layout of cooling channels, Journal of Energy Storage. 31 (2020) 101720. https://doi.org/10.1016/J.EST.2020.101720.

[143] S.M. Aithal, Natural convection in a cubical cavity with a coaxial heated cylinder, International Journal of Heat and Mass Transfer. 118 (2018) 961–975. https://doi.org/10.1016/j.ijheatmasstransfer.2017.11.046.

[144] S.M. Aithal, Turbulent natural convection in a square cavity with a circular cylinder, Journal of Thermophysics and Heat Transfer. 30 (2016) 843–853. https://doi.org/10.2514/1.T4873.

[145] S.R. Sondur, B. Meuris, A.M. Mescher, Benchmarked simulations of natural convection airflow in a square cavity, Numerical Heat Transfer; Part A: Applications. 84 (2022) 252–268. https://doi.org/10.1080/10407782.2022.2105120.

[146] A. Ben-Nakhi, M.A. Mahmoud, Conjugate turbulent natural convection in the roof enclosure of a heavy construction building during winter, Applied Thermal Engineering. 28 (2008) 1522–1535.

[147] M. Omri, N. Galanis, Numerical analysis of turbulent buoyant flows in enclosures: Influence of grid and boundary conditions, International Journal of Thermal Sciences. 46 (2007) 727–738.

[148] T. Wu, C. Lei, On numerical modelling of conjugate turbulent natural convection and radiation in a differentially heated cavity, International Journal of Heat and Mass Transfer.

91 (2015) 454–466.

[149] U.D.F. Manual, ANSYS FLUENT 12.0, Theory Guide. (2009).

[150] A. Bejan, Convection Heat Transfer, second, John Wiley and Sons Inc., 1995.

[151] A.I. Zografos, W.A. Martin, J.E. Sunderland, Equations of properties as a function of temperature for seven fluids, Computer Methods in Applied Mechanics and Engineering. 61 (1987) 177–187.

[152] J. Wang, J.K. Carson, M.F. North, D.J. Cleland, A new structural model of effective thermal conductivity for heterogeneous materials with co-continuous phases, International Journal of Heat and Mass Transfer. 51 (2008) 2389–2397. https://doi.org/10.1016/j.ijheatmasstransfer.2007.08.028.

[153] P. Belleoud, D. Saury, D. Lemonnier, Coupled velocity and temperature measurements in an air-filled differentially heated cavity at Ra=1.2E11, International Journal of Thermal Sciences. 123 (2018) 151–161. https://doi.org/10.1016/j.ijthermalsci.2017.09.018.

[154] I. V. Miroshnichenko, M.A. Sheremet, Turbulent natural convection heat transfer in rectangular enclosures using experimental and numerical approaches: A review, Renewable and Sustainable Energy Reviews. 82 (2018) 40–59. https://doi.org/10.1016/J.RSER.2017.09.005.

[155] R. Hidki, L. El Moutaouakil, Z. Charqui, M. Boukendil, Z. Zrikem, Natural convection in a square cavity containing two heat-generating cylinders with different geometries, Materials Today: Proceedings. 45 (2021) 7415–7423. https://doi.org/10.1016/J.MATPR.2021.01.626.

[156] S. Pandey, Y.G. Park, M.Y. Ha, An exhaustive review of studies on natural convection in enclosures with and without internal bodies of various shapes, International Journal of Heat and Mass Transfer. 138 (2019) 762–795. https://doi.org/10.1016/j.ijheatmasstransfer.2019.04.097.

[157] A. Jobby, M. Khatamifar, W. Lin, A Comprehensive Review on the Natural Convection Heat Transfer in Horizontal and Inclined Closed Rectangular Enclosures with Internal Objects at Various Heating Conditions, Energies. 18 (2025). https://doi.org/10.3390/en18040950.

[158] Z. Begum, M. Saleem, S.U. Islam, S.C. Saha, Numerical Study of Natural Convection Flow in Rectangular Cavity with Viscous Dissipation and Internal Heat Generation for Different Aspect Ratios, Energies. 16 (2023). https://doi.org/10.3390/en16145267.

[159] Y.M. Seo, Y.G. Park, M. Kim, H.S. Yoon, M.Y. Ha, Two-dimensional flow instability induced by natural convection in a square enclosure with four inner cylinders. Part I: Effect of horizontal position of inner cylinders, International Journal of Heat and Mass Transfer. 113 (2017) 1306–1318. https://doi.org/10.1016/j.ijheatmasstransfer.2017.02.011.

[160] I. Sarbu, C. Sebarchievici, Aspects of indoor environmental quality assessment in buildings, Energy and Buildings. 60 (2013) 410–419. https://doi.org/10.1016/j.enbuild.2013.02.005.

[161] A.M. Akbarpoor, A.H. Poshtiri, F. Biglari, Performance analysis of domed roof integrated with earth-to-air heat exchanger system to meet thermal comfort conditions in buildings, Renewable Energy. 168 (2021) 1265–1293. https://doi.org/10.1016/j.renene.2020.12.110.

[162] A.M. Akbarpoor, Z.M. Gilvaei, A.H. Poshtiri, L. Zhong, A hybrid domed roof and evaporative cooling system: Thermal comfort and building energy evaluation, Sustainable

Cities and Society. 80 (2022) 103756. https://doi.org/10.1016/j.scs.2022.103756.

[163] A. Mirzazade Akbarpoor, A. Haghighi Poshtiri, Cooling urban buildings with a combined meander EAHE–DEC system: Energy and water consumption analysis, Journal of Building Engineering. 108 (2025) 112850. https://doi.org/10.1016/j.jobe.2025.112850.

[164] P. Azimi, B. Stephens, HVAC filtration for controlling infectious airborne disease transmission in indoor environments: Predicting risk reductions and operational costs, Building and Environment. 70 (2013) 150–160. https://doi.org/10.1016/j.buildenv.2013.08.025.

[165] P. Shrestha, J.W. DeGraw, M. Zhang, X. Liu, Multizonal modeling of SARS-CoV-2 aerosol dispersion in a virtual office building, Building and Environment. 206 (2021) 108347. https://doi.org/10.1016/j.buildenv.2021.108347.

[166] C.A. Faulkner, J.E. Castellini Jr, W. Zuo, D.M. Lorenzetti, M.D. Sohn, Investigation of HVAC operation strategies for office buildings during COVID-19 pandemic, Building and Environment. 207 (2022) 108519. https://doi.org/10.1016/j.buildenv.2021.108519.

[167] R.B. Simmons, S.A. Crow, Fungal colonization of air filters for use in heating, ventilating, and air conditioning (HVAC) systems, Journal of Industrial Microbiology. 14 (1995) 41–45. https://doi.org/10.1007/BF01570065.

[168] R.B. Simmons, D.L. Price, J.A. Noble, S.A. Crow, D.G. Ahearn, Fungal colonization of air filters from hospitals, American Industrial Hygiene Association Journal. 58 (1997) 900–904. https://doi.org/10.1080/15428119791012252.

[169] D.L. Price, R.B. Simmons, S.A. Crow, D.G. Ahearn, Mold colonization during use of

preservative-treated and untreated air filters, including HEPA filters from hospitals and commercial locations over an 8-year period (1996-2003), Journal of Industrial Microbiology and Biotechnology. 32 (2005) 319–321. https://doi.org/10.1007/s10295-005-0226-1.

[170] M. Ljaljević-Grbić, J. Vukojević, M. Stupar, Fungal colonization of air-conditioning systems, Archives of Biological Sciences. 60 (2008) 201–206. https://doi.org/10.2298/ABS0802201L.

[171] F. Noris, J.A. Siegel, K.A. Kinney, Biological and metal contaminants in HVAC filter dust, ASHRAE Transactions. 115 PART 2 (2009) 484–491.

[172] Z. Wang, H.P. Guzman, Y. Zou, I. Xagoraraki, K. Lin, SARS-CoV-2 Detection in Heating, Ventilation, and Air Conditioning Filters of University Lecture Rooms, ACS ES&T Air. 2 (2025) 1280–1291. https://doi.org/10.1021/acsestair.5c00056.

[173] H. Xie, B. Yu, J. Wang, J. Ji, A novel disinfected Trombe wall for space heating and virus inactivation: Concept and performance investigation, Applied Energy. 291 (2021) 116789. https://doi.org/10.1016/j.apenergy.2021.116789.

[174] E.J. Braga, M.J.S. de Lemos, Turbulent heat transfer in an enclosure with a horizontal permeable plate in the middle, Journal of Heat Transfer. 128 (2006) 1122–1129. https://doi.org/10.1115/1.2352779.

[175] E.J. Braga, M.J.S. de Lemos, Laminar and turbulent free convection in a composite enclosure, International Journal of Heat and Mass Transfer. 52 (2009) 588–596. https://doi.org/10.1016/j.ijheatmasstransfer.2008.07.012.

[176] P.H.S. Carvalho, M.J.S. De Lemos, Turbulent free convection in a porous square cavity using the thermal equilibirum model, International Communications in Heat and Mass Transfer. 49 (2013) 10–16. https://doi.org/10.1016/j.icheatmasstransfer.2013.10.003.

[177] P.H.S. Carvalho, M.J.S. de Lemos, Role of porosity and solid-to-fluid thermal conductivity ratio on turbulent combined heat and mass transfer in a porous cavity, International Journal of Heat and Mass Transfer. 132 (2019) 221–237. https://doi.org/10.1016/j.ijheatmasstransfer.2018.11.137.

[178] C. Liu, Z. Dai, B. He, Q.F. Ke, The effect of temperature and humidity on the filtration performance of electret melt-blown nonwovens, Materials. 13 (2020) 1–12. https://doi.org/10.3390/ma13214774.

[179] B. Konves, Understanding Fiberglass, Polyester, and Pleated AC and Furnace Filters, (2024). https://www.acfilters4less.com/fiberglass-vs-polyester-vs-pleated-ac-furnace-filters.html (accessed October 13, 2025).

[180] A.M. Elsaid, M.S. Ahmed, Indoor Air Quality Strategies for Air-Conditioning and Ventilation Systems with the Spread of the Global Coronavirus (COVID-19) Epidemic: Improvements and Recommendations, Environmental Research. 199 (2021). https://doi.org/10.1016/j.envres.2021.111314.

[181] T. Sibanda, R. Selvarajan, H.J.O. Ogola, C.C. Obieze, M. Tekere, Distribution and Comparison of Bacterial Communities in HVAC Systems of Two University Buildings: Implications for Indoor Air Quality and Public Health, Environmental Monitoring and Assessment. 193 (2021) 47. https://doi.org/10.1007/s10661-020-08823-z.

[182] G. Buonanno, L. Ricolfi, L. Morawska, L. Stabile, Increasing ventilation reduces SARS-

CoV-2 airborne transmission in schools: A retrospective cohort study in Italy's Marche region, Frontiers in Public Health. 10 (2022) 1087087. https://doi.org/10.3389/fpubh.2022.1087087.

[183] L.D. Knibbs, L. Morawska, S.C. Bell, P. Grzybowski, Room ventilation and the risk of airborne infection transmission in 3 health care settings within a large teaching hospital, American Journal of Infection Control. 39 (2011) 866–872. https://doi.org/10.1016/j.ajic.2011.02.014.

[184] V.A. Vartiainen, J. Hela, A. Luoto, P. Nikuri, E. Sanmark, A. Taipale, I. Ehder-Gahm, N. Lastovets, P. Sormunen, I. Kulmala, The effect of room air cleaners on infection control in day care centres, Indoor Environments. 1 (2024) 100007. https://doi.org/10.1016/j.indenv.2024.100007.

[185] M. Zaatari, A. Novoselac, J. Siegel, The relationship between filter pressure drop, indoor air quality, and energy consumption in rooftop HVAC units, Building and Environment. 73 (2014) 151–161. https://doi.org/10.1016/j.buildenv.2013.12.010.

[186] S. Pandey, A. Karvinen, J. Hakala, Unveiling the potential of far-UVC: Assessing irradiance and dose-response for microbial inactivation in UV systems, International Journal of Thermofluids. 27 (2025) 101187. https://doi.org/10.1016/j.ijft.2025.101187.

[187] J.A. Siegel, Primary and secondary consequences of indoor air cleaners, Indoor Air. 26 (2016) 88–96. https://doi.org/10.1111/ina.12194.

[188] H. Zhao, X. Kong, W. Yao, X. Fei, J. Zhao, S. Zhao, T. Feng, Control technology of pathogenic biological aerosol: Review and prospect, Building and Environment. 243 (2023) 110679. https://doi.org/10.1016/j.buildenv.2023.110679.

[189] Z. Feng, S.J. Cao, F. Haghighat, Removal of SARS-CoV-2 using UV+Filter in built environment, Sustainable Cities and Society. 74 (2021) 103226. https://doi.org/10.1016/j.scs.2021.103226.

[190] C. Doig, A.L. Seagar, B. Watt, K.J. Forbes, The efficacy of the heat killing of Mycobacterium tuberculosis, Journal of Clinical Pathology. 55 (2002) 778–779. https://doi.org/10.1136/jcp.55.10.778.

[191] A.S.N.W. Pahalagedara, E. Gkogka, M. Hammershøj, A review on spore-forming bacteria and moulds implicated in the quality and safety of thermally processed acid foods: Focusing on their heat resistance, Food Control. 166 (2024). https://doi.org/10.1016/j.foodcont.2024.110716.

[192] M.E.R. Darnell, D.R. Taylor, Evaluation of inactivation methods for severe acute respiratory syndrome coronavirus in noncellular blood products, Transfusion. 46 (2006) 1770–1777. https://doi.org/10.1111/j.1537-2995.2006.00976.x.

[193] M. Shaffer, K. Huynh, V. Costantini, J. Vinjé, K. Bibby, Heat inactivation of aqueous viable norovirus and MS2 bacteriophage, Journal of Applied Microbiology. 135 (2024) 1–13. https://doi.org/10.1093/jambio/lxae033.

[194] N. Soni, D. Sharma, V. Nimesh, V. Mahendra Reddy, Solar energy assisted thermal treatment model to decontaminate airborne viruses in hospital, Thermal Science and Engineering Progress. 36 (2022) 101516. https://doi.org/10.1016/j.tsep.2022.101516.

[195] American Society of Heating, Refrigerating, and Air-Conditioning Engineers (ASHRAE), Guideline 26, Guideline for field testing of general ventilation filtration devices and systems for removal efficiency in-Situ by particle size and resistance to flow, (2012).

[196] Y.-S. Cheng, B.T. Chen, Aerosol sampler calibration, in: American Conference of Governmental Industrial Hygienists, 2008.

[197] P. Abdolghader, C. Brochot, F. Haghighat, A. Bahloul, Procedure to measure the penetration of one mechanical filter for nanoparticles–Validation by comparison, Measurement. 147 (2019) 106840. https://doi.org/10.1016/j.measurement.2019.07.068.

[198] A. Bastani, C.-S.S. Lee, F. Haghighat, C. Flaherty, N. Lakdawala, Assessing the performance of air cleaning devices–A full-scale test method, Building and Environment. 45 (2010) 143–149. https://doi.org/10.1016/j.buildenv.2009.05.008.

[199] M.G. Khararoodi, F. Haghighat, C.-S. Lee, Removal of indoor air ozone using carbon-based filters: Systematic development and validation of a predictive model, Building and Environment. 219 (2022) 109157. https://doi.org/10.1016/j.buildenv.2022.109157.

[200] J. Wu, J. Chen, J.S. Olfert, L. Zhong, Filter evaluation and selection for heating, ventilation, and air conditioning systems during and beyond the COVID-19 pandemic, Indoor Air. 32 (2022) 1–13. https://doi.org/10.1111/ina.13099.

[201] K. Kang, T. Kim, C.W. Shin, K. Kim, J. Kim, Y.G. Lee, Filtration efficiency and ventilation performance of window screen filters, Building and Environment. 178 (2020) 106878. https://doi.org/10.1016/j.buildenv.2020.106878.

[202] S. Bell, Measurement good practice guide no. 11 (issue 2), A Beginner's Guide to Uncertainty of Measurement. National Physical Laboratory Teddington, Middlesex, United Kingdom. (2001).

[203] G. Yao, Z. Liu, J. Shi, H. Liu, M. Ding, J. He, Comprehensive evaluations of the bioaerosol

filtration performance of high- and medium-efficiency filters under different influencing factors, Building Simulation. 17 (2024) 2249–2262. https://doi.org/10.1007/s12273-024-1184-8.

[204] R. Maus, A. Goppelsröder, H. Umhauer, Survival of bacterial and mold spores in air filter media, Atmospheric Environment. 35 (2001) 105–113. https://doi.org/10.1016/S1352-2310(00)00280-6.

[205] P.C. Kemp, H.G. Neumeister-Kemp, G. Lysek, F. Murray, Survival and growth of micro-organisms on air filtration media during initial loading, Atmospheric Environment. 35 (2001) 4739–4749. https://doi.org/10.1016/S1352-2310(01)00280-1.

[206] A. Forthomme, A. Joubert, Y. Andrès, X. Simon, P. Duquenne, D. Bemer, L. Le Coq, Microbial aerosol filtration: Growth and release of a bacteria-fungi consortium collected by fibrous filters in different operating conditions, Journal of Aerosol Science. 72 (2014) 32–46. https://doi.org/10.1016/j.jaerosci.2014.02.004.

[207] W.C. Hinds, Y. Zhu, Aerosol technology: properties, behavior, and measurement of airborne particles, in: Second, John Wiley & Sons, 2022.

[208] R.V. GmbH, GKHM 280-CIB EC Fan Performance Data, (2025).

[209] American Society of Heating, Refrigerating and Air-conditioning Engineers, (2021). https://www.ashrae.org/technical-resources/filtration-disinfection.

[210] C. Chen, W. Ji, B. Zhao, Size-dependent efficiencies of ultrafine particle removal of various filter media, Building and Environment. 160 (2019) 106171. https://doi.org/10.1016/j.buildenv.2019.106171.

[211] A.H. Al-abdalall, S.A. Al-dakheel, H.A. Al-Abkari, Impact of air-conditioning filters on microbial growth and indoor air pollution, in: Low-Temperature Technologies, IntechOpen, 2019: pp. 179–206. https://doi.org/10.5772/intechopen.88548.

[212] J.C. Bonnevie Perrier, L. Le Coq, Y. Andres, P. Le Cloirec, SFGP 2007-Microbial growth onto filter media used in air treatment devices, International Journal of Chemical Reactor Engineering. 6 (2008). https://doi.org/10.2202/1542-6580.1675.

[213] W. Yu, L. Wang, Q. Wang, X. Wang, G. Li, J. Wang, H. Awbi, Design selection and evaluation method of PM2. 5 filters for fresh air systems, Journal of Building Engineering. 27 (2020) 100977. https://doi.org/10.1016/j.jobe.2019.100977.

[214] F. Ahmed, W.R. Shultes, Hygienic Design of HVAC Systems for Hospitals, in: ASHRAE Transactions, American Society of Heating, Refrigeration and Air Conditioning Engineers, Inc., 2022: pp. 505–512.

[215] X. Tian, Q. Ou, C. Pei, Z. Li, J. Liu, Y. Liang, D.Y.H. Pui, Effect of main-stage filter media selection on the loading performance of a two-stage filtration system, Building and Environment. 195 (2021) 107745. https://doi.org/10.1016/j.buildenv.2021.107745.

[216] X. Tian, Q. Ou, J. Liu, Y. Liang, D.Y.H. Pui, Influence of pre-stage filter selection and face velocity on the loading characteristics of a two-stage filtration system, Separation and Purification Technology. 224 (2019) 227–236. https://doi.org/10.1016/j.seppur.2019.05.031.

[217] X. Tian, Q. Ou, J. Liu, Y. Liang, D.Y.H. Pui, Particle loading characteristics of a two-stage filtration system, Separation and Purification Technology. 215 (2019) 351–359. https://doi.org/10.1016/j.seppur.2019.01.033.

[218] J.C. Bonnevie Perrier, L. Le Coq, Y. Andrès, P. Le Cloirec, SFGP 2007 - Microbial growth onto filter media used in air treatment devices, International Journal of Chemical Reactor Engineering. 6 (2008). https://doi.org/10.2202/1542-6580.1675.

[219] A. A-Abdalall, S.A. Al-dakheel, H.A. Al-Abkari, Impact of Air-Conditioning Filters on Microbial Growth and Indoor Air Pollution, in: T. Morosuk, M. Sultan (Eds.), Low-Temperature Technologies, IntechOpen, Rijeka, 2019. https://doi.org/10.5772/intechopen.88548.

[220] M. Hyttinen, P. Pasanen, J. Salo, M. Björkroth, M. Vartiainen, P. Kalliokoski, Reactions of ozone on ventilation filters, Indoor and Built Environment. 12 (2003) 151–158. https://doi.org/10.1177/1420326X03012003002.

[221] M. Hyttinen, P. Pasanen, P. Kalliokoski, Adsorption and desorption of selected VOCs in dust collected on air filters, Atmospheric Environment. 35 (2001) 5709–5716. https://doi.org/10.1016/S1352-2310(01)00376-4.

[222] M. Hyttinen, P. Pasanen, M. Björkroth, P. Kalliokoski, Odors and volatile organic compounds released from ventilation filters, Atmospheric Environment. 41 (2007) 4029–4039. https://doi.org/10.1016/j.atmosenv.2007.01.029.

[223] X. Zhou, X. Dong, R. Ma, X. Wang, F. Wang, Characterizing the partitioning behavior of formaldehyde, benzene and toluene on indoor fabrics: Effects of temperature and humidity, Journal of Hazardous Materials. 416 (2021) 125827. https://doi.org/10.1016/j.jhazmat.2021.125827.

[224] G. Beel, B. Langford, N. Carslaw, D. Shaw, N. Cowan, Temperature driven variations in VOC emissions from plastic products and their fate indoors: A chamber experiment and

modelling study, Science of the Total Environment. 881 (2023) 163497. https://doi.org/10.1016/j.scitotenv.2023.163497.

[225] Z. Zuo, J. Wang, C.H. Lin, D.Y.H. Pui, VOC outgassing from baked and unbaked ventilation filters, Aerosol and Air Quality Research. 10 (2010) 265–271. https://doi.org/10.4209/aaqr.2009.10.0064.

[226] B. Stephens, J.A. Siegel, Comparison of test methods for determining the particle removal efficiency of filters in residential and light-commercial central HVAC systems, Aerosol Science and Technology. 46 (2012) 504–513. https://doi.org/10.1080/02786826.2011.642825.

[227] V. Gnielinski, On heat transfer in tubes, International Journal of Heat and Mass Transfer. 63 (2013) 134–140. https://doi.org/10.1016/j.ijheatmasstransfer.2013.04.015.

Appendix A (Structured Mesh for Validation of Numerical Simulation)

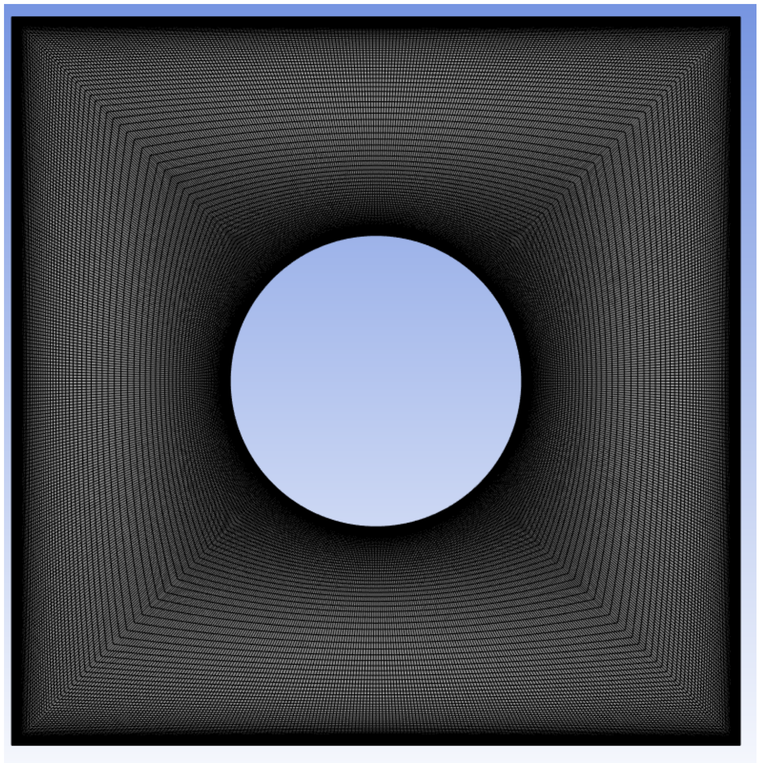

Fig. A.1. A schematic representation of the numerical grid used for the validation of the numerical simulation in Section 3.5.4.

Appendix B (ASHRAE 52.2 General Requirements)

ASHRAE 52.2 [22] provides a design guideline for measuring the capability of HVAC filters in removing specific particles from the airstream and their resistance to airflow. This standard introduces critical dimensions and arrangements of the test apparatus as well as the required features of different equipment (e.g., aerosol generator and aerosol sizer) to obtain a reliable result in filter testing. Fig.B.1 depicts a schematic view of the open-circuit wind tunnel suggested by ASHRAE 52.2. Some of the general requirements for designing the experimental setup are as follows:

1. The test duct is primarily of square cross section, 610 × 610 mm (24 ×24 in.).
2. The temperature of the air at the test device shall be between 10°C and 38°C (50°F and 100°F) with a relative humidity of 45% ± 10%.
3. An orifice plate and a mixing baffle shall be located downstream of the aerosol injection point for better mixing.
4. The application of the bend is optional, but it helps the homogenization of particles.
5. Uniformity of air velocity and aerosol concentration profiles (the coefficient of variation (CV) should be within ± 10% of the mean values in the test section).
6. Air-cleaner testing should be conducted at airflow rates not less than 0.22 m^3/s (472 cfm), nor greater than 1.4 m^3/s (3000 cfm).
7. The test aerosol shall be poly-disperse solid-phase (dry) potassium chloride (KCl) particles generated from an aqueous solution. The aerosol generator shall provide a stable test aerosol of sufficient concentration over the 0.30 to 10 µm diameter size range without overloading the aerosol particle counter.

8. Isokinetic sampling (to within 10%) shall be maintained on both primary and secondary probes (i.e., the direction and velocity magnitude of the airflow within the sampling probe should be equal to that of the air in the duct).
9. The aerosol particle counter shall be based on optical particle sizing and counting (i.e., light scattering). These instruments are commonly known as "optical particle counters" and also as "optical aerosol spectrometers." The particle counters shall count and size aerosol particles in the 0.30 to 10 µm diameter size range.

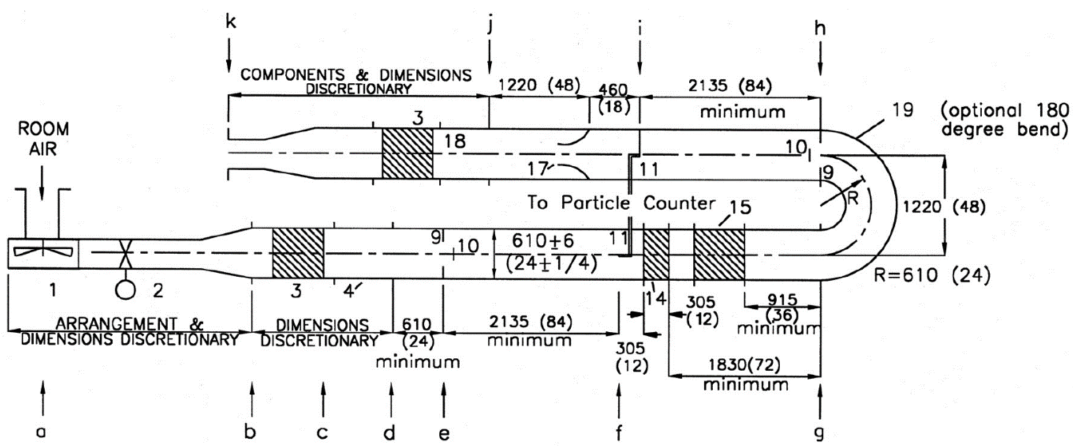

Overall View of Test Duct

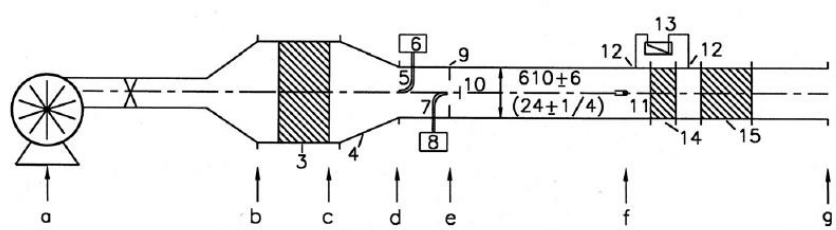

Upstream Duct Detail

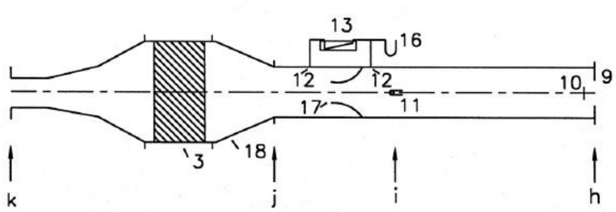

Downstream Duct Detail

1. Blower	**10. Perforated diffusion plate**
2. Flow control valve	**11. Location of sample probe**
3. HEPA filter bank	**12. Static tap**
4. Transition, if any, from filter bank to 610 × 610 mm (24 × 24 in.) ducting. Maximum transition half angle = 45°.	**13. Manometer** **14. Air-cleaning device and transitions (if any)**
5. Aerosol injection tube	**15. Final filter (installed only during dust loading)**
6. Aerosol generator	**16. Vertical manometer**
7. Dust feed pipe	**17. Main flow measurement nozzle**
8. Dust feeder	**18. Transition, if needed**
9. Mixing orifice	**19. Bend, optional**

Fig. B.1. Schematic views of the open-loop test apparatus recommended by ASHRAE 52.2 (i.e., dimensions are in mm (in)) [22].

Appendix C (Advanced Testing Infrastructure: Closed-Loop Aerosol Wind Tunnel)

(a)

(b)

(c)

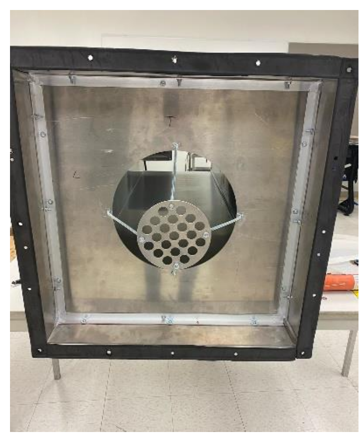

(d)

(e)

(f)

(g)

Fig. C.1. Advanced filtration testing assembly and setup, including (a) ductwork sections, (b) centrifugal fan, (c) HEPA filter, (d) mixing baffle, (e) aerosol generator nozzle, (f) aerosol sampling tube, and (g) closed-loop aerosol wind tunnel.

Appendix D (Ph.D. Publications)

D.1. Peer-Reviewed Journal Papers

D.1.1. Published

1. **A. Mirzazade Akbarpoor**, M. Salimi, E. Rasouli, M. Shahbakhti, A. Nouri, A Heat-Driven Disinfection Technology for Enhancing Indoor Air Quality in HVAC Systems, Journal of Building Engineering. 115 (2025) 114513. https://doi.org/10.1016/j.jobe.2025.114513.

2. **A. Mirzazade Akbarpoor**, M. Salimi, E. Rasouli, M. Shahbakhti, A. Nouri, An Energy-Efficient Heat-Driven Technology for Airborne Pathogen Inactivation: Integration of Two-Stage HVAC Filtration with Thermal Disinfection, Applied Thermal Engineering. (2026) 129140. https://doi.org/https://doi.org/10.1016/j.applthermaleng.2025.129140.

3. E. Rasouli, M. Salimi, **A. Mirzazade Akbarpoor**, M. Shahbakhti, A. Nouri, Effect of Aerodynamic Disturbances on Particle Detachment from Fibrous Filters in an Air Disinfection System, Journal of Building Engineering. (2025) 114653. https://doi.org/10.1016/j.jobe.2025.114653.

D.1.2. Under Review

1. E. Rasouli, M. Salimi, **A. Mirzazade Akbarpoor**, M. Shahbakhti, A. Nouri, Numerical Investigation of Flow Disturbance and Particle Release Risk Mitigation in a Filter Disinfection System, Indoor & Built Environment, (Submitted on February 2, 2026).

2. **A. Mirzazade Akbarpoor**, M. Salimi, A. Shabani, M. Shahbakhti, A. Nouri, Natural-Convection-Based Thermal Disinfection of Air Filters: Performance and Energy Evaluation in HVAC Systems, Thermal Science and Engineering Progress. (Submitted on January 31, 2026).

3. Z. Moghtader Gilvaei, **A. Mirzazade Akbarpoor**, M. Salimi, M. Shahbakhti, A. Nouri, Integration of Infrared Thermal Irradiation in HVAC Systems for Filter Disinfection, Journal of Building Engineering, (Submitted on January 14, 2026).

D.1.3. In Preparation

1. A. Shabani, M. Salimi, **A. Mirzazade Akbarpoor**, M. Shahbakhti, A. Nouri, A Novel Energy-Efficient Technology for Disinfecting Air Filters: Integration of Pleated Filters with Heating Wires, Building & Environment, (To be Submitted in April 2026).

D.2. Technical Posters

1. **A. Mirzazade Akbarpoor**, M. Salimi, E. Rasouli, M. Shahbakhti, A. Nouri, A Novel Heat-Based Technology for Disinfecting Pleated Air Filters in HVAC Systems. Faculty of Engineering Graduate Research Symposium (FEGRS 2025), University of Alberta, (August 2025).

2. E. Rasouli, M. Salimi, **A. Mirzazade Akbarpoor**, M. Shahbakhti, A. Nouri, Influence of Aerodynamic Disturbances on Particle Release from Fibrous Filters in Disinfection Systems. Faculty of Engineering Graduate Research Symposium (FEGRS 2025), University of Alberta, (August 2025).

3. Z. Moghtader Gilvaei, **A. Mirzazade Akbarpoor**, M. Salimi, M. Shahbakhti, A. Nouri, Thermal Disinfection of HVAC Filters Using Radiant Ceramic Heaters, Faculty of Engineering Graduate Research Symposium (FEGRS 2025), University of Alberta, (August 2025).